UNIVERSIDADE FEDERAL DE SANTA CATARINA
CENTRO TECNOLÓGICO
PROGRAMA DE PÓS-GRADUAÇÃO EM ENGENHARIA ELÉTRICA

Manfred Georg Kratzenberg

OTIMIZAÇÃO MULTIDIMENSIONAL DE CÉLULAS SOLARES DO TIPO PEROVSKITA

Florianópolis
2020

Manfred Georg Kratzenberg

MULTIDIMENSIONAL OPTIMIZATION OF PEROVSKITE-TYPE SOLAR CELLS

Tese submetida ao Programa de Pós-Graduação em Engenharia Elétrica da Universidade Federal de Santa Catarina para a obtenção do título de doutor em Engenharia Elétrica e Eleetronica
Orientador: Prof. Carlos Renato Rambo, Dr.

Florianópolis
2020

Ficha de identificação da obra elaborada pelo autor,
através do Programa de Geração Automática da Biblioteca Universitária da UFSC.

Kratzenberg, Manfred Georg
OTIMIZAÇÃO MULTIDIMENSIONAL DE CÉLULAS SOLARES DO TIPO PEROVSKITA / Manfred Georg Kratzenberg ; orientador, Carlos Renato Rambo, 2020.
215 p.

Tese (doutorado) - Universidade Federal de Santa Catarina, , Programa de Pós-Graduação em Engenharia Elétrica, Florianópolis, 2020.

Inclui referências.

1. Engenharia Elétrica. 2. Célula solar perovskita. 3. Modelo analítico de eficiência. 4. Otimização Numérica Multidimensional. I. Rambo, Carlos Renato. II. Universidade Federal de Santa Catarina. Programa de Pós Graduação em Engenharia Elétrica. III. Título.

Manfred Georg Kratzenberg

MULTIDIMENSIONAL OPTIMIZATION OF PEROVSKITE-TYPE SOLAR CELLS

O presente trabalho em nível de doutorado foi avaliado e aprovado por banca examinadora composta pelos seguintes membros:

Profª. Izete Zanesco, Drª.
Pontifícia Universidade Católica do Rio Grande do Sul

Prof. Ivan Helmuth Bechtold, Dr.
Universidade Federal de Santa Catarina

Prof. Roberto Francisco Coelho, Dr.
Universidade Federal de Santa Catarina

Certificamos que esta é a **versão original e final** do trabalho de conclusão que foi julgado adequado para obtenção do título de doutor em Engenharia Elétriaca.

Bartolomeu Ferreira Uchoa Filho:47636211491
Assinado de forma digital por Bartolomeu Ferreira Uchoa Filho:47636211491
Dados: 2020.06.05 11:29:44 -03'00'

Prof. Bartolomeu Ferreira Uchôa-Filho, Dr.
Coordenador do Programa

Documento assinado digitalmente
Carlos Renato Rambo
Data: 04/06/2020 17:40:02-0300
CPF: 134.748.198-28

Prof. Carlos Renato Rambo, Dr.
Orientador

Florianópolis, 2020.

Este trabalho é dedicado aos meus colegas e professores do LAMATE, da FOTOVOLTAICA, da pós-graduação do PPGEEL, e aos meus queridos membros de família na Alemanha e no Brasil, e principalmente, às gerações futuros, que se devem confrontar cada vez mais com os efeitos de mudança climática em decorrencia ao aquecemento global.

AGRADECIMENTOS

Gostaria de agradecer a todos aqueles que contribuíram diretamente e indiretamente na minha tese e formação, especialmente, a minha amada esposa Maria Terezinha de Souza e os meus queridos entes familiares no Brasil e na Alemanha, pelo apoio e singular paciência. Agradeço o meu orientador, professor Carlos Renato Rambo, pelo apoio com discussões relacionados à modelagem das células solares, que contribuíram na viabilização dessa tese. O seu conhecimento e a sua experiência na área química e física de materiais elétricos foram elementos-chaves para avançar na matéria estudada. Prezo pela sua experiência, seu caráter e sua amizade, sendo essas características, essenciais na finalização das etapas demandadas.

Também agradeço a CAPES pela bolsa fornecida durante meu doutorado e aos professores do Programa de Pós-graduação em Engenharia Elétrica (PPGEEL) da Universidade Federal de Santa Catarina (UFSC), pelos conhecimentos transmitidos. Quero deixar um agradecimento especial aos colegas do PPGEEL, pelo: apoio e troca de ideias e conhecimentos em relação ao uso das ferramentas computacionais e modelagem. Agradeço-os pela alegria e o bom humor, proporcionando assim, um ambiente amigável e descontraído.

Fico grato pelo pela colaboração dos alunos do laboratório LAMATE, especialmente o Rafael Bomaro Ferreira e o Fernado Wruck em relação a minha coorientação em dois trabalhos, um orientado e outro de conclusão de curso. Agradeço aos alunos do grupo de pesquisa FOTOVOLTAICA da UFSC, em especial ao professor Ricardo Rüther e aos alunos desse laboratório, pela colaboração no projeto da ANEEL de sistema fotovoltaico interligado a rede de eletricidade utilizando bateria. Também agradeço a sociedade brasileira e o seu sistema de educação superior, assim como o curso PPGEEL por ter viabilizado meus estudos nas áreas de engenharia elétrica e de células solares. Agradeço, aos pesquisadores da área perovskita que conseguiram em pouco tempo proporcionar uma ampla base de conhecimento, modelagem e simulações, que resultaram num crescimento exponencial de publicações desde a descoberta dessa célula em 2009. Por fim, agradeço aos revisores das revistas científicas e aos professores das minhas bancas de qualificação e de defesa da tese pelas suas contribuições com as revisões e sugestões de melhorias.

We have this handy fusion reactor in the sky called the sun. You don't have to do anything. It just works. It shows up every day and produces ridiculous amounts of power.

Elon Musk, CEO of Tesla Motors, and SpaceX, 2015

RESUMO

Os pesquisadores na área de desenvolvimento de células solares fotovoltaicos devem ter o conhecimento teórico que indica quais ideais propriedades uma célula solar deve apresentar, sendo que estes resultem na sua máxima possível eficiência. Tal conhecimento orienta no aperfeiçoamento de cada uma das propriedades, a partir do uso de apropriados (i) materiais e (ii) processos de manipulação na fabricação das células. Nesse sentido (i) o objetivo intermediário é de aperfeiçoar cada uma das propriedades consideradas de material, sendo (ii) o objetivo final de obter um aumento significante da eficiência da célula, a partir do melhoramento multidimensional das propriedades numa célula fabricada. A informação sobre as propriedades ideais pode ser obtida por meio da simulação do modelo matemático de uma célula solar, e especialmente sob otimização numérica desse modelo em espaço multidimensional das suas propriedades. Apresentamos a otimização multidimensional da eficiência usando um modelo analítico de uma célula solar perovskita, do tipo pin e analisamos diferentes desenhos de aperfeiçoamento da célula. A partir de uma análise de sensibilidade mostramos que a eficiência é função de diferentes propriedades configuradas de material, e também da espessura da camada de absorção dessa célula. A presente otimização numérica melhora a eficiência dessa célula do valor inicial de 15,7% para o valor máximo de 27.8%, considerando-se a sensitividade de sete variáveis num espaço de nove dimensões analisadas pelo algoritmo. Propomos diferentes desenhos de célula que analisamos em detalhe para obter um maior conhecimento sobre o processo de otimização. Sob o uso de armadilhas de luz na camada absorção a espessura dessa camada pode ser reduzida de 400 nm para 160 nm, perdendo apenas 0.2% de eficiência. Essa configuração resulta em uma redução significante da camada de absorção e assim do uso de Pb. A partir de análises de sensitividade da célula otimizada, mostramos o melhoramento mínimo necessário para cada propriedade, e a partir de uma análise combinatória das propriedades ideais, propomos uma sequencial ideal de inclusão de variáveis para o seu aprimoramento.

Palavras-chave: Célula solar perovskita. Modelo analítico de eficiência. Otimização Numérica Multidimensional.

RESUMO EXPANDIDO

Introdução

A otimização de células solares é realizada no estado da arte em função de uma ou duas variáveis por vez, tanto nos modelos de simulação, como também em células fabricadas, já que o resultado de tais otimizações é facilmente acompanhável, plotando a eficiência em função dessas variáveis em um gráfico. No entanto, a partir do modelo que simula os processos de deriva e difusão de elétrons e lacunas, sabe-se que a eficiência de uma célula solar é função de múltiplas propriedades de material. A partir da inerente aleatoriedade do processo de otimização no espaço uni- ou bidimensional, obtém se teoricamente um tempo de otimização infinito para se otimizar uma célula solar. Por exemplo, no caso das células de silício monocristalino esse processo pode demorar várias décadas (NREL, 2020). Tal morosidade existe também, porque o melhoramento de uma das propriedades, pode ser parcial ou plenamente compensada a partir da decadência de uma, ou das demais propriedades não analisadas. De forma adicional, os melhoramentos em baixa dimensionalidade não mostram o aumento da eficiência a partir da característica da não linearidade em espaço multidimensional. Essa não linearidade resulta em um efeito sinergético do aumento da eficiência, que apenas aparece na otimização em espaço multidimensional como mostrado nessa tese. A partir da modelagem matemática do modelo de deriva e difusão de elétrons e lacunas poder-se-ia prever um aumento da eficiência sob consideradas propriedades ideais de material. No entanto, não sabendo as propriedades ideais, os métodos de análise uni- e bidimensionais presentemente usados na avaliação dessas simulações não conferem a modelagem multidimensional. Desta forma serão também necessárias infinitas simulações para obter a máxima eficiência da célula. Portanto, para conhecer-se melhor uma célula solar, principalmente no que tange à otimização da sua eficiência, são necessários métodos de otimização multidimensionais, sob uso de restrições do espaço de variáveis. Estes métodos resultam na configuração ótima de propriedades de material para dadas restrições de faixa das variáveis envolvidas, viabilizando assim a extração de um maior conhecimento sobre a célula e em especial a sua otimização.

Objetivos

A multidimensionalidade das propriedades de material inviabiliza uma análise mais profunda de uma célula solar, sob métodos convencionais de plotagem gráfica. Sendo assim, as pesquisas no estado da arte não analisam uma célula solar de forma adequada e resulta assim em um longo tempo para otimizar a sua eficiência de forma que se aproxima ao valor teórico máximo. O objetivo desse trabalho de tese é de propor um novo método multidimensional utilizado para obter um maior conhecimento sobre a otimização da célula solar perovskita. O proposto método resulta, a partir da variação das restrições das variáveis da otimização, em vários desenhos otimizados da célula, cuja análise comparativa resulta no maior conhecimento sobre a maximização da eficiência da célula perovskita. Propomos métodos de fabricação de células solares a partir de uma resenha, para obter-se um melhoramento das variáveis no sentido como foi obtido pela otimização multidimensional. O conhecimento adquirido também envolve uma metodologia, elaborada a partir de uma análise de sensibilidade e de uma análise combinatória de variáveis envolvidas, que resulta em

recomendações para o pesquisador que fabrica células, mostrando em qual ideal sequencia de inclusão de variáveis se deve melhorar as propriedades para obter-se um maior aumento da eficiência da célula. Os resultados podem ser usado na otimização da eficiência de células fabricadas, já que indicam ao pesquisador quais propriedades apresentam uma maior sensitividade, e portanto, devem ser melhoradas em primeiro lugar.

Metodologia

Partimos do modelo de deriva e difusão de elétrons e lacunas, e usamos também um método numérico multidimensional de otimização. Usamos um modelo analítico da célula perovskita, que foi derivado do modelo de deriva e difusão em (SUN; ASADPOUR; NIE; MOHITE et al., 2015). Sendo analítico, esse tem a vantagem de apresentar um reduzido tempo de processamento computacional na simulação dos pontos da curva J-V, ou seja, a curva da densidade de corrente em função da tensão de terminal. Configuramos o algoritmo de otimização multidimensional para repetir muitas otimizações, cada uma sob diferentes restrições das propriedades de material e da camada de absorção da célula perovskita. Essas diferentes configurações resultam em diferentes desenhos da célula que apresentam diferentes eficiências otimizadas, embasados em diferentes propriedades de material em espaço multidimensional. A análise comparativa dos parâmetros de desempenho destes desenhos resulta em um maior conhecimento sobre a célula analisada, e especialmente sobre a sua otimização. Revisamos os métodos de manipulação das propriedades de material de uma célula perovskita para o fim do melhoramento da eficiência. Usamos o modelo analítico de uma célula perovskita, derivados da modelagem da deriva e difusão de elétrons e lacunas, e realizamos uma análise de sensitividade uni- e bidimensional das propriedades de material, para validar o potencial de sucesso com métodos tradicionais de otimização. Usamos um algoritmo de otimização multidimensional que inclua o uso de restrições de faixa individualizada no espaço multidimensional de propriedades de material para otimizar a eficiência do modelo analítico da célula. Sob a modificação das restrições individualizadas no espaço multidimensional das propriedades de material, propomos diferentes desenhos futuros da célula, mostrando o aumento da eficiência a partir do melhoramento das propriedades de material. Mostramos também diferentes desenhos com eficiências iguais, baseados em propriedades variadas, especialmente a partir das armadilhas de luz inseridas na camada de absorção. Extraímos detalhes importantes desses desenhos hipotéticos, que resulta no maior conhecimento sobre a célula e especialmente sob a sua otimização. Por exemplo, registramos um aumento da tensão em circuito aberto e no ponto máximo de potência, que permite reduzir a espessura da camada de absorção da célula para 160 nm, limitando assim a perda de eficiência para 0,2% em comparação com uma camada de 400 nm. Análises de sensitividade mostram a importância de cada uma das variáveis para sustentar uma alta eficiência otimizada. Uma análise combinatória de (i) variáveis ideais, e (ii) não ideais, onde as primeiras foram obtidas da melhor celula modelada, e as últimas de uma célula medida resulta em uma ideal sequência na inclusão dessas variáveis na otimização de células fabricadas. Nessa otimização são sucessivamente incluídas aquelas variáveis que apresentam a maior sensitividade. O método sugere um ideal roteiro para implementar melhoramentos nas (i) propriedades de material da célula, e (ii) na espessura de sua camada de absorção.

Resultados e discussões

Sob o uso de um assumido alto fator de melhoramento das propriedades de f_B = 160, a eficiência da célula analisada, de 15,7%, pode ser aumentada sob uso de diferentes métodos para se atingir a eficiência do estado da arte de 24,2% (25.2% em 2020). Por exemplo, tal aumento pode ser obtido sob (i) melhoramento das propriedades de material, em combinação com o uso de armadilhas de luz, sendo essas armadilhas nanopartículas plasmônicas inseridas na camada de absorção da célula. (ii) Em outra configuração tal aumento de eficiência é obtido apenas sob o melhoramento das propriedades de matérias. No segundo caso há maior exigência em relação ao fator melhoramento das propriedades de material (f_B). Na configuração (i) pode se obter o maior aumento da eficiência com o valor máximo de 27,8% para f_B = 160 em uma célula com camada de absorção de 400 nm. Se a camada de absorção é reduzida para 160 nm obtivemos apenas 0,2% de perda de eficiência que cai para 27,6%, já que há um aumento da tensão no ponto da máxima eficiência nessa configuração de camada de espessura menor. Mostramos que o melhoramento multidimensional das propriedades de material da célula apresenta uma grande vantagem no incremento da eficiência da célula perovskita se comparado com o melhoramento das propriedades em uma ou duas dimensões. Esta vantagem é evidente a partir da comparação de dois diferentes casos. No primeiro considera-se o somatório dos aumentos de eficiência por melhoramento unidimensional de propriedade. Esse somatório resulta num aumento de apenas 4,5%. No segundo caso considera se um melhoramento das propriedades na mesma magnitude, mas na forma multidimensional, e este caso resulta no aumento da eficiência de 11,9%, ou seja, a eficiência aumenta de 15.7% para 27,6%. Identificamos que a diferença desses dois casos decorre a partir das não linearidades no modelo da deriva e difusão de elétrons e lacunas. Como resultado recomendamos fortemente a introdução e a adoção de um protocolo de otimização, que considera melhoramentos multidimensionais das propriedades na pesquisa relacionada a otimização de células fabricadas. Evidentemente tal protocolo irá também melhorar a otimização de outras células solares. O protocolo deve incluir a medição e o melhoramento multidimensional das propriedades de material. A partir de análises de sensitividade nos verificamos a importância de cada uma das variáveis na obtenção da máxima eficiência. Chegamos a conclusão que uma sintonização adequada deve priorizar o mantimento da relação entre a espessura da camada de absorção (t_0) e o comprimento do decaimento ótico médio (λ_{ave}) para assegurar o valor máximo de uma célula otimizada. As duas variáveis formam um vértice, que resulta em pontos de máxima eficiência, tanto numa célula otimizada como em uma célula não otimizada. O método combinatório de melhoramento de variáveis mostra que a redução das velocidades de recombinação de elétrons (s_f) e lacunas (s_b) resulta no maior aumento da eficiência de uma célula não otimizada. Valores ideais dessas variáveis resultam em um aumento da eficiência por 2,37% e 1,94%, respectivamente. Uma vez tendo melhorados essas variáveis a tensão inerente (V_{bi}) resulta num aumento ainda maior de 3,03%. Além disso, as variáveis de coeficiente de difusão de elétron (D_n), e de lacunas (D_p) são também de alta importância nessa mesma sequência de prioridade. Os valores otimizados dessas variáveis resultam num aumento adicional da eficiência de 1,17% e 1,75%, respectivamente.

Considerações Finais

Métodos de otimização multidimensional devem ser usados com maior vigor nas pesquisas relacionadas ao aumento da eficiência de células solares. Estes viabilizam a extração de conhecimento adicional relacionado a esse processo, a qual não pode ser obtido com outros métodos. O objetivo é obter protocolos úteis na fabricação de células solares em laboratório, ou em escala industrial, que encurtam consideravelmente o seu tempo de desenvolvimento. Será interessante experimentar a utilidade deste método em outros dispositivos, como células de múltiplas junções, baterias, supercapacitores, por exemplo. Uma vez tendo um modelo matemático do dispositivo disponível, pode se usar outras funções objetivas, como por exemplo, a capacidade de carga de uma bateria, ou um supercapacitor. Principalmente nos dias de hoje, em que há uma rápida transição para novas tecnologias limpas de energia, métodos de adequação mais velozes dos dispositivos considerados, acrescenta grande valor nessa transição.

Palavras-chave: Célula solar perovskita. Modelo analítico de eficiência. Otimização Numérica Multidimensional.

ABSTRACT

To obtain significant improvements in the Power Conversion Efficiency (PCE) of solar cells, researchers should know which material properties and cell design constitute cells with the highest possible cell efficiency. Such knowledge can orient in the improvement of each of the cell's material properties, and in the selection of appropriate manufacturing methods to improve these material properties obtaining a higher PCE. We postulate that such knowledge is obtainable by simulation and numerical optimization of the cell's PCE, which we present for the considered pin-type Perovskite Solar Cell (PSC) in a multidimensional variable space. Our analyses and review show and compare, which material properties lead to the highest cell efficiency. By utilization of a sensibility analysis, which uses the analytical model of the pin-type PSC, we show that its efficiency is a nonlinear function of several material properties and the absorber layer thickness in a multidimensional function space of variables. The presented numerical optimizations improve the PSC's efficiency from an initial 15.7% up to 27.8%. We consider variable improvements at different scales in a nine-dimensional hypercube space of cell properties and the absorber layer thickness. We thus show the high development potential of this solar cell. We present the combined variable specification necessary to obtain such high efficiency, and we found that seven of the nine analyzed variables show efficiency sensitivity. We also preset further model optimizations that consider limited variable improvements and lead to a lower PCE, which leads to additional knowledge concerning the optimization of the cell with and without light trapping for different absorber layer thicknesses and improvement scales. We found that the Pb content of the optimized PSC can be reduced significantly with a small PCE loss of only 0.2% if light trapping is used in thin absorber layers. Our sensitivity analyses show the minimal necessary variable improvement for each of the considered variables, and our presented combinatorial approach validates 91 possible variable combinations, suggesting an ideal sequence of variable tunings.

Keywords: Perovskite Solar Cell. Analytic solar cell model. Multidimensional Numerical Efficiency Optimization.

LIST OF FIGURES

LIST OF TABLES

LIST OF ACRONYMS

ANEEL	Agência Nancional de Energia Elétrica
a-Si	Amorphous solar cells
CAPES	Coordenação de Aperfeiçoamento de Pessoal de Nível Superior
CdTe	Cadmium telluride solar cells
CIGS	Copper Indium Selen solar cells
FAPI	Formamidinium lead iodide absorber layer
FDTD	Finite Difference Time Domain modeling
IPM	Interior Point Search Method
KKT	Karush-Kuhn-Tucker conditions
LAMATE	Laboratório de Materiais Elétricos – UFSC
LCOE	Levelized Cost of Electric Energy
LIB	Lithium-ion battery
LP	Linear programming techniques
LSM	Line Search Method
MPP	Maximum Power Point
MAPI	Methylammonium lead triiodide PSC absorber layer
NLP	Nonlinear Programming
NP	Nanoparticles
OTM	Optical Transfer Matrix method
OPV	Organic photovoltaic cells
PCE	Power Conversion Efficiency
PPGEEL	Programa de Pós-graduação em Engenharia Elétrica
PSC	Perovskite Solar Cell
PV	Photovoltaic
RAM	Random Access Memory
SBPMAT	Sociedade Brasileira de Pesquisa em Materiais
SSE	Solvent-Solvent Extraction method
SRV	Surface recombination velocity
SUV	Sport utility vehicle
UFSC	Universidade Federal de Santa Catarina

LIST OF CHEMICAL SYMBOLS

ABX_3	General molecular expression of perovskite materials (A large cation, B small cation, X halide series anion)
Ag	Silver
AM 1.5	Air Mass = 1.5
Cs	Cesium
CH_3NH_3	Methylammonium organic cation
$CH_3NH_3PbI_3$	Methylammonium lead triiodide PSC absorber (MAPI)
$CH(NH_2)_2PbI_3$	Formamidinium lead triiodide absorber layer (FAPI)
$CH_3NH_3PbI_{3x}Cl_x$	Methylammonium lead iodide-chloride PSC absorber
$FAPbI_3$	Formamidinium lead triiodide absorber layer (FAPI)
$(MA,FA,Cs)PbI_3$	Triple cation absorber layer
$MAPbBr_3$	Methylammonium lead bromide absorber layer
$MAPbBr_{3-x}Cl_x$	Methylammonium lead bromide-chloride absorber layer
$MAPbCl_3$	Methylammonium lead trichloride PSC absorber
$MAPbI_3$	Methylammonium lead triiodide PSC absorber (MAPI)
$MAPbI_{3x}Cl_x$	Methylammonium lead triodide-chloride absorber layer
$CH_3(NH_2)_2^+$	Formamidinium organic cation.

LIST OF SYMBOLS

A	Substitution parameter of the photocurrent density [-]
B	Substitution parameter of the photocurrent density [-]
D_n	Diffusion coefficient of electrons [cm²/s]
D_p	Diffusion coefficient of holes [cm²/s]
E	Built-in electrical field [V/m]
E_g	Effective band gap energy [eV]
f_B	Boundary-expansion or variable-improvement factor [-]
$f_{B\text{-}max}$	Maximal boundary amplification factor [-]
$G_{AM1.5}$	Solar irradiance with air mass 1.5 [mW/cm^2]
$G(x)$	Generation rate of charges as a function of x [$s^{-1}cm^{-3}$]
G_{eff}	Effective charge carrier generation [$s^{-1}cm^{-3}$]
G_{max}	Maximum or total charge carrier generation [$s^{-1}m^{-2}$]
J_b	Electron recombination current density of the backside charge conduction layer at $x = t_0$ [mA/cm²]
J_{dark}	Measurable current density in the dark [mA/cm²]
J_f	Electron recombination current density of the frontside charge conduction layer at $x = 0$ [mA/cm²]
J_{light}	The measurable current density under light exposure [mA/cm²]
$J_{MPP,i}$	Maximum power point current density [mA/cm²]
J_n	Electron current density at the backside charge conduction layer [mA/cm²]
J_p	Hole current density at the frontside charge conduction layer [mA/cm²]
J_{sc}	Short circuit current density [mA/cm²]
m	Factor which relates t_0 and λ_{ave} in the Beer-Lambert law [-]
P_{MPP}	Maximum power point power density [mW/cm^2]
k_B	Boltzmann constant $1.38064852 \times 10^{-23}$ [J/K]
q	Electric charge of an electron or hole [mAs]
s_b	Surface recombination velocity of holes (s_p) [cm/s]

s_f	Surface recombination velocity of electrons (s_n) [cm/s]
T	Cell temperature [K]
t_0	Absorber layer thickness [nm]
$t_{0\text{-}min}$	Minimum absorber layer thickness [nm]
V	Terminal voltage of the solar cell [V]
V_{bi}	Built-in voltage [V]
V_{MPP}	Maximum power point voltage [V]
V_{oc}	Open-circuit voltage [V]
$x = 0 \ldots t_0$	Solar irradiance penetration depth [m]
$X_j = X_1 \ldots X_9$	X_j is one of the nine model variables of the PSC model
$X_{j,me}$	A model variable extracted from the measured J-V curve, X_j, is one of the nine model variables of the PSC model
$X_{j\text{-}min} \ldots X_{j,max}$	Maximal variable-expansion range for the variable j

Greek symbols

α_b	Back recombination current density scaling coefficient [-]
α_f	Front recombination current density scaling coefficient [-]
Δn	Excess minority carrier concentration of electrons [cm^{-3}]
Δp	Excess minority carrier concentration of holes [cm^{-3}]
$\Delta\phi_{bi}$	Built-in potential ($q\ V_{bi}$) [mJ/cm^2]
η_i	Optimized PCE for the i-th optimization iteration [%]
η_{max}	Optimized efficiency value [%]
λ	Wavelength of the solar irradiance [nm]
λ_{ave}	Average optical decay length [nm]
μ_n	Drift coefficient or mobility of electrons [$cm^2V^{-1}s^{-1}$]
μ_p	Drift coefficient or mobility of holes [$cm^2V^{-1}s^{-1}$]
ρ	Density of charge carriers [m^{-3}]

Indices

$i = 1 \ldots N$	Iterations in the optimization of the efficiency
$j = 1...9$	Index, which counts the nine variables
$k = 1...M$	Iterations in the optimization of the power curve
$f_B = 1 \ldots f_{Bmax}$	Boundary amplification factor

TABLE OF CONTENTS

1. INTRODUCTION

Climate change is the 800-pound gorilla 27 in the living room that the media dances around. But in the scientific community, it's a settled question: 95 percent of scientists believe this is happening with 100 percent confidence temperatures are rising. With 90 percent confidence, we believe it's human activity and not natural cycles that is driving the increase in temperature on the Earth.

Michio Kaku, Physicist, 23. February 2014

Solar energy is the only ready-to-mass-deployable resource that is both: (i) large enough and (ii) acceptable enough to be exploited in a long term time frame as discussed in (PEREZ; ZWEIBEL; HOFF, 2011) and (PEREZ; PEREZ, 2009). The authors validate this affirmation comparing the recoverable energy from finite and renewable energy global energy reserves. They estimate the total recoverable energy potential, in the unit of [TW years], as related to (i) finite sources (Coal, 900; Uranium, 90…300; Petroleum, 240; and Natural Gas, 215) and renewable energy sources (ex. Solar 23000; Wind, 25…70; Hydropower 3…4), estimated on an annual generation base. It comes to attention that the potential of solely the solar energy resources on a yearly base is much higher than the sum of the finite energy resources. If compared to the estimated total energy consumption on a global level in 2050, which is 28 TWyears, especially the yearly available solar energy potential of 2300 TWyears is large. Therefore, considering the exploitation of only a tiny fraction of this available solar energy resource could meet the demand with a nearly infinite room of growth.

The cost of a photovoltaic system is constituted by the expenditures of (i) the photovoltaic generator and (ii) the balance of the system (BOS), where the latter encompasses all system components excluding the photovoltaic modules. The BOS of a grid-connected system is typically constituted by the costs of the (i) inverter, (ii) electric metering unit, (iii) the cabling, and (iv) the mounting system of the photovoltaic (PV) modules. While the BOS costs showed a continuous decrease, recently, in 2014, the costs of the solar generator of a PV system showed to be lower than the BOS (LOUWEN; VAN SARK, 2020). However, presently the PV generator is still the system component with the highest cost. Therefore, it is expected that the future commercially available PV – modules, as based on the third generation perovskite solar cell technology for the conversion of solar energy, enables large-scale electric energy production at still lower manufacturing costs (CAI; WU; CHEN; YANG

et al., 2017). A consideration which implies some future developments as discussed in the reference section.

Third-generation solar cells are conceived for extra thin and flexible coatings, which can be coated with simple ink deposition methods. The first conceived third-generation solar cells were dye-sensitized and organic solar cells, which are already used in building integrated photovoltaic (BIPV) systems creating attractive design elements, as shown in (SHUKLA; SUDHAKAR; BAREDAR, 2016) and (MORITZ, 2019). PSCs are third-generation solar cells that present the highest state-of-the-art efficiency, and they are classified as hybrid cells, being constituted of an absorber layer made of organic and inorganic materials. As detailed in section 2.4, page 45, the Methylammonium ($CH_3NH_3PbX_3$), is presently the most analyzed PSC cell type, but recent work also analyzed Formamidinium ($CH_3(NH_2)_2PbX_3$) cell types, because of its higher absorption behaviors. Furthermore, the introduction of Cesium in a ($Cs_{0.17}FA_{0.83}Pb(Br_{0.17}I_{0.83})$) cell type results in higher long term stabilities and efficiencies. The substitution of the X_3 term with the halides (I_3^-), (Br_3^-), and (Cl_3^-) provides an adjustable bandgap, a characteristic which is essential in the development of PSC-based multiple junction solar cells.

State-of-the-art research related to the efficiency increase of PSCs focuses on cell prototyping, in which authors try to optimize solar cells by reasoning and hypothesis testing of inherent physical principles. In this context, efficiency increases are typically shown as a function of the improvement of one- or two variables. Such one and two-dimensional optimizations are adopted since the efficiency, in such a restricted variable space, can be optimized by the simple two- and three-dimensional plots, which show the PCE values as a function of these variables.

However, the benefits of analytical or numerical models, as derived from a solar cell's drift-diffusion equations, can give more useful information. In using such models, the cell's current density – voltage (J-V) curve can be simulated as a function of multiple material properties. Therefore, we assumed that it is especially useful if the whole set of material properties is improved rather than only one or two properties, a behavior that we analyzed in this thesis. Our objective is to provide more knowledge and insights about the optimization process of perovskite solar cells and propose high-efficiency low-cost designs for future PSC developments. Additionally, we suggest several high-efficiency designs, as obtained by light trapping in combination with absorber layer thickness reductions, and we discuss how the

PCE of state-of-the-art cells can be increased by different methods. To access this knowledge and design proposals, we postulate a multidimensional numerical optimization of a solar cell's drift-diffusion model, and our analyses of the optimized solar cell results to a comprehensive, in-depth understanding of the optimization of a PSC.

Having a multidimensional mathematical model at hand, it is of fundamental importance to answer the following questions to obtain the highest possible cell efficiency: (i) which model variables or material properties should be concomitantly improved, to achieve the highest efficiency values, (ii) should the value of the considered variables be increased or decreased, (iii) to which specific value each one of these model variables has to be improved, (iv) which one of the taken variables account for the most significant PCE increase. Our research focus is to provide answers to these research questions providing knowledge to accelerate the future development of perovskite solar cells. The general concept of our research, simulations, and optimization can be transferred straightforwardly to further solar cell types.

1.1 HYPOTHESIS

We validate the following hypothesis: The multidimensional optimization of the perovskite solar cell model, using as optimization variables (i) the cell's material properties, and (ii) its absorber layer thickness, results in a much higher efficiency increase, in comparison to any of the possible one- and tow-dimensional optimizations.

1.2 OBJECTIVES

To obtain significant increases in the optimization of solar cells, we argue in this thesis that the substitution of the state-of-the-art one- and two-dimensional cell optimizations, by the simultaneous improvement of multiple material properties, is novel and of substantial advantage. In this context, researchers should know, which combined material properties and cell design parameters result in the highest efficiency increase. For the same objective, it is also of importance to know which ideal relationships in-between these variables must be adjusted. Such knowledge becomes available by numerical optimizations and simulations, which we present for a Perovskite Solar Cell (PSC) in a hypercube space of model variables.

The main objectives of this work are:

- The optimization of the variables of an analytical model of a PSC by utilization of a multidimensional numerical optimization algorithm to obtain a significant increase in the cell's efficiency,
- Compare the results of the multidimensional efficiency optimization with the results of the state-of-the-art one and two-dimensional optimizations in analyzing any possible variable combinations in the latter case,
- The complete specification of the necessary material properties and the absorber layer thickness defined as a precondition so that cells with such an improved state-of-the-art efficiency can be manufactured, based on adequate material property improvements,
- Proposing several different PSC design concepts, which consider ideal and quasi-ideal material properties for different absorber layer thicknesses and short-circuit currents, as obtained by light trapping, in order to access new knowledge related to a PSC's optimization,
- Use sensitivity analyzes of the optimized PSC to show the minimal necessary material property improvement for each of the considered model variables to enable the maximum model efficiency,
- Providing detailed information to display, which combination of improved material properties, leads to the highest PCE increases, leading to a ranking of the most to the least efficiency-sensitive material properties,
- Analyzing why a multidimensional optimization is much more effective as in comparison to the one- and two-dimensional optimizations,
- Showing by a review, based on the obtained optimization results, how state-of-the-art manufacturing processes can manipulate material properties and the absorber layer thickness most effectively for high solar cell efficiencies.

2. BIBLIOGRAPHY REVIEW

When something is important enough, you do it even if the odds are not in your favor.

Elon Musk, CEO of Tesla Motors and Space X, 2017

We present a short general introduction to the perovskite solar cells highlighting especially the distinctive flexibility of this solar cell platform, which is unique in the concept that allows a continuous band gap tuning ability in single and multiple band gap cells. We review the advantage of perovskite solar cells, especially its low-cost concepts, as combined with high efficiencies, and a necessary low long-term degradation of its efficiency. Such characters will possibly enable the use of perovskite solar cells for the generation of electrical energy at a large-scale and extra low-cost. Especially the use of (i) low-cost materials, (ii) its low manufacturing cost, and (iii) its high efficiency in single and multiple junction cells will probably leave its mark in the future of the generation of electrical energy. A precondition for such a large impact is that its presently high long-term degradation must be reduced. We show that degradation mechanisms are still being discovered in PSCs. Again, the flexibility of this solar cell platform allows for several chemical modifications of the absorber material, leading in higher long-term stability, which is, in some cases, paired with high efficiencies. This large possibility of chemical manipulations enables a multitude of functions to be included in the platform, which allowed for each degradation mechanism an action, which counteracts the related effects. A future combination of these measures gives a positive outlook for a future PSC, which presents long term stability and a long lifespan.

We review the state-of-the-art modeling approaches, as used for the simulation of PSCs. Simplified models do only consider radiative recombination losses and are typically used to calculate the upper-efficiency limit of different perovskite solar cell types. More detailed simulation models also consider further recombination losses, which are usually related to the material properties of the perovskite solar cells. Such approaches are typically based on the drift-diffusion equations of electrons and holes. These multidimensional models are separated into two different groups: (i) the most used numerical simulation models, which can also be found in several simulation programs; and (ii) the analytical models, which considering some simplifications, and are based on an extensive derivation process involving the solution of five second-order differential equations (APPENDIX A.1, page 156).

A multidimensional model also needs a multidimensional approach to improve the cell's several material properties. We review multidimensional methods as used in the optimization of several technological devices, and introduce the here used optimization algorithm in Section 2.9, page 66. Once knowing the necessary material properties of a high-efficiency PSC, it is quintessential to understand how to improve these properties best to obtain values that are close to the optimized solar cell properties. Such methods of improvement we review in sections 2.10.2 to 2.10.8, page 72.

2.1 GENERAL SCOPE

Photovoltaic (PV) power plants based on the widely used silicon solar cells were already cost-competitive without subsidies in several countries seven years ago (BREYER; GERLACH, 2013), an affirmation, which is based principally on the calculus of the local cost of electric energy and the annual solar irradiance. Meanwhile, climate-change problems (Section 2.2, page 36) demand the large-scale implementation of non-CO_2 emitting power plants (EDENHOFER; PICHS-MADRUGA; SOKONA; SEYBOTH *et al.*, 2011), which stresses substantial investments because of the higher initial cost of photovoltaic power plants if compared to thermal power plants. E.g., considering the comparison of an arbitrary renewable power plant with a non-renewable coal or gas firing thermoelectric power plant, for the specific case that both plants do present a similar levelized cost of electric energy (LCOE), the renewable plant has a higher initial investment cost, but as it shows a nearly zero fuel consumption, it has depreciable operation costs.

The LCOE is a method, which allows the comparison of different power generation plants by the validation of a whole set of different expenses within the plant's lifetime, which are: (i) investment, (ii) interests, (iii) maintenance and (iv) fuel costs. The method levels these costs to the present date, which allows a direct comparison of the energy price of power plants that own different cost structures in investment and operation. Therefore, if (i) manufacturing cost reductions and (ii) higher efficiencies of photovoltaic modules may permit a significant further cost reduction in the generation of electrical energy, more utility PV generation plants can be implemented with the same investment, because of the reduced initial investment cost. The manufacturing cost is also an essential aspect as PSC solar cell technologies allow a printing alike coating of the cell's semiconductors at low temperatures and out of vacuum

conditions (RONG; HOU; HU; MEI *et al.*, 2017). A high solar cell efficiency is one of the essential issues to convert solar energy at low generation costs. This affirmation can be understood, as by doubling of the module efficiency, only half of the module area is necessary to generate a similar energy. In such a case, the costs related to following items reduce by approximately 50%, for the same project power: (i) the module encapsulation, (ii) the mounting rack and the installation material of modules, (iii) the workforce necessary for the installation of the solar panels, and finally (iv) the land use of the considered photovoltaic project.

2.1.1 The birth of photovoltaics and first-generation solar cell technologies

The photovoltaic effect was discovered by occasion during experiments made by the physicist Alexandre Edmond Becquerel in 1839 (PV-RESOURCES, 2015). Later in 1905, Albert Einstein laid out the most comprehensive theoretical work about the photoelectric effect (KLASSEN, 2011) and won the Nobel Prize for his work. Einstein provided, parallel to the wave theory of light, a quantum theory of the electromagnetic radiation, as based on the flux of photons (BARANOV, 2016) . In 1915 the chemist Jan Czochralski invented the process in which a large single crystal, called ingot, is grown slowly from a silicon melt. It took a long time until the first irradiance-proof solar cells were manufactured in 1958, from wafers, sawn from those ingots, which result in monocrystalline silicon solar cells. Those cells were used as independent photovoltaic power supplies for the first launched satellites. The first cells, as utilized in terrestrial applications, were initially produced from the same ingots, as used in the manufacturing process of microchip. The resulting bottlenecks of the waver supplies were later circumvented by the introduction of a silicon material especially provided for crystalline silicon solar cells. While this material contains somewhat higher impurities, if compared to microchip grade silicon, it has the advantage of a lower cost per unit weight. The bottleneck of the slow crystal-growing process was avoided by the casting of silicon in forms, which results in the multi-crystalline wafers. However, there are further bottlenecks in manufacturing. E.g.: (i) the monocrystalline and multi-crystalline ingots need several days to cool down to a temperature necessary for the additional manufacturing steps; (ii) the wavers have to be sawn from the ingots which need time; (iii) each small cell has to be subjected to several processes such as etching, doping, passivation, and the coating of its

electrodes; (iv) most of these processes have to be accomplished under vacuum conditions; (v) the cells have to be interconnected by the soldering of an electrical bus bar (GOODRICH; HACKE; WANG; SOPORI *et al.*, 2013; MCEVOY; CASTANER; MARKVART, 2012). While automatization can reduce the cost of these processes, it cannot reduce the time lag and the necessary energy as related to these processes, which increases the footprint of the manufacturing plant, and therefore, the related cost.

2.1.2 First, second and third-generation solar cell technologies

First-generation solar cells are monocrystalline and polycrystalline silicon solar cells, which were introduced historically as the first commercially available photovoltaic modules. Such cells are indirect band gap cells, needing, therefore, a momentum as provided by a phonon to convert a photon in free charge carriers. As a result, these cells need to have a considerable thickness of generally 200 μm to be able to absorb the sun's irradiance.

The later introduced second-generation solar cells, also called thin-film solar cells, such as (i) Copper Indium Gallium Selene (CIGS), (ii) Cadmium-Telluride (Cd-Te) and (iii) amorphous silicon solar cells (a-Si), use lower quantities of the necessary, highly purified materials, because of its thinner active layers. Therefore, it was initially expected that photovoltaic modules with cells made of these materials become available at a lower price per Watt peak. This character showed not up initially, principally because of its lower efficiency in comparison with crystalline silicon solar cells (GREEN, 2001). The third-generation solar cells, such as organic and perovskite solar cells are extra thin printable cells. Especially perovskite solar cells (PSCs) are of interest because of its high efficiency, and it is expected that future PV modules made of single-junction PSCs convert solar energy at the lowest costs (CAI; WU; CHEN; YANG *et al.*, 2017). This lower cost is associated to (i) its composition, using lower-cost materials; (ii) its lower material use, because of its extra thin absorber layers; (iii) a much lower coating temperature, which results in lower energy consumption, (iv) the out-of-vacuum manufacturing process; (v) a manufacturing process using low-cost printing and roll-to-roll methods; (vi) the high PCE of a single-junction PSC; and finally (viii) its band gap flexibility which enables a manufacturing of high efficiency multiple-junction solar cells.

2.1.3 Advantages of second-generation cell technologies

The time- and energy-demanding processes as necessary for the manufacturing of silicon photovoltaic modules are not required for the manufacturing of second-generation thin-film Cd-Te, CIGS and a-Si modules, as its layers are coatable in a conveyor belt assembly (MCEVOY; CASTANER; MARKVART, 2012). While these modules use semiconductor materials that are not as abundantly available as silicon, there are much thinner, resulting thus in lower material use. However, second-generation modules must still be coated under vacuum conditions and at relatively high temperatures, which increase the manufacturing's energy consumption and cost.

2.1.4 Advantages of third-generation cell technologies

The earliest third-generation organic photovoltaic cell (OPV) cell, with a reasonable efficiency of 1%, was conceived as a two-layer design by (TANG, 1986), apud (SUN; SARICIFTCI, 2017). Then, in 1991, Michael Grätzel created the first dye-sensitized solar cell (O'REGAN; GRÄTZEL, 1991), and in (KOJIMA; TESHIMA; SHIRAI; MIYASAKA, 2009), the first hybrid solar cells was discovered. In comparison to first- and second-generation modules, the manufacturing process of third-generation dye-sensitized, organic, and perovskite solar modules is more advantageous, as it involves (i) much lower process temperatures; and (ii) simple, low-cost manufacturing processes, such as printing processes (RONG; HOU; HU; MEI *et al.*, 2017). Furthermore, the third generation PSCs present recently also a higher state-of-the-art PCE that second-generation cells (NREL, 2020). The manufacturing of third-generation cell technologies needs less sophisticated machinery, as the coating of its layer can be accomplished by low-cost methods, i.e., under low temperatures, and ambient conditions, as known in the coating of inks. The extra thin films of such cells lead not only to low material use and cost but also present high adaptability of the resulting photovoltaic modules, which lead to its easy use in building-integrated photovoltaics (BIPV).

One of the first buildings, which use third-generation BIPVs is the Swiss Tech Convention Center, shown in (JACOBY, 2016), using dye-sensitized solar cells as manufactured by the company Solaronix. Furthermore, the color-rich surfaces as of printed organic cells on flexible membranes create new design possibilities of buildings and facades,

as shown in (ARCHITEKTUR; DER TECHNIK; LA ARQUITECTURA, 2017) and (MORITZ, 2019). Recently, the charge conduction layers of organic photovoltaic cells are made from fullerene-free materials, which present smaller molecule sizes. The use of such materials leads to both, (i) distinguished efficiencies up to 17 %, for a cell, in which both charge conduction layers are made of fullerene-free materials (ZHAN; LI; LAU; CUI *et al.*, 2020); and reasonable long-term stabilities of its efficiency, with an expected T_{80} lifetime[i] larger than 20 years (XU; XIAO; ZHANG; WEI *et al.*, 2020).

As a result, of its highest cell efficiency in-between the third-generation solar cells, the perovskite solar cells are most promising to be used in BIPV but also in photovoltaic power plants. Perovskite photovoltaic modules present the lowest energy amortization time, which is only 2…3 months if compared to further solar cell manufacturing technologies (GONG; DARLING; YOU, 2015). As the ambient moisture influences positively the crystallization process of the PSC's absorber layer, the manufacturing of PSCs has not to be accomplished under vacuum conditions, leading, therefore, to a pore-free absorber layer coating at low costs (RONG; HOU; HU; MEI *et al.*, 2017). After its deposition, the humidity of this layer is evaporated by a thermal annealing process. The PSC manufacturing is divided principally into two different techniques; (i) vapor phase techniques and (ii) solution-based methods, which are presented in (BRITTMAN; ADHYAKSA; GARNETT, 2015) and (ZHOU; YANG; WU; VASILIEV *et al.*, 2015). Highest efficiencies of 22.7% and 23.2% perovskite solar cells are obtained with the combination of different materials in a $(FAPbI_3)_{0.95}(MAPBr_3)_{0.05}$ PSC as shown in (JUNG; JEON; PARK; MOON *et al.*, 2019) and in (JEON; NA; JUNG; YANG *et al.*, 2018) while manufacturing methods of the state-of-the-art efficiency of 25.2% (NREL, 2020) is presently unknown. The former authors present a complete review and classification of the different manufacturing methods used for the fabrication of single-junction PSCs. Another advantage of thin-film third-generation PSC-junctions is that they are stackable, and its cell bandgaps are adjustable. This characteristic results in multijunction PSCs to extra high cell efficiencies.

2.2 OUTREACHING IMPACT

While electric energy generated from fossil fuels is conceived as to have a positive carbon dioxide balance effect, because of its related CO_2 emissions, renewable energy

generators based biofuels present a nearly neutral CO_2 balance effect, because of the sequestration of the atmosphere's CO_2 by the growing vegetation, used as biofuel. Systems which have a negative balance effect of CO_2 are most favorable in this comparison, as they can provide the electrical energy, which enables a reduction of CO_2 by its absorption in the earth's intact vegetation (BALDWIN, 2006). Systems with a negative balance effect are (i) wind turbines; (ii) photovoltaic systems; and (iii) solar thermal systems, such as power towers, parabolic trough, and dish-engine systems. Because of its thermal insulation property, the gas CO_2 is one of the responsible actors to maintain the earth's temperature about the temperature of space. However, the increase in the atmosphere's CO_2 content results in the so-named radiative forcing effect. The increased thermal insulation, as related to the higher CO_2 content, results in an increased blocking of the upward infrared radiation to space. As a result, the total upward energy flow is lower than the downward energy flow, being the latter defined by the incoming solar irradiance. Such a radiative imbalance, or forcing effect, results in the global warming of the atmosphere and the oceans, originating climate change, as discussed, e.g., in (BUTLER; MONTZKA, 2016). In-depth scientific evidence was first provided by NASA researcher Hansen (HANSEN; SATO; RUEDY, 1997), based on a global 3D-simulation of the earth's atmosphere and oceans, over several years. Consequently, in the past, the main argument for the substitution of the most polluting coal-fired power plants with renewable power plants was its contribution to the decrease in CO_2 emission.

However, the recent cost-competitiveness of renewable power plants, and its tendency to sinking generation costs, presently provides another argument for renewable power plants providing a lower-cost alternative of the generation of electric energy. Therefore, in the future (i) not only a reduction in the CO_2 emission but also (ii) a reduction of the total CO_2 content, as stored in the atmosphere, can e expected, because of the expected increase in the generation of electrical energy by renewable power plants. As an outcome not only (i) the non-renewable energy resources are conserved, avoiding, therefore, a future exposition to high energy prices, because of increased resource scarcity; but also (ii) electric energy can be converted at lower costs by renewable power plants, and as a complementary function; (iii) the risks and costs as related to climate change can be mitigated.

2.2.1 A proposal of a future with fully renewable energy generation

Solely the use of those renewable energy systems, which energy generation is related to wind-, water-, and solar energy sources (WWS), is expected to generate the energy for all sectors in a future scenario in 2050 (DELUCCHI; JACOBSON, 2011; JACOBSON; DELUCCHI, 2011), i.e. (i) electric energy generation, (ii) transportation, (iii) heating, (iv) cooling, and (v) industrial use. Such a configuration mitigates, therefore, the risks and costs related to (i) local pollution mainly generated by the transport sector, and (ii) CO_2 pollution, as associated with the current energy production and consumption. The authors estimate that the amount of wind plus solar energy available in likely developable locations exceeds the projected worldwide energy demand for all purposes in 2050 by more than an order of magnitude. Based on simulations with (i) different energy storage capacities in a 30 s interval; and (ii) a global 3D atmospheric circulation model, used to simulate the supply of renewable resources, (DELUCCHI; JACOBSON, 2011; JACOBSON; DELUCCHI, 2011) conclude that the main barriers for such a transition of a fully renewable energy generation matrix are primarily of social and political origin, but not of technological or economic nature.

As contrary to the concept that the firm energy of thermal and nuclear power plants can supply energy when renewable sources are not available, the concept of (JACOBSON; DELUCCHI, 2011) is based on several different energy storages inbound in a smart power grid. In their simulations, they use: (i) seasonal heat storage units, which provide district heat at costs less than 1 US dollar per kWh; (ii) insulated ice storage units for air condition systems of buildings; (iii) thermally insulated reservoirs of cold and warm water, for air conditioning systems of building complexes such as, e.g., universities; (vi) heat pumps for heating and cooling of rooms, and the production of warm water in residents; (v) demand response to control the heating and cooling of these systems, as well as further non-priority consumer equipment; (vi) hydrogen storage units; (viii) concentrated thermal solar power plants with low-cost rock heat storages, which enable the generation of electrical energy for nearly 24 hours per day; (ix) the storage capacities of pumped hydropower plants; and finally (x) the storage of conventional hydropower plants, where (a) the lower, and the upper limits of its storage unit, as well as, (b) its minimal dispatch to maintain the related river bed, have to be respected.

While the current LCOE of Nuclear power plants is 91...112 USD/MWh, coal power plants is 90...120 USD/MWh, and natural gas plants is 75...90 USD/MWh (CAI; WU; CHEN; YANG *et al.*, 2017), state-of-the-art utility PV power plants, already present a lower cost range of LCOE of ~ 42...75 USD/MWh (KOST; SHAMMUGAM; JÜLCH; NGUYEN *et al.*, 2018). A cost which should decrease additionally in the future, because of larger-scale manufacturing of silicon cells, and low-cost manufacturing of high efficiency photovoltaic technologies, such as perovskite solar cells. As discussed by the Stanford University Professor in one of its lectures (JACOBSON, 2018), on an economical line of thought the lower costs in the WWS scenario (DELUCCHI; JACOBSON, 2011; JACOBSON; DELUCCHI, 2011) are also associated to a 59% reduction of the global energy demand, as a result of (i) the avoidance of low-efficiency combustion processes, which results in a 23% reduction on average; (ii) the stopping of mining and transport of fossil fuels and uranium (13% reduction); (iii) the efficiency of heat pumps (16%); and general measures to improve the efficiency of electric energy use (7%).

The main reason for the exclusion of the Nuclear fission generators are (i) its risk related to power station accidents; (ii) the large half-time of the irradiation of nuclear waste; (iii) the large time from project to operation of nuclear power plants up to 20 years, and its uncertainty in social acceptance, which translates to an investment risk; and finally (iv) to avoid risks as related to nuclear weapon proliferation in a large scale. While the expected business costs of such a WWS energy supply are very similar in comparison to the cost of an energy supply using state-of-the-art power supply systems, because of the needed storage units, the social costs, related to the lower local air pollution and climate change effects, favorize the WWS supply presenting a 40% lower cost in comparison to the conventional energy supply (JACOBSON; DELUCCHI; CAMERON; FREW, 2015).

For such a solution, the electrical power grid must be validated, and its capacities must be actualized to some small extent. Energy transport, because of the variability in the generation, down to the range of some seconds, must be enabled. However, the cost of such an actualization should be relatively low because of the generation of large parts of the energy close to the consumer side, because of the distributed generation character of the renewable energy sources and especially the building-integrated PV systems. A further benefit of reduced energy transport is also obtained as, e.g., the photovoltaic conversion profile

coincides at a daily and seasonal base for most of the time with the demand of the cooling power, especially in tropical and subtropical areas.

Additionally, the renewable energy generation presents a generation complementarity at different time scales, from some seconds to the seasonal time scale. These complementarities are related (i) to different renewable power sources, as also installed in (ii) different locations, which present different supply profiles. The storage density of the commercially available graphite-based lithium-ion batteries (LIB) presents at the state-of-the-art 377 $mAhg^{-1}$; and, an increase in this capacity can be expected by further developments towards the theoretical maximum limit of 5268 $mAhg^{-1}$, for a LIB with a monolayer h-borophene anode (LI; TRITSARIS; ZHANG; SHI *et al.*, 2020). Such an increase will result in a further rise in the range of electric cars, which is already 603 km for the long-range sport utility vehicle (SUV) Tesla, Model S, which inclusively presents a front- and an extendable back-luggage space.

Because of such long ranges, the particular case that too many cars are needed to be charged at a unique charging point can be avoided charging vehicles mostly over-night at low current consumption and low effective energy prices. Even better, many charging stations can be installed close to high voltage transmission lines, at lower logistic costs as in comparison to gasoline fuel stations, which typically need a larger infrastructure, and need to be replenishment by tanker trucks. Supercharging units obligate the driver for a rest of 15 minutes, while a Tesla Model 3, e.g., is partly charged for a range of 277 km. Therefore, the recharge with electric charging stations can potentially lead to lower bottlenecks, for the same investment, and a securer transport, as in comparison to the refueling of the present vehicle fleet.

While in 2016 the LIBs presented half of the cost of an EV for personal transport, electric vehicles will become cost competitive in 2030…2035, as in comparison to conventional vehicles, because of its lower battery costs in the future, as evaluated in (KAPUSTIN; GRUSHEVENKO, 2020), based on different forecast models. Some of the mentioned refueling stations can be extended with hydrogen fuel for longer distance vehicles. Such an extended concept presents also low logistic and fuel-costs, as DR-generated hydrogen can be locally produced, being stored by electrolysis and hydrogen tanks, needing again, no replenishment with pipeline or tanker trucks.

2.2.2 The actual penetration of photovoltaic conversion in power grids

Presently the total conversion of the worldwide installed PV-systems does only cover a tiny fraction of 2% of the words consumption of electric energy (IRENA, 2019). While the PV conversion of solar energy showed a large increase in recent years, the 2 % generation is still low, considering that solely the annual increase of the electric energy consumption is 4% (IRENA, 2019). Furthermore, higher annual growth rates can be expected because of (i) the increased use of electric vehicles; (ii) the rapid improvement of living standards in developing countries and growing economies; and (iii) the global population growth.

However, the growth of the PV energy conversion is expected, as its energy is already cost-competitive in some countries if compared with the price of the consumption of electric power, attaining the so-called grid parity. These countries present (i) high energy prices and (ii) a sufficiently high enough annual average of the solar irradiance (KAMRAN; FAZAL; MUDASSAR; AHMED *et al.*, 2019). E.g., based on the LCOE calculations PV-systems in Germany, Australia, Italy, Denmark, and Spain have attained grid parity even before 2012, where its high costs of electric energy present the main reason for the cost competitiveness of solar energy. In Brazil, Turkey, France, and Japan, grid parity was attained since 2015. Even with the low generation cost as related to PV systems, the withdrawal of subsidies as introduced in some of these countries has resulted in a significant reduction of new PV-system installations. Therefore, even lower costs are interesting to scale up the production of solar energy systems.

2.2.3 The need for extra low-cost photovoltaic systems

If compared to wind power plants, photovoltaic power plants are the most promising resource for CO_2 reduction, as capacity targets are better archivable in most countries (AL IRSYAD; HALOG; NEPAL, 2019). Furthermore, solar energy costs have been fallen remarkably, and especially the investments in PV plants have low investment risks because of relatively simple resource assessment, social acceptability, and a short construction period. However, PV plants present a higher initial investment cost for the same generation of energy as in comparison to power plants with the use of fossil-fuel. Therefore, it is essential to develop with urgency extra low cost and high-efficiency solar cell technologies, as can

become available with optimized single- and multiple junction PSCs, if the long-term stability of its efficiency can be improved.

2.2.4 Cost of photovoltaic technologies

In the last 40 years, the cost per Watt peak of photovoltaic modules decreased ~ 300 times, resulting in a low current price of approximately US$ 0.25/W_p (THE FREEING ENERGY PROJECT, 2019) apud Bloomberg New Energy Finance. However, even with this low cost, the extensive conversion to electric energy, and its contribution to the reduction of climate gas emissions, is still not significant, as discussed in Section 2.2.2. As presented in (CAI; WU; CHEN; YANG *et al.*, 2017), the LCOE generated by systems based on crystalline silicon PV modules is in the range of 95…195 USD/MWh and is decreasing continuously. They show that the lower value of this range is already cost-competitive with the upper LCOE of (i) nuclear power, (ii) hydropower, and (iii) coal-fired power plants, and as a result grid parity is obtained in some countries. While the cost per watt peak of photovoltaic modules, made of multicrystalline silicon cells, is rapidly decreasing following the Swanson's law (KOBOS; ERICKSON; DRENNEN, 2006), this reduction appears to be still insufficient to explore the sun's energy in a significantly large scale, if compared to the global energy consumption (section 2.2.2). The Swanson's law defines by its so-called learning curve that every doubling of manufactured solar modules reduces the module price by approximately 20%.

If the fraction of the PV generation increases in a power grid, the cost of its injected energy will rise in the future because of the necessary adaptions, as required, to mitigate the related variability of its solar energy conversion as discussed in (HIRTH; UECKERDT; EDENHOFER, 2015). As a result, it will be more fruitful to use advanced low-cost manufacturing technologies in the future for a needed large-scale upscaling of the globally installed PV systems, keeping the total investment costs low. In this context, it is expected that breakthrough solar cell technologies, such as perovskite solar cells, lead in the future to the lowest-cost electric energy production at all, if compared to any further renewable or non-renewable energy technologies (CAI; WU; CHEN; YANG *et al.*, 2017). The low cost is obtained as its layers are coatable by low-cost roll-to-roll printing technologies, such as screen printing or gravature printing methods, where the latter already leads to efficiencies of 17.2%

(KIM; YANG; SUHONEN; VÄLIMÄKI *et al.*, 2019). Blade coating is another low-cost manufacturing method in the laboratory, which can be easily converted to the slot-dye coating process, as applicable in roll-to-roll manufacturing. The blade coating presents already a high PCE of 17.3% (YANG; LI; REESE; REID *et al.*, 2017).

As estimated in (CAI; WU; CHEN; YANG *et al.*, 2017), the lower and upper range of the LCOE of a PV-system, of 30 and 60 USD/MWh, based on modules with single-junction perovskite solar cells will be lower than the lowest LCOE of any other power plant. However, (CAI; WU; CHEN; YANG *et al.*, 2017) based its cost estimations on a T_{80} lifetime of 15 years, where T_{80} defines a 20 % PCE degradation in this lifetime under realistic operation conditions. Such a lifetime does presently not correspond to the state-of-the-art of perovskite solar cells. At present, tested PSCs under simulated realistic operation conditions in a climate chamber, show degradation of approximately 10 % per year, which results therefore in an expected T_{80} lifetime of only two years (TRESS; DOMANSKI; CARLSEN; AGARWALLA *et al.*, 2019). As a result, the PSC's degradation under realistic operation conditions must be decreased by the factor 7.5, before its converted energy presents a lower LCOE than the energy generated by any other power plant.

2.2.5 Long development times of solar cells

As many costs of a photovoltaic system are related to the area of the installed photovoltaic generator, the optimization of a solar cell's efficiency is one of the most valuable methods to decrease the costs of its converted energy. The essential character of single-junction solar cells is that its PCE is a function of multiple material properties, as defined by the models derived from its drift-diffusion equations. As a result, the fundamental nature of its efficiency optimization is that such a process needs presently a very long time, which takes in some cell types up to several decades until its optimized efficiency proximate to a cell's theoretical upper efficiency limit. E.g., it took more than 40 years to optimize monocrystalline silicon solar cells form a PCE of 13% to 26.1% (NREL, 2020). Such a long time is needed, as presently authors still optimize cells in the lower dimensional space, where solely one or two of the cell's material properties are improved at a time, ignoring, therefore, the improvement or the worsening of the remaining material properties. Because of the possible random

variation of the non-measured properties, such a process needs nearly infinite material optimizations to attain the cell's maximal possible efficiency.

Because of the required solutions for high-efficiency low-cost photovoltaic modules, we consider state-of-the-art lower-dimensional optimizations and its related long development times, as not being ideal to be used in the future for the developments of solar cells. Optimization of manufactured cells should work out much quicker, because of the high demand in generated electric energy at a low cost, which can be provided to a large extent by solar energy. This thesis aims to provide supportive information for the future optimization processes of perovskite solar cells, based on the proposed multidimensional improvement of its material properties. The general formulation, as presented here, is transferrable to optimize further solar cells, using an analytical or a numerical model, as elaborated from its drift-diffusion equations of electrons and holes. Therefore, the here proposed multidimensional optimizations have a large application field in different solar cell technologies.

2.3 PEROVSKITE SOLAR CELLS

The perovskite material was first discovered in the Ural Mountains of Russia by Gustav Rose in 1839; and was later named after the Russian mineralogist Lev Perovski, who founded the Russian Geographical Society in 1845 (OLALERU; KIRUI; WAMWANGI; RORO *et al.*, 2020). Rose discovered that perovskite materials are organized in a typical general material structure, defined as ABX_3 (Figure 2.1, page 46). This structure was later confirmed in a work relating to tolerance factors (GOLDSCHMIDT, 1926), being representative concerning the stability and the distortion of crystal structures (UBIC; SUBODH, 2009). In this context, values of the tolerance factor most proximate to the unity indicate the most stable perovskite molecules.

Early research in hybrid solar cells (WONG; WANG; HE; DJURIŠIĆ *et al.*, 2007) led to the concept of the so-known PSC (KOJIMA; TESHIMA; SHIRAI; MIYASAKA, 2009), a third generation hybrid thin-film cell, with an absorber constituted of an organic-inorganic compound of semiconductor materials. Second- and third-generation thin-film solar cells provide potentially a viable alternative to the most used mono and multicrystalline silicon solar cells in photovoltaic modules, because of its lower material use and manufacturing cost. Especially perovskite thin-film solar cells are advantageous, once its

degradation problems are solved, as discussed in section 2.6, page 52, because of its (i) high efficiency, (ii) lower material use, (iii) lower coating temperatures, and its (iii) direct band gap, which enables the coating of extra thin absorber layers if compared to silicon solar cells, where the cell's thickness has to be higher because of its inherent indirect band gap. In the case of the manufacturing of perovskite photovoltaic modules, PSCs with highly reproducible efficiency curves have to be manufactured (AHN; SON; JANG; KANG *et al.*, 2015), resulting, therefore, in low cell mismatch losses in those modules. Considering solely radiative recombination losses, the theoretical maximal efficiency of this cell is 30% (YIN; SHI; YAN, 2014), disregarding in this estimation further recombination losses, e.g., as related to trap states, limiting diffusion lengths, pinholes, undesired conduction effects, and further recombination effects. Because of its outstanding material properties, and its relatively easy manufacturing, the organic-metal-halide PSC showed a rapid evolution of its record efficiency values, which increased from 3.8% to 25.2% in only one decade, showing the steepest efficiency increase in comparison to further solar cells (NREL, 2020).

2.4 FLEXIBLE PLATFORM OF PEROVSKITE ABSORBER LAYERS

The general expression ABX_3 (Figure 2.1) stands for (i) a large organic cation A, (ii) a small inorganic cation B, and (iii) a halide anion X_3, resulting, therefore, in the organic-metal-halide constitution of the perovskite material.

Halide anion: For the halide anion (X_3) authors use iodide (I_3^-), chlorine (Cl_3^-), and bromine (Br_3^-), in this exact sequence of most frequent use (SALIBA; MATSUI; SEO; DOMANSKI *et al.*, 2016). In some configurations, the anion is constituted by the combination of two halide species, e.g., Cl and I, or Cl and Br, which results in an absorber layer made of $MAPbI_{3-x}Cl_x$ or $MAPbBr_{3-x}Cl_x$, where the x defines the relative material constitution of these halides. If x = 0, the absorber layer composition is $MAPbI_3$ for the first, and $MAPbBr_3$ for the second absorber layer configuration. However, if x = 3, the constitution of both absorber layer formulations is $MAPbCl_3$. The continuous variation of X in these formulations enables a precise band gap tuning of PSCs, obtaining the fixed material band gaps of 3.1, 2.3 and 1.6 eV for PSCs with pure halides (I_3^-), (Br_3^-) and (Cl_3^-). For the variation between x = 0…3, intermediate material band gaps are obtained in the range of 1.6…3.1 eV

for the $MAPbI_{3-x}Cl_x$ and 1.6…2.3 eV for the $MAPbBr_{3-x}Cl_x$ cell. This band gap tuning is allowed, because of the crystal lattice expansion of the perovskite molecule. Therefore, the tuning results in a remarkable advantage of PSCs, being especially useful in the design of low-cost multiple band gap cells. However, the $MAPbCl_3$ cell and $MAPbBr_3$ cell are not only of value in the engineering of a multiple junction PSC, but they can also be used for a fine-tuning of a PSC to the solar spectrum for a specific location, obtaining, therefore, some small additional efficiency gains.

Figure 2.1- Organic-inorganic hybrid perovskite compound, based on metal halides adopting the general perovskite structure ABX_3 in 3D PSC, where (i) A is the large organic cation, as constituted e.g. by Cs, or $CH_3NH_3^+$; (ii) B is the small inorganic cation, as constituted by Pb or Sn ; and (iii) X represents the anion from the halide series as constituted by Cl, Br^-, or I^+.

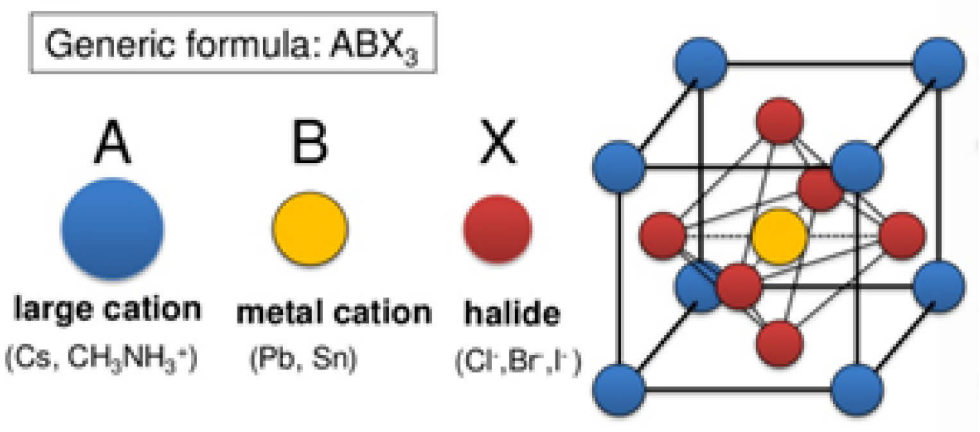

Source: (CHANG, without date).

Inorganic cation: The most used materials for the inorganic cation (B) are lead (Pb^{2+}), and tin (Sn^{2+}). Recently, the Pb was also substituted with Bismuth leading to an absorber layer of $(CH_3NH_3)_3Bi_2I_9$, which presents an efficiency of 1.62% (JAIN; EDVINSSON; DURRANT, 2019). However, presently most research articles are available about Pb-based perovskite solar cells, because of its higher state-of-the-art efficiency, which might change in the future.

Finally, we like to mention that 2D-PSC structures also present the advantage that the distance between its two or more, so-called 2D perovskite layers, can be manipulated. This manipulation results in an additional band gap tuning and additionally makes further new material properties available (GRANCINI; ROLDÁN-CARMONA; ZIMMERMANN;

MOSCONI *et al.*, 2017). As to see from this short review, and as also will be seen from the short review about the PSC's degradation mitigation in section 2.6, page 52, the possibilities of the manipulations of (i) the band gap and (ii) the further material properties seem to be nearly endless in the perovskite platform, which is of great advantage for the future development of highly efficient and stable PSCs.

We note that a single-junction Methylammonium lead iodide cell ($MAPbI_3$), as here optimized, is a cell that should result in the highest single-junction cell efficiency because of the nearly ideal cell band gap. In the optimization of the present cell, the effective cell band gap is 1.2 eV, a value that leads to a theoretical efficiency limit of 32.57%, which is only 0.34% lower than the highest Shockley-Queisser thermodynamic efficiency limit for single-junction solar cells, which demands an ideal band gap of 1.4 eV (RÜHLE, 2016).

We note that (i) the band gap of the perovskite material and (ii) the PSC's band gap are different items that present, therefore, different values. Whereas the material band gap of the absorber layer material is 1.5 eV (- 3.9 eV - (-5.4 eV)), the cell's band gap is 1.2 eV (Figure 3.1a, page 81). The cell's band gap is defined as the difference between the tilted lines of the absorber layer in this figure, outlined as the difference between the highest occupied molecular orbit (HOMO) and lowest unoccupied molecular orbit (LUMO) (e.g. - 4.2 eV - (- 5.4 eV) = 1.2 eV).

2.5 ADVANTAGES OF PEROVSKITE SOLAR CELLS

The remarkable advantages of perovskite solar cells in comparison to the similar organic solar cells, and the dominating silicon photovoltaic technology, is discussed here. Unique material properties make PSCs especially valuable for its use in solar energy conversion, and another of its attractive features is its potential viability for the manufacturing of low-cost, high-efficiency, flexible thin-film photovoltaic modules, as based on low material costs. Third generation hybrid perovskite solar cells are often compared to the third generation OPV cells, as they share similar low-cost manufacturing methods for the coating of its layers using ink coating technologies. However, PSCs are most different, because of its significant higher state-of-the-art efficiency (25.2%), which is similar in comparison to the first generation monocrystalline (26.1%), but higher than the first generation multicrystalline (22.8%), the second generation Copper Indium Gallium Selen (CIGS) (23.4%) and Cadmium

Telluride (CdTe) (22.1%), and much higher than the further third-generation solar cells, such as OPV (17.4%), quantum dot (16.6%), and dye-sensitized solar cells (12.3%), as visualized in (NREL, 2020).

In order to attain cost competitiveness in comparison with non-renewable power plans, the long term degradation of the PSC's efficiency should be validated under realistic operation conditions, resulting in a lifetime of at least 15 years (CAI; WU; CHEN; YANG *et al.*, 2017). Here we have to remark that the third-generation organic solar cells, already present very low PCE degradation under realistic operation conditions, which leads in an expected lifetime of over 20 years, if its fullerene type charge conduction layers are substituted with non-fullerene containing materials (XU; XIAO; ZHANG; WEI *et al.*, 2020). However, OPV cells present a lower state-of-the-art efficiency, which reduces its cost-competitiveness, considering its use in utility power plants, connected to the grid, which restrings its use in the application of, e.g., Building integrated photovoltaic systems (BIPV), where rater design than PCE plays an important role.

Such cost competitiveness with conventional power plants is essential in the future, when the fraction of the generation by photovoltaic and wind power systems raise, to mitigate the costs as related to the PV plant's variable generation profile (HIRTH; UECKERDT; EDENHOFER, 2015). In a future of high penetration of the renewable energy generators in the power grid, the total generation cost of wind and photovoltaic systems will increase. This because of the needed energy storage, or otherwise, because of power plants that present an adjustable firm energy, as necessary to mitigate the variability of the generated power by renewable plants. Consequently, it is of advantage to decrease the cost of the photovoltaic generator further, as being presently still the highest cost component of a PV system.

2.5.1 Low-cost materials

Perovskite solar cell absorber layers consist of a mixture of abundant and low-cost raw materials, such as lead (Pb), tin (Sn), carbon (C), hydrogen (H), and nitrogen (N). The indium (I), used in single-junction PSC, can be substituted in future perovskite-based multijunction solar cells by the non-rare halides bromide (Br) and chloride (Cl). This substitution is advantageous as Br and Cl result in the higher demanded band gap for its upper junctions. Therefore, such materials are useful and lead to the absorption of a broader solar spectrum, which results in higher efficiencies. In low-cost PSCs, these non-rare materials can

be combined with inexpensive materials used for the coating of the charge conduction layers, made of metal oxides (YOU; MENG; SONG; GUO *et al.*, 2016). The authors composed the p-type and the n-type charge conduction layers with NiO_x and ZnO. As a result, they inclusively obtained an improved long-term-stability for the measured efficiency, as these charge conduction layers do provide a better barrier to avoid the diffusion of materials from the adjacent layers through the charge conduction layers.

2.5.2 Low-cost manufacturing techniques

As the manufacturing process of third-generation thin-film solar cells is much simpler, in comparison to the known monocrystalline, and multicrystalline silicon solar cells, they are manufacturable at a low-cost and in a large-scale. The monocrystalline cells are made from a grown unique crystal, called ingot in a slow-growing process. In contrast, in multicrystalline cell manufacturing, this ingot is substituted with a molten block of silicon. After the cooling of these blocks, which need several days, they are sawn to silicon wafers using diamond wire saws. Then, solar cells are obtained, after doping passivation of each of the wafers, which still need to be interconnected electrically and laminated to a photovoltaic module (GOODRICH; HACKE; WANG; SOPORI *et al.*, 2013; MCEVOY; CASTANER; MARKVART, 2012). Such demanding processes are not necessary for the manufacturing of thin-film solar cells, such as Copper Indium Gallium Selenium (CIGS), or the Cadmium Telluride (CdTe) solar cells, as they are coatable in a conveyor belt production line (MCEVOY; CASTANER; MARKVART, 2012). However, these thin-film cells must be coated and treated under high temperatures and vacuum conditions.

In comparison, the manufacturing process of the third generation organic, and perovskite solar cells, is more advantageous as it involves: (i) much lower process temperatures, and (ii) simple and known, low-cost manufacturing processes, such as printing processes as discussed in (RONG; HOU; HU; MEI *et al.*, 2017), (YANG; LI; REESE; REID *et al.*, 2017) and (KIM; YANG; SUHONEN; VÄLIMÄKI *et al.*, 2019). A complete review of the different manufacturing methods used for the fabrication of single-junction PSCs, as categorized in (i) vapor-phase; and (ii) solution-based methods, such as, e.g., printing methods; are presented in (BRITTMAN; ADHYAKSA; GARNETT, 2015) and (ZHOU; YANG; WU; VASILIEV *et al.*, 2015). Another interesting manufacturing method, also

usable for large-scale coating, is the solvent-solvent manufacturing method (ZHOU; YANG; WU; VASILIEV et al., 2015), which already results in PCE of 15.2 %. In this method, a precursor solution, constituted by components of PbI_2 and MAI, is printed on a substrate, already pre-coated with a transparent conductive and a charge conduction layer. The obtained dispositive is then immersed in a Diethyl ether $(C_2H_5)_2O$ bath, which forms by a chemical reaction to built-up the perovskite absorber layer. One of the advantages of this manufacturing process is that the perovskite layer thickness can be adjusted accurately by variation of the immersion time.

2.5.3 Low-cost devices based on single-junction cells

The combination of the use of (i) low-cost materials, (ii) a low-cost manufacturing process, in the manufacturing of a cell which results in a (iii) relatively high efficiency, results together in the pre-evaluation that electric energy converted by PSC modules leads to the lowest LCOE, of only 30…60 US$/MWh. The lower and the upper value of this range is lower than the LCOE of any further state-of-the-art renewable and non-renewable energy generation technologies (CAI; WU; CHEN; YANG *et al.*, 2017).

Therefore, in a single-junction solar cell configuration, PV-modules based on PSCs have the potential for most-far reaching cost reductions in the generation of electrical energy (CAI; WU; CHEN; YANG *et al.*, 2017), considering however that the cell's long term stability under realistic operation conditions can be increased (Section 2.2.4, page 42). The authors estimate that PV modules, based on single-junction PSCs, can generate electric energy at the lowest LCOE. Even the upper value of 60 US$/MWh, as projected by the authors, is lower in comparison to any further state-of-the-art renewable and non-renewable energy generation technologies. The costs are estimated assuming two different module types, with efficiencies in the range of 10-12% and 15-20%, and a lifetime under realistic operation conditions of 15 years, which is, however, presently not the state-of-the-art for perovskite solar cells. In both configurations, the materials of the active layers are responsible for only 12…14% of the module's material cost. The costs of the manufacturing plant were estimated on a 100 MW/year plant capacity, considering its overhead, and depreciation costs.

The plant costs of the lower efficiency PV-module were estimated based on the production of existing plants of dye-sensitized solar modules. For the plant with the higher

module efficiency, plant costs are estimated based on the manufacturing cost of a second-generation module manufacturing. Both cases consider a correction factor based on the efficiencies of the manufactured modules. The generation cost of electric energy is calculated based on the total costs of a grid-connected PV-system, which includes (i) its mounting rack, (ii) wiring, (iii) power conditioning, (iv) installation, (v) operation & maintenance, (vi) capital recovery, and (vii) land use, and where only the module costs are substituted, with the estimated module price for the considered manufacturing plant.

2.5.4 Extra low-cost devices based on multiple-junction cells

Multiple-junction solar cells do present the inherent advantage that the energy of a broader spectrum of the solar irradiance can be converted to electric power, which results in higher efficiencies. E.g., four junction solar cells present a state-of-the-art PCE of 47.1% and 39.2% for concentrated and non-concentrated solar irradiance (NREL, 2020). However, the state-of-the-art III-V multiple-junction solar cells are presently only used (i) in space applications or (ii) terrestrial projects with concentrated solar irradiance, because of its high manufacturing cost per area. Such cells are based the higher-cost materials, such as Gallium, Arsenide, and Indium (LIN, 2020), and very slow-growing coating techniques, such as epitaxial growth (TANABE, 2009), which result in a very high cost per Watt peak if compared to silicon photovoltaic modules.

The band gap tuneability, as related to the combination of different perovskite materials, makes a simple band gap tuning available, which is advantageous in the tuning of the used junctions in a multiple-junction PSC. Coating two of two in-series connected PSC junctions results in multiple-junction perovskite solar cell. The first research activities with all-perovskite multiple junction cells resulted in PCE values of 6.7% and 15.2% for triple and tandem junctions (MCMEEKIN; MAHESH; NOEL; KLUG *et al.*, 2019). The author's triple-junction cell presents inclusively two tunnel junctions to reduce the contact resistance between the three different perovskite junctions. In the comparison to state-of-the-art multijunction cells (DIMROTH; GRAVE; BEUTEL; FIEDELER *et al.*, 2014), PSCs are of particular interest, because high-efficient multijunction PSCs are manufacturable from low-cost materials and by low-cost manufacturing processes, which can be up-scaled to large areas via, e.g., an all-gravure printing process (KIM; YANG; SUHONEN; VÄLIMÄKI *et al.*,

2019). The property of continuous band gap tuning provides a further opportunity space for the optimization of multiple-junction PSCs, if compared to the present III-V multiple band gap tuning.

Furthermore, they are also usable in multijunction cells, being this in combination with (i) silicon, (ii) further second-generation solar cells, or (iii) in a concept solely built-up with perovskite layers. The latter has the advantage of overcoming the slow-growing rates as related to the state-of-the-art second-generation multiple-junction solar cells (PALMSTROM; EPERON; LEIJTENS; PRASANNA *et al.*, 2019), enabling, therefore, a higher velocity mass-production of extra low-cost photovoltaic modules. The authors already obtained a PCE of 23.1% with a proposed all-perovskite tandem solar cell. The mechanical flexibility of third-generation solar cells allows the fabrication in a multiple-junction roll-to-roll manufacturing process, e.g., using the all-gravure printing process. In single-junction PSCs, such a printing already results in a high efficiency of 17.2% (KIM; YANG; SUHONEN; VÄLIMÄKI *et al.*, 2019).

2.6 MITIGATION OF THE CELL'S LONG-TERM DEGRADATION

Under realistic operation conditions, the present lifetime of a PSC photovoltaic module is estimated to be only two years by extrapolation, based on an annual degradation of 10% per year (TRESS; DOMANSKI; CARLSEN; AGARWALLA *et al.*, 2019), which restricts the scope of its practical applications considerably. Therefore, future developments must reduce the long term degradation of cell's PCE (KALTENBRUNNER; ADAM; GŁOWACKI; DRACK *et al.*, 2015; PARK; GRÄTZEL; MIYASAKA; ZHU *et al.*, 2016; YANG; WANG; LIU; CHENG *et al.*, 2016; YOU; MENG; SONG; GUO *et al.*, 2016) to make PSC's commercially useful. Such a behavior can be obtained by (i) the substitution of methylammonium cation; (ii) the use of improved inorganic charge conduction layers, which also present a lower cost than in comparison to the most used organic charge conduction layers; and (iii) the cell's encapsulation (BUSH et al. (2017) - figure 3b), or lamination of the perovskite photovoltaic module in between other methods.

While the degradation of perovskite solar cells was initially thought only to be a function of the (i) the higher energy ultraviolet irradiance; (ii) temperature cycles during operation; and (iii) small amount of humidity, which penetrates through the cell's encapsulation protection; more recent findings showed that there are further problems which have to be resolved too. These are (iv) small amounts of oxygen, which also can penetrate the lamination of a photovoltaic module and then migrate through the charge conduction layer. Then, by bonding with an absorber layer's hydrogen, this O_2 converts into moisture within the absorber layer, which starts a degradation process. Furthermore, (v) the electric field, as built up under MPP operation, or under the open-circuit condition of the PSC, leads to the further migration of ions. Some of such degradation effects, e.g., as related to the electric field, also appeared at its initial development with second-generation solar cells and were then later resolved (KHENKIN; ANOOP; KATZ; VISOLY-FISHER, 2019).

From the following short review, we conclude that there is at least one solution available to avoid each of these multidimensional degradation issues. Furthermore, some of the measures, which increase the cell's PCE, as discussed in Section 2.10.1, page 70, do simultaneously provide improved long term stability of the cell's efficiency. These details, and the fitness of the perovskite platform for chemical modifications, in general, give a thorough outlook that a combination of the different measures might be able to mitigate the present degradation problems of PSCs.

Degradation and self-healing: Recent research revealed that some of the degradation effects as associated with UV-irradiance and temperature cycles are of no permanent character. E.g., degradation as a function of UV-light exposure can be partially self-healed by the cells temporary displacement in the dark (NIE; BLANCON; NEUKIRCH; APPAVOO *et al.*, 2016). Therefore, it can be considered that some of the previews UV degradation tests, which did not analyze these self-healing effects, overestimate the PSC's degradation presenting, therefore, a too high degradation effect because of the continuous light exposure. Such degradation tests should be accomplished under simulated under realistic conditions with day-night irradiance and temperature cycles.

Improved self-healing property under exposition to UV-light: The most challenging aspect of PSCs is its degradation and efficiency loss under light-exposition. Under this condition, and also during the manufacturing of a PSC, are produced Pb^0 and I^0

defects, which represent (i) recombination sites of charge carriers and (ii) deteriorate PSCs efficiency over time (WANG; ZHOU; HU; HUANG *et al.*, 2019). However, the authors inactivate such states is by its oxidations, using a tiny quantity of the rare earth metal Europium (Eu), which is used as a so-named redox shuttle. The advantage of these redox shuttles is that its ion pairs Eu^{3+} and Eu^{2+} can be regenerated in a closed cycle, converting the Pb^0 and I^0 trap states in Pb^{2+} and I^- ions as specified by the following two equations

$$2Eu^{3+} + Pb^0 \rightarrow 2Eu^{2+} + Pb^{2+} \quad (2.1)$$

$$Eu^{2+} + I^0 \rightarrow Eu^{3+} + I^- \quad (2.2)$$

As to see from the first passivation in equation (2.1), the Pb^0 trap state is converted in Pb^{2+}, while the $2Eu^{3+}$ is transformed in $2Eu^{2+}$. In the following passivation, as presented in equation (2.2), the I^0 trap state, is converted in I^-, while the Eu^{2+} is back-transformed in Eu^{3+}. Theoretically, such a transformation of temporary trap states can, therefore, work forever, avoiding thus the cell's efficiency loss and degradation under exposition to light. Initial research activities with such a closed trap regeneration cycle resulted in UV-light stability, which retained 92% of the cells PCE of 21.52% in 1500 hours of light exposure. As the electric field does also reduces the PCE, an MPP tracked exposure retained 91% of the cell's PCE after 500 hours of continuous operation.

Degradation under permanent exposition to UV-light: One of the most challenging aspects of PSCs is its permanent degradation and efficiency loss under light-exposition. The authors (SHI; CHEN; WU; CAI *et al.*, 2020) simulated quasi-vacuum conditions, as appearing in near-space applications, avoiding, therefore, almost wholly the degradations related to ambient oxygen and humidity. They examined the absorber layer's surface visually and measured the cell's efficiency, showing that PSCs present a permanent degradation as a function of its exposition to simulated and uninterrupted irradiance. This permanent degradation results in the effect that some small spots of the absorber layer degrade, especially under exposure to green and blue light spectrums, where the latter presents the highest photon energy. However, it is not understood why only some small areas degrade, while approximately 99 % of the cell's absorber layer surface is visually intact. Furthermore, it is also not known if, in the case of a day-night exposure profile, such a

localized degradation can be avoided, as related to a recovery effect discussed in (NIE; BLANCON; NEUKIRCH; APPAVOO *et al.*, 2016).

Light degradation under ambient temperature: One of the most promising configurations is presented in (TURREN-CRUZ; HAGFELDT; SALIBA, 2018), proposing an inorganic PSC made of $Cs_{10}Rb_5FAPbI_3$. In a 1000 h continuous exposition under MPP-tracking, this cell shows a small initial degradation of approximately 2%, in the first 500 hours, which then stabilizes, showing visually no further degradation. An effect that presents similarity with the known initial degradation of crystalline silicon solar cells, showing a 3% degradation typically within the first year of operation (GREEN, 2005). Because of the discussed self-healing effect, this initial degradation can even be lower than 2% under exposition to cycling irradiance. However, as the experiment in (TURREN-CRUZ; HAGFELDT; SALIBA, 2018) was set-up under ambient temperature conditions, it is not known if a further degradation under temperature cycling, as appears under realistic operation conditions, can deteriorate the cell's efficiency further.

Degradation under temperature stress cycles: In power plants, photovoltaic modules and its solar cells are exposed to temperature stress cycles. E.g., during the day in low latitude locations, it is usual that the PV modules heat up till 70…80 ºC while cooling down in the night to around 20ºC, or even to colder temperatures in deserts or locations with high altitudes. Such a temperature profile leads in perovskite solar cells to thermal stresses, as its internal perovskite material changes its crystal lattice from the orthogonal phase, as present in low temperatures, to the tetragonal and the cubic phases, as related to high operating temperatures (WANG; WRIGHT; ELUMALAI; UDDIN, 2016). The resulting crystal structure changes lead to the deterioration of the cell's efficiency over time. Temperature cycle-dependent deterioration can be avoided by partial or the complete substitution of the A-cation, and the X-anion, which results in a tuning of (i) the crystallographic tolerance factor (t), and (ii) the octahedral factor (μ) (WANG; WRIGHT; ELUMALAI; UDDIN, 2016). This classification is essential as μ determines the stability of the octahedral phase in perovskite solar cells. In an example the authors manufactured such a cell, by the incorporation of a thiocyanate anion (SCN^-) into the absorber layer, adding a small amount of $Pb(SCN)_2$ to the PbI_2 solution in the cell manufacturing, which results in a composed $MAPbI_{3-x}(SCN)_x$ absorber layer that presents enhanced stability. The authors also revised several further

chemical modifications, which do not only reduce the degradation as a function of temperature cycles, but also take account to further PCE degradation effects.

Degradation by penetration of oxygen: Further studies indicate that degeneration also happens as a function of the penetration of oxygen, which diffuses through the charge conduction layer. This oxygen is thought of as building up a light-induced generation of H_2O in the absorber layer, using a hydrogen atom of the methylammonium. Such an effect results in a moisture-related degradation process of this layer (YU, 2019). The recent discovery of tight oxygen resistant charge transport layers, as obtained by the deposition of atomic layer deposition (ALD) of a metal- oxide charge conduction layer (YU, 2019), shows one way to avoid such an O_2 penetration. However, such metal-oxide layers can also result in additional trap states at its interface with the perovskite layer, presenting typically defects of oxygen, and metal cations of different valences such as, e.g., Ti^{3+} or Ti^{4+} (SINGH; SINGH; MIYASAKA, 2016). Meanwhile, a promising method to passivate these trap states is the contact passivation of the metal oxide layer (TAN; JAIN; VOZNYY; LAN *et al.*, 2017). The authors present excellent stability, showing that its attained PCE of 20% is retained by (i) 97% after 500 hours of light exposure and (ii) by 90% after 500 hours MPP tracking under AM 1.5 conditions. These values the authors measured only after dark recovery. The underlying self-healing effect of perovskite solar cells suggests that its degradation should be accessed under more realistic situations, exposing the cell to a simulated day/night illumination profile with a 24 h full cycle, which should, therefore, result in even lower degradation effects.

Degradation by humidity: Another promising approach to obtain a long term stabilization is the manufacturing of 2D-PSCs (SMITH; HOKE; SOLIS-IBARRA; MCGEHEE *et al.*, 2014). A 2D-PSC is defined by a perovskite absorber layer which has several interleaved layers of organic cell material. In this context, especially the combination of a conventional PSC, which is conceived as a 3D perovskite solar cell, with the 2D-PSC results in lower long term degradations (GRANCINI; ROLDÁN-CARMONA; ZIMMERMANN; MOSCONI *et al.*, 2017). Under one sun testing irradiance, the author obtained no PCE degradation during 1 ¼ year of storage in a closed chamber with controlled humidity, and without exposition to light. Basically, in these mixed 2D/3D PSC, the hydrophilicity inherent to the 3D perovskite solar cell is reduced to a large extent by the

introduction of the hydrophobic spacing cations, which are placed in-between the 2D-PSC plates (CHEN; SUN; PENG; ZHANG *et al.*, 2017).

Degradation under exposition to the internal electric field: The electric field of a solar cell, as generated under MPP operation conditions, leads to the internal migration of organic and halide ions, leading, therefore, to local trap-states, which degrade the efficiency and result also to a hysteresis of the cells J-V curve (WEI; MA; WANG; DOU *et al.*, 2018). Furthermore, if these ions migrate through the charge conduction layers, they can result in the deterioration of the electrodes. The authors show that the fixation of these ions can avoid such migration effects by a ubiquitous cation interaction based on introduced Rubrene. The calculated interaction energy with Rubrene is with 1.5 eV, which is much higher than the low activation energy of MA+ ions is, avoiding, therefore, an escape from its lattice structure. The avoided migration of ions improved the long-term stability of the PSC's efficiency considerably.

Degradation by the migration of electrode parts: Similarly, the metal particles of the electrodes can migrate through the charge conduction layers at operating temperatures of 80 ºC, which also results in the deterioration of the PSC's efficiency. E.g., gold from the top electrode of a PSC can migrate through the hole transport layer (DOMANSKI; CORREA-BAENA; MINE; NAZEERUDDIN *et al.*, 2016). Such migration can be avoided using a Cr metal interlayer between the electrode and the hole transport layer.

2.7 RESIDUALS IN PEROVSKITE SOLAR CELLS

Rather than the third-generation organic solar cells, PSCs contain a small amount of Pb in its absorber layer, and several authors attempted to reduce the toxicity inherent to this heavy-metal. Such methods consider the complete (DEVI; MEHRA, 2019; DIXIT; PUNETHA; PANDEY, 2019), or partial substitution of this element (LIU; LI; FAN; MAI, 2018). While initially, such methods lead to much lower efficiencies in manufactured cells, if compared with the high state-of-the-art efficiency, more recent research shows that the partial substitution of Pb with Sn in a cell with a $(FASnI_3)_{0.6}(MAPbI_3)_{0.4}$ absorber layer can result in high efficiencies of 20% (TONG; SONG; KIM; CHEN *et al.*, 2019). If compared to the Pb based perovskite solar cells, the Sn-based PSCs present a lower band gap and the higher

diffusion coefficients, which are advantageous and might result in high efficiencies in the future as obtained by simulations (section 2.8.1, page 60).

State-of-the-art Pb based PSCs with an absorber layer of 450 nm do already contain a low quantity of heavy-metal residuals, which is similar to state-of-the-art photovoltaic modules (GREEN; HO-BAILLIE; SNAITH, 2014; STASIULIONIS, 2015). Additionally, Pb based PSCs present by its own, a 90-300 times lower heavy-metal content in its life cycle analysis, if compared to coal-fired power plants for the similar energy production (FTHENAKIS; KIM; ALSEMA, 2008). The advantage of solar cells is that the encapsulation of the photovoltaic module contains its heavy-metal content and, therefore, it can be recycled, not exposing the environment as a result. Interestingly, the thickness reduction of the absorber layer, as here proposed for high-efficiency PSCs, reduces the use of the perovskite material in a PSC, resulting in 2.8 times lower quantity of lead (Pb) residuals in a photovoltaic module. This lower residual content places PSC's in a favorable position by the reduction of its toxicity, in comparison to silicon solar cells. However, the absorber layer in PSCs is dissolvable in water, and therefore, they should ideally have an improved encapsulation, or hydrophobic character, as inherent to, e.g., a 2D-PSC absorber layer (CHEN; SUN; PENG; ZHANG *et al.*, 2017), which avoids or reduces leakage in the case of a module break.

Furthermore, in the future, adequate recycling policies should enable the option of recycling for all photovoltaic modules, improving the presently implemented routine of voluntary recycling, as adopted by some manufacturers (MCDONALD; PEARCE, 2010). Presently the price of the recycled materials of silicon modules is approximately 0.17 US dollar / kg, being lower than its recycling cost, which currently is 0.62 US dollar / kg (HSU; KUO, 2020). However, it is thought that in the future, the economic benefit from large-scale recycling even helps to expand the PV sector, as discussed in (TAMAS VEKONY, 2020), apud (HSU; KUO, 2020), if its recycling cost becomes lower than 0.17 US dollar / kg.

2.8 MODELING OF PEROVSKITE SOLAR CELLS

State-of-the-art PSCs are mostly optimized based on cell prototyping, where the cell's efficiency is increased in small steps as a function of one or two different measured variables, as permitted by graphical visualization in one- or two-dimensional function spaces. Such an optimization has the inherent disadvantage that variations in the not measured

material properties are unknown. Therefore, efficiency gains because of the improvement of one or more of the material properties can be entirely or partially nullified by the worsening of one or more other, not controlled properties, without even being noticed. This situation should be controlled better in future cell manufacturing.

The benefits of mathematical modeling of the PSC's efficiency, by use of an analytical model, a numerical model, or a combination of such models (AGARWAL; NAIR, 2014; 2015) can result in valuable understanding, and accelerate potentially the cell's development process. These models are derived (i) from the PSC's drift-diffusion equations of electrons and holes, (ii) the Poisson equations, which simulates the electrical field, and (iii) a method which calculates the short circuit current density. The model's drift-diffusion equations do simulate the cell's current-voltage curve typically as a function of multiple material properties and the absorber layer thickness. The highest PCE at the state-of-the-art, based on such simulation studies, results in 25% for a single-junction PSCs (AGARWAL; NAIR, 2014; 2015).

Short circuit current density: The cell's J_{sc} is simulated independently, using a simplified Beer-Lambert model (SUN; ASADPOUR; NIE; MOHITE *et al.*, 2015), or the higher resolution transfer matrix method (TMM), also named as optical transfer matrix method (OTM), which do typically not include light-trapping schemes. Both modeling methods are used in the program Scolore, an in Python-written open-source software (ALONSO-ÁLVAREZ; WILSON; PEARCE; FÜHRER *et al.*, 2018), which inclusively enables the simulation of multiple-junction solar cells. A J_{sc} modeling that also includes light trapping, is accomplished with finite difference time domain modeling (FDTD) scheme (CAI; PENG; CHENG; GU, 2015), which simulation is based on a spatial resolution. It enables a J_{sc} simulation as a function of (i) the use of plasmonic light-trapping nanoparticles, in different light-trapping schemes; (ii) the absorber layer thickness; (iii) providing also a simulation for the case without light trapping. Some authors also present an efficiency optimization in a one-dimensional optimization of the cells charge conduction layer thickness (PHILLIPS; RASHED; TREHARNE; KAY *et al.*, 2016; ZHAO; LIU; LIN; CHEN *et al.*, 2018), using the Optical Transfer Matrix (OTM) scheme for its modeling.

2.8.1 Numerical perovskite solar cell models and their optimization

Most simple solar cell models are based on the one diode or the two diode model, where the solar cell's behavior and its IV-curves are simulated by a circuit of discrete electronic elements, such as diodes, resistors, and current sources (KRATZENBERG; MOYA; ROMERO, 2014). As the resulting equation is implicit, its solution has to be obtained numerically. More sophisticated model simulations are based on the Poisson and the drift-diffusion equations. In this concept, an independent simulation of the short circuit current density, as based on the generation of charge carriers, while the drift-diffusion equations and the Poisson model its transport. A complete representation of these equations includes the (i) solar irradiance absorption, (ii) the resulting charge carrier generation, (iii) the drift and diffusion of these carriers, and (iv) finally also considers several recombination effects within the solar cell. These models consider Dirichlet-type boundary conditions to find a solution to these differential equations numerically, and the boundary conditions are used to solve the second-order drift-diffusion equations by an iterative process. Its solution results in the solar cell's current densities of electrons and holes as a function of its terminal voltage under the cell's exposition to a reference light source, and when it is localized in the dark (LIU; ZHU; WEI; LI *et al.*, 2014).

A very detailed numerical model is presented in Foster *et al.* (2014), where the author divides the PSC in a total of seven different regions, which are modeled separately: (i) the bulk of the perovskite absorber layer, (ii) the boundary region at the interface between the electron acceptor and the adjacent absorber layer, (iii) the bulk of the electron acceptor layer, (iv) the boundary region between the acceptor of electrons and its adjacent electrode, (v) the boundary region at the interface between the donor of electrons and its adjacent absorber layer, (vi) the bulk of the donor layer, and finally (iv) the boundary region between the donor and its adjoining electrode. The model allows calculating the cell's HOMO and LUMO potentials as a function of the irradiance penetration depth.

MAPI: The authors (IFTIQUAR; YI, 2016) used the AFORS-HET program, another numerical 1D-solar cell simulator and observed by numerical simulations that a MAPI cell lead to a PCE > 20 % if the absorber layer's defect density is lower than 4 x 10^{14} cm^{-3} and the cell's thickness is at least 400 nm. The observed that the principally the open-circuit voltage, and therefore the PCE, is a function defect density. (LIU; ZHU; WEI; LI *et al.*, 2014) used the

1D-program named as analysis of microelectronic and photonic structures (AMPS), for the simulation of a MAPI cell. They found high PCE values of 22.2% for low trap densities at the absorber layer interface of 10^9 cm^{-2}, and defect densities in the absorber layer lower than, or equal to 10^{12} cm^{-3}. Using the 1D solar cell capacitance simulator (SCAPS), an open-source code simulation program, the authors (DEVI; PARREY; AZIZ; DATTA, 2018) found that for a pin-type MAPI cell with a 500 nm thick absorber layer a maximal PCE of 23.83%. In this cell, the most used TiO_2 electron conduction layer must be substituted by CdS layer, which results in a high built-in voltage of 1.37 V. For a 1000 nm thick absorber layer, the cell's PCE increase to 24.5%. Using the same simulator in simulations with an nip-type MAPI cell (AZRI; MEFTAH; SENGOUGA; MEFTAH, 2019) found the ideal bandgap alignment is obtained by the selection ZnO and TiO_2 for the p-type charge conduction layer, because of the nearly ideal alignment of its conduction band with the PSC's LUMO layer resulting in a simulated efficiency of 25.02%. In a similar form, they obtained an excellent band alignment of HOMO levels, between the CuSCN n-type layer and the perovskite layer.

$MAGeI_3$: Using the SCAPS simulated the authors in (HIMA; LAKHDAR, 2020) found that a substitution of the Pb with Ge in a nip-type $MAGeI_3$ cell can result to an efficiency of 23.8%, using a 1 μm thick absorber layer. The authors analyzed four different hole transport layers of the pin-type cell (PEDOT:PSS CuSCN, $CUSbS_2$ and NiO) and found this high PCE because of an adequate energy alignment between the copper (I) thiocyanate (CuSCN) and the perovskite material, leading to the highest built-in potential ($\Delta\phi_{bi}$) (see $\Delta\phi_{bi}$ in Figure 3.1a, page 81). The authors (KANOUN; KANOUN; MERAD; GOUMRI-SAID, 2019) used SCAPS to investigate the absorber layer thickness, the material of the hole transport layer, the defect density, the hole mobility, and the metal electrode work function. They find the highest PCE of 21%, for a 600 nm thick absorber layer, using CU_2O hole transport material. This efficiency reduced to 11% if the defect density increases from 1 x 10^{14} to 1 x 10^{18} cm^{-1}. Furthermore, a mobility of at least 100 cm^2 V^{-1} s^{-1} is necessary to enable this highest PCE.

$MASnI_3$: In (HOSSAIN; DAIF; AMIN; ALHARBI *et al.*, 2015) the authors used a one-dimensional solar cell capacitance simulator (SCAPS) to optimize a $MASnI_3$, obtaining a PCE of 15.64%. The author (AMU, 2014) used the numerical SCAPS model to optimize a Sn-based $MASnI_3$ and suggest device efficiencies > 18% as based on the variation of the tuning

of the perovskite doping concentration. As shown in (ANWAR; MAHBUB; SATTER; ULLAH, 2017), the highest PCE of 20.23% is obtained with a Cu_2O hole transport layer and ZnO-nanorod electron transport layer. They found this PCE for an ideal thickness of the absorber layer of 600 nm, and a defect density at both interfaces with the value of $\leq 1 \times 10^{10}$ cm^{-3}.

$FASnI_3$: The authors (DIXIT; PUNETHA; PANDEY, 2019) used SCAPS and simulated a $FASnI_3$ cell obtaining a maximal simulated and measured efficiency of 9.99%. They also showed that the V_{0C} and the FF are functions of the doping concentration and the defect density. This low maximum efficiency is obtained for (i) low operation temperatures, (ii) a 450 nm thick absorber layer and (iii) a band gap between 1 and 1.4 eV.

In general, the solution of a numeric model is very time demanding and leading, e.g., to an optimization time of approximately 60 min for a singular numerical optimization process of a planar organic solar cell (KRATZENBERG, 2015b). The time demanding process in the simulation of such a model occurs as the whole solar irradiance spectrum is subdivided into several sub-band spectra, where for each of these sub-band spectra, a set of differential equations must be solved by a numeric method. We have to comment here that the modeling methods as cited in this section improve the efficiency as a function of one, or two material properties at a time, but do not consider a simultaneous improvement of multiple material properties as proposed in this thesis.

2.8.2 Analytical solar cell models

The authors (DORN; SOUKUP, 1994) show the first derivation of an analytical solar cell model, using the drift-diffusion equations of electrons and holes of a silicon solar cell. For an organic bulk heterojunction solar cell, an analytical model was also presented in (CHOWDHURY; ALAM, 2014), discussing the benefit of its reduced computational cost. Its model shows a separate analytical solution for each sub-band spectrum of the sun's irradiance. The same research group introduced later the analytical models of four different types of single-junction perovskite solar cells in (SUN, 2018; SUN; ASADPOUR; NIE; MOHITE *et al.*, 2015): (i) the pin-type, (ii) the nip-type, (iii) the ppn-type and (iv) the npp-type. The authors show that in a one-dimensional optimization of the absorber layer thickness,

the pin-type and the nip-type PSC presented the highest measured and modeled efficiency of 15.7% and 15.4%.

In comparison, the ppn-type and the npp-type cells resulted in the lower PCEs of 11.2% and 8.6%. This analytical model is obtained by the solutions of five second order differential equations (DE): (i) the four drift-diffusion equations and (ii) the Poisson equation. The drift-diffusion equations are modeling the transport of electrons and holes for the cases when the solar cell is exposed to a reference solar irradiance, and when it is localized in the complete dark, while the Poisson equation simulates the electric field in the solar cell. The solution for these five second order DEs the authors obtained by the specification of two Dirichlet-type boundary equations for each DE (section APPENDIX A.1, page 155).
Additionally, the absorption of light and the generation of charge carriers the authors modeled by a general Beer-Lambert exponential decay curve. Usually, the absorption of light in a material is a function of the considered wavelength, resulting in a wavelength-dependent absorption length, and, therefore, an individual Beer-Lambert exponential decay curve. However, the approximation by a general Beer-Lambert curve model the absorption of light for the whole spectrum in which the PSC shows light sensitivity. This approximation considers a general solution for (i) the generation of charge carriers G(x) and (ii) the average absorption length, also called as average optical decay length λ_{ave}. As a result, the cell's short circuit current density is simulated by a unique exponential decay curve (Figure 3.1b, page 81). This approach leads to small, but a depreciable deviation of only 0.1% absolute error in comparison to the measured efficiency with a manufactured PSC as shown in (SUN; ASADPOUR; NIE; MOHITE *et al.*, 2015).

The complete formulation of the analytical pin-type model of the here analyzed planar heterojunction PSC and its derivation scheme we presented in section APPENDIX A.1, page 155. Apart from the measurements with the manufactured solar cells, (NIE; TSAI; ASADPOUR; BLANCON *et al.*, 2015), apud (SUN; ASADPOUR; NIE; MOHITE *et al.*, 2015), accomplished extensive numerical simulations, involving the solution of the Maxwell current density equations, the Poisson equation, and the drift-diffusion equations. The results from these simulations were used in (SUN; ASADPOUR; NIE; MOHITE *et al.*, 2015) to validate the behavior of the derived analytical models. Because of its simplifications as discussed in section APPENDIX A.1, page 156, this analytical model is of advantage, as it presents several orders of magnitude lower computational cost in a single optimization, as in

comparison to the numerical simulation model. The authors (TARETTO; SOLDERA; KOFFMAN-FRISCHKNECHT, 2017) proposed an analytical model for a MAPI cell, which present a low FF and concluded that for this cell both recombination losses at the interface and in the bulk of the cell have to be considered.

This fast simulation is of benefit in arbitrary applications, where the model simulations have to be accomplished multiple times. E.g., in the access of the cells' mismatch losses in a photovoltaic module, which performance is based on the simulation of the complete set of single solar cells, each presenting a small variation of its J-V curve performance parameters. Another example is the maximization or optimization of the model's efficiency as a function of multiple model variables as presented here.

2.8.3 Recombination and further losses

One disadvantage of the model presented in (SUN; ASADPOUR; NIE; MOHITE *et al.*, 2015) might be, that it does not consider recombination losses in the bulk of the absorber layer (equations (A.27) and (A.28), page 168). While the depreciation of bulk recombination might be correct, for the cell's short circuit current, it is possibly not valid for its open-circuit voltage, as well as its MPP voltage, as discussed in (TARETTO; SOLDERA; KOFFMAN-FRISCHKNECHT, 2017). However, strictly speaking, some of the recombination processes in the bulk of the perovskite absorber layer are already contemplated in (SUN; ASADPOUR; NIE; MOHITE *et al.*, 2015), as taking place by the formulation of the front and back surface recombination velocities of electrons and holes, s_f and s_b. These recombination velocities are not only related to recombination effects at the transition surfaces between the charge conduction layer and the absorber layer but are also existent at the transition surfaces between the single perovskite crystals in the bulk of the absorber layer. Such effects are especially accentuated in non-passivated surfaces with crystal grain sizes lower than 5 μm (YANG; YAN; YANG; CHOI *et al.*, 2015).

The limited diffusion length defines another recombination process, as simulated in the model of (SUN; ASADPOUR; NIE; MOHITE *et al.*, 2015). If a diffusing electron or hole charge carrier did not pass its charge conduction layer, in its predetermined diffusion paths length (L_n, L_p), as specified by equations (A.33) and (A.34), page 169, for a fixed lifetime, recombination happens, which reduces the diffusion coefficient, and therefore the cell's

efficiency. Furthermore, presuming that for a fixed $L_{n,}$ and L_p the electrons and holes diffusion velocities are to slow, then the connected limited lifetimes ($\tau_{n,}$ τ_p) are not sufficient enough to transport these charge carriers behind its charge conduction layer, and recombination happens, which also reduces the cell's D_n and its efficiency. To thick absorber layers lead, therefore, even in an increased recombination of charge carriers. On the other hand, too thin absorber layers, for a given absorption rate, as defined by the average optical decay length (λ_{ave}), do result in losses as too much of the solar irradiance is reflected at the back reflector and escape from the solar cells absorber layer back to the sky. However, such an effect can be reduced by light trapping, which not only increases the J_{sc}, and therefore the PCE, but also allows an absorber layer reduction while maintaining almost the same high efficiency in thin absorber layers, down to a certain thickness.

Another recombination process is defined by a too low built-in voltage (V_{bi}). As in PSCs the transport of charge carries is defined in a dominant form by the drift, rather than the diffusion force of charge carriers, a too low V_{bi}, leads to the effect that the internal electrical field is not strong enough to transport the charge carriers behind its inherent charge conduction layer, therefore, leading to recombination effects at the transition surface from the absorber to the charge conduction layer.

While the present solar cell model considers these recombination effects and losses, further influences can lead to additional recombination effects in the absorber layer of manufactured solar cells, which can, however, be avoided by adequate manufacturing. E.g., nanoscale-pinholes in the absorber layer, which can lead to parasitic charge carrier conduction. The use of, e.g., the diethyl ether dripping during spin coating, avoid pinholes in suitable manufacturing (AHN; SON; JANG; KANG *et al.*, 2015). High-resolution imaging techniques, such as the Scanning Electron Microscopy (SEM), can be used to identify pinholes (AHN; SON; JANG; KANG *et al.*, 2015) and provide, thus, a manufacturing quality control, concerning such effects.

2.8.4 The theoretical upper limit of the efficiency

While the highest state-of-the-art PCE of a manufactured PSC is already 25.2% (NREL, 2020), perovskite solar cells show still a high improvement potential. Considering in a simplified PSC model, only optical recombination losses, the maximal efficiencies of 30%

(YIN; SHI; YAN, 2014), 30.88% (SHA; REN; CHEN; CHOY, 2015) and 31.3% (MARTYNOV; NAZMITDINOV; MOIÀ-POL; GLADYSHEV *et al.*, 2017) can be obtained theoretically in single-junction MAPI cells. Furthermore, using zero surface recombination velocities and ideal light trapping in a drift-diffusion model, a PCE of 29.9% can be obtained (REN; WANG; SHA; CHOY, 2017). These upper limits are, as expected, below the highest attainable PCE of single-junction cells with the thermodynamic limit of 33.7% for the black-body irradiance spectrum (SHOCKLEY; QUEISSER, 1961), and 33% for a measured irradiance spectrum (RÜHLE, 2016). With our used analytical solar cell model such high efficiencies are only approximated, obtaining a high maximal efficiency of 27.8% for an arbitrary selected maxima improvement of the material properties with an improvement factor of f_B = 160 (Figure 4.3, page 106), and 32.1% for extreme high property improvements considering material properties improvement of f_B = 1000 (Figure B.1, page 193) material properties improvements.

2.9 MULTIDIMENSIONAL OPTIMIZATIONS

Multidimensional optimizations are state-of-the-art to solve many engineering problems to find, e.g. (i) the optimal power flow in electric power grids (CROW, 2009), (ii) the lowest cost design of a wind turbine synchronous generator (BAZZO; KÖLZER; CARLSON; WURTZ et al., 2017), or the minimal series resistance in a GaAs solar cell (ALGORA; DÍAZ, 2000).

2.9.1 Multidimensional optimization of solar cell models

In the analyses of a cell's drift-diffusion model, a multidimensional optimization is useful to demonstrate that the simultaneous variable improvement results in much higher efficiency increases than in state-of-the-art one- and two-dimensional optimization techniques. Additionally, the multidimensional optimization can lead (i) to a better understanding of the optimization process and (ii) to the proposal of advanced solutions for future high-efficient solar cell design concepts as proposed in this thesis.

However, in the area of perovskite solar cells, most of the authors use only one-dimensional (TARETTO; SOLDERA; KOFFMAN-FRISCHKNECHT, 2017) or two-dimensional model optimizations (SUN; ASADPOUR; NIE; MOHITE *et al.*, 2015), as similar as used in the research of manufactured solar cells. In the area of amorphous silicon solar cells (a-Si) (VICENTE; WOJCIK; MENDES; ÁGUAS *et al.*, 2017) use simple heuristic search methods, to improve the cell's efficiency. Its optimization is based on statistical modeling using the multivariate analyses. The method is based on the random variation of model variables, with the following statistic evaluation of observed tendencies. As a result, the method estimates an area where the global maximum is localized. The authors (VICENTE; WOJCIK; MENDES; ÁGUAS *et al.*, 2017) improved the efficiency by 24%, resulting in an optimized PCE of 8.85%.

The use of the Nonlinear Programming (NLP) optimization algorithm for the efficiency maximization of an analytical solar cell model, as here proposed, is of importance as it not only leads to the exact solution of the global maximum but also reduces the number of necessary repetitive simulations of the cell's J-V curve, to obtain this optimal PCE. Rather than indicating an area where the maximum efficiency can be localized, it results in the exact location of the optimal efficiency value, which shows no variation in two decimal cases by repeated optimizations. The low computational cost and the exact solution allows the use of the model for a large number of optimizations under variable boundary conditions or restrictions, whose results we use in this thesis to elaborate design proposals of the PSC, and in-deep analysis of the optimized solar cell, especially concerning the specification of its ideal material properties, as here presented. The use of an NPL optimization for solar cells was first introduced for a planar organic solar cell (KRATZENBERG, 2015a) and a pin-type perovskite solar cell (KRATZENBERG, 2015b) and also appeared in the poster presentation of (KRATZENBERG; RAMBO; RÜTHER; BEYER, 2015). Furthermore, it was used to elaborate several optimal solar cell designs (KRATZENBERG; RAMBO; RÜTHER, 2019).

2.9.2 Optimization algorithms

Optimization techniques work in a multidimensional variable space and come historically for the first time available in the area of linear programming techniques (LP) and were then generalized to nonlinear programming techniques (NLP) (YE, 2011). The linear or

nonlinear specifications refer to the improvement of linear and nonlinear continuous functions, which are locally differentiable, and for which a global minimum or maximum has to be localized. The LP and NLP techniques do have a considerable speed advantage in comparison to (i) the population-based meta-heuristic methods (NAZARI-HERIS; MOHAMMADI-IVATLOO; GHAREHPETIAN, 2017) or (ii) the statistical optimization methods (VICENTE; WOJCIK; MENDES; ÁGUAS *et al.*, 2017), as they advance in the direction of the global minimum or maximum by the calculation of a combined multidimensional gradient in hypercube function space.

Evolution based search methods, such as the particle swarm optimization, advance a whole population of points, which has the unique advantage, in comparison to the NLP that its algorithm has a better ability to avoid local maximums, which is of particular interest in the optimization of complicated functions, which have several local maximums. However, the resulting lower computational cost with the LP and NLP techniques is of particular benefit for the optimization of models, which have to be maximized or minimized in a multidimensional function space, where each optimization step considers a single simulation of the analyzed function or model to find the global PCE maximum, as in the case of the present optimization of a PSC model. Furthermore, the low computational cost allows the repetition of many separate optimizations, which are here used for the detailed analysis of the perovskite solar cell model.

The first iterative optimization techniques in the area of LP techniques were used in the optimization of continuous functions and came available with the Newton and Simplex methods. The latter approach was successfully used for approximately 50 years (LESAJA, 2009). For each one of the model variables of an analyzed function, the upper and lower limits represent the simplest delimitation of the considered function space. In the case of two-dimensional function spaces, such restrictions result in a rectangular search space, and in multidimensional optimizations, these limits result in a hypercube space of model variables. Additionally, to these range constraints, further equality and inequality constraints can be specified, which can define specific relations between the model variables and can restrict the optimization to sections or areas of particular formats or shapes within the function space. Convex or concave functions, in a hypercube space, can be optimized by the identification of a stationary point by setting the first derivative to zero, using Fermat's theorem. A stationary point is a location, which shows no gradient in the considered function. While the global or

local maximums in a maximization are also stationary points, many of the identified stationary points are not related to such maximums, as they can represent simple locations with no gradients in the multidimensional space. In these cases, the introduction of Lagrange multipliers gives a better solution to the global maximum within such a function space (YE, 2011). Whereas the Lagrangian multipliers are only usable with equality constraint equations, the Karush–Kuhn–Tucker (KKT) conditions present first-order conditions, which generalize the Lagrangian multiplier constraints in the sense that also inequality constraints are imposable to the LP and NLP problems. The KKT conditions give, therefore, a hypothesis to the global maximum in a concave function space, which is additionally delimitated to specific areas by the determined inequality constraints (ARORA, 2004).

The here used routine *fmincon* of the Matlab™ program is based on the state-of-the-art NLP techniques using inclusively Interior Point Methods (IPM), which do reduce the computational effort by a factor of 40, if compared to the SM method (YE, 2011). While in the SM, the main idea is to walk from vertex to vertex to find in iterative steps the global maximum of a function, the IPM optimization is conducted in a way that it walks from point-to-point within the interior of a feasible region, localized in the proximity of an optimum vertex line as illustrated in (LESAJA, 2009). The optimization algorithm restraints progressively the area of this feasible region while it advances along an identified vertex line in the course of the search process. This process leads, therefore, to a successive approximation to the global optimal point. Furthermore, the interior-point methods do incorporate two powerful tools (BYRD; HRIBAR; NOCEDAL, 1999): (i) the sequential quadratic programming (SQP) techniques, which can additionally handle nonlinearities, within the inherent constraint equations and (ii) trust region strategies (TRS), which allows the algorithm to treat concave and non-concave regions in a unique treatment.

Additionally, the IPM incorporated in *fmincon* also includes a line search method (LSM) (BYRD; HRIBAR; NOCEDAL, 1999), which presents a modification strategy in the KKT system. Whereas the KKT, of an IPM, solely defines the direction in which the search algorithm must advance, the LSM extends this specification by the calculation of an adequate step-width for advances in this search direction. This correct step-width ensures that, in a single optimization step, a crescent merit function is obtained, which means that in such a step the modeled solar cell efficiency can only increase but not decrease. The basic idea of the working principle of the LSM is that it advances in orthogonal steps and identifies by use of a

step width estimation in the multiple function space the specific point at which the stepping trajectory forms a tangent to one of the isopleths of the function to be optimized (CMU (2000) - figure 22) in a hypercube space of variables. Isopleths are height lines of unique energy level or, in the present case, a unique efficiency level in a concave function space. The correct working principles of how the LSM controls by matrix calculus the correct step-wide in a multidimensional function are presented, e.g., in (LUCAS; KIM; CHIN; GUO, 2008).

2.10 HOW TO INCREASE THE CELL'S EFFICIENCY

In this thesis, we present design proposals of high-efficiency perovskite solar cells based on the improvement of its material properties. However, only from this research, it is not known which manufacturing methods can be used to manipulate the manufacturing process to configure a manufactured PSC that presents the specified properties, and therefore, a high PCE. Only with such information, the knowledge obtained from the multidimensional optimization returns in know-how, as essential for the development of perovskite solar cells. In the following sections, we (i) review several high-efficiency cell designs, and (ii) present references, which showed nearly ideal material properties, if compared to the ideal properties obtained in our multidimensional optimizations in section 4.2, page 105.

2.10.1 High-efficiency single-junction perovskite concepts

If compared to other solar cell types, the single-junction PSC presents the highest gradient of the record efficiency values of manufactured cells in (NREL, 2020), because of its excellent material properties. Furthermore, there is a large variety of perovskite materials that can be used for the constitution of PSCs (GANOSE; SAVORY; SCANLON, 2017). One favorite PSC is the $CH_3NH_3PbI_3$, also abbreviated as MAPI (ROLDAN-CARMONA; GRATIA; ZIMMERMANN; GRANCINI *et al.*, 2015). The authors observed that the use of stochiometric excess of the PbI_2 precursor solution, concerning the MAI precursor, results in an improved crystallinity, and therefore, electron transport from the absorber layer to the electron conduction layer, which leads to measured efficiency of 19.1%. The authors (AHN; SON; JANG; KANG *et al.*, 2015) developed a perovskite solar cell with a highly reproducible PCE via Lewis Base Adduct of Lead (II) Iodide. The authors demonstrated how the treatment

with diethyl ether during the spin coating process avoids pinholes in the absorber layer. Its manufactured cells lead to an efficiency of (18.7 ± 0.7) %, with the maximal certified value of 19.7%.

The authors (YANG; NOH; JEON; KIM *et al.*, 2015) developed a PCE with a PCE of 20.2% using as absorber layer material formamidinium lead iodide $CH(NH_2)_2PbI_3$, also abbreviated with FAPI, which presents a broader absorption spectrum. The authors (SALIBA; MATSUI; SEO; DOMANSKI *et al.*, 2016) show that a triple cation cell made of $(MA,FA,Cs)PbI_3$ results in a high PCE of 21.1%. They demonstrate that large uniform crystals, extending from the electron to the hole conduction layer, are produced by seed-assisted crystal growth. This cell also presents a low long-term degradation and high reproducibility of the PCE values in manufactured prototypes.

The authors (YANG; PARK; JUNG; JEON *et al.*, 2017) present an introduction of additional iodide ions in the organic cation solution, as used for the coating of a mixed $(FAPbI_3)_{0.95}(MAPBr_3)_{0.05}$ absorber layer. These additional iodide ions reduced the concentration of deep-level material defects. The fine-tuning concerning the energy level of its absorber layer results in a band gap of 1.51 eV. The resulting cell presents reduced interstitial, and antisite crystallographic defects, obtaining an efficiency of 22.1%. While the former defect present atoms in a crystalline structure where there is usually no atom, the latter happens when atoms of different materials exchange positions in an ordered alloy or compound. The authors (JUNG; JEON; PARK; MOON *et al.*, 2019) propose a device with a special concept including two absorber layers in a single-junction PSC. They combined a wide- with a narrow-band gap absorber layer, which results in a PCE of 22.7%, and a J_{sc} of 24.88 mA/cm^2.

As in the previously presented cell, the wide band gap absorber layer is constituted by $(FAPbI_3)_{0.95}(MAPBr_3)_{0.05}$, and this layer is coated on the top of a narrow band gap absorber layer, as made by an in situ reaction of n-hexyl trimethyl ammonium bromide. This concept not only results in an efficiency increase but also presents improved long-term stability of its PCE. In a 1400 h test run under 1-Sun illumination, the device's PCE degraded by only 10%. The authors (JEON; NA; JUNG; YANG *et al.*, 2018) used a fluorene-terminated spiro-OMeTAD alike hole transport layer (9,9 -dimethyl-9H-fluoren-2-yl), abbreviated as DM-HTL, which allowed a fine-tuning of its energy level. The cell resulted in an efficiency of 23.2%, with a short circuit current density of J_{sc} = 24.9 mA/cm^2, an open-circuit voltage of

V_{0C} = 1.14 V, and a fill factor of FF = 81%. The developed absorber layer made of $(FAPbI_3)_{0.95}(MAPBr_3)_{0.05}$ also resulted in a higher long-term stability of the PCE.

2.10.2 The surface recombination velocities

As identified by the combination of s = 91 possible variable combinations in section 0, page 95, the reduction of the surface recombination velocities s_f and s_b leads to the highest independent PCE improvement, if compared to the improvement of the further variables. Therefore, we recommend that a suitable optimization of manufactured PSCs should start with and mainly focus on the reduction of the surface recombination velocities. Principally s_f must be reduced, as close to the front charge conduction layer, most of the free charge carriers are converted form photons in excitons and the resulting electrons and holes, by the division of the excitons. The lowest measured values of these variables were obtained in (WANG; FU; JARIWALA; SINHA *et al.*, 2018), which reduced the surface recombination velocities to the values of 10 cm/s and 20 cm/s (Appendix Table B.5, page 197) using the materials TiO_2, and PVK, for the coating of the electron, and the hole transport layers. Considering the s_f and s_b as obtained in (SUN; ASADPOUR; NIE; MOHITE *et al.*, 2015), the use of such charge conduction layers reduced the surface recombination velocities by $1/f_B$ = 1.92 and 10 times (19.2 m/s / 10 m/s = 1.92 and 200 m/s / 20 m/s = 10). The authors used a time-resolved photoluminescence method to experimentally analyze the surface recombination velocities of 14 different electron- and hole-extracting layers, including TiO_2, SnO_2, ZnO, PCBM, ITIC, ICBA, TPBi, PEDOT:PSS, PTAA, PVK, NiO, MoO_3, WO_3, and spiro-OMeTAD.

2.10.3 The built-in voltage

In perovskite solar cells the charge carrier transport is dominated by the drift force, as produced by the built-in electrical filed (ZHANG; WANG; YUAN; WANG *et al.*, 2019). Earlier PSCs showed a to low value of the built-in electrical field, providing an insufficient drift force to separate charge carriers and sustain its transport, which therefore results in the nonradiative recombination of charge carriers (CHUNG; KIM; KIM; KIM, 2009; YUAN; REECE; SHARMA; PODDAR *et al.*, 2011). As discussed by the authors, small V_{bi} will make the charge carriers be either (i) captured in trap states or (ii) accumulated at the transport layer interfaces, because of the insufficient drift force provided.

The authors in (ZHANG; WANG; YUAN; WANG *et al.*, 2019) developed a method to increase the PSC's performance via the combination of (i) internal doping of the intrinsic layer using a polarized ferroelectric polymer (PFE) and (ii) the external control by an electric field during the annealing process, where the coated cell is positioned between two plates with different voltage potentials (ZHANG; WANG; LI; LIU *et al.*, 2018). A group of PFE materials is used for the doping of a small part of the $MAPbI_3$ layer, being localized between the perovskite and the hole transport layers, to enhance the built-in electric field. As the authors found out, this additional PFE layer also improves the crystallization of the $MAPbI_3$ absorber layer and reduces the nonradiative recombination in PSCs. This combined effect leads to a substantial reduction in the V_{bi} losses of 0.14 V, as measure by electroluminescence, resulting in the high V_{bi} of 1.36 V. However, too high built-in fields, obtained as a result of a too high doping of the charge conduction layers, not only result in high built-in voltages but can also lead to PCE losses, as carrier lifetimes are an inverse function of doping density, as discussed in (GREEN, 2009).

2.10.4 The diffusion coefficients

Considering the lifetime and diffusion length as dependent properties, many authors measured an efficiency increase, because of a higher and not shorter measured lifetime. However, we consider that the lifetimes and the diffusion lengths as independent properties, which specify in its conjunction the diffusion coefficient, also defined as the diffusivity.
Our multidimensional optimization shows that the cell's efficiency increases as a function of increased diffusion coefficients. The diffusion of electrons and holes defines the spreading of these charge carriers in random directions and is defined by the Fick's law (KITAI, 2011). As the diffusion coefficients of electrons and holes are determined by the expression (4.1), they can be increased by either, (i) the augmentation of the electron or hole diffusion lengths L_n and L_p, or (ii) the reduction of its lifetimes τ_n and τ_p, whereas the manipulation of L_n and L_p is more advantageous, because of its quadratic formulation in these equations.

Diffusion length: Perovskite solar cells present a high upper bound of the diffusion length of charge carriers. For example, in a solar cell based on a single perovskite crystal, large diffusion lengths of 175 μm and 3 mm were measured under one sun and weak light

conditions (DONG; FANG; SHAO; MULLIGAN *et al.*, 2015). The authors measured a lifetime of (82 ± 5) μs using a separate method, as defined by the transient photovoltaic and impedance spectroscopy. However, in the manufacturing of perovskite solar cells, as accomplished with a solution-based process, results in much lower diffusion lengths. A reduction of recombination sites by a Lewis Base passivation resulted in a decreased number of trap states at the perovskite crystal terminations and enabled a relatively high diffusion length of charge carriers with values higher than 3 μm (NOEL; ABATE; STRANKS; PARROTT *et al.*, 2014). High diffusion lengths of electrons and holes, of approximately 1.9 μm and 1.5 μm, were observed for $CH_3NH_3PbI_{3-x}Cl_x$ perovskite pin-type cells, as measured by electron beam-induced current (EDRI; KIRMAYER; MUKHOPADHYAY; GARTSMAN *et al.*, 2014). High diffusion length of electrons and holes of 1.7 μm and 6.3 μm, were also observed by (LI; YAN; LI; WANG *et al.*, 2015) for a pin-type MAPI cell. The authors measure a lifetime of superior to 100 ns using the photoluminescence method, where the fluorescent lifetime of a spin-coated MAPI absorber layer depends on the film thickness and increases with the thickness increase of the absorber layer up to approximately 250 nm.

While many authors determine the diffusion length indirectly, by (i) the measurement of the electron and hole lifetimes, (ii) an estimated diffusion coefficient from former references, and (iii) the use of equations (A.33) and (A.34), page 169, we think that such a procedure is not correct, as these properties should be determined by direct measurements. For the diffusion lengths, such measurement can be accomplished by the scanning photocurrent microscopy (SPCM), as used in (XIAO, 2019).

Lifetime: The electron and the hole lifetimes are the limited times in which these charge carriers can diffuse in the absorber layer, and therefore, they might also be defined as the transport time before its recombination happens. These times are related to the fast decay of a cell's photoluminescence, which is used as a measurement method for the determination of the lifetime. Whereas it is usually conceived that the higher lifetime increases the efficiency, the authors (SONG; CUI; WANG; WEI *et al.*, 2015) show that if a post-annealing process treats the coated PSCs with a temperature of 160 ºC, (i) an n-type doping of the absorber layer, and (ii) a lifetime reduction of electrons and holes from 44 ns to 22.6 ns are obtained. Such a treatment increases the cell's efficiency from 6% to 16.4%, not only as a function of the lifetime reduction, but also as a function of the increase of the short circuit

current density, as the post-annealing process does also improve the absorption of this solar cell.

2.10.5 The average optical decay length

The process of cell's light absorption and its conversion in free charge carriers is defined in (SUN; ASADPOUR; NIE; MOHITE *et al.*, 2015) using the average optical decay length (λ_{ave}), as based on the Beer-Lambert law (equation (A.18), page 164). Lower λ_{ave} values increase the absorption of light, which results in a growth of the short circuit current density (J_{sc}). Another measure to specify the light absorption is given by the absorption coefficient, which can be measured as a function of the wavelength. Absorption coefficients of MAPI, as used (SUN; ASADPOUR; NIE; MOHITE *et al.*, 2015), are still higher than highest-efficient single-junction GaAs cells, basically over the whole wavelength range (YIN; SHI; YAN, 2014). Such a high absorption of PSC is remarkable, because the GaAs cells are among the highest-efficiency single-junction state-of-the-art solar cells, presenting a PCE of 28% (NREL, 2020). As a result of its higher light absorption, the theoretical efficiency limit of an ideal MAPI cell is 30% (YIN; SHI; YAN, 2014).

Furthermore, the absorbance figures published elsewhere show that the absorbance values of a formamidinium lead trihalide (FAPI) PSCs are still significantly higher than the corresponding values of the MAPI cells (EPERON; STRANKS; MENELAOU; JOHNSTON *et al.*, 2014; GREEN; JIANG; SOUFIANI; HO-BAILLIE, 2015). The authors observed this behavior over almost the whole analyzed spectrum range up to 800 nm, which should, therefore, lead to a theoretical upper limit superior to 30% for the FAPI cells. In fact, a mixed absorber layer PSC made of $(FAPbI_3)_{0.95}(MAPBr_3)_{0.05}$, lead to the highest state-of-the-art efficiencies based on the reports in several scientific publications (section 2.10.1, page 70).
The correct selection of the post-annealing temperature and time leads to a further increase in the absorbance values of perovskite solar cells (FEDELI; GAZZA; CALESTANI; FERRO *et al.*, 2015; KHATIWADA; VENKATESAN; ADHIKARI; DUBEY *et al.*, 2015). The latter authors obtained the highest absorption coefficients for annealing temperatures of 120 ºC, and 110 ºC; for a MAPI, and a mixed $MAPbI_{3-x}Cl_x$ (x = 0.19) PSC, while the highest efficiencies they obtained for 120 ºC and 80 ºC. The MAPI presents a PCE increase by factor 1.04 if this temperature is increased from 80 ºC to 120 ºC, indicating that higher post-annealing

temperatures lead to ta slight advantage only for MAPI, but not for the mixed halide PSCs. Post-annealing also has an ideal time of 10 min, which leads to the highest absorption coefficients of MAPI cells annealed at 80 ºC (KUMAR; SOLEIMANIOUN; SINGH; SINGH *et al.*, 2020), as longer times lead to the cell's degradation.

Light trapping: Different light-trapping techniques (TANG; TRESS; INGANÄS, 2014) also lead to a considerable improvement of the light absorption in PSCs. If, e.g., spherical metal NPs of distributed size are inserted into the absorber layer, a collective oscillation of the electrons' conduction band happens because of the NP's optical excitation with light waves. These oscillations present a frequencies, which are similar to the NP's inherent resonance frequency and provokes a strong spherical scattering of light partitioning from each of the NP's center, which leads then to the plasmonic light-trapping effect (HSU; JUANG; CHEN; HSIEH *et al.*, 2015), (CAI; PENG; CHENG; GU, 2015). The spherical light scattering increases the total optical path length of the irradiances' rays within the absorber layer, which increases, therefore, its absorption (CAI; PENG; CHENG; GU, 2015). As this resonance frequency is a function of the NP's size, a carefully engineered and tuned distribution of the particle sizes, added to the solar cell's absorber layer do increase the absorption of ultraviolet and visible light. Such sizable spherical NPs can be cost-effectively synthesized and deposited by Nanosphere Lithography (NSL) (LUCAS; KIM; CHIN; GUO, 2008; SALEEM; TILAKARATNE; LI; BAO *et al.*, 2016).

The light-trapping effect inherent to plasmonic NPs can be modeled by the finite difference time domain method (FDTD) method (CAI; PENG; CHENG; GU, 2015), and the numerical simulations, using this method of high spatial resolution, predict highest J_{sc} increases for lumpy Ag particles inserted into the backside of the PSC's absorber layer. Results with manufactured PSC show a J_{sc} increase by 1.2 and, while the PCE increases 1.22 times on average (LIU, 2017). The author used a 130 nm thick absorber layer and added distributed size NPs with an average diameter of 11 nm. However, simulations in (CAI; PENG; CHENG; GU, 2015) show in the best case, a J_{sc} increase by the factor 1.5 rather than 1.2 for the same absorber layer thickness. The lower J_{sc} increase in manufactured cells may be ascribed to (i) undesired conduction effects, as related to a high volume density of NPs, (ii) pinholes, in thin absorber layers, but might also be related to a (iii) a different sizing of the NPs or (iv) its location within the cells absorber layer.

2.10.6 The absorber layer thickness

In our optimizations, we obtained the highest efficiencies for two ideal absorber layer thicknesses, which both consider light trapping (Section 4.2, page 105). In the first, the absorber layer thickness of 400 nm is the same as without light trapping, and light trapping increases the cell's current density considerably, therefore, also increasing the cell's efficiency. In the second case, the absorber layer is reduced to 160 mm, which results in a something lower short circuit current density, but because of the higher MPP voltage, the efficiency is only 0.2 % lower as in the former case. We consider both cases as ideal concepts, the first case because of its slightly higher PSC, and the second case, because of the lower absorber layer thickness, and therefore, the more moderate Pb use.

Meanwhile, in both cases, the absorber layer thickness hast to stand in a close relationship to the average optical decay length (λ_{ave}) for high efficiencies. Therefore, an adequate tuning of the absorber layer thickness as a function of λ_{ave} is necessary in any case (Figure 4.2e and Figure 4.2f, page 102). Techniques that allow an adjustment of the absorber layers are specified, e.g., in (ZHOU; YANG; WU; VASILIEV *et al.*, 2015) using the solvent-solvent extraction method, which results in a maximal efficiency of 15.2%. Furthermore, for the spin-coating process the absorber layer thickness can be tuned independently by the manipulation of (i) the PbI_2 : CH_3NH_3I precursor concentration, of a MAPI cell; and (ii) the rotation speed of the spin coater as shown in (ZHANG; ZHANG; PANG; HUANG *et al.*, 2016). The authors obtained a maximal PCE of 9% for a MAPI cell with a 300 nm thick absorber layer, showing at this thickness the largest grain size, which results in the largest charge carrier mobility.

2.10.7 Quantity of excess holes and electrons

The number of excess holes and electrons that participate in the recombination process, $\Delta p = p - p_0$, and $\Delta n = n - n_0$, as used for the modeling in equations (A.6) and (A.7), page 160, are already located within the region of the highest efficiency (Figure 4.2d, page 102). Furthermore, it can be seen that Δp and Δn are not improved by the optimization algorithm (Table 4.1, page 103; Figure 4.2d, page 102). Because of its registered irrelevance in the optimization process, we do not analyze how these properties can be improved further.

2.10.8 The thicknesses of the electron and hole conduction layers

As shown by measurements in (MARINOVA; TRESS; HUMPHRY-BAKER; DAR *et al.*, 2015), the thickness variation of the charge conduction layers modifies the PCE minimally. E.g., for a thickness reduction of the spiro-OMeOTAD hole conduction layer, from 600 nm to an ideal value of 200 nm, the measured PCE increased from (12.3 ± 1.2) % to the value of (13.5 ± 0.4) %. For this thickness reduction, the measured series resistance decreased from 40.2 Ω/cm^2 to the value of 21.8 Ω/cm^2. (KIM; OHKITA, 2017) analyzed the influence of the thickness of the hole transport layer and found an efficiency increase from 18% for a 310 nm thick spiro-OMeTAD layer to a value of 19.2% for an ideal thickness of 130 nm. The measured series resistance reduced from 9 Ω/cm^2 to the value of 6 Ω/cm^2 for this thickness reduction.

The authors (ZHAO; LIU; LIN; CHEN *et al.*, 2018) analyzed the thickness of a NiO hole conduction layer and found an ideal thickness of approximately 30 nm by simulation, which lead to the highest PCE of 21.5%. This NiO thickness reduction leads to a significant efficiency increase, which raises from initially 17%, for a thickness of 220 nm, to the maximum value of 21.5% from a 30 nm thickness, an effect mainly related to the increased FF in the case of a thin NiO layer, because of its lower series resistance. For the measured efficiency values, they obtained an efficiency rise from 14.19%, for a 76 nm thick NiO layer, to the value of 17.03%, for a 40 nm thick NiO hole conduction layer. They also analyzed the thickness-dependent efficiency of the PCBM electron conduction layer and found a measured efficiency increase from 14.07%, for a 78 nm thick electron conduction layer, to 16.86% for an ideal thickness of 55 nm.

In analyzing the materials TiO_2, WO_3, ZnO Nb_2O_5, CdS and $Cd_{0.4}Zn_{0.6}S$ (PHILLIPS; RASHED; TREHARNE; KAY *et al.*, 2016) found that the short circuit current density depends mostly on the used material of the electron conduction layer in a nip-type perovskite cell, rather than on its thickness. The authors found by simulation with the OTM method that the Trioxide de tungsten (WO_3) results in a superior J_{sc} basically for all n-type layer thicknesses, if compared to the further materials, resulting in the highest J_{sc} of 22.5 mA/cm^2 for a ~ 65 nm thick electron conduction layer, which leads to a 3.4% increase of J_{sc} if compared to a 170 nm thick layer.

3. METHODOLOGY AND MODELING

A theory can be proved by experiment; but no path leads from experiment to the birth of a theory.

Albert Einstein, Physicist

Some fundamental questions should be answered to develop a PSC, which presents the highest possible PCE. These are: (i) which multiple material properties and cell design parameters are necessary to be improved simultaneously; (ii) should the value, of each considered variable, be increased or decreased; (iii) to which exact value each variable must be ideally tuned; and (iv) which of the variables presents the highest sensitivity in respect to the increase of the cell's efficiency, and should, therefore, prioritized in its variable tuning. We answered these questions here using a drift-diffusion model, as proposed in (SUN; ASADPOUR; NIE; MOHITE *et al.*, 2015), and (SUN, 2018), by searching the maximum efficiency in a multidimensional function space of material properties and manufacturing parameters, using a numerical optimization algorithm. The answers to these questions we obtained by the adequate setup of the optimization algorithm and analyses of the optimized results, as coming available using the multidimensional optimization algorithm.

3.1 OPTIMIZATION IN A HYPERCUBE SPACE OF VARIABLES

We selected the analytical solar cell model, as introduced in (SUN; ASADPOUR; NIE; MOHITE *et al.*, 2015), as it allows a modeling as a function of several measurable material properties, and results in a short simulation time of its JV-curve, which allows extensive analyses of considered MAPI perovskite solar cell. The (i) complete model formulation, (ii) its assumed simplifications, and (ii) its derivation method we present in , page 155. The selected NLP optimization model as shown in section 2.9.2, page 67, we choose because of (i) its multidimensional character, (ii) allowing equality and non-equality constraints, and (iii) its short simulation time, (iv) combining several advanced methods. Compared to the use of (i) a numerical PSC model, and (ii) random search methods, the selected model and optimization method reduce the computational optimization cost significantly. This reduced cost enabled us to accomplish a large set of optimizations, using in each of these optimizations, different constraints for the model's variable set.

The approximations made in (SUN; ASADPOUR; NIE; MOHITE *et al.*, 2015) for the selected analytical model result in a low fitting deviation of only 0.1%, between the measured and the simulated PCE values. This small deviation is insignificant, considering that outdoor-spectral variations can lead to PCE uncertainties up to 3% in thin-film cells (RÜTHER; KLEISS; REICHE, 2002). The used model defines the cell's electron and hole transport schemes in the dark and under light exposure, as obtained from a set of four second-order drift-diffusion differential equations, and its boundary equations in (SUN; ASADPOUR; NIE; MOHITE *et al.*, 2015). A fifth second-order differential expression, as defined by the Poisson equation, and its two boundary equations, the authors used for the simulation of the electric field. In Figure 3.1a, page 81, we present a detailed charge transport scheme of the used pin-type PSC, while Figure 3.1b illustrates the charge generation of this cell as a function of different average optical decay lengths (λ_{ave}), which corresponds to different absorption properties.

The proposed numerical optimization of this analytical PSC model uses a nested optimization scheme to improve the cell's efficiency. This scheme considers the modification of the cell's material properties and its absorber layer thickness at various improvement scales via equations (3.1) to (3.11), pages 83 to 88. The proposed general scale of the variable improvements, as here adopted for the most of the considered variables, we define by the concept of a hypothetical boundary-expansion factor (f_B), as given in equation (3.5), which defines the positive and negative range of variation of an analyzed variable or material property. The utilization of a considered fixed short circuit current density (J_{sc}), as used for the one-dimensional thickness optimization in (SUN; ASADPOUR; NIE; MOHITE *et al.*, 2015), is here improved by considering of an absorber layer thickness-dependent current density, connected to the use of light trapping with plasmonic silver (Ag) nanoparticles as presented in (CAI; PENG; CHENG; GU, 2015). In this context, equation (3.11) specifies a correction of the constant J_{sc} under consideration of light-trapping effects in a manufactured PSC.

Based on Finite Difference Time Domain (FDTD) simulations in (CAI; PENG; CHENG; GU, 2015), our optimized solar cell architectures present spherical light-trapping nanoparticles in thin absorber layers. These nanoparticles can increase the short circuit current

density of a pin-type PSC without light trapping J_{sc} = 23 mA/cm^2), for a broad range of absorber layer thicknesses between 50 and 400 nm.

Figure 3.1 - Energy band diagram and diagram of the normalized charge generation $G(x)$ by the Beer-Lambert law

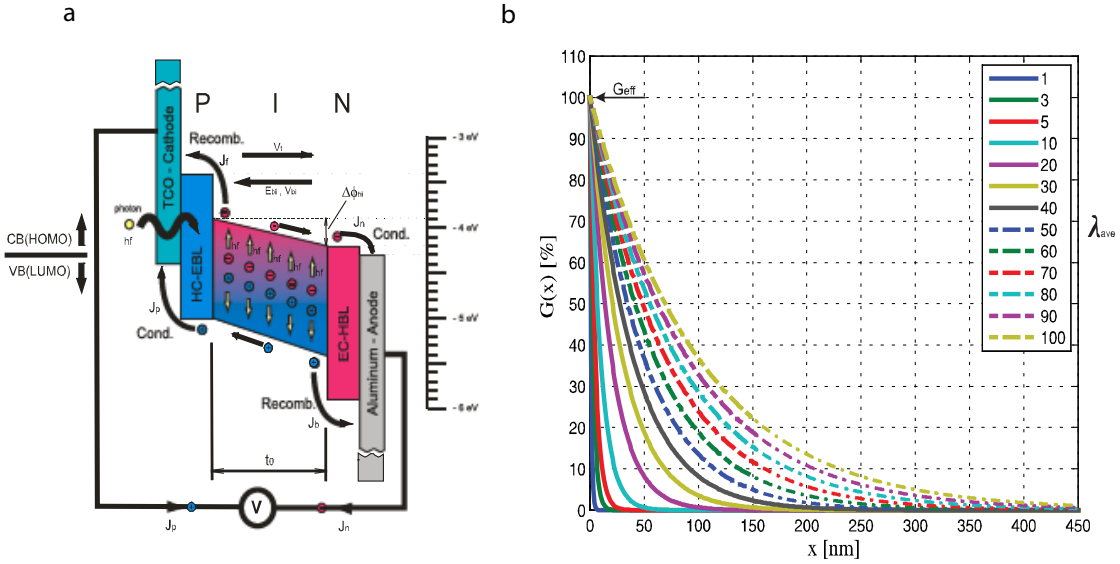

(a) Energy potential diagram and charge carrier trajectories of a planar pin-type heterojunction perovskite solar cell, as modeled in (SUN; ASADPOUR; NIE; MOHITE *et al.*, 2015), presenting from left to right side the: (i) transparent top cover (not visualized here); (ii) cathode layer made of a Transparent Conductive Oxide (TCO); (iii) p-type hole conduction and electron blocking layer, made of organic material PEDOT:PSS; (iv) i-type intrinsic charge generation layer, or absorber layer, with thickness t_0 = 450 nm made of the hybrid MAPI perovskite material; (v) n-type electron conduction and hole blocking layer, made of organic material PCBM; and (vi) anode layer made of aluminum. The figure was adapted from figure S1.1a in (SUN; ASADPOUR; NIE; MOHITE *et al.*, 2015). (b) Approximation of the normalized charge generation profiles $G(x)$ as a function of the penetration depth (x = 0…450 nm) on the abscissa, calculated for several average optical decay lengths of λ_{ave} = 1 to 100 nm using the Beer-Lambert formulation considering cells with (λ_{ave} < 100) and without light trapping (λ_{ave} = 100 nm).

3.2 INDEPENDENT AND DEPENDENT OPTIMIZATION VARIABLES

We intend to provide supporting knowledge, and know-how, for research laboratories and the manufacturing industry of PSCs to enable the manufacturing of cells with higher and highest efficiencies. Our used analytical model makes use of the following independent model variables: the surface recombination velocities of the cell's front and back

charge conduction layers (s_f, s_b), the diffusion coefficients of electrons and holes (D_n, D_p) the built-in voltage (V_{bi}), the average optical decay length (λ_{ave}), the number of excess electrons and holes (Δn, Δp), and the absorber layer thickness (t_0). Apart from these independent variables, we remark that the present optimization improves involuntarily also the model's dependent variables, which are: (i) the mobilities of electrons and holes (μ_n , μ_n), (ii) its diffusion lengths (L_n, L_p), and (iii) its lifetimes (τ_n, τ_p). These variables are not necessary to be used as optimization variables as, (i) μ_n and μ_n are a function of the independent diffusion coefficients (D_n and D_n), because of the Einstein relation (equations (A.40) to (A.44) , page 172), and (ii) as the diffusion coefficient D_n and D_p, also named as diffusivities, are calculated from the diffusion lengths of electrons and holes (L_n, L_p) and its lifetimes (τ_n, τ_p), as presented in equation (4.1), page 108, which are measurable with independent methods.

3.3 THE MULTIDIMENSIONAL OPTIMIZATION

The analytical model results in the shape of two J-V curves of the PSC cell, (i) its photogeneration curve for irradiance considering an air mass of 1.5 (AM1.5), and (ii) its curve under exposition to the complete dark. While the former curve models the current density, without considering recombination effects, the latter curve accounts for the different recombination effects within the solar cell. The superposition of both curves results in the measurable J-V curve under AM1.5 irradiance (Figure 4.4, page 111). Its current density (J_{light}) interprets, therefore, recombination effects under standard operating conditions. The multiplication of the current density J_{sc} with the terminal voltage (V) of this curve leads to the cell's power curve.

The present work considers nested optimization scheme, where (i) the first optimization maximize the cell's efficiency, as a function of its material properties and the absorber layer thickness; and (ii) a nested optimization maximize the cell's output power, using its power curve as a function of its terminal voltage, which results in the cell's current density (J_{MPP}), its voltage (V_{mpp}), and the power density (P_{mpp}), as all defined for the maximum power point (MPP). Based on the optimization results and further references, we discuss in section 2.10, page 70, how the PSC's efficiency can be increased for a manufactured PSC, by the combination of several intentional manufacturing methods, which

should result in a cell, which presents a set of ideal material properties, and its related ideal absorber layer thickness.

3.3.1 Modeling

In this work, we propose the numerical efficiency optimizations the PSC's analytical model in a multidimensional function space, which is specified by the following objective function

$$\eta_{max} \rightarrow \max [\ \eta_i(X_{1,i}\ldots X_{9,i})\ ] \quad ; \quad i = 1\ldots N \ , \tag{3.1}$$

where the efficiency η_i in the i-th iteration is a function of the model's nine model variables ($X_{1,i}\ldots X_{9,i}$), building up a nine-dimensional hypercube space, in which the variables have to be optimized. The maximum efficiency (η_{max}) in this space is obtained after $i = 1\ldots N$ model simulations. In searching for the optimal variable values, the optimization algorithm sets up each of the nine model variables to a different value, in every single iteration i, if compared to the step (i-1), using a combination of advanced search methods (Section 2.9.2, page 67). Therefore, each iteration i results in a separate model simulation, using the variable values as obtained by the tunings of the model variables by the optimization algorithm. For the setup of the optimization problem or initial condition of the variables $X_1\ldots X_9$, we considered the values as obtained by the one-dimensional optimization in (SUN; ASADPOUR; NIE; MOHITE *et al.*, 2015), which we resume in Section 3.3.2, page 88. In each of the N steps, the used Matlab™ optimization algorithm, named as *fmincon* improves the values of the whole set of model variables. This algorithm uses Nonlinear Programming (NLP) optimization technique (BYRD; HRIBAR; NOCEDAL, 1999), based on (i) interior point search (IPM), and (ii) line-search (LSM) optimization methods, to find the maximum possible model efficiency in the hypercube optimization space. When the cell's relative efficiency increase is below a specified threshold value, the optimization algorithm identifies the maximum cell efficiency and stops the optimization process. In each of the $i = 1\ldots N$ model simulations, a new calculation of (i) the J-V curves, (ii) the maximum power point (MPP) power density, and (iii) the cell's efficiency (η_i) are accomplished, using equation (3.2). This efficiency we calculate as a function of the nine used model variables $X_{1,i}$ to $X_{9,i}$, representing eight quantum physical

material properties and the absorber layer thickness.

$$\eta_{MPP,i} = (U_{MPP,i}\ J_{MPP,i}(X_{1,i}...X_{9,i})) / G_{AM1.5} = P_{MPP,i} / G_{AM1.5} \quad (3.2)$$

In equation (3.2) $G_{AM1.5}$ = 100 mW/cm² is the standardized solar irradiance at Air Mass 1.5. We obtained the PSC's maximum output power density $P_{MPP,i}$ [mW/m^2] in the i-th optimization step and model simulation by another objective function as follows

$$P_{MPP,i} \rightarrow \max (P_k (J_{light,1} (G_{AM1.5}, V_k, X_{1,i}...X_{9,i})... J_{light,M}(G_{AM1.5}, V_k)) \ ; \ k = 1...M , \quad (3.3)$$

where each $P_{MPP,i}$ is obtained by maximization of cell's power density curve in $k = 1...M$ iteration steps, and where the optimized $P_{MPP,i}$ is related to the PSC's material properties in the i-th optimization step. The cell's analytical model calculates $J_{light,k}$ as a function of the whole set of model variables ($X_{1,i}...X_{9,i}$), its terminal voltage (V_k), and its temperature. In this second optimization, we do not modify the device's material properties and remark that we nested the power density optimization of the equation (3.3) in the efficiency optimization of equation (3.1). This nested optimization process (Appendix Figure B.2, page 196) we subject to the following specific boundary conditions

$$X_{j,min} \leq X_j \leq X_{j,max} \ ; \ j = 1...9 , \quad (3.4)$$

where $X_{j\text{-}max}$ and $X_{j\text{-}min}$ are the maximal and minimal constraints for each one of the nine model variables X_j to be optimized. A single optimization process considers a variable-specific range ($X_{j\text{-}min}$ ...$X_{j,max}$) for each of the nine model variables, allowing the optimization algorithm to modify the associated variables in its specified ranges. By equation (3.5), we define these variable-specific constraints for arbitrary variable range expansions, which provide the precondition to configure a large set of optimizations, each under different boundary conditions. Since we cannot know in advance, which property improvements will be configurable in future cell developments, we set up arbitrary-defined and adjustable range constraints, by a proposed boundary-expansion factor (f_B), which we also named as variable improvement factor, in equation (3.5), where the terms f_B and $1/f_B$ define specific amplification and reduction factors for a model variable in a single optimization process,

which enables the optimization algorithm to search for higher and lower values at different scales for each of the considered material properties within the range of $X_{j\text{-}min}$ and $X_{j\text{-}ma}$

$$X_{j\text{-}min} = (1/f_B)\, X_{j,me} \leq X_j \leq X_{j,me}\,(f_B) = X_{j,max} \quad ; \quad j = 1\ldots9 \ , \tag{3.5}$$

$_x$. In each singular efficiency optimization, the application of f_B results in the values of the upper and lower boundary limits of the model variables ($X_{j\text{-}min}$ and X_{jmin}). In equation (3.5) $X_{j,me}$ represents the variable values of the setup configuration of the optimization process, and $X_{j\text{-}min}$ and $X_{j\text{-}max}$ are the minima and the maxima limits for each of the $j = 1\ldots9$ model variables, as specified in equation (3.4). Our optimizations we accomplish for different absorber layer thicknesses and light trapping effects using $f_B = 1\ldots f_{B\text{-}max}$ optimizations, at an increment of the unity, where $f_{B\text{-}max} = 160$ is the considered maximal boundary amplification factor. Therefore, in the best case, the optimization algorithm can increase or decrease a property by the factor of 160. With the improvement factors in the range of $f_B = 1\ldots f_{B\text{-}max}$, we analyze arbitrary material property improvements as defined by the 160 optimizations for $f_B = 1\ldots f_{B\text{-}max}$. While we judge this range as most probable, for the interested reader, we show higher PCE increases in Appendix Figure B.1, page 193, considering arbitrary material improvements up to an $f_B = 1000$. For the built-in voltage (V_{bi}), the absorber layer thickness (t_0), and the average optical decay length (λ_{ave}), we configured variable-specific constraints as defined by equations (3.6) to (3.10). Built-in voltages with values ($V_{bi} > 1.4$ V) do not lead to any further increases in the cell's efficiency (Figure 4.2b, page 102). Hence, we additionally imposed the inequality constraint of equation (3.6) to the optimization, avoiding, therefore, unrealistic high values of this variable.

$$V_{bi\text{-}min} \leq V_{bi} \leq V_{bi\text{-}max} \tag{3.6}$$

Furthermore, we provide by equation s (3.7) a modification gradient for the built-in voltage, with the objective that 160 different Vbi's are calculated, as similar as accomplished for the remaining material properties in equation (3.5). In this case, we use the f_B factor to increase Vbi in a sequence of ($f_{B\text{-}max} - 1$) small steps of ΔV_{bi},, which increase the Vbi from its lower limit of $V_{bi\text{-}min} = 0.76$ V to its defined upper limit of $V_{bi\text{-}max} = 1.4$ V.

$$\Delta V_{bi} = (V_{bi\text{-}max} - V_{bi\text{-}min}) \ / \ (f_{B\text{-}max} - 1) \tag{3.7}$$

Where $V_{bi\text{-}min}$ is the setup value of the built-in voltage, as specified in section 3.3.2, page 88. Therefore, we consider a total of 160 optimizations in which we increase $V_{bi\text{-}min}$ we iteratively by the value ΔV_{bi} from one to the next optimization as follows

$$V_{bi} = V_{bi\text{-}min} + (f_B - 1)\ \Delta V_{bi} \tag{3.8}$$

As specified by this equation, for $f_B = 1$ the value of V_{bi} is $V_{bi\text{-}min}$, while for $f_B = 160$, this concept results in the last of 160 optimizations with $V_{bi} = V_{bi\text{-}max}$. Thinner absorber layer with light trapping techniques can result in lower Pb contents of the PSC's absorber layer. In this case, we suppose that each of the different available coating techniques of the absorber layer presents a specific minimum thickness ($t_{0\text{-}min}$) to avoid losses related to, e.g., pinholes (QIU; MERCKX; JAYSANKAR; DE LA HUERTA *et al.*, 2016); and conduction effects, in the case of light trapping (ATWATER; POLMAN, 2010). E.g., techniques that result in very smooth absorber layers such as the solvent-solvent coating technique (ZHOU; YANG; WU; VASILIEV *et al.*, 2015), allow a coating of extremely thin absorber layers without presenting pinholes. We set up an additional constraint for t_0, which considers an adjustable minimum thickness ($t_{0\text{-}min}$) as the lower boundary in an optimization process. For the upper limit ($t_{0\text{-}max}$) we assumed a maximal possible t_0 of 1 μm, obtaining the following inequality constraint.

$$t_{0\text{-}min} \leq t_0 \leq 1\ \mu m \tag{3.9}$$

In the Beer-Lambert law, the average optical decay length (λ_{ave}) stands in a defined relationship with the absorber layer thickness (t_0), which is expressed by equation (A.17), page 164, resulting in low reflection losses of approximately 1%. This small reflection losses at the cell's back reflector, are visible from Figure 3.1b, page 81, which we configured using the equation of the Beer-Lambert law. Considering an λ_{ave} of 100 nm, as calculated in (SUN; ASADPOUR; NIE; MOHITE *et al.*, 2015) for the case without light trapping, a 450 nm thick absorber layer results is a value of $0.01\,G_{eff}$, where this value defines the effective generation of charge carriers in [$s^{-1}cm^{-3}$] close to the back-reflector. The setup configuration for t_0 and λ_{ave} (Section 3.3.2, page 88) results in the value of $m = t_0 / \lambda_{ave}$ = 450 nm / 100 nm = 4.5, for the case without light trapping, which should also be considered for cells with light trapping,

assuming a similar relation of the absorption to the reflection losses. Light trapping increases the J_{sc} (CAI; PENG; CHENG; GU, 2015) and reduces the average optical decay length (λ_{ave}), simultaneously. We used the calculated m = 4.5 to specify an additional equality constraint for λ_{ave} with equation (3.10), defined here as the m-constrained value of λ_{ave}. We defined the constraint of $\lambda_{ave}(t_0)$ for light trapping as a function of t_0, solving equation (A.17), page 164, for λ_{ave}, as follows

$$\lambda_{ave}(t_0) = t_0 / m = t_0 / 4.5 \, . \qquad (3.10)$$

If λ_{ave} is, instead, in the same form constrained as the remaining model variables, by use of the f_B factor, a relationship arises, as defined by the vertex lines in Figure 4.2f, page 102. This relationship results, with an relationship of m = 5.5, as derived from this figure, in lower λ_{ave} values, and a somewhat higher optimized efficiency because of the improved absorption (Table 4.2 to Table 4.4, page 107 – last two columns).

However, improved absorption properties, as obtained by light trapping, and the resulting higher short circuit current density, should ideally result in a PCE improvement, while presenting a similar relationship of the absorption to the reflection as in a cell without light trapping. In the Beer-Lambert formulation (Figure 3.1b, page 81), this means a similar m has to be considered. Therefore, we calculated an m – constrained λ_{ave} in equation (3.10), as a function of a considered absorber layer thickness, which results in a lower PCE, presenting, consequently, a more conservative formulation. In the presented m – constrained optimizations, we constraint the remaining material properties by the f_B – factor, as specified in equations (3.5) to (3.9), pages 85 to 86, adding, however, an additional equality constraint, as defined by equation (3.10).

Using, however, the values of λ_{ave} and t_0 of Figure 4.2f, as obtained from a f_B constrained optimization, a calculated m = 5.5 is obtained, considering ideal material properties of a PSC, which corresponds to lower reflection losses and higher PCEs. Therefore, the selection of m = 4.5 is a conservative estimation of the simulated reflection losses. In our optimizations, we consider spherical Ag nanoparticles localized in the absorber layer, close to its backside (CAI; PENG; CHENG; GU, 2015). Whereas higher efficient light-trapping schemes by shape-optimized plasmonic nanoparticles are possible (KAKAVELAKIS; PETRIDIS; KYMAKIS, 2017), we only adopt the case with spherical nanoparticles, because

of the available, and here adopted current densities, as specified by FDTD simulations in (CAI; PENG; CHENG; GU, 2015). Under the simulated light-trapping configuration, the short circuit current densities are for a large range of t_0 higher than the J_{sc} values obtained in (SUN; ASADPOUR; NIE; MOHITE *et al.*, 2015). Therefore, we specify in equation (3.11) a correction factor for the short circuit current density in the case of light trapping, which value is a function of the absorber layer thicknesses as follows

$$CF_{lt}(t_0) = J_{sc\text{-}Cai}(t_0) / J_{sc\text{-}Sun} \, . \tag{3.11}$$

Fortunately, in the configuration without light trapping, both authors present a similar short circuit current density for the used MAPI absorber layer, if considering an absorber layer thickness of 450 nm. Therefore, we adopted in the setup of our simulations directly the short circuit current densities and absorber layer thicknesses as obtained by FDTD simulations in (CAI; PENG; CHENG; GU, 2015) for different absorber layer thicknesses.

3.3.2 Setup conditions

We used the cell properties and the absorber layer thickness (t_0), as obtained in (SUN; ASADPOUR; NIE; MOHITE *et al.*, 2015), as setup-conditions, or initial condition in our multidimensional optimizations. Using the OTM method, the authors calculated the fundamental optical parameters, which are (i) the effective generation of charge carriers, G_{eff} = 1.4356 x 10^{13} $cm^{-3}s^{-1}$, and (ii) the average optical decay length (λ_{ave} = 100 nm). Both parameters represent material-specific properties that are independent of the absorber layer thickness. By the derived equation for the total generation of free charge carriers (equations (A.1) and (A.2), page 157), a total charge carrier generation of G_{max} = 1.4356 x 10^{17} $cm^{-2}s^{-1}$ is calculated, which the authors validated with the measured short circuit current density of qG_{max} = 23 mA/cm², where q is the electric charge. The built-in voltage is V_{bi} = 0.78 V, and the diffusion coefficients are $D_n = D_p$ = 0.05 cm^2/s. The authors obtained an ideal t_0 of 450 nm by a one-dimensional optimization of this variable. After the manufacturing of the PSC with the optimized absorber layer thickness, the authors obtained by a curve fitting (i) an electron surface recombination velocity (SRV) at the transition from the absorber layer to the frontside charge transport layer, with $s_f = s_n$ = 200 cm/s, (ii) a hole SRV at the transition to the backside charge transport layer, with $s_p = s_b$ = 19.2 cm/s, and (iii) the number of the

excess minority carrier concentrations of electrons and holes (Δn=8.426 x 10^6 cm^{-3}, Δp=1.3003 x 10^8 cm^{-3}). They obtained an optimized PCE of 15.7%, in a cell with an open-circuit voltage of V_{0C} = 0.87 V. The measured semiconductor temperature was 300.56 K, which results in a thermal voltage of $V_t = k_B T/q$ = 25.9 mV. These setup values result in the cell design as specified in Table 4.5, page 113 - design 6. In our optimizations, we used a short circuit current density qG_{max} = 23 mA/cm^2 for a 450 nm thick absorber of a MAPI-PSC, as calculated in (SUN; ASADPOUR; NIE; MOHITE *et al.*, 2015), for a simulation without light trapping.

For light trapping with spherical nanoparticles, we adopted the values as obtained by the FDTD simulations in (CAI; PENG; CHENG; GU, 2015), using short circuit current densities $qG_{max,}$ for absorber layer thickness in the range of t_0 = 50…400 nm, as specified by equation (3.11). For several different absorber layer thicknesses (t_0), we used the following short circuit current densities ($q\ G_{max}$), in units of [mA/cm^2], as obtained for light-trapping conditions in (CAI; PENG; CHENG; GU, 2015): 22.5 (t_0= 50 nm), 23.05 (80 nm), 23.9 (160 nm), 24.18 (320 nm), 24.5 (400 nm).

3.4 SENSITIVITY ANALYSES

In our previous work, we numerically optimized a PSC's efficiency as a function of seven efficiency-sensitive model variables using the analytical model, which resulted in the high maximal PCE of 27.5% (KRATZENBERG; RAMBO; RÜTHER, 2019), as also detailed in section 4.2, page 105. Knowing the ideal material properties is an essential aspect concerning the optimization of PSCs, as the measurements of the values of these properties can validate if a manufacturing method improves or worsens a necessary property for high cell efficiencies. It is state-of-the-art knowledge that the J_{sc} increases as a function of light trapping in cells over a large range of t_0, leading, however, to a J_{sc} decrease for very thin absorber layers (CAI; PENG; CHENG; GU, 2015).

However, the improvement of the material properties, combined with light trapping in thin absorber layers, can lead to a considerable increase in the PSC's state-of-the-art efficiency. E.g., we showed in section 4.2, page 105 that a 160 nm thick absorber layer results in only 0.1…0.2% lower PCE if compared to another optimized design with t_0 = 400 nm, because of the V_{MPP} increase in thin absorber layers. Furthermore, this cell design, with

specified material properties, shows a 2.5-fold reduction of the cell's Pb content, demonstrating, therefore, that high-efficiency PSCs can be manufactured with relatively low residual content.

However, we do not specify how a material property tuning should be ideally accomplished in the development of high-efficiency cells with low Pb content. In this context, a solar cell researcher should know in which best sequence the seven PCE-sensitive variables should be selected ideally for its improvement tunings in cell manufacturing. To find out more details about each of the variables, and its importance, we accomplish a complete set of one-dimensional sensitivity analyses, validating the sensitivity of a whole set of performance parameters as a function of each of the considered material properties. We compare these sensitivity analyses for (i) a non-optimized and (ii) a fully optimized solar cell design.

3.4.1 Methods

In the sensitivity analyses of the non-optimized and optimize solar cells, we improved one model variable at a time with arbitrary sensitivity factors in the range of f_s = 1…160, using equations (3.12) to (3.17), page 92, and compare the improvement of several performance parameters in section 4.3, page 120.

Non-optimized perovskite solar cell: The authors in (SUN; ASADPOUR; NIE; MOHITE *et al.*, 2015), obtained an optimized PSC cell configuration tested in model and experiment by use of a one-dimensional optimization of t_0. We used that cell configuration as setup design in a multidimensional material property optimization, and we labeled it as the cell configuration of a non-optimized PSC design in the following text. In our one-dimensional sensitive analyses, we define a variable as being most important or sensitive; if starting from the non-optimized design, the improvement of the value of a considered material property results in the steepest efficiency increase as a function of this variable improvement.

Optimized perovskite solar cell: As more interesting to know is the variables' importance, as specified by the most efficiency-sensitive variables, of an optimized solar cell, principally as the state-of-the-art PCE of 25.2% is already proximate to the here proposed optimized solar cell design. As in the non-optimized solar cell, we analyze a variable range

between the non-optimal till the optimal variable values. For one-dimensional sensitivity analyses of the optimized cell design, we define the variable as being most important, which shows the highest efficiency-sensitivity, or drop in PCE, when leaving its optimal variable value, in the direction of the non-optimal variable value. We defined the improvement range of a considered variable by its model variable and a sensitivity factor f_s, which we determined in a similar form as in section 3.3, page 82. However, the resulting model variables are different as we use here specific signs of the analyzed variables and not ranges as used in a multidimensional optimization to specify the variables as a function of f_s. Because of the cell's strong non-linearity, as discussed in sections 4.1, page 98, and 4.2, page 105, it is not known if the material properties of a non-optimized cell present the same rank of efficiency-sensitivity as in comparison to a non-optimized PSC. Therefore, we analyze this question here in more detail.

3.4.2 Modeling

In two different sensitivity analyses, we modify the material properties and the absorber layer thickness by a sensitivity factor (f_s), which values correspond to the used values of the boundary amplification factor (f_B), as proposed in section 3.3, page 82. We solely introduce the new formulation of a sensitivity factor f_s to underline the clear distinction of the formulation of the sensitivity formulation. While the optimization algorithm identifies automatically if a variable should be increased or decreased within a range of lower and higher material properties, as defined by f_B, in a sensitivity analysis, the sign of the variable modification must be known beforehand, to adopt a correction with f_s, which either increases or decreases, the value of a model variable. In the present sensitivity analyses, we adopt the obtained signs of the model variables as already obtained by the multidimensional optimization in section 4.2, page 105, to increase or decrease the material properties in the same direction as selected by the optimization algorithm. Our sensitivity analysis analyzes each of the model variables in the ranges between the non-optimized and the optimized solar cell configuration, as specified, considering $f_B = 1 \ldots 160$, as used in section 3.3. We know from the optimizations in section 4.2 that the cell's efficiency rises as a function of higher D_n and D_p values. Therefore, the increase of these variables is determined as follows

$$X_{opt} = X_{nopt}\, f_s\,, \tag{3.12}$$

where f_s is the sensitivity factor (f_s = 1…160 $\in \mathbb{N}$), as chosen for an arbitrary variable improvement. This equation defines that the optimized values of D_n and D_p can be found by gradually increasing the non-optimized values by the sensitivity factor f_s from 2 to 160. The variable X_{nopt} (f_s = 1) stands for the non-optimal initial values of D_n or D_p, and X_{opt} stands for its optimized values, as found by the multidimensional optimization. We adopt here the initial and optimal values as obtained in (KRATZENBERG; RAMBO; RÜTHER, 2019), also defined in Table 3.1, page 94. Furthermore, we know from our multidimensional optimizations, that the surface recombination velocities of electrons and holes, as related to the front and the back layer of the PSC (s_f and s_b) must decrease as much as possible. Therefore, equation (3.13) determines the decrease in s_f and s_b as follows

$$X_{opt} = X_{nopt} / f_s\,, \tag{3.13}$$

where f_s = 1…160; X_{nopt} stands for the initial values of s_f and s_b, as used for the setup in the optimizations in section 3.3; and X_{opt} stands for the improved or optimized surface recombination velocities. For the V_{bi} and t_0 we considered a reduced variable improvement range in sections 3.3 and 4.2, which we specify in a resumed form in Table 3.1, page 94. For these two variables, we define a variable modification gradient by the following equation

$$\Delta X_i = (\ |X_{opt} - X_{nopt}|\ )\ /\ (f_{s\text{-}max} - 1)\,, \tag{3.14}$$

Where ΔX_i stands for the gradual variable improvements, representing ΔV_{bi}, Δt_0 and $\Delta\lambda_{ave}$ and $f_{s\text{-}max}$ = 160 is the maximal sensitivity factor. The improved t_0, $V_{bi,}$ and t_0 values we calculate by equations (3.15) to (3.17).

$$V_{bi} = \mathrm{V_{bi\text{-}nopt}} + (f_s - 1)\ \Delta V_{bi} \tag{3.15}$$

$$t_0 = \mathrm{t_{0\text{-}nopt}} - (f_s - 1)\ \Delta t_0 \tag{3.16}$$

$$\lambda_{ave} = \lambda_{ave\text{-}\mathrm{nopt}} - (f_s - 1)\ \Delta\lambda_{ave} \tag{3.17}$$

While for $f_s = 1$ this sensitivity analysis uses the values of the non-optimized setup conditions with $V_{bi} = V_{bi\text{-}nopt}$, $t_0 = t_{0\text{-}nopt}$ and $\lambda_{ave} = \lambda_{ave\text{-}nopt}$, the values of the optimized model are calculated with the maximal sensitivity factor $f_s = f_{s\text{-}max} = 160$, resulting in the values $V_{bi\text{-}opt}$, $t_{0\text{-}opt}$ $\lambda_{ave\text{-}opt}$. As a result, the whole set of variables vary in the range between X_{nopt} and X_{opt} as specified in Table 3.1.

In this sensitivity analysis, we consider dependent and independent variables. The independently modified model variables as here analyzed are the absorber layer thickness (t_0) and material properties λ_{ave}, V_{bi}, $D_{n,}$ $D_{p,}$ $s_{f,}$ s_f are the s, which present a PCE-sensitivity in one- and two-dimensional sensitivity analyses. Our dependent variables are constituted as a function of the variation of each of these independent variables, using the analytical solar cell model, as presented in (SUN; ASADPOUR; NIE; MOHITE *et al.*, 2015). The dependent variables are the performance parameters of PSC's J-V curve, which are the: (i) maximum power point voltage (V_{MPP}), and current density (J_{MPP}); (ii) open-circuit voltage (V_{oc}); (iii) short circuit current density (J_{sc}); and (iv) fill factor (FF). Our numerical design of experiments is planned under the criteria as provided in (MONTGOMERY, 2017), setting up a systematic set of numerical analysis and simulations to identify the different effects and sensitivities, while the actual model variables are set up by the equations (3.12) to (3.17), showing the modulations of the cell's material properties and its t_0, as a function of f_s.

Increased m-factor in a non-optimized and fully optimized solar cell: The *m*-factor in equation (A.17), page 164, defines the relationship between t_0 and λ_{ave}. Based on the absorber layer thickness of 450 nm and an average optical decay length of 100 nm, considering the setup of the model as presented in (SUN; ASADPOUR; NIE; MOHITE *et al.*, 2015), an *m* of 4.5 is obtained. However, analyzing the gradients of the straight maximal efficiency vertex line in Figure 4.2f, on page 102, an *m* of 5.5 is obtained, as tuned by the optimization algorithm for the optimized solar cell model in the multidimensional space, using an f_B - constrained optimization, instead of an m-constrained optimization. The *m*-factor can be considered as a measure for the reflection losses, and in this sense, a something higher *m* means that something lower reflection losses at the back reflector do appear. Looking, e.g., to Figure 3.1b, on page 81, it can be seen that our setup conditions or the conditions of the non-optimized solar cell correspond to reflection losses of approximately 1 %, with $\lambda_{ave} = 100$ nm and $X = t_0 = 450$ nm. As also to see from the same figure, if λ_{ave} is decreased, or t_0 is

increased, as related to a higher *m*, then this reflection losses decrease. By an additional simulation, we analyzed the PCE as a function of the tow different *m*'s, which result in efficiencies of 27.6% and 27.8% for the *m*-values of 4.5 a 5.5. Therefore, for the fully optimized solar cell, our simulation leads to a small deviation with a 0.2% lower PCE as we adopted a general *m* of 4.5 in the present sensitivity analyses.

3.4.3 Setup conditions

Whereas the section 3.4.1, page 90 specified the on-dimensional improvement ranges, as a function of the presented sensitivity factor f_s, which are identical for the considered non-optimized and the optimized solar cell, here we specify with Table 3.1 the utilized set-up conditions or range limitations for these improvements. The variables X_{nopt} specifies the model variables for the non-optimized setup of the model, and the variables X_{nopt} define the model variables for the optimized configuration of the model variables. Then, in a one-dimensional variable improvement of λ_{ave}, e.g., this variable is modified in the range of λ_{ave} = 100…35.6 nm, a range at which the sensitives of a whole set of performance parameters are validated, for both cell configurations, for a non-optimized PSC, and a fully optimized cell.

Table 3.1 - Setup of the sensitivity analyses, as defined by the optimal and non-optimal variables, used for the definition of the variable modification range in the present sensitivity analyses. Variable value changes, in the range, between the non-optimized (X_{nopt}), and the optimized variable (X_{opt}). Sensitive variables are the absorber layer thickness (t_0); average optical decay length (λ_{ave}); surface recombination velocity of the front (s_f), and the back interface (s_f) of the perovskite absorber layer; and diffusion coefficients of electrons (D_n), and holes (D_p).

Variable	s_f	s_b	V_{bi}	D_n	D_p	t_0	λ_{ave}
Unit	[cm/s]	[cm/s]	[V]	[cm^2/s]	[cm^2/s]	[nm]	[nm]
X_{nopt}	200	19.2	0.76	0.05	0.05	450	100
X_{opt}	1.25	0.12	1.4	8	8	160	35.56

3.5 VARIABLE RANKING

Another promising method for the specification of a sequence of the most efficiency-sensitivity, or most essential variables, we propose in this section, as based on the equation of the binomial coefficient in equation (3.18), which we use for the combination of model variables. We used this equation to obtain suggestions for the variable tuning, or property tuning, in future cell research with manufactured solar cells in the laboratory, and at industrial scale. Our objective is to specify how the efficiency of a manufactured PSC can be increased best, ranking its material properties in the order from the highest to the lowest efficiency-sensitive variable. This ranking we based on the analysis of a total of 91 possible variable combinations using the optimized and non-optimized material properties of seven efficiency sensitive variables. The results of the obtained simulations we combine with additional information from the results of the sensitivity analyses using an optimized cell design to create a more qualified decision in the variable tuning of manufactured PSCs.

3.5.1 Modeling

Apart from the sensitivity analyses, we analyze, which ideal combinations of k optimized model variables ($k = 1 \ldots n$; $n = 7$), leads to the highest optimized efficiencies, in a multidimensional space of $n\text{-}1$ material properties, and t_0, saying in the space of n model variables. Such knowledge can also be used to decide which variables should be manipulated first in a manufactured solar cell, subjected to an optimization process. Because of the PSC model's nonlinearities, it is crucial to evaluate the PCE values as obtained of a whole set of possible variable combinations, using the seven sensitive model variables. Here we rank the efficiency as obtained by 91 possible combinations of two sets of variables, which are the non-optimized (X_{nopt}) and the optimized (X_{opt}) model variables in Table 3.1, page 94. The objective is to advise the manufacturers of perovskite solar cells, which like to tune its variables one-by-one in a stepwise optimization. In such a tuning, the most efficiency-sensitive, and therefore, most the most promising variables or material properties should be improved first, in a sequential selection. As a result, the most effective manufacturing methods are used first to increase the PSC's efficiency.

Conversely, the least sensitive variables and property improvement methods are selected at last. In this sequential selection, we used the combinatorial approach as specified

by equation (3.18), to set up the variables as selected by this method to its optimized value (X_{opt}), while the non-selected variables we set up to its non-optimal values (X_{nopt}). With $n = 7$ sensitive variables, and $k = 1…7$ specifying the number of a variable set, we obtain seven variable sets, each with s variable combinations (Table 4.8, page 130). The possible variable combinations, as related to each variable set, we configure by the equation of the binomial coefficient (1994), as follows

$$\binom{n}{k} = \frac{n!}{k!(n-k)!} \quad ; \quad 1 \geq k \geq 7 \; ; \quad k \wedge n \in \mathbb{N} \, . \tag{3.18}$$

This equation defines the total number of s possible combinations in each of the seven variables sets, where each set is based on the combination of the number of k arbitrary selected model variables, taken out of our variable set of $n = 7$ sensitive variables, resulting in a total of 91 possible variable combinations. We configure the combinations of the different model variables to be tested, using the Matlab™ function *nchoosek*, using equation (3.18). And at last, we evaluate the optimized efficiencies for each of the possible variable combinations, to find for each of the seven sets a unique combination, which results in the highest PCEs, as presented in section 4.4.1, page 129.

Observation: In the current model setup further optimizations are not necessary for the here presented simulations, as the simplification by equation (3.10), page 87 interprets correctly the relation of the bi-dimensional linear vertex line, which only appears in-between t_0 and λ_{ave} in the multidimensional function space (KRATZENBERG; RAMBO; RÜTHER, 2019). As such, a maximal-efficiency vertex line was not found in the relationship between the further model variables, and as model restrictions are not found for additional model variables, simulations can be considered as being sufficiently able to substitute the model optimizations. However, considering the case that light trapping is used before the improvement of the further model variables, then small uncertainties can be introduced because of the variation of the m-factor between the values of $m = 4.5$, as obtained by (SUN; ASADPOUR; NIE; MOHITE *et al.*, 2015) and $m_c = 5.52$, as derived from Figure 4.2, page 102.

3.5.2 Setup conditions

For the setup conditions, we used the same samples as presented in Table 3.1, page 94. However, the combinatorial approach results in a specific selection criterion, which select the model variables with the highest efficiency-sensitivity first in a sequence of variable inclusions. E.g., to validate the $s = 7$ combinations with $k = 1$ variable taken out of a set of $n = 7$ variables, the prepared software based on the selection algorithm sets up all model variables with the values of X_{nopt}, excluding only one variable, which is set up with the value of X_{opt} at a time. The selection by the highest efficiency resulted in the favorite variable s_f. For the case of $k = 2$ variables are taken out of a set of $n = 7$ variables, we used the general setup of X_{nopt} again for the whole set of variables excluding only two variables, which are set up with the value of X_{opt}, at a time. In this second variable selection, we obtained the highest PCE with the combination of the variables s_b and s_f, including, therefore s_b to the selected group of variables. In the whole sequence of variable selections, we fortunately obtained for a clear series, where the algorithm of the binomial coefficient included only one new variable, for each increase of k, to the group of selected variables.

4. RESULTS

Some people don't like change, but you need to embrace change if the alternative is disaster.

Elon Musk, CEO of Tesla Motors and SpaceX

State-of-the-art one- and two-dimensional optimizations can over a long time, in repeated research efforts, lead to a cell's maximal efficiency limit, as shown for several different cells in (NREL, 2020), which usually need several decades. Therefore it is interesting to know the maximal efficiency increase in the combination of all possible variable combinations, which we explore in section 4.1 for the considered MAPI cell. We present a complete set of the accomplishable one- and two-dimensional sensitivity analyses, as obtained by the possible variable combinations, to identify the potential or the maximal efficiency increase by state-of-the-art methods. This sensitivity analyzes we simplify by on- and two-dimensional optimizations. However, the results of the proposed multidimensional optimization of a solar cell's efficiency, as based on its drift-diffusion model, is much more effective (Section 4.2, page 105). Based on our results, and principally the multidimensional optimizations, we propose different cell designs, which increase the state-of-the-art efficiency of the simulated and manufactured PSCs significantly.

4.1 ONE- AND TWO-DIMENSIONAL OPTIMIZATIONS

One- and two-dimensional optimizations are the state-of-the-art of the optimizations in cell manufacturing and modeling, as the cell's efficiency can be easily plotted as a function of one or two considered variables. Hence, we analyze in more detail such an optimization process to obtain information about the expected efficiency increase and non-linearities, as related to the used PSC model.

4.1.1 Results

As shown by the proposed combinatorial approach (section 4.4, page 128), the material properties which are most-efficiency sensitive are: (i) the front surface recombination velocity (s_f), (ii) the back surface recombination velocity (s_b), (iii) the built-in voltage (V_{bi}),

and the diffusion coefficient of electrons (D_n) in the analyzed pin-type MAPI cell. Being the most promising variables, we examine its behavior in more detail in Figure 4.1a-b.

Figure 4.1- Efficiency growth as function of two model variables (a) as a function of the built-in voltage (V_{bi}) and the diffusion coefficient of electrons (D_n); and (b) as a function of the front and back surface recombination velocities (s_f and s_b). The efficiency as obtained in (SUN; ASADPOUR; NIE; MOHITE *et al.*, 2015) is presented by a white cross.

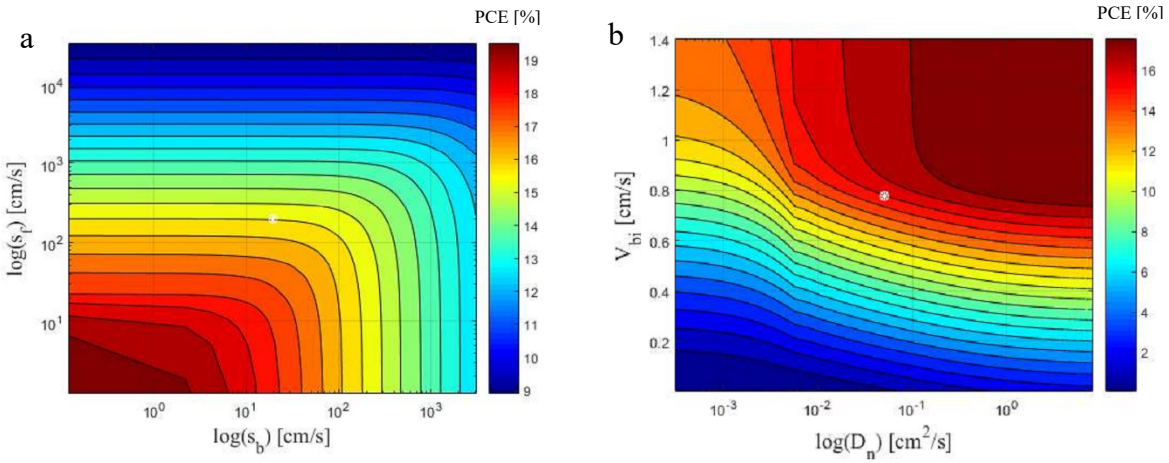

Source: (WRUCK, 2018)

Figure 4.2a-e, page 102, shows some further typical one- and two-dimensional sensitivity analyses, where we calculate the PCE as a function of the improvement of the cell's model variables. The figure was configured in (WRUCK, 2018), which inclusively shows a set of further one- and two-dimensional dependencies of the PSC's efficiency. However, for the visualization of the efficiency gains, as obtained by the possible combinations of nine analyzed model variables, a large set of 45 such figures would be necessary. Therefore, we propose a substitution of these sensitivity analyses, by use of two-dimensional numerical optimizations in Table 4.1, page 103, using the NLP optimization algorithm *fmincon* of the MATLAB™ program. In this table Δn is the number of excess electrons per unit volume that are available for the recombination process within the p-type layer, Δp is the number of excess holes per unit volume that are available for the recombination process within the n-type layer, D_p is diffusion coefficient of holes and the remaining variables were already introduced. The table shows the optimized efficiency values and the used model variables, as obtained from 90 optimizations in the one-dimensional space and 280 optimizations in the two-dimensional optimization space, considering 10 different

boundary- extensions factors f_B and considering as setup configuration, the variable values obtained in (Sun et al., 2015) presenting the initial efficiency of 15.7%. Table 4.1 presents only the highest attainable PCE values of those sensitivity analyses, as a function of different boundary-expansion factors f_B, from which the corresponding variable values can be calculated back, using the boundary amplification factor f_B. For this back-calculation, it must be known if an efficiency increase is obtained by the increase or the decrease of the considered model variable, as identified by an f_B constrained optimization presented in Appendix Table B.1, page 189. We obtained in this two-dimensional efficiency optimization the same signs as identified for the multidimensional optimization in Appendix Table B.1, showing that the variables s_f, s_b, and λ_{ave}, must decrease for high efficiencies, while the variables D_n, D_p, and V_{bi} must increase. The variable t_0 is unique as it presents in all cell designs an ideal value.

Figure 4.2a-d shows some further one- and two-dimensional efficiency optimizations, analyzing some particular behaviors, and Figure 4.2e-f examines the sensitivity of t_0 and λ_{ave}, comparing two different setups of this two-dimensional sensitivity analyses. While in Figure 4.2e, the remaining variables confer to our setup condition, in Figure 4.2f, these variables are configured with the ideal values, as obtained by a multidimensional, f_B – constrained optimization, using f_B = 160. Both figures consider light trapping with independently adjustable t_0 and λ_{ave}, but the multidimensional optimizations (Figure 4.2f) result in much higher efficiency values for low values of t_0 and λ_{ave}.

The slight right shift of the grey vertex lines in Fig 2f indicates that improved material properties demand an improved light trapping for arbitrary t_0 values, because of its lower optimal λ_{ave} for the same t_0. Based on the results of our f_B – constrained multidimensional optimization (Appendix Table B.1, page 189), and based on the figures presented in (WRUCK, 2018), we conclude that a variable relationship, which results in maximum efficiency vertex lines, only appears in-between the variables t_0 and λ_{ave}, and not in-between the further model variables.

4.1.2 Discussion

While nearly two orders of magnitude reduction of s_f can increase the efficiency from 15.7% to almost 17%, more than two orders of magnitude improvement of the s_b lead interestingly in nearly zero increase of the PCE (Figure 4.1a). However, the simultaneous reduction of s_f, and s_b shows a more significant efficiency increase to the value of 19.5%.

The improvement of the V_{bi} to 1.4 V alone results in an efficiency increase to approximately 16.5%. In contrast, a rise in D_n alone by two orders of magnitudes results in a something higher PCE of ~ 17.2%, as to see from the darkest area in Figure 4.1b. Meanwhile, the simultaneous improvement of V_{bi} and D_n results in a similar value of ~ 17.2%. Considering that the D_n improvement can only be obtained on a limited range, e.g., much less than an order of magnitude, then the combined improvement with V_{bi} still enables this small improvement from 15.7% to 17.2%.

The reduction of the average optical decay length from λ = 100 nm to the value of 80 nm, as, e.g., obtainable by a weak light trapping, leads in a tiny PCE increase of only 0.05 % (Figure 4.2b), showing that (SUN; ASADPOUR; NIE; MOHITE *et al.*, 2015) already accomplished nearly ideal optimization of the relationship between λ_{ave} and t_0 by its one-dimensional thickness optimization. While the rise in D_p, from initially 0.05 to the values of 1 and 2.5 m^2/s leads to PCEs of 16.5% and 17.5%, the increase of D_n, from initially 0.05 to 1 m^2/s leads on its own to no improvement of the PCE at all in Figure 4.2c. The maximal PCE increase we obtained by the rise of both D_p and D_n to the values of 2.5 and 1 m^2/s, leading to a meager PCE increase to the value of 18.3%. The setup conditions do present excess concentration of electrons and holes Δn, and Δp, which are both already ideal, and therefore, the optimization algorithm is not able to find improvements for these variables (Figure 4.2d).

As seen in (SUN; ASADPOUR; NIE; MOHITE *et al.*, 2015), the MAPI cell presents an ideal absorber layer thickness of t_0 = 450 nm in a one-dimensional optimization. This finding is also reflected in Figure 4.2e and Figure 4.2f. The former shows a very slight PCE increase can be obtained for lower absorber layer thicknesses if the average optical decay length is reduced simultaneously. In Figure 4.2f, the whole set of material properties are improved, using a multidimensional optimization, which enables a more significant efficiency increase.

Figure 4.2 - One- and two-dimensional sensitivity analyses, showing the model efficiency as a function of different model variables.

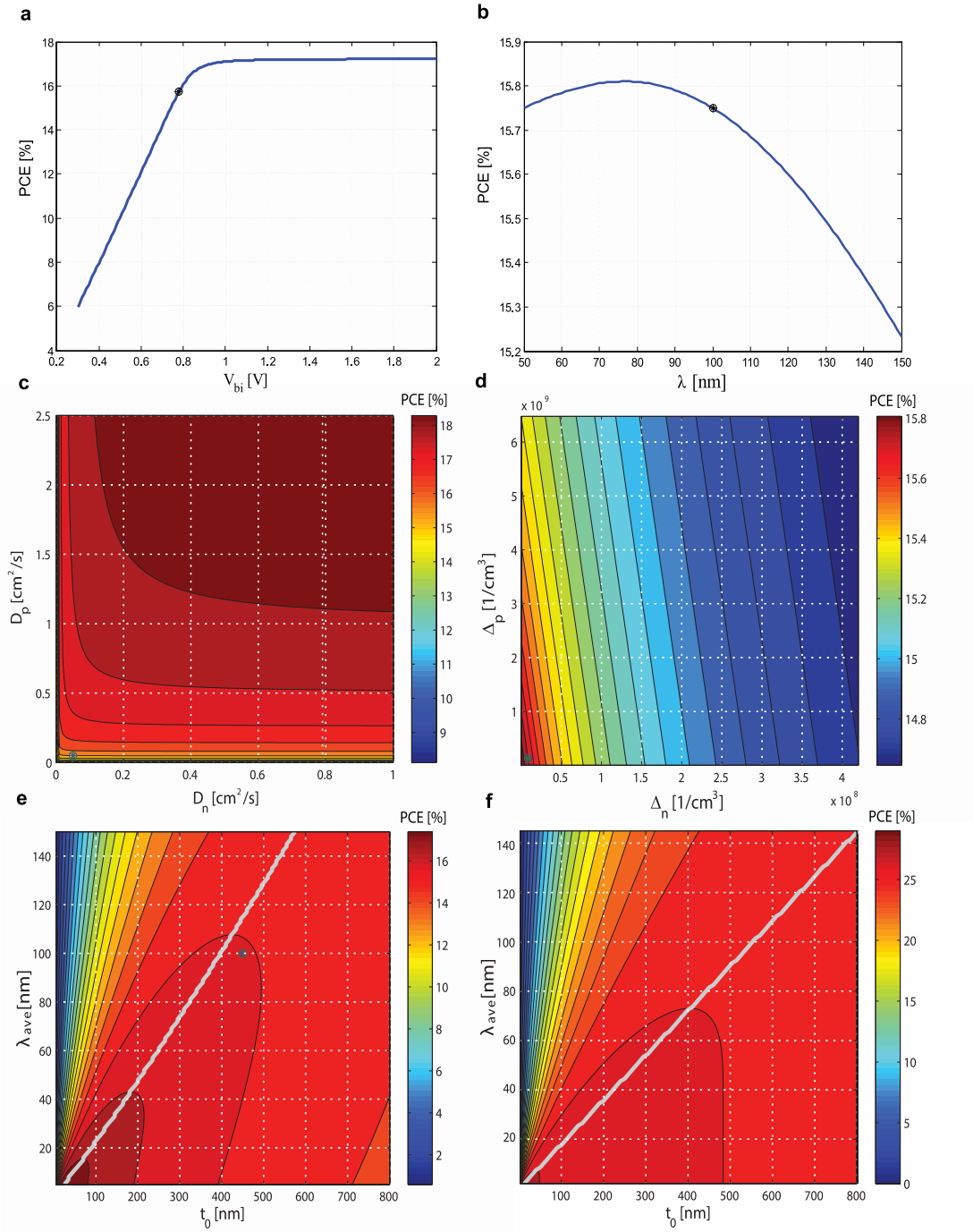

(a) the average optical decay length λ_{ave}; (b) the built-in voltage V_{bi}; (c) the diffusion coefficients of electrons and holes D_n and D_p; (d) the excess concentration of electrons and holes Δn and Δp; and finally, in (e) and (f), the absorber layer thickness t_0, and the average optical decay length λ_{ave}, where the grey vertex lines show the maximum attainable efficiency values in these two-dimensional presentations. (a) – (e) the remaining model variables are set up to the values as obtained in (SUN; ASADPOUR; NIE; MOHITE *et al.*, 2015); (f) the remaining model variables are set up by our f_B – constrained multidimensional optimization for f_B = 160; the measured efficiency values of 15.7% in (a) – (e) appear as a star within a surrounded circle.

Table 4.1 – Efficiency as function of material properties and absoraber layer thickness in one- and two-dimensional optimizations.

$f_B = 1.1$

	s_f	s_b	Δn	Δp	V_{bi}	D_n	D_p	t_0	λ_{ave}
s_f	15.8	15.9	15.8	15.8	16.8	15.9	15.9	15.9	15.9
s_b		15.8	15.8	15.8	16.7	15.8	15.8	15.8	15.8
Δn			15.7	15.7	16.7	15.8	15.8	15.8	15.8
Δp				15.7	16.7	15.8	15.8	15.8	15.8
V_{bi}					16.7	16.8	16.7	16.7	16.8
D_n						15.8	15.8	15.9	15.9
D_p							15.8	15.8	15.8
t_0								15.8	15.8
λ_{ave}									15.8

$f_B = 1.5$

	s_f	s_b	Δn	Δp	V_{bi}	D_n	D_p	t_0	λ_{ave}
s_f	16.2	16.2	16.2	16.2	17.6	16.5	16.2	16.2	16.2
s_b		15.8	15.8	15.8	17.2	16.1	15.8	15.8	15.8
Δn			15.7	15.7	17.2	16.1	15.8	15.8	15.8
Δp				15.7	17.2	16.1	15.8	15.8	15.8
V_{bi}					17.2	17.4	17.2	17.2	17.3
D_n						16.1	16.1	16.1	16.2
D_p							15.8	15.8	15.8
t_0								15.8	16.1
λ_{ave}									15.8

$f_B = 5$

	s_f	s_b	Δn	Δp	V_{bi}	D_n	D_p	t_0	λ_{ave}
s_f	17.1	17.3	17.1	17.1	18.3	17.8	17.3	17.1	17.3
s_b		15.8	15.8	15.8	17.3	17.2	15.8	15.8	15.8
Δn			15.7	15.7	17.2	17.0	15.8	15.8	15.8
Δp				15.7	17.2	17.0	15.8	15.8	15.8
V_{bi}					17.2	17.9	17.3	17.2	17.4
D_n						17.0	17.2	17.0	17.2
D_p							15.8	15.8	15.8
t_0								15.8	17.2
λ_{ave}									15.8

$f_B = 20$

	s_f	s_b	Δn	Δp	V_{bi}	D_n	D_p	t_0	λ_{ave}
s_f	17.8	18.5	17.8	17.8	18.4	18.1	18.4	17.8	18.1
s_b		15.8	15.8	15.8	17.3	18.3	15.8	15.8	15.8
Δn			15.7	15.7	17.2	17.7	15.8	15.8	15.8
Δp				15.7	17.2	17.7	15.8	15.8	15.8
V_{bi}					17.2	18.2	17.3	17.2	17.4
D_n						17.7	18.2	17.7	18.0
D_p							15.8	15.8	15.8
t_0								15.8	18.2
λ_{ave}									15.8

$f_B = 40$

	s_f	s_b	Δn	Δp	V_{bi}	D_n	D_p	t_0	λ_{ave}
s_f	17.9	19.0	17.9	17.9	18.4	18.1	19.0	18.0	18.4
s_b		15.8	15.8	15.8	17.3	18.7	15.8	15.8	15.8
Δn			15.7	15.7	17.2	17.9	15.8	15.8	15.8
Δp				15.7	17.2	17.9	15.8	15.8	15.8
V_{bi}					17.2	18.3	17.3	17.2	17.4
D_n						17.9	18.7	17.9	18.3
D_p							15.8	15.8	15.8
t_0								15.8	18.7
λ_{ave}									15.8

$f_B = 60$

	s_f	s_b	Δn	Δp	V_{bi}	D_n	D_p	t_0	λ_{ave}
s_f	18.0	19.3	18.0	18.0	18.4	18.1	19.3	18.0	18.5
s_b		15.8	15.8	15.8	17.3	19.0	15.8	15.8	15.8
Δn			15.7	15.7	17.2	18.0	15.8	15.8	15.8
Δp				15.7	17.2	18.0	15.8	15.8	15.8
V_{bi}					17.2	18.3	17.3	17.2	17.4
D_n						18.0	19.0	18.0	18.4
D_p							15.8	15.8	15.8
t_0								15.8	19.0
λ_{ave}									15.8

$f_B = 80$

	s_f	s_b	Δn	Δp	V_{bi}	D_n	D_p	t_0	λ_{ave}
s_f	18.0	19.5	18.0	18.0	18.4	18.1	19.5	18.1	18.5
s_b		15.8	15.8	15.8	17.3	19.2	15.8	15.8	15.8
Δn			15.7	15.7	17.2	18.0	15.8	15.8	15.8
Δp				15.7	17.2	18.0	15.8	15.8	15.8
V_{bi}					17.2	18.4	17.3	17.2	17.4
D_n						18.0	19.2	18.0	18.5
D_p							15.8	15.8	15.8
t_0								15.8	19.2
λ_{ave}									15.8

$f_B = 100$

	s_f	s_b	Δn	Δp	V_{bi}	D_n	D_p	t_0	λ_{ave}
s_f	18.0	19.7	18.0	18.0	18.4	18.1	19.6	18.1	18.5
s_b		15.8	15.8	15.8	17.3	19.4	15.8	15.8	15.8
Δn			15.7	15.7	17.2	18.0	15.8	15.8	15.8
Δp				15.7	17.2	18.0	15.8	15.8	15.8
V_{bi}					17.2	18.4	17.3	17.2	17.4
D_n						18.0	19.3	18.1	18.5
D_p							15.8	15.8	15.8
t_0								15.8	19.3
λ_{ave}									15.8

$f_B = 120$

	s_f	s_b	Δn	Δp	V_{bi}	D_n	D_p	t_0	λ_{ave}
s_f	18.1	19.8	18.1	18.1	18.4	18.1	19.7	18.1	18.6
s_b		15.8	15.8	15.8	17.3	19.5	15.8	15.8	15.8
Δn			15.7	15.7	17.2	18.0	15.8	15.8	15.8
Δp				15.7	17.2	18.0	15.8	15.8	15.8
V_{bi}					17.2	18.4	17.3	17.2	17.4
D_n						18.0	19.4	18.1	18.5
D_p							15.8	15.8	15.8
t_0								15.8	19.5
λ_{ave}									15.8

$f_B = 160$

	s_f	s_b	Δn	Δp	V_{bi}	D_n	D_p	t_0	λ_{ave}
s_f	18.1	20.0	18.1	18.1	18.4	18.1	19.9	18.1	18.6
s_b		15.8	15.8	15.8	17.3	19.7	15.8	15.8	15.8
Δn			15.7	15.7	17.2	18.1	15.8	15.8	15.8
Δp				15.7	17.2	18.1	15.8	15.8	15.8
V_{bi}					17.2	18.4	17.3	17.2	17.4
D_n						18.1	19.6	18.1	18.6
D_p							15.8	15.8	15.8
t_0								15.8	19.6
λ_{ave}									15.8

Considering a 160 nm thick absorber layer and light trapping by spherical NPs, the efficiency increases to the value of 27.61% (corresponds to Figure 4.3, page 106, Table 4.4, page 110). If nearly ideal light-trapping conditions are considered, as eventually obtained by shape-optimized NPs, the PCE increases to 29% (Appendix Table B.1, page 189). The maximal efficiency grey vertex lines Figure 4.2e-f, show that in any cell design configuration, the absorber layer must be tuned as a function of the average optical decay length. In the comparison of a geographical topology, such vertex lines can be thought of as rising mountain ridges, or better hill ridges, which lead to the top of the hill that corresponds to the point of the maximal cell efficiency.

Table 4.1, page 103, shows that the most efficiency-sensitive variables in a one-dimensional improvement are D_n and s_f, which both increase the PCE value from 15.7% to 18.1% for a $f_B = 160$. Therefore, it is expected that two-dimensional efficiency optimizations, which involve these two variables, also leads to the highest efficiency increase. Interestingly, the highest two-dimensional efficiency increase with 20% is obtained by a 160-time reduction of the surface recombination velocities s_b and s_f. In comparison, the second-highest PCE of 19.9% we attained by the improvement of the variables D_p and s_f. Similar behavior also appears for lower improvements of the related variables, showing a lower PCE increase, however, as to see, e.g., for $f_B = 20$ in Table 4.1, page 103. We consider that such unexpected behavior, of changes of the variable sensitivities, appears because of the related nonlinear behavior in the two-dimensional space, which also should appear in the multidimensional space. For a two-dimensional space, such non-linearities appear in Figure 4.1 and Figure 4.2.

The aggregation in two-dimensional spaces can result in a much higher PCE increases, as in comparison to the gains as obtained by one-dimensional property improvements using the considered variables. This higher increase still happens if one of these variables leads, in a one-dimensional improvement, to nearly zero PCE increase (Table 4.1, page 103, and Figure 4.1, page 99). In the manufacturing of cells, this makes the PCE optimization a most challenging process leading; therefore, to a long development process as many of these variable spaces must be analyzed in a combination. If more variables are analyzed, the number of two-dimensional plots increases significantly because of the increasing number of possible combinations. Therefore, our proposed two-dimensional numerical optimization, (Table 4.1, page 103), simplifies the related work in a sense that variable-combinations that result in the highest PCE are identifiable, without the otherwise

necessary plots. However, in principle, maximal efficiency vertex lines are only possible to verify if figures of all possible variable combinations are plotted. Such vertex lines are important to validate, as otherwise, an undesired efficiency reduction can be obtained. However, such abundant analyses can be avoided by the use of multidimensional optimizations, which also result in much higher cell efficiencies, as shown in the next section.

4.2 MULTIDIMENSIONAL PROPERTY OPTIMIZATIONS

To avoid the disadvantages of the one- and two-dimensional optimizations, as principally defined by the tiny efficiency increases, future cell manufacturing should be oriented by the concepts of multidimensional optimization. Therefore, we elaborate on several different high- and highest-efficiency concepts in the following subsections. Rather than considering ideal light trapping as presented in Table B.1, page 189, we based our optimizations at more realistic concepts, as obtained by the plasmonic light-trapping effect, related to nanoparticles, which current densities were simulated by the high spatial resolution finite difference time domain (FDTD) method in (CAI; PENG; CHENG; GU, 2015).

4.2.1 Results

We present six sets of optimization results in Figure 4.3, on page 106, considering six different absorber layer thicknesses, each with a total of 160 different multidimensional optimizations ($f_B = 1\ldots160, \in \mathbb{N}$). For these m – constrained optimizations, the variable λ_{ave} is constrained by the equation (3.10), while the remaining variables are f_B – constrained as specified by equation (3.4) to (3.10), and set up by equation (3.11). As defined in equation (3.9), we consider that each coating technique of the absorber layer presents its associated minimum thickness ($t_{0\text{-}min}$) for the deposition of perfect absorber layers, and therefore, we elaborate optimized cell designs for different absorber layer thicknesses. Light trapping with spherical nanoparticles (solid curves in Figure 4.3) shows a significant efficiency advantage in comparison to the case without light trapping (dotted curve) in almost all development-states as expressed by the f_B – factor. In a 160 nm thick absorber layer, such a light trapping shows only a 0.1...0.2% lower efficiencies, in comparison to the configuration with the highest PCE, as obtained for t_0 = 400 nm, which presents the highest PCE in this figure.

Figure 4.3 - Optimized efficiency as a function of the 160 boundary-expansion factors (f_B = 1…160, for all $f_B \in \mathbb{N}$) for six absorber layer thicknesses from t_0 = 50…450 nm, optimization variables (D_n , D_p , V_{bi} , s_f , s_b), while $\lambda_{ave}(t_0) = t_0$ /4.5 is the calculated average optical decay length: (i) without light trapping, $t_{0\text{-}min}$ = 450 nm, λ_{ave} = 100 nm; (ii) light trapping with spherical plasmonic nanoparticles, t_0 = 50….400 nm, with corrected short circuit current densities. Used qG_{max} values, in units of [mA/cm^2], as obtained in (Cai et al. 2015 and Sun et al. 2015), which are: 22.5 (t_0 = 50 nm), 23.05 (80 nm), 23.9 (160 nm), 24.18 (320 nm), 24.5 (400 nm), and 23 (450 nm, without light trapping).

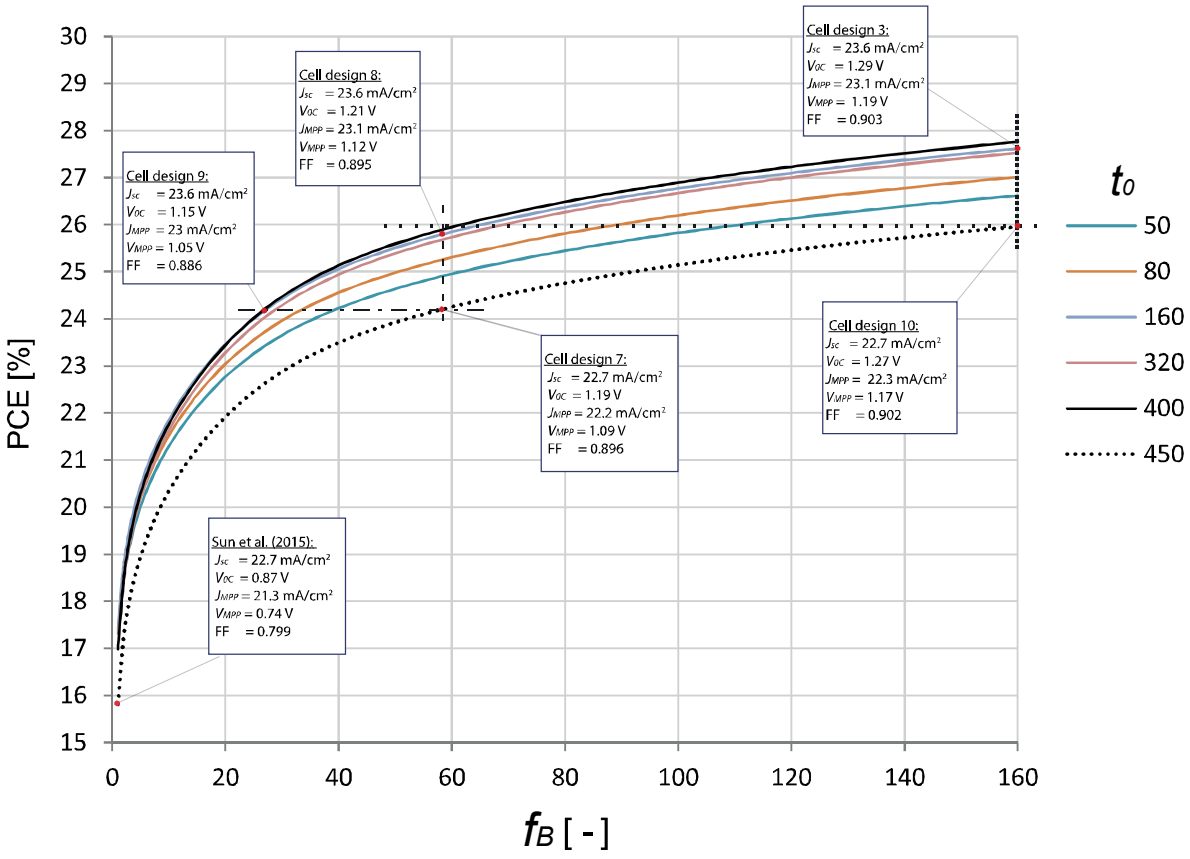

Meanwhile, a PSC with t_0 = 160 offers the advantage of containing a 2.5-fold lower Pb content. Therefore, we give the most emphasis to two different cell designs in our discussions, a fully optimized design with a 160 absorber layer, and a similar cell design with a 400 nm thick absorber layers. Because of the ascendant character of the curves in Figure 4.3, we present in Appendix Figure B.1, page 193, the PCE for arbitrary material improvements up to an improvement factor of f_B = 1000. In Table 4.2 to Table 4.4, we show alternative representations for some optimizations in Figure 4.3, presenting in these tables also the values of the optimized material properties. Table 4.2 considers the state-of-the-art absorber layer thickness of 450 nm without light trapping.

Figure 4.3 and Figure 4.4 present the results for thinner absorber layers of 400 nm and 160 nm, using a short circuit current density values, as obtained by light trapping with spherical nanoparticles (CAI; PENG; CHENG; GU, 2015), and considering an *m* – constrained specification of λ_{ave}, as defined in equation (3.10). For the interested reader, we additionally present the PCE and λ_{ave} values, which consider f_B – constrained λ_{ave} constraints setups as presented by equation (3.5). However, we advise that these values should be observed with caution because of the related low reflection losses, which might be unrealistic. Lower λ_{ave} values lead to a higher absorption, which results in higher decay of G(x), as a function of x, (Figure 3.1b, page 81), leading, as a result to lower reflection losses for a fixed absorber layer thickness.

Table 4.2 – Optimized model variables (boldface symbols), as obtained from eleven optimizations in the nine-dimensional function space with specific boundary-expansion factors f_B, presenting the best PCE of 25.96%, for t_0 = 450 nm, without light trapping (λ_{ave} = 100 nm); qG_{max} = 23 mA/cm^2.

f_B	s_f	s_b	Δn	Δp	V_{bi}	D_n	D_p	μ_n	μ_p	t_0	λ_{ave}	η	λ_{ave}^*	η^*
[-]	[cm/s]	[cm/s]	[1/cm^3]	[1/cm ^{3}]	[V]	[cm²/s]	[cm²/s]	[cm²/Vs]	[cm²/Vs]	[nm]	[nm]	[%]	[nm]	[%]
5.00	40.00	3.84	8.43E+06	1.30E+08	0.80	0.25	0.25	9.65	9.65	*450.00*	100.00	*18.96*	48.13	19.15
10.00	20.00	1.92	8.43E+06	1.30E+08	0.82	0.50	0.50	19.30	19.30	*450.00*	100.00	*20.34*	10.00	20.57
20.00	10.00	0.96	8.43E+06	1.30E+08	0.86	1.00	1.00	38.61	38.61	*450.00*	100.00	*21.92*	5.00	22.17
30.00	6.67	0.64	8.43E+06	1.30E+08	0.90	1.50	1.50	57.91	57.91	*450.00*	100.00	*22.88*	3.33	23.14
40.00	5.00	0.48	8.43E+06	1.30E+08	0.94	2.00	2.00	77.22	77.22	*450.00*	100.00	*23.49*	2.50	23.76
60.00	3.33	0.32	8.43E+06	1.30E+08	1.01	3.00	3.00	115.82	115.82	*450.00*	100.00	*24.26*	1.67	24.53
80.00	2.50	0.24	8.43E+06	1.30E+08	1.09	4.00	4.00	154.43	154.43	*450.00*	100.00	*24.76*	27.89	25.04
100.00	2.00	0.19	8.43E+06	1.30E+08	1.17	5.00	5.00	193.04	193.04	*450.00*	100.00	*25.14*	26.85	25.43
120.00	1.67	0.16	8.43E+06	1.30E+08	1.25	6.00	6.00	231.65	231.65	*450.00*	100.00	*25.46*	25.85	25.75
140.00	1.43	0.14	8.43E+06	1.30E+08	1.32	7.00	7.00	270.26	270.26	*450.00*	100.00	*25.73*	25.01	26.02
160.00	1.25	0.12	8.43E+06	1.30E+08	1.40	8.00	8.00	308.87	308.87	*450.00*	100.00	*25.96*	0.63	26.26

Observations: (i) The values in italic formatted numbers correspond to the values of the lower curve in Figure 4.3, page 106; (ii) optimizations consider the *m*-constrained specification of λ_{ave} *;* the values in the columns as marked with *, we obtained in f_B – constrained setup of λ_{ave}.

The J-V curves, and the power density curves, of nine high-efficiency design proposals we present in Figure 4.4a-b. Some of these schemes visualize in more detail the simulated design proposals of Figure 4.3, page 106. Highest-efficiency designs (1) to (5) use light trapping for t_0 = 50…400 nm, with f_B = 160, while design concept (6) presents the J-V curve as measured and modeled in (SUN; ASADPOUR; NIE; MOHITE *et al.*, 2015). Cell design concept (7) confers to the cell with the former state-of-the-art efficiency of 24.2% (the present state-of-the-art PCE is 25.2%), considering improved material properties, but no light

trapping. Design (8) shows how (7) can be improved by light trapping, and concept (9) shows a similar efficiency as (7), with less ideal properties, but with light trapping. Table 4.5 presents the J-V performance parameters of these design proposals, and Table 4.6, page 114, visualizes the relative improvements of these parameters, comparing in each row two different design proposals, as selected from Table 4.5.

Table 4.3 – Optimized model variables (boldface symbols), as obtained from eleven optimizations in the nine-dimensional function space with specific boundary-expansion factors f_B for a PSC with t_0 = 400 nm, where light trapping with spherical nanoparticles compensates the reduced absorption in this absorber layer; qG_{max} = 24.5 mA/cm^2.

f_B	s_f	s_b	Δn	Δp	V_{bi}	D_n	D_p	μ_n	μ_p	t_0	λ_{ave}	η	λ_{ave}^*	η^*
[-]	[cm/s]	[cm/s]	[1/cm^3]	[1/cm^3]	[V]	[cm²/s]	[cm²/s]	[cm²/Vs]	[cm²/Vs]	[nm]	[nm]	[%]	[nm]	[%]
5.00	40.00	3.84	8.43E+06	1.30E+08	0.80	0.25	0.25	9.65	9.65	*400.00*	88.89	*20.29*	41.76	20.50
10.00	20.00	1.92	8.43E+06	1.30E+08	0.82	0.50	0.50	19.30	19.30	*400.00*	88.89	*21.76*	8.89	22.01
20.00	10.00	0.96	8.43E+06	1.30E+08	0.86	1.00	1.00	38.61	38.61	*400.00*	88.89	*23.45*	4.44	23.72
30.00	6.67	0.64	8.43E+06	1.30E+08	0.90	1.50	1.50	57.91	57.91	*400.00*	88.89	*24.47*	2.96	24.76
40.00	5.00	0.48	8.43E+06	1.30E+08	0.94	2.00	2.00	77.22	77.22	*400.00*	88.89	*25.13*	2.22	25.42
60.00	3.33	0.32	8.43E+06	1.30E+08	1.01	3.00	3.00	115.82	115.82	*400.00*	88.89	*25.95*	1.48	26.25
80.00	2.50	0.24	8.43E+06	1.30E+08	1.09	4.00	4.00	154.43	154.43	*400.00*	88.89	*26.48*	24.56	26.79
100.00	2.00	0.19	8.43E+06	1.30E+08	1.17	5.00	5.00	193.04	193.04	*400.00*	88.89	*26.90*	23.71	27.17
120.00	1.67	0.16	8.43E+06	1.30E+08	1.25	6.00	6.00	231.65	231.65	*400.00*	88.89	*27.23*	22.83	27.54
140.00	1.43	0.14	8.43E+06	1.30E+08	1.32	7.00	7.00	270.26	270.26	*400.00*	88.89	*27.52*	22.15	27.83
160.00	1.25	0.12	8.43E+06	1.30E+08	1.40	8.00	8.00	308.87	308.87	*400.00*	88.89	*27.76*	21.50	28.08

Observations: (i) The values in italic formatted numbers correspond to the cell with t_0 = 400 nm in Figure 4.3, page 106; (ii) optimizations consider the *m*-constrained specification of λ_{ave} ; the values in the columns as marked with *, we obtained in f_B – constrained setup of λ_{ave} .

In our simulation, we optimize the efficiency in a general form, as a function of the improved diffusivities (D_n and D_p), not considering the modeling of (i) the diffusion length, or (ii) the lifetime of charge carriers separately. However, using the relationship

$$D_{n,p} = L_{n,p}^2 \,/\, \tau_{n,p} \;, \tag{4.1}$$

as obtained by solving equation (A.33) and (A.34), page 169, for the diffusion coefficient, the efficiency can also be expressed as a function of the diffusion length, or the lifetime of the minority charge carriers. We use our optimized diffusivity $D_n = D_p$ in the range of 0…8 cm^2/s, where the higher value is specified for the design with the highest PCE, and calculate the necessary improvements of the (i) lifetime, (ii) diffusion length, or (iii) the simultaneous improvement of both of these variables, specifying the values of these properties for the

optimized diffusivity. For the setup condition, we consider the state-of-the-art values of diffusion lengths of $L_n = L_p = 1$ μm (STRANKS; EPERON; GRANCINI; MENELAOU *et al.*, 2013), the diffusivities of $D_n = D_p = 0.05$ cm^2/s ((SUN; ASADPOUR; NIE; MOHITE *et al.*, 2015) apud (STRANKS; EPERON; GRANCINI; MENELAOU *et al.*, 2013)), which result in a calculated lifetimes of $\tau_{n,p} = 200$ ns. To calculate this lifetime, we use equations (A.33) and (A.34), page 169, and solving them for its lifetimes as follows

$$\tau_{n,p} = L_{n,p}^2 / D_{n,p} . \tag{4.2}$$

Considering a fixed value of $\tau_n = \tau_p = 200$ ns, as used for the setup conditions, and the optimized $D_n = D_p = 8$ cm^2/s, then the diffusion length is calculated with 12.65 μm by equations (A.33) and (A.34), page 169. Therefore, the initial diffusion length of 1 μm must be increased by the adequate manipulation of the material properties, resulting in a 12.65-fold increase of this diffusion length, configuring $D_n = D_p = 8$ cm^2/s. As a result, the demanded diffusion coefficient improvement in the range of 0.05…8 cm^2/s can be configured by a demanded diffusion length improvement in the range of 1…12.65 μm, for a fixed $\tau_n = \tau_p =$ 200 ns.

Considering instead a fixed diffusion length of $L_n = L_p = 1$ μm, and the optimized $D_n = D_p = 8$ cm^2/s, then the $\tau_n = \tau_p$ is calculated with 1.25 ns, using equation (4.2). Therefore, the initial lifetime of 200 ns must be reduced by adequate manipulation of the material properties, resulting in a 160-fold lifetime reduction in order to configure the optimized diffusion coefficients of 8 cm^2/s. As a result, the demanded diffusion coefficient improvement in the range of 0.05…8 cm^2/s can be configured by a demanded lifetime decrease from the initial lifetime of 200 ns down to the value of 1.25 ns, for a fixed $L_n = L_p = 1$ μm.

We conclude that the manipulation of the diffusion length is much more effective because of its 160/12.65 = 12.8 fold increased sensitivity as defined by the quadratic formulation in equation (4.2). In a combined improvement of the lifetime and the diffusion length we consider, e.g., only a 40-fold lifetime reduction, which leads to the value of 5 ns. Applying again the relationship as defined by equation (A.33) and (A.34), page 169, the diffusion lengths must be doubled to the value of $L_n = L_p = 2$ μm, resulting in a combination of improved (i) lifetimes, and (ii) diffusion lengths, which lead to the optimized diffusivities

of $D_n = D_p = 8$ cm^2/s. As to see from the exemplary calculi using equation (4.2), the reduced lifetime in a highly efficient PSC can only appear if it is compensated by a higher transport velocity of charge carriers, saying a higher diffusion coefficient, not reducing, therefore, the diffusion length of 1 µm. An effect which is also to see from the equations (A.33) and (A.34), page 169, which specify that the same diffusion lengths can be obtained by (i) shorter lifetimes if these shorter lifetimes are compensated by higher diffusion coefficients. As to see from these exemplary calculi, the excellent diffusion lengths of PSCs are in any case longer than 1 µm, which is much larger than the considered absorber layer thickness in our simulations. Therefore, recombination effects because of a limited diffusion length have not to be considered in modeled cases.

Table 4.4 – Optimized model variables (boldface symbols) and efficiencies from eleven nine-dimensional optimizations as a function of several boundary-expansion factors (f_B) for a PSC with $t_0 = 160$ nm, where light trapping by spherical nanoparticles compensates the reduced absorption in this thin absorber layer; $qG_{max} = 23.9$ mA/cm^2.

f_B	s_f	s_b	Δn	Δp	V_{bi}	D_n	D_p	μ_n	μ_p	t_0	λ_{ave}	η	λ_{ave}^*	η^*
[-]	[cm/s]	[cm/s]	[1/cm^3]	[1/cm^3]	[V]	[cm²/s]	[cm²/s]	[cm²/Vs]	[cm²/Vs]	[nm]	[nm]	[%]	[nm]	[%]
5.00	40.00	3.84	8.43E+06	1.30E+08	0.80	0.25	0.25	9.65	9.65	*160.00*	35.56	*20.46*	7.11	21.20
10.00	20.00	1.92	8.43E+06	1.30E+08	0.82	0.50	0.50	19.30	19.30	*160.00*	35.56	*21.85*	3.56	22.67
20.00	10.00	0.96	8.43E+06	1.30E+08	0.86	1.00	1.00	38.61	38.61	*160.00*	35.56	*23.46*	1.78	24.34
30.00	6.67	0.64	8.43E+06	1.30E+08	0.90	1.50	1.50	57.91	57.91	*160.00*	35.56	*24.43*	1.19	25.35
40.00	5.00	0.48	8.43E+06	1.30E+08	0.94	2.00	2.00	77.22	77.22	*160.00*	35.56	*25.06*	0.89	26.00
60.00	3.33	0.32	8.43E+06	1.30E+08	1.01	3.00	3.00	115.82	115.82	*160.00*	35.56	*25.84*	0.59	26.82
80.00	2.50	0.24	8.43E+06	1.30E+08	1.09	4.00	4.00	154.43	154.43	*160.00*	35.56	*26.37*	9.08	27.36
100.00	2.00	0.19	8.43E+06	1.30E+08	1.17	5.00	5.00	193.04	193.04	*160.00*	35.56	*26.77*	0.60	27.77
120.00	1.67	0.16	8.43E+06	1.30E+08	1.25	6.00	6.00	231.65	231.65	*160.00*	35.56	*27.10*	0.90	28.11
140.00	1.43	0.14	8.43E+06	1.30E+08	1.32	7.00	7.00	270.26	270.26	*160.00*	35.56	*27.37*	8.44	28.40
160.00	1.25	0.12	8.43E+06	1.30E+08	1.40	8.00	8.00	308.87	308.87	***160.00***	35.56	***27.61***	0.71	28.65

Observations: (i) The values in boldface formatted numbers correspond to cell design (3) in Figure 4.3, page 106, and Figure 4.4, page 111, and the highest-efficiency cell in Figure 4.4 and Figure 4.5, page 115; (ii) the values in italic formatted numbers correspond to the PSC with $t_0 = 160$ nm in Figure 4.3; (iii) optimizations consider the *m*-constrained specification of λ_{ave}; the values in the columns as marked with *, we obtained in f_B – constrained setup of λ_{ave}**.**

4.2.2 Discussions

Cell designs: Figure 4.3, and Figure 4.4, pages 106 and 111; as well as Table 4.2 to Table 4.6, pages 107 to 114; visualize how different measures can optimize the efficiency of a PSC in different development states by (i) the improvement of the material properties, as expressed by the f_B – factor; (ii) light trapping for a constant f_B – factor, as used for $t_0 < 450$

nm; and (iii) the combination of these methods. While the material property improvements mainly raise the V_{MPP}, light trapping increases both parameters V_{MPP}, and the J_{MPP}. Such developments can be discussed, comparing the cell designs in Table 4.5, which results in cell comparisons of Table 4.6, page 114.

Figure 4.4 – Current density – terminal voltage (J-V) curves and power density – voltage curves of the proposed cell designs.

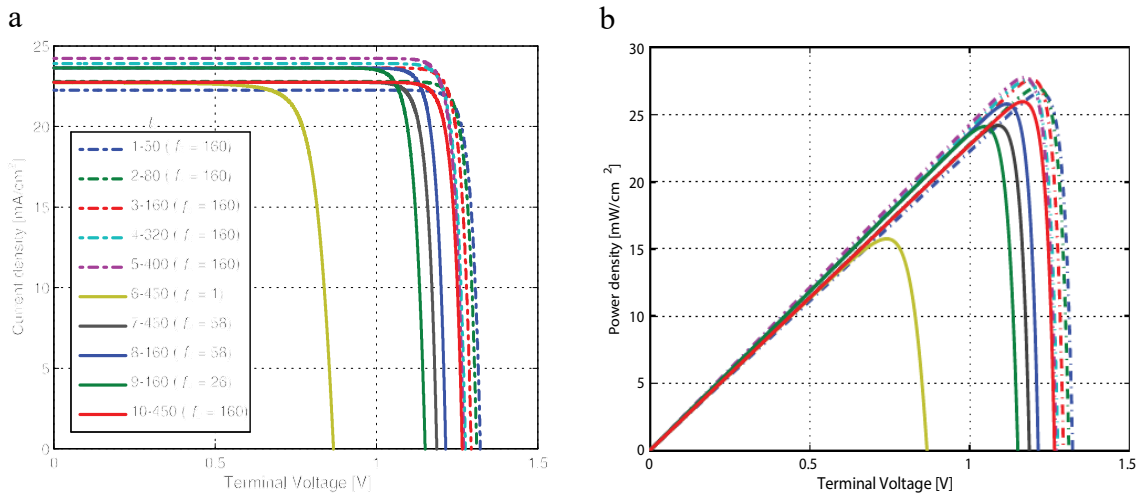

(a) J-V and (b) power density curves of ten solar cell designs, as obtained by nine multidimensional optimizations, specified here by different absorber layer thicknesses (t_0) and boundary-expansion factors (f_B): (1) t_0 = 50 nm, f_B = 160; (2) t_0 = 80 nm, f_B = 160; (3) t_0 = 160 nm, f_B = 160; (4) t_0 = 320 nm, f_B = 160; (5) t_0 = 400 nm, f_B = 160; (6) t_0 = 450 nm, f_B = 1 (SUN; ASADPOUR; NIE; MOHITE *et al.*, 2015); (7) t_0 = 450 nm, f_B = 58; (8) t_0 = 160 nm, f_B = 58; (9) t_0 = 160 nm, f_B = 26, (10) t_0 = 450, f_B = 160.

Considering that the cell with the former state-of-the-art efficiency of 24.2%, is based on light trapping (Table 4.5, design 9), an improvement of the further material properties results in cell design (3) and raises the PCE by a relative increase of 14.6% (Table 4.6 - row 13). This increase is mostly based on a 14.1% rise in V_{MPP}. However, assuming that the state-of-the-art cell uses no light-trapping scheme (Figure 4.3 and Table 4.5, design 7); its PCE can be increased by 6.6% using light trapping with spherical nanoparticles, obtaining design (8). This increase is a function of a 4% rise in J_{MPP} and a 2.5% increase in V_{MPP} (Table 4.6 - row 6).

Figure 4.4, on page 111, compares the J-V curves and the power curves of (i) the setup cell design concept and (ii) the most ideal cell design concept as considered here with a 160 nm thick absorber layer (Table 4.4 - design 3). The dash-dotted curves represent the cell

as optimized in (SUN; ASADPOUR; NIE; MOHITE *et al.*, 2015), and the continuous curves characterize the ideal cell design. This design concept is a result of a multidimensional material property improvement of a cell with spherical plasmonic nanoparticles localized in a 160 nm thick absorber layer. The PCE of this cell is only 0.2% lower in comparison to the highest obtained efficiency in a cell with t_0 = 400 nm (Table 4.3, Figure 4.3 and Table 4.5 – cell design 5). Light trapping with spherical nanoparticles and the improvement of the device's material properties result in a significant PCE increase, rising the PSC's efficiency from initially 15.7% (design 6), to 27.6% as obtained by cell design (3), and to 27.5%, as obtained by cell design (5).

The nonlinear advantage in higher-dimensional optimizations: Summing up the nine one-dimensional efficiency increases in Table 4.1, page 103, we registered a total contribution of 4.5% for a boundary-expansion factor of f_B = 160. However, the combined contribution of these variables, in a multidimensional optimization, results with the maximum value of 27.6% (Table 4.4, page 110) in a much higher efficiency rise of 27.6% - 15.7% = 13.4%, considering the same f_B – factor. Consequently, the summed single contributions of the one-dimensional PCE growths result in a 4.5% efficiency increase, and because of further effects, we obtained an additional efficiency increase, with a value of 13.4% – 4.5% = 8.9%. We registered a similar behavior also in the comparison of the one- and the two-dimensional optimizations in section 4.1, page 98, and assign this additional PCE increase to the nonlinearities, as inherent to the analyzed PSC's drift-diffusion model. As an outcome, higher-dimensional optimizations are much more effective, in comparison to the state-of-the-art one- and two-dimensional optimizations.

A further nonlinear behavior we observed for the proper efficiency increases in Figure 4.3, page 106, since the highest PCE gradients appear for low f_B values, which correspond to small material property improvements in the hypercube space. Therefore, the multidimensional efficiency optimizations are most effective for cells, which efficiency is close and principally lower, than the state-of-the-art PCE. The light-trapping characteristics enhance this effectiveness in the multidimensional optimizations because of the resulting higher efficiency gradients of the related curves in Figure 4.3, page 106.

Table 4.5 - Optimization setup configurations (f_B, t_0, λ_{ave}, qG_{max}, J_{sc}) and perovskite performance parameters (V_{0C}, V_{MPP}, FF, PCE), as calculated from the J-V curve characteristics, including also cell designs as presented Figure 4.3, page 106, and Figure 4.4, page 111.

Cell designs	f_B [-]	t_0 [nm]	λ_{ave} [nm]	$q\,G_{max}$ (#) [mA/cm^2]	J_{SC} [mA/cm^2]	V_{0C} [V]	J_{MPP} [mA/cm^2]	V_{MPP} [V]	FF [-]	PCE [%]
(1)	160	50	11.1	22.5	22.3	1.32	21.8	1.22	0.905	26.6
(2)	160	80	17.8	23.1	22.8	1.31	22.3	1.21	0.904	27.0
(3)	160	160	35.6	23.9	23.6	1.29	23.1	1.19	0.903	27.6
(4)	160	320	71.1	24.2	23.9	1.28	23.4	1.18	0.902	27.5
(5)	160	400	88.9	24.5	24.2	1.27	23.7	1.17	0.902	27.8
(6)	1	450	100.0	23.0	22.7	0.87	21.3	0.74	0.799	15.7
(7)	58	450	100.0	23.0	22.7	1.19	22.2	1.09	0.896	24.2
(8)	58	160	35.6	23.9	23.6	1.21	23.1	1.12	0.898	25.8
(9)	26	160	35.6	23.9	23.6	1.15	23.0	1.05	0.886	24.1
(10)	160	450	100.0	23.0	22.7	1.27	22.3	1.17	0.902	26.0

(#) Adopted short circuit current densities as obtained in (Cai et al. 2015 and Sun et al. 2015). Observation: In the Beer-Lambert model simulations as presented in (SUN; ASADPOUR; NIE; MOHITE *et al.*, 2015) and section APPENDIX A.1, page 156 the Jsc is to some minute extent lower than qGmax, as used in the setup of this model (see Matlab^{TM} program in Supplementary Material). An effect, which disappears for large values (m > 10) in equation (A.14), page 163. In the modeling presented, we used m = 4.5, which results in a feeble reduction of the J_{sc}, in comparison to qG_{max}. A meliorated model of the short circuit current density would, therefore, present slightly higher maximum efficiencies than those obtained in this section and table, because of the corrected J_{sc} values, which result, e.g., to a 0.2 mA/cm^2 higher short circuit current density in cell design (1).

High efficiencies with thin absorber layers: The highest and second highest values of J_{sc} and J_{MPP} we obtained with the light-trapping cell designs (5) and (4) in Table 4.5, page 113. These designs present the thickest absorber layers of t_0 = 400 and 320 nm. Meanwhile, the highest and second highest PCE values we obtained with cell designs (5) and (3), which present a t_0 of 400 and 160 nm. In the case of V_{0C} and $V_{MPP,}$ the highest value appears, for the cell with the thinnest absorber layer, as presented in cell design (1). This cell also presents the highest fill factor (FF). The relatively high efficiency in the cell with an absorber layer thickness of only 160 nm (design 3) can be explained as a result of the increased J_{MPP}, as related to light trapping, in combination with the high V_{MPP} in thin absorber layers. Such a combination leads to the second-highest efficiency, being only 0.2% lower in comparison to the design with the highest efficiency of 27.8% (design 5), with a t_0 of 400 nm.

Table 4.6 – Relative increase or decrease of six performance parameters in fourteen comparisons of the ten discussed cell designs of Table 4.5.

Row	Design improvements	J_{SC} [%]	V_{0C} [%]	J_{MPP} [%]	V_{MPP} [%]	FF [%]	PCE [%]
1	Sun – Design (9)	4.0	32.8	8.3	41.2	10.8	53.0
2	Sun - Design (7)	0.1	36.9	4.5	47.0	12.1	53.6
3	Sun - Design (10)	0.1	46.0	4.7	57.5	12.8	64.8
4	Sun - Design (3)	4.0	49.2	8.8	61.2	13.0	75.3
5	Sun - Design (8)	4.0	40.1	8.6	50.7	12.3	63.7
6	Design (7) - Design (8)	3.9	2.3	4.0	2.5	0.2	6.6
7	Design (9) - Design (8)	0.0	5.5	0.3	6.7	1.4	7.0
8	Design (9) - Design (7)	-3.8	3.1	-3.5	4.1	1.2	0.4
9	Design (7) - Design (10)	0.0	6.6	0.2	7.1	0.6	7.3
10	Design (8) - Design (10)	-3.8	4.2	-3.7	4.5	0.4	0.7
11	Design (10) - Design (3)	3.9	2.2	4.0	2.3	0.2	6.4
12	Design (8) - Design (3)	0.0	6.5	0.1	6.9	0.6	7.1
13	Design (9) - Design (3)	0.0	12.4	0.4	14.1	2.0	14.6
14	Design (7) - Design (3)	3.9	9.0	4.1	9.6	0.8	14.1

The highest values of V_{0C} and FF in the thinnest absorber layer we account for the simultaneous (i) reduction of t_0, and (ii) the light-trapping effect. High V_{0C} in PSC's are obtained as a function of its inherent photon-recycling effect (PAZOS-OUTÓN; SZUMILO; LAMBOLL; RICHTER *et al.*, 2016), which improves by light trapping (SHA; REN; CHEN; CHOY, 2015) that also increases the fill factor (FF) (SHA; REN; CHEN; CHOY, 2015). Thin absorber layers (i) allow for lower diffusion lengths of electrons and holes and (ii) increase the electrical field of the PSC, which can result in lower recombination of charge carriers.

We say here which can result in lower recombination effects because if a certain level of built-in voltage, and therefore, built-in electrical field, is attained, further increase of V_{bi} leads to no efficiency increase as evident from section 4.3, page 120. Even without a light trapping, thin absorber layer increase the FF and the V_{oc}, as also evaluated by numerical simulations in (DEVI; PARREY; AZIZ; DATTA, 2018). Therefore, we suggest to use coating techniques that allow the coating of extra thin absorber layers, and result in high efficiencies, using, e.g., the solvent-solvent extraction methods (ZHOU; YANG; WU; VASILIEV *et al.*, 2015), or further available techniques (LIU, 2017).

The former technique results in smooth, and thickness-adjustable absorber layers, in the range of t_0 = 20…410 nm. However, for the light trapping with spherical nanoparticles, we do not recommend the coating of absorber layers thinner than 160 nm, as even light trapping cannot compensate for the reduced current density as related to thin absorber layers.

The more effective shape-optimized nanoparticles can improve such a scenario, providing higher efficiency even for thinner absorber layers.

Figure 4.5 - J-V and power curves of the initial and optimized PSCs for AM 1.5 reference solar irradiance of 100 mW/cm², with marked maximum power point (MPP) values: (i) Curves for the solar cell configuration of the manufactured and modeled PSC in (Sun et al. 2015) (J_{light}, J_{dark}, P). And (ii) curves for the simulated solar cell model, as obtained by the multidimensional optimization, with a maximum PCE of 27.6 % for f_B = 160 and t_0 = 160, ($J_{light\text{-}max}$, $J_{dark\text{-}max}$, P_{max}). Stars and circles show the MPP points of these curves presenting power densities of 15.7 mW/cm^2 and 27.6 mW/cm^2, which correspond in this normalized presentation to efficiencies of η_{MPP} = 15.7% and 27.6% (Matlab^{TM} program for the configuration of these curves, as a function of the cell's material properties, in Appendix section C.2).

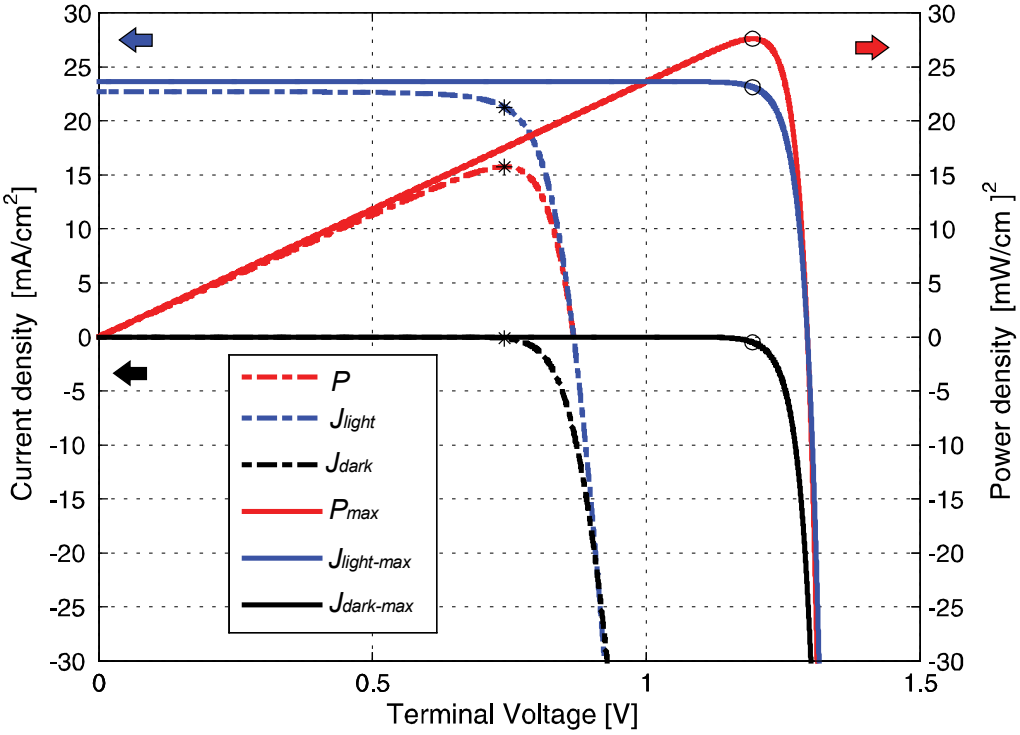

However, there are presently no simulated or measured short circuit densities available for such an improved scheme. We note that PSCs with $t_0 \approx 450$ nm present already low Pb contents per cell area, which are similar to the total heavy-metal content of state-of-the-art silicon photovoltaic modules (GREEN; HO-BAILLIE; SNAITH, 2014; STASIULIONIS, 2015). Fortunately, the thickness reduction of the absorber layer to t_0 = 160 nm, as enabled here by light trapping, leads to an additional decrease in the cell's Pb residual.

While the open-circuit voltage of the cell as measured and modeled in (SUN; ASADPOUR; NIE; MOHITE *et al.*, 2015) present a high open-circuit voltage of 0.74 V, as similar to crystalline solar cells; its high fill factors of 0.8 is similar to the state-of-the-art FF of multicrystalline, CIGS, and CdTe cells, as measured by an independent laboratory (GREEN; DUNLOP; LEVI; HOHL-EBINGER *et al.*, 2019). The best of our analyzed or proposed cell designs do present, with an increase of the FF to the value of ~ 0.9, a slightly higher value in comparison to the highest efficient GaAs with FF = 0.87. The open-circuit voltage of our optimized cells is, with values of ~ 1.3 V, higher than the values of GaAs, and the perovskite cells as presented in (GREEN; DUNLOP; LEVI; HOHL-EBINGER *et al.*, 2019), which show $V_{0C's}$ of ~ 1.13 V. The highest J_{sc} for the here optimized cells, as considered for light trapping, is with 23.7 mA/cm^2 still lower than the value of 24.9 mA/cm^2, as measured for a PSC with an efficiency of only 20.9% in (GREEN; DUNLOP; LEVI; HOHL-EBINGER *et al.*, 2019). Therefore, we think that by the selection of a better absorber material, the PCE of the presented optimized cell designs might still be improved to some extent.

Accuracy and comparison of the obtained results: The modeling of the short circuit current density, as used in our simulations, presents high accuracies for the cases with and without light trapping. In both cases, we set up our simulations with values of the short circuit current density as obtained by high-resolution simulations. Without light trapping, we used the values as simulated by the OTM modeling (SUN; ASADPOUR; NIE; MOHITE *et al.*, 2015), and in the light-trapping configurations, we used the values obtained by FDTD simulations in (CAI; PENG; CHENG; GU, 2015). More details about these methods we discuss in APPENDIX C.2, page 201. Furthermore, we consider reasonable low uncertainties in the Beer-Lambert modeling (sections APPENDIX C.2, page 201; APPENDIX C.3, page 202). In this context, we remark that large deviations in the λ_{ave} value result in only tiny efficiency deviations for the same f_B value Table 4.2 to Table 4.4, page 107). Therefore, even assuming hypothetically high uncertainties in the Beer-Lambert law, and its related λ_{ave}, this would result in only small deviations of the optimized efficiency values.

The highest achieved efficiency for the single-junction PSCs of 27.76% (Table 4.3, page 106), is higher than (i) the state-of-the-art efficiency of 25.2%, and (ii) the highest simulated efficiency of 25% (AGARWAL; NAIR, 2014; 2015). Additionally, a large set of our optimized solar cell designs increase these state-of-the-art PCEs of manufactured and

simulated solar cells (Figure 4.3, page 106). As expected, all cell designs show a lower efficiency than the lowest value of the theoretical upper limit with the PCE = 29.9% (REN; WANG; SHA; CHOY, 2017).

The contributions in this work: The material property improvements, as optimized by the multidimensional NLP optimization algorithm, are arbitrary, and we controlled these arbitrary variable improvements using a proposed improvement factor (f_B). These improvements must not coincide with the property values of manufactured PSCs since the latter can arise at individual scales for each property. We used the presented concept of general property improvement to (i) illustrate the substantial efficiency increase in the case of multidimensional property improvements; (ii) present high- and highest-performance cell designs with low Pb contents and discuss, which techniques enable its manufacturing; (iii) estimate and discuss the percentual increases of several performance parameters at different development stages; (iv) identify dependencies in-between model variables, and (v) present a complete set of possible two-dimensional sensitivity analyses. Accordingly, we acquired a better understanding and provided useful knowledge for the efficiency optimization of manufactured PSCs. The presented results can be used as a roadmap, showing to which extent the PSC's efficiency and curve parameters can be increased, by different measures, and at different developmental stages. Our proposed designs, consider one-, two- (Table 4.1, page 103), and multidimensional improvements of the cell's material properties (Figure 4.3, page 106). We define the multidimensional improvement as the simultaneous improvement of (i) the whole set of material properties and (ii) the absorber layer thickness, as accomplished by a numerical optimization process.

Diffusion coefficients of electrons and holes: It is generally conceived that longer diffusion length of electron and hole charge carriers lead to longer diffusion distances of these charge carriers without being subjected to a recombination process. As they recombine with a high probability at the end of its diffusion length, the L_n and L_p should be high enough that these charge carriers can reach its selective charge conduction layers, which is especially crucial for cells with thick absorber layers. A similar abstraction is also to conceive for the lifetime of electrons and holes, τ_n and τ_p, and it is generally assumed that with a long lifetime charge carriers can diffuse at longer distances in the absorber layer, therefore being less prone to recombine.

However, as an evident result of our multidimensional optimizations, we got to know that the so-called lifetime should be ideally as short as possible. In our optimization, we choose the diffusion coefficients of electrons and holes, D_n and D_p, also named as diffusivities, as optimization variables and, the multidimensional optimization shows that the diffusivities should be as large as possible. As a result of equation (4.1), page 108, we observe that shorter lifetimes and longer diffusion lengths result is higher diffusivities, as the lifetime stands in the denominator and the diffusion length stands in the nominator of this equation. As the diffusivity, with the units of [cm^2/s], expresses a spatial expansion velocity of the electrons and holes, as higher as this velocity is in this expansion process, for fixed values of the diffusion length, as shorter is the transport time, usually conceived as lifetime. As a result, higher diffusivities also result in higher efficiencies, which can be based on shorter lifetimes, longer diffusion lengths, or a simultaneous improvement of both of these variables.

Such a conclusion is supported with the findings in (SONG; CUI; WANG; WEI *et al.*, 2015), which shows that the PCE increases from 6.4% to 16.4% as a function of a reduced monomolecular lifetime, which decrease from 44 ns to 27.6 ns, using a post-annealing process at 160 ^oC. However, the authors show that this annealing process also improves the cell's absorption coefficient at a wavelength of 635 nm, which increases from the value of 2.9 x 10^{-4} s^{-1} to 4.0 s^{-1}. Thus, it is not fully evident if the higher PCE is obtained because of a shorter lifetime or a higher absorption coefficient. However, the authors registered an increase in both (i) the open-circuit voltage and (ii) the J_{sc}. Therefore, the higher PCE, as obtained by the post-annealing process, is possibly related to both (i) a shorter lifetime and (ii) a higher absorption of the solar irradiance. Furthermore, the authors (CHIRVONY; SEKERBAYEV; PÉREZ-DEL-REY; MARTÍNEZ-PASTOR *et al.*, 2019) discuss that the very short photoluminescence lifetimes in MAPI films result in high diffusion coefficients and PCE values. However, as the efficiency is a multidimensional function of the cell's material properties, only multidimensional efficiency analyses and optimizations, as accomplished in the present work, can give conclusive results concerning these dependencies.

Recommendations for cell optimizations: Material property improvements lead to the highest relative efficiency increase in cells whose PCE is less or equal than state-of-the-art efficiency (Figure 4.3, Table 4.6, page 114 - row 2). Otherwise, light-trapping techniques are most efficient in cells, whose non-optimized PCE is already higher or equal than the state-of-

the-art PCE (Figure 4.3, Table 4.6 - rows 6 and 11). While the material properties improvement does principally increase V_{MPP}, light trapping results in the raise of both J_{MPP} and V_{MPP}. Being the state-of-the-art efficiency based on light trapping (design 9), or not (design 7), we increased this PCE by approximately 14%. This increase is a result of (i) additional material property improvements (Table 4.6 - row 13), and (ii) its combination with light trapping (Table 4.6 - row 14). In all cell configurations, λ_{ave} should always be configured as a function of t_0; being this in (i) an m-constraint relationship, or (ii) in a f_B – constrained relationship.

The former is easy to calculate, and the latter results in slightly higher efficiency values (last two columns at the right side of Table 4.2 to Table 4.4, page 107) if the low reflection losses are configurable in a manufactured cell. Since the remaining properties stand not in such a relationship to each other, the multidimensional optimizations, as presented here, can be substituted by simple model simulations, in cell manufacturing and research. These simulations are accomplishable using (i) the constraint condition in equation (9), and alternatively (ii) a two-dimensional sensitivity analysis of Figure 4.2f, page 102. We suggest that PSC manufacturing should be based on thickness-adjustable thin film coating techniques (LIU, 2017; ZHOU; YANG; WU; VASILIEV *et al.*, 2015). Otherwise, adjustable light-trapping techniques (CAI; PENG; CHENG; GU, 2015) can be used to set up an ideal λ_{ave}, for a fixed absorber layer thickness. Such techniques enable the tuning of a perfect relationship between t_0 and λ_{ave}, which enables high efficiencies. Finally, we like to advise that some solar cell types have an ideal built-in electric field (GREEN, 2009), as related to an ideal built-in voltage. We observed, however, such an effect in our optimizations and simulations within the constraint of $V_{bi} \leq 1.4$ V.

With the presented multidimensional optimizations, we have demonstrated that the state-of-the-art efficiency of PSCs can be increased substantially and assign this effect chiefly to the nonlinear behavior of the drift-diffusion model of electrons and holes. We found that material property improvements raise the V_{MPP} predominantly, while light trapping increases the J_{MPP} mainly. Cell designs with plasmonic nanoparticles for light trapping show similar high efficiencies for a wide range of absorber layer thicknesses, because of the related increases of V_{MPP} in thin absorber layers. Small material property improvements, as expressed by low f_B values, result in the highest PCE gradients, and therefore, PCE sensitivity (Figure 4.3, page 106). Light trapping raises the PCE and increases this sensitivity, especially for low

f_B factors. For high f_B values, light trapping is most effective, resulting in the highest PCE increases. Our proposed ideal cell, as obtained by light trapping, combined with the improvement of the device's material properties, presents a high PCE value of 27.6% for the absorber layer thickness of only 160 nm, reducing, therefore, significantly cell's Pb content.

4.3 SENSITIVITY ANALYSES

The presented sensitivity analyses are of importance to validate the significance of a variable in the improvement of a nonoptimized and optimized solar cell model. In the former case, it shows by which variable modification the efficiency can be most effectively increased, and, in the latter case, it shows which variable is most important to maintain a high optimized solar cell efficiency. By knowing the efficiency (PCE) and power density at the MPP point (P_{MPP}), we also know the current density (J_{MPP}), the voltage, as well as the short circuit current density (J_{sc}), and the open-circuit voltage (V_{0C}) of the considered cell configuration. Knowing the behavior of these additional performance parameters is essential in elaborating better knowledge, especially related to the optimized cell. With this knowledge, we can respond to critical questions, why, or because of the degradation of which performance parameter, an optimized solar cell efficiency can reduce as a function of single non-ideal material properties.

4.3.1 Results

In Figure 4.6 to Figure 4.8, we present the results from a set of one-dimensional sensitivity analyses of the considered pin-type PSC, analyzing two different cell designs. In the left-side diagrams (Figure 4.6 a-c and Figure 4.7 a-c), we analyze the considered non-optimized PSC. And in the right-side graphs (Figure 4.6 d-f and Figure 4.7 d-f), as well as in Figure 4.8, we validate the sensitivity of the cell design as obtained by the multidimensional numerical optimization in section 4.2, page 105. In both sensitivity analyses, we only improved one of the model variables at a time, scaling the variable modification with the sensitivity factor, as defined in the modeling section of the sensitivity analyses.

In the abscissa scaling, we select for the optimized cell $f_s = 1\ldots160 \in \mathbb{N}$ and the non-optimized cell $f_s = 1\ldots80$, because of saturation of the improvement, as observable by the low gradients for values for $f_s > 80$. While in Figure 4.6 and Figure 4.7, only the abscissa values

are normalized, in Figure 4.8, we also normalized the ordinate values, which allows us to compare the behavior of the whole set of performance parameters as a function of the variation of single material properties. The conversion of the abscissa scale is identical, as in Figure 4.6 and Figure 4.7. Table 4.7 presents the resulting sequence of the most- to the least efficiency sensitive model variables, as selected by the analyses in Figure 4.6 to Figure 4.8. While in the case of the non-optimized solar cell, we evaluate the sensitivity by the attained PCE for high values of f_s; for the optimized PSC, we ranked these independent model variables, by the criterion of its highest PCE-gradient values, as appearing for the highest f_s values. An identical validation cannot be implemented because of the saturation character of the PCE values for high f_s values in the case of Figure 4.6a.

Table 4.7 – Variables presented by its selected importance, from the 1-th to the 7-th important variable, as selected by the efficiency gradients for high f_s vales, comparing the non-optimized and the optimized PSC design.

	1-th	**2-nd**	**3-th**	**4-th**	**5-th**	**6-th**	**7-th**
PCE$_{nopt}$	t_0	s_f	D_n	V_{bi}	λ_{ave}		
PCE$_{opt}$	λ_{ave}	s_f	D_n	s_b	D_p	V_{bi}	t_0

The properties s_b and D_p do not present any importance in the one-dimensional optimization, because of its zero gradients in Figure 4.6a. In the case of the optimized model, an increased λ_{ave}, as related to lower f_B values (Figure 4.8f) leads to lower absorption of the solar irradiance, and because of its highest gradient, we rank λ_{ave} as the most efficiency-sensitive variable. Because of its high gradients in Figure 4.8 for the upper scale f_s values, we rank the variables s_f, D_n, s_b, D_p, V_{bi} as the most important variables, in this sequence. The variable t_0 is the least important, as a slightly increased absorber layer thickness does even lead to a small PCE increase.

Figure 4.6 - One-dimensional sensitivity analyses of two different solar cell designs: (a-c) perovskite solar cell with t_0 = 450 nm as obtained in (SUN; ASADPOUR; NIE; MOHITE *et al.*, 2015); (d-f) PSC with optimized efficiency and low absorber layer thickness, as proposed by a multidimensional optimization in (KRATZENBERG; RAMBO; RÜTHER, 2019), presenting a 160 nm thick absorber layer. In the latter cell design, the cell's absorption is improved by light trapping using spherical nanoparticles. Analyzed dependent variables or performance parameters: (a, c) the power conversion efficiency (PSC); (b, d) the fill factor (FF); and (c, f) the maximum power point voltage (V_{MPP}).

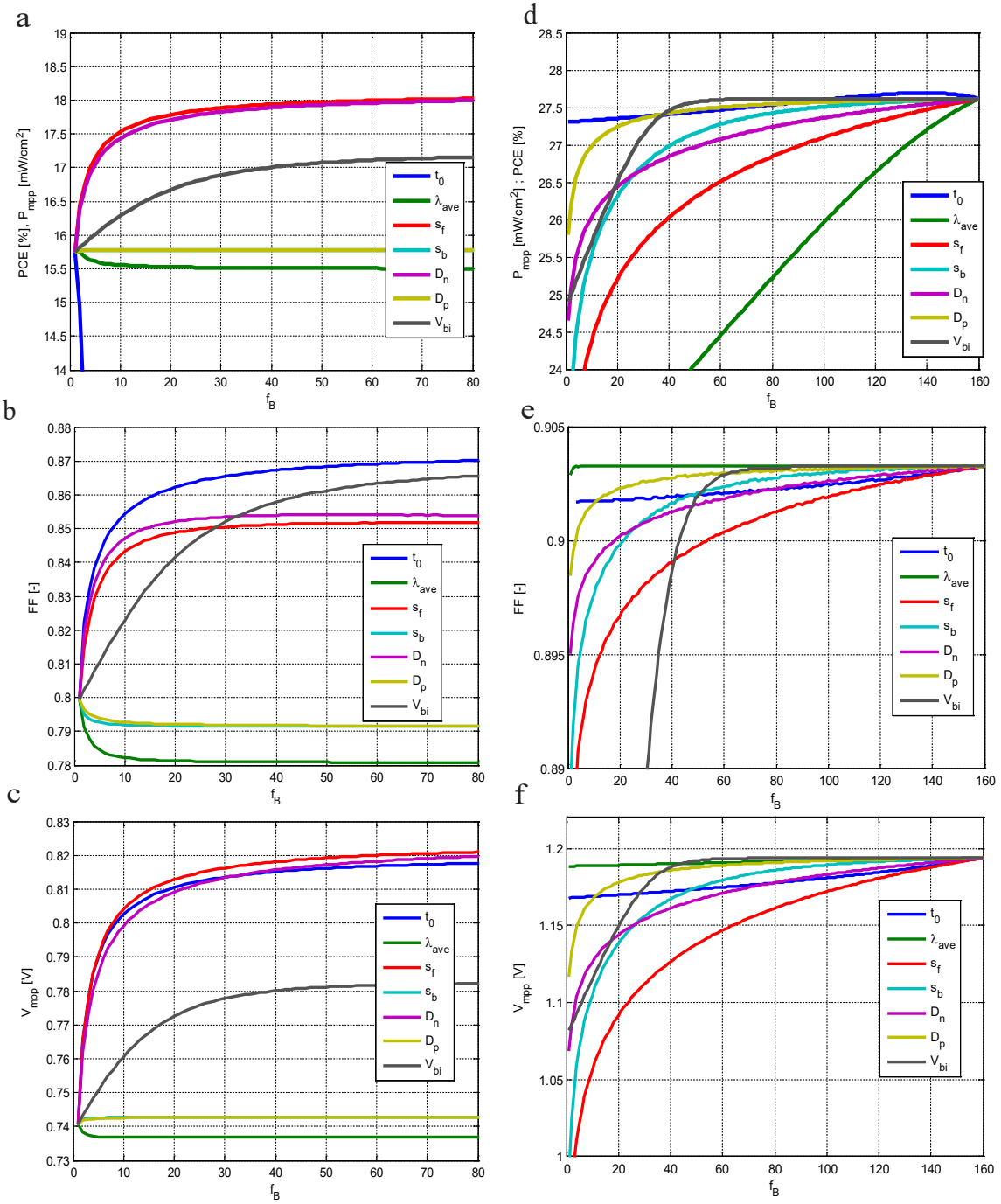

Figure 4.7 - Additional analyzed dependent variables, or performance parameters, extending the presentations of Figure 4.6, and presenting in the additional figures (a, c) the open-circuit voltage (V_{oc}); (b, d) the maximum power point current density (J_{MPP}); and (c, f) the increased short circuit current density (J_{sc}), because of light trapping.

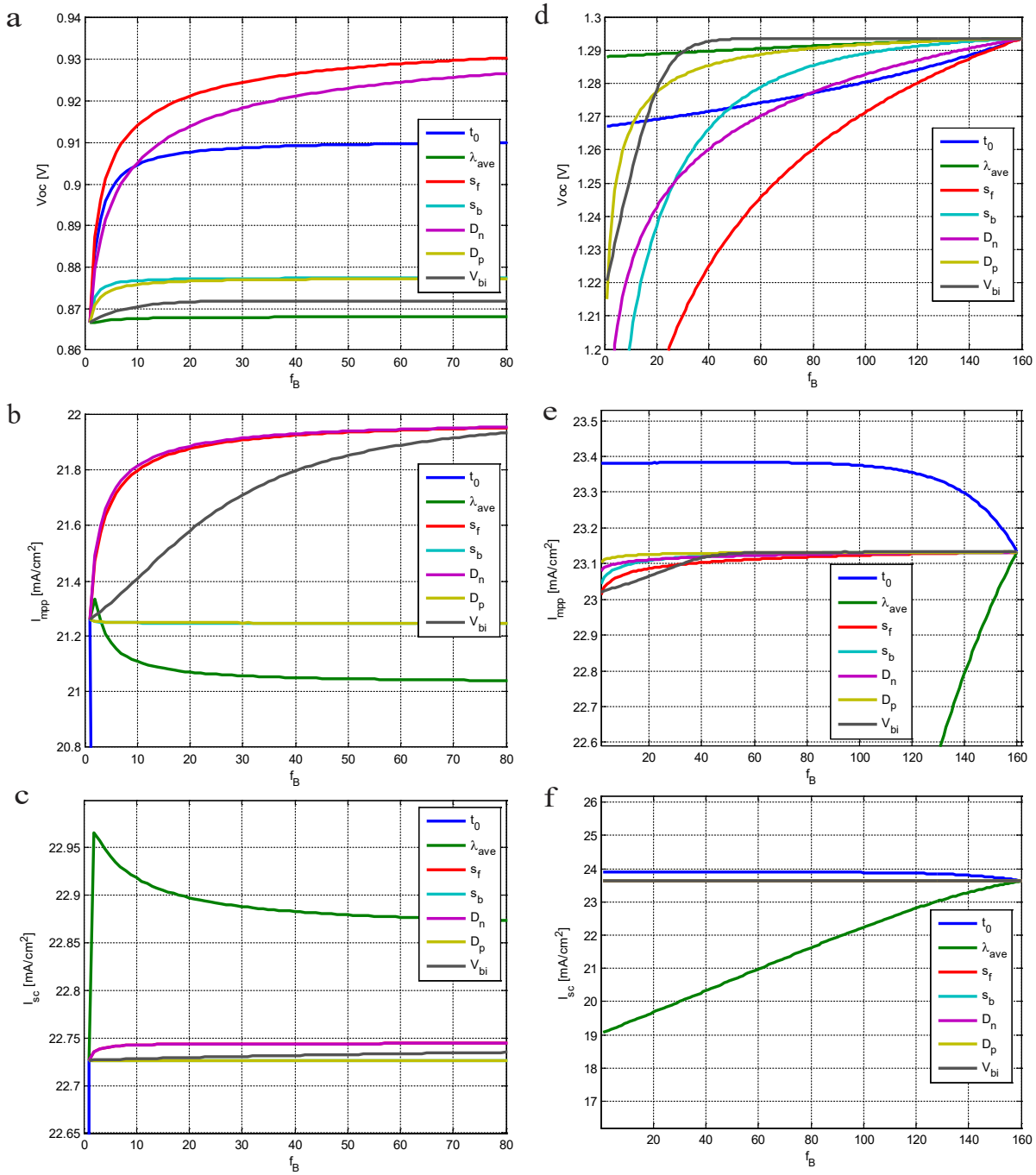

Figure 4.8 - Normalized presentation of the sensitivity analyses of the optimized PSC. (a-g) Normalized performance parameters of the J-V curve, in the ordinate, as a function of the variable improvements of different model variables, as expressed by the $f_S = f_B$ factor, in the abscissa. The sensitivity factors of f_S = 1…160 correspond to values X_{nopt} (f_S =1) and X_{opt} (f_S =160), using the values of Table 3.1, at page 94.

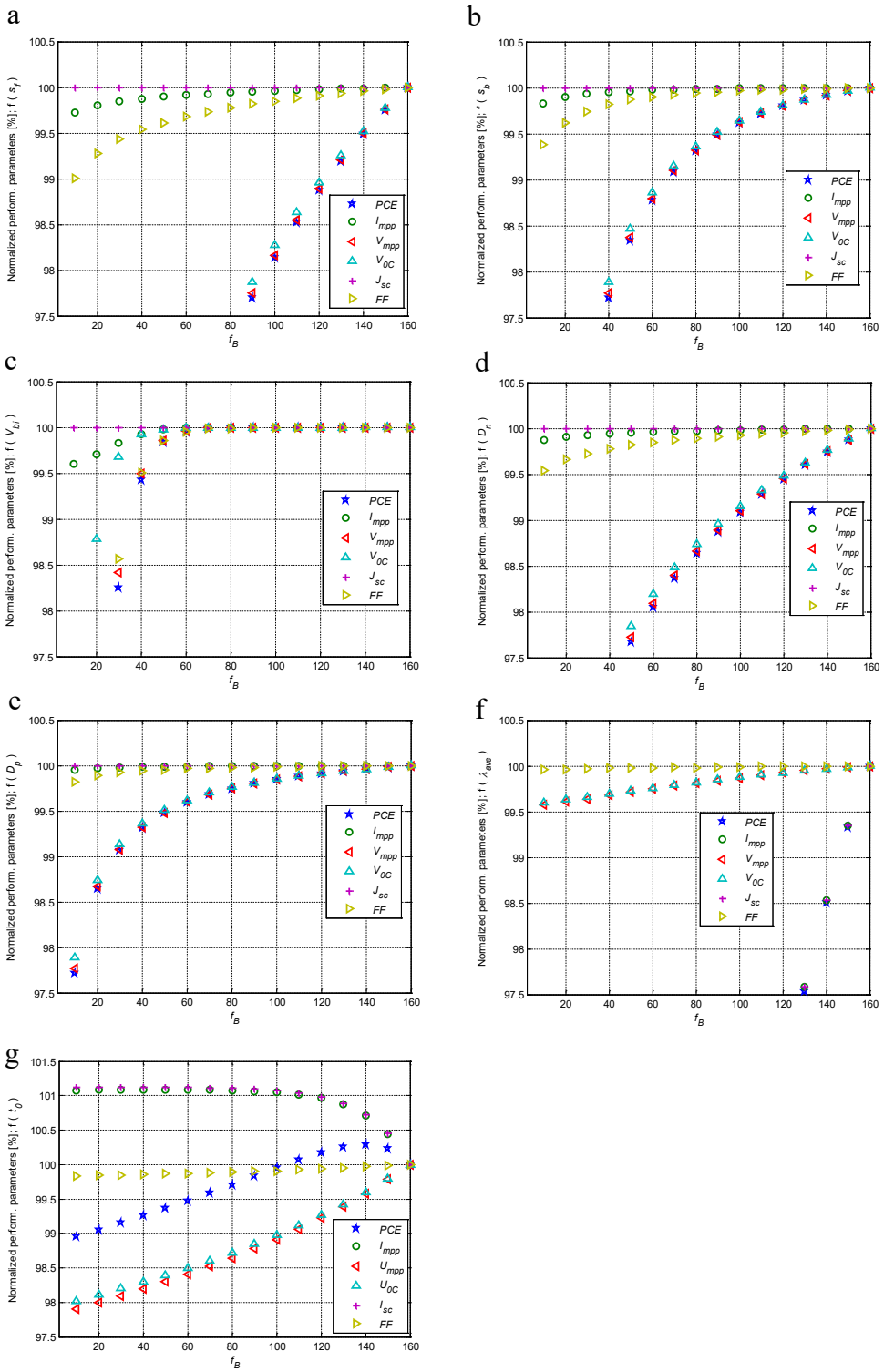

4.3.2 Discussions

As to see from Figure 4.6a, the analyzed variables increase the PCE of a non-optimized cell only to a shallow extent, resulting in a maximal PCE growth of only 2.3 %. We observe that solely in the sensitivity of the optimized PSC (Figure 4.6d) appear (i) high obtained PCE values, and (ii) high PCE gradients. For the non-optimized cell (Figure 4.6a), one-dimensional efficiency optimizations result in saturation of the PCE with nearly zero gradients, even for high sensitivity factors. These observations lead again to the conclusion that high and highest efficiencies can only be obtained if the whole set of material properties is improved. Some of the variables, e.g., t_0 and λ_{ave}, lead even to the decrease of the PCE with a considerable gradient. This decrease is evident as these two variables built-up a maximal efficiency vertex line (KRATZENBERG; RAMBO; RÜTHER, 2019) and must maintain, therefore, a demanded relationship, or at least, in the relationship of equation (A.17), page 164, to enable high PCEs.

Not complying with this relationship, they result in substantial PCE losses, as also visible in the sensitivity analysis of the non-optimized (Figure 4.6a) and optimized (Figure 4.6d) PSC. Both types of sensitivity analyses give evidence that apart from λ_{ave} and t_0, the third and the fourth most essential variables are s_f and D_n (Table 4.7, page 121), as noticeable the steep PCE reduction gradients, visible in both sensitivity analyses (Figure 4.61a and Figure 4.61d). If adequate passivation techniques reduce the number of electron recombination sites, as related to the transition interfaces of the front p-type layer to the absorber layer, the resulting reduction of s_f will lead to a substantial decrease in the electron recombination, thus increasing the cell's PCE. If the diffusion coefficient of electrons (D_n) is increased, e.g., by the longer diffusion length, then the cell's efficiency increase as more electrons can reach the back- charge conduction layer. By the way, the high sensitivities related to s_f and D_n are comprehensible, as most of the charge carriers are generated for low layer penetration depths of photons in the absorber layer (Figure 3.1b, page 81).

(GREEN, 2009) suggests that an ideal built-in field and, therefore, built-in voltage might be present to enable the highest efficiencies in some solar cells. While, the multidimensional optimization in section (4.2, page 105) has given no additional information to this question, the here presented sensitivity analyses give a clear answer to the question of the ideal V_{bi}. In comparison to the rest of the model variables, the V_{bi} presents a specific

behavior, as values of f_s > 80 (V_{bi} > 1.08 V) already enable the highest PCE values (Figure 4.8c and Figure 4.6d). This behavior provides the insight that the optimization of V_{bi} is less critical in comparison to the other variables. Once attained a minimal necessary threshold value of V_{bi} ≈ 1.08 V, it is of no further importance to increase this variable further to enable the development of high- and highest-efficient PSCs. Therefore we recommend to tune the V_{bi} solely to the value of ~1.1 eV, but not higher, as very high built-in electrical fields can even reduce the cell's efficiency, because of the necessary, excessive doping of the charge transport layers, as discussed in (GREEN, 2009).

By calculus, the power and efficiency are a function of V_{mpp} and the J_{mpp} as being both used for the calculation of the cell's power density P_{MPP}. The PCE of an optimized PSC decreases at the same magnitude as the V_{mpp} in Figure 4.8d, being a function of higher s_f values, which are represented by lower f_B values. The origin of this decrease V_{oc}, which also degrades at a very similar proportion as the PCE in the normalized representation of this figure. Meanwhile, the current density in the MPP point do degrade only very slightly, because of the lower FF, while the J_{sc} does not reduce at all as a function of higher s_f values. If compared to the remaining representations of Figure 4.8, the variables s_b (Figure 4.8b), D_n (Figure 4.8d), and D_p (Figure 4.8e) show similar patterns of performance parameter degradations, leading however to different degradation rates.

The Figure 4.8c shows that the performance parameters V_{MPP}, and FF show exceptionally high and similar normalized sensitivities as a function of a lower V_{bi}, as expressed by a lower f_B, which also leads to a similar gradient of the PCE degradation. V_{bi} of the upper range of f_B, and therefore V_{bi}, does not lead to any degradation at all, but lower range V_{bi} values lead to a significant reduction of the FF, $V_{MPP,}$ and PCE, especially pronounced for f_s < 50. This more specific pattern of degradation does not appear with the degradation of s_f, s_b, D_n, and D_p. We also observe that only the V_{bi} degradations lead to an FF-originated V_{MPP} and, therefore, PCE decrease, while the degenerations of s_f, s_b, D_n, and D_p lead to a V_{0C} originated degradation pattern of V_{MPP} and, therefore, PCE. In general, the variable λ_{ave} shows the highest-efficiency sensitivity (Figure 4.8f) as a function of a f_s value decrease, and therefore, an increase in λ_{ave}. Its PCE decrease is directly related to the lower J_{sc}, and thus, J_{mpp} values, being only to a very low extent related to lower V_{mpp} values.

A cell without light trapping presents an ideal absorber layer thickness of 450 nm, as a function of an average optical decay length of λ_{ave} of 100 nm, as inherent to the perovskite

material. The use of plasmonic nanoparticles results in a reduced λ_{ave} of 35.6 nm and permits a t_0 reduction to a here considered ideal absorber layer thickness of 160 nm (Table 3.1, page 94). The optimized efficiency of such a configuration is very similar to a cell with light trapping in a 450 nm thick absorber layer (Table 4.5, page 113). As λ_{ave} and t_0 must stand in a closed relationship, the modification of only one of these variables results in a substantial decrease of the PCE (Figure 4.6a, and Figure 4.6d, page 122). For the second case of an optimized model, this is also visible in Figure 4.8f, and Figure 4.8g, on page 124. Figure 4.8f presents the highest PCE degradation gradient in comparison to the further figures in Figure 4.8.

This high degradation appears as in this figure the non-ideal λ_{ave}, as presented $f_B = 1$, corresponds to λ_{ave} = 100 nm, and stands for a lower absorption, which needs a thicker absorber layer of 450 nm, or light trapping. Therefore, its light absorption is insufficient, with a thickness of 160 nm in the optimized cell configuration. In Figure 4.8g, $f_B = 1$ represents a thicker absorber layer of 450 nm, and f_B = 160 represents the lower t_0 of 160 nm. As an optimized cell with 160 nm thick absorber layer shows a 0.2 % lower PCE, if compared to the same cell with 400 nm (Table 4.5, page 113), the short circuit current density of the former cell increase to some low extent (1 %) for higher t_0. However, as thicker absorber layers present a lower V_{0C} and V_{mpp}, this compensation behavior results in an effective PCE decrease in Figure 4.8g for thick absorber layers. This decrease is possibly the reason of the saddle-point, as appearing in Figure 4.2, page 102, and as evident from the results for the f_B constraint optimization with ideal light trapping in Appendix Table B.1, page 189, which both show that an ideal t_0 has to be adjusted, as a function of a considered arbitrary λ_{ave}.

Some curiosities: In Figure 4.6a and Figure 4.6d, the absorber layer thickness reduces from t_0 = 450 nm ($f_s = 1$) to the ideal 160 nm ($f_s = 160$). Therefore, a PCE decrease is expected with the reduction of the t_0 without light trapping because of its reduced absorption. The λ_{ave} decrease from 100 nm (f_s = 1), to the ideal value of 35.6 nm (f_s = 160) in those figures, because of light trapping. Its PCE also decreases, as expected, as the demanded tuned relationship of m = t_0 / λ_{ave} is not holding anymore. This decrease is especially accentuated for the optimized solar cell (Figure 4.6d), as the lower absorption with λ_{ave} = 100 nm is insufficient for the generation of enough free charge carriers.

Based on the result of the present sensitivity analyses, we advise again that optimizations, in which the complete set of efficiency-sensitive material properties are improved, are essential to obtain high PCE. As the most crucial measure, we recommend for any cell design, an adequate tuning of the relationship between t_0 and λ_{ave}, as otherwise substantial efficiency losses, are the result. These losses are explainable because of the unique relationship which these variables must comply, which leads to a maximal-efficiency vertex line. After these variables, we identified s_f, and D_n as the most efficiency-sensitive variables. The remaining variables are different in the ranking of its importance for the non-optimized and the optimized PSC, because of the related non-linearities of its drift-diffusion model, which lead to different rankings in cells with different development states.

This variable V_{bi} is unique, as its value must be increased at least only to its threshold value of approximately 1.08 V (f_s = 80, Figure 4.8f), to enable the maximal cell efficiency, in an optimized solar cell, but not in a non-optimized cell. Therefore, the ranking of this variable is distinct in the non-optimized and optimized PSC. The normalized representation, as proposed in Figure 4.8, is useful to analyze the origin of the efficiency decreases in our sensitivity analyses, which shows up by the superposition and therefore correlation of the curves of its performance parameters. We found that a reduced V_{bi} decreases the PCE mainly as a function of a FF reduction, which results in a V_{MPP} decrease, as these variables are highly correlated (Figure 4.8c). However, increased SRVs and reduced diffusion coefficients decrease the PCE mainly as a function of a V_{0C} reduction, which also leads to a V_{MPP} reduction, where these variables also present a high correlation because of its nearly complete superposition in Figure 4.8a, b, d and e.

4.4 VARIABLE RANKING

Comparing the ranking of the most important to the least essential model variables, as obtained by the sensitivity analyses of the non-optimized and optimized solar cell model (Table 4.7), we observed that this classification is distinct, principally for the least important variables. We consider that sensitivity analyses of a non-optimized PSC give only a rough estimation of the most sensitive or most essential variables to be included sequentially in the tuning of the PSC's material properties of a highly efficient cell, as the ranking of a cell optimized in the multidimensional space is distinct. However, the sensitivity analyses of an

optimized cell might also not be representative, especially for cells with low efficiencies, where the non-optimized cell should be more representative.

As a solution to this problem, we think that the combinatorial approach based on the equation of the binomial coefficient, as introduce in section 0, page 95, is the most assertive method. This method starts with the variable that is most efficiency-sensitive in the non-optimized solar cell, and it ends with the least sensitive variable in the multidimensional optimization. Furthermore, it analyzes a large set of 91 possible variable combinations. Therefore, we consider that this method is most representative in the transition of a non-optimized to an optimized solar cell, as it is characteristic for both cases for the non-optimized and the optimized solar cell. Furthermore, based on a large set of combinations, it selects only the variable combinations, which result in the highest efficiency increases. Therefore, the combinatorial approach proposes an ideal transition from a non-optimized to an optimized PSC design, selecting sequentially the variables which lead in the highest PCE increases, by the least improvements in the material properties.

4.4.1 Results

In this ranking, we select from a resulting set of s possible combinations for a considered variable number k, the specific variable combination, which results in the highest PCE. The variable k shows how many variables are selected from our set of seven variables. For the selected variables, we adopt the values of the optimized solar cell, and for the non-chosen variables, we use the value of the non-optimized solar cell. E.g., for $k = 2$, we take out only two variables from a set of 7 variables, which result in $s = 21$ variable combinations. In this set, we obtained the highest efficiency for the combination of the material properties s_f and s_b. In taking out $k = 3$ variables at a time, we found the highest PCE of $s = 35$ possible variable combinations for the specific combination of s_f, s_b, and V_{bi}. As expected, we obtained a sequential inclusion of model variables in the group of optimized variables, which means that for an increment of k there appears one new additional variable in this selected set. Therefore, we suggest this obtained sequence of variable inclusion as variable importance or selection criterion in the tuning of the material properties of manufactured PSC cells. We present in Table 4.8 the rank of variables, as obtained by the combinatorial selection scheme, from the least to the most important variable.

Table 4.8 - Results of the combinatorial approach, selecting from the total of n = 7 sensitive variables a total of seven subsets, where k defines the number of variables included in each subset, and s establishes the number of analyzed variable combinations. Each selected subset is composed of the variables, which appear at the left side of its column. E.g., for k = 4, the selected variables which result in the highest PCE are s_f, s_b, $V_{bi,}$ and D_n. The correlation coefficient (R) shows the correlation of a J-V performance parameter with the PCE and shows here that the PCE is improved mostly as a function of higher V_{MPP} values.

k	***1***	***2***	***3***	***4***	***5***	***6***	***7***	
s	*7*	*21*	*35*	*35*	*21*	*7*	*1*	
Selected variable	s_f	s_b	V_{bi}	D_n	D_p	λ_{ave}	t_0	R
PCE	18.07	20.01	23.04	24.21	25.96	27.31	27.62	
ΔPCE	2.37	1.94	3.03	1.17	1.75	1.62	0.31	
V_{MPP}	0.823	0.911	1.038	1.090	1.167	1.168	1.194	0.992
J_{MPP}	21.97	21.96	22.19	22.22	22.25	23.38	23.13	0.813
V_{0C}	0.933	1.053	1.134	1.187	1.266	1.267	1.294	0.988
J_{sc}	22.74	22.74	22.74	22.74	22.74	23.90	23.63	0.686
FF	0.852	0.835	0.893	0.897	0.902	0.902	0.903	0.888

4.4.2 Discussions

The combinatorial approach is different in its constitution, because of the sequential inclusion of optimized model variables, where each new variable addition results in a new, most ideal set of variables, and ideal PCE. Therefore, this sequential variable inclusion results in several optimized cell designs, presenting different optimized efficiencies.

The reduction of s_f leads to an efficiency increase of ΔPCE = 2.37% (Table 4.8), raising the PCE from 15.7% to 18.8%, and the inclusion of s_b results in an additional PCE rise of 1.94%. However, the highest efficiency growth of ΔPCE = 3.03%, is obtained by the inclusion of the V_{bi}, being this the third most outstanding variable. However, the increase of V_{bi} leads only to this highest PCE increase if beforehand s_f and s_b are reduced, as the improvement of these variables results in the highest one- and two-dimensional efficiency increases.

A similar behavior also appears with D_p, which only results in a high ΔPCE of 1.75%, if beforehand D_n is improved, which leads by its own in a lower ΔPCE of 1.17, as also being evident from Figure 4.2, page 102. We conclude that first and prioritizing optimization efforts must focus on the improvement of the three most important variables, which are s_f, s_b, and V_{bi}, being in its conjunction the quintessential in the efficiency optimization of manufactured PSCs. While such an optimization leads to an optimized PCE of 23.04%, the

state-of-the-art efficiency of a manufactured PSC is already 25.2% (NREL, 2020). To increase this state-of-the-art PCE, the further model variables, which are D_n, D_p, $\lambda_{ave,}$ and t_o need also be improved. They lead in its conjunction in an additional PCE increase of ΔPCE = 4.58%, which raises the PCE beyond the state-of-the-art efficiency (Table 4.8). We conclude that it is crucial to improve the whole set of material properties to enable the increase in PSC's state-of-the-art efficiency. However, the tuning of the absorber layer from 450 nm to 160 nm hast the least impact with an increase of only 0.3 %, moving in an ideal point of maximal efficiency vertex line in this last optimization.

From the correlation coefficient (R) in Table 4.8, we found the PCE values correlate mostly with the raising of values of V_{MPP}, and V_{OC}, in this sequence. The J_{MPP} presents only a small correlation with the PCE, which is understandable because of the constant J_{sc} without light trapping in columns 1 to 5 in this table. Light trapping with tuned λ_{ave} and t_0 values results in a summed ΔPCE value of 1.62 + 0.31 = 1.93 % (Table 4.8). A tuned light trapping is only better than the improvement of D_n (ΔPCE = 1.17 %) and D_p (ΔPCE = 1.75 %), if these variables are improved beforehand the use of light trapping. The sum of the two ΔPCE values related to D_n and D_p, is with 2.92% circa 1% higher than the increase obtained by light trapping but is lower than the summed improvements of the SRV, which is 4.31%.

We conclude that (i) passivation techniques in general, and (ii) the growth of the built-in electric field, as related to V_{bi} (Figure 4.8, page 124), are primordial for obtaining high-efficiency PSCs. Such a ranking is reasonable as PSCs do present a dominant charge transport by the drift rather than the diffusion of charge carriers (JIANG; YANG; ZHOU; TO *et al.*, 2015). Because of the distinct variable importances, comparing Table 4.7, page 121 with Table 4.8, we also conclude that the sensitivity analyses, in general, are not representative in an adequate ranking of the most important variables, even if accomplished for a model optimized in the multidimensional space.

D_p is a further lowest-ranked variable in Table 4.8, apart from the variables λ_{ave} and t_0. This low rank is reasonable, as most photons are converted in electrons and holes close to the front p-type layer. Therefore, a reduction of D_p is of minor importance because of the short flight distance between the location of the hole generation and its selective p-conduction layer. Thus, a short diffusion length of holes is already satisfactory to transport the holes to its transport layer. The rise of D_n is more important than the rise of D_p, as it enables the transport of the generated electrons, as appearing in a superior density close to the front p-type layer, to

the back n-type layer, because of the increased diffusion lengths. The s_f is more critical than the s_b as close to the front p-type layer, most of the photons are converted into electrons and holes, and therefore, the probability of recombination is also higher if a major number of defects are related to the front charge conduction layer.

The least ranked variables in the combinatorial approach (Table 4.8) are the variables λ_{ave} and t_0, which. However, we like to remember that the relationship in-between these two variables must be maintained, by the tuning of t_0, or the tuning of λ_{ave} as obtainable by the configuration of the light trapping with plasmonic nanoparticles. Otherwise, substantial efficiency losses appear, as to see from in Figure 4.6a, page 122, for t_0; and in Figure 4.6d, for λ_{ave}.

As light trapping is presently not used in manufactured high-efficiency solar cells, the state-of-the-art efficiency of 25.2% is already very close to the maximal attainable PCE without light trapping, which presents the value is 25.96% (Table 4.8), based on a J_{sc} of 22.74 mA/cm^2. Considering a higher J_{sc} of 24.9 mA/cm^2 without light trapping in recently developed, high-efficiency solar cells (JEON; NA; JUNG; YANG *et al.*, 2018; JUNG; JEON; PARK; MOON *et al.*, 2019), this maximal attainable PCE should be, to some small extent, higher in simulations with such cells.

As the ranking starts with one- and two-dimensional analyses (k = 1 and k = 2), our results for these k's match with the results of the maximal efficiencies as obtained for the one- and two-dimensional sensitivity analyzes or optimizations in Table 4.1, page 103. Therefore, k = 3, leads to a similar way to the highest efficiency for three-dimensional sensitivity analysis, as would be obtained by a cubic matrix of PCE values, and k = 4…7 increases the dimensionality of these resulting matrices. Comparing the ranking of the most important to the least important model variable as obtained by (i) the sensitivity analyses of an optimized cell (Table 4.8) and (ii) the combinatorial approach (Table 4.7, page 121), we observed that these rankings lead to different results, because of the models non-linearity. However, it is obvious that the V_{bi}, once passing its threshold level, as found in the sensitivity analyses of an optimized cell, is placed in the upper ranking of at optimized cell (Table 4.7). Manly, because of the large set of 91 possible variable setups and simulations, we choose the results of Table 4.8, as a reference method for the best selection of model variables.

Based on a set of different sensitivity analyses, we recommend as the most crucial measure in the efficiency optimization the analyzed PSCs, an adequate tuning of the

relationship between t_0 and λ_{ave}, as otherwise are obtained substantial efficiency losses. These losses are explainable because of the variable's necessary relationship, which leads to a maximal-efficiency vertex line. However, for a fixed λ_{ave} = 100 nm, as related to a MAPI cell without light trapping, this is easy to accomplish, just by the tuning of the absorber layer to a fixed value of 450 nm (SUN; ASADPOUR; NIE; MOHITE *et al.*, 2015). Apart from the tuning of this relationship, we consider the combinatorial approach as the most decisive approach for the identification of the variable importance, because of the validation with 91 possible variable combinations. Based on this method, we identified s_f and s_b as the most efficiency-sensitive variables in the optimization of the pin-type PSCs.

The third most crucial variable measure is the increase in V_{bi}, which leads to the highest efficiency growth of ΔPCE = 3.04% (Table 4.8, page 130), which is astounding, as the V_{bi} has only to be increased to at least 1.08 V (f_s = 80, Figure 4.8, page 124), to enable this high growth. As to see from this figure for higher V_{bi} values there is no improvement of any performance parameter of the PSC. The fourth and last essential properties are the diffusion coefficients of electrons and holes (D_n and D_p). Light trapping is the least important measure, as its PCE growth depends on the improvement of the further material properties. It improves the maximal attainable efficiency from 26% to 27.6%, increasing the state-of-the-art efficiency significantly. We like to note that the state-of-the-art PCE is probably not obtained with a MAPI but with a FAPI alike cell because of the higher absorption of this material as evident from the resulting higher J_{sc} as discussed in section 2.10.1, page 70. Therefore, the maximal PCE, as obtained with an optimized cell that uses light trapping with this material, will lead to an even higher maximal PCE as presented here.

5. CONCLUSIONS AND FUTURE WORK

The first step is to establish that something is possible; then – probability will occur.

Elon Musk, CEO of Tesla Motors and SpaceX

5.1 CONCLUSIONS

We initiated this work as we found that the efficiency optimization of solar cells is a lagging process that needs too much time, up to several decades, using traditional one- and two-dimensional analysis and improvement methods. The main reason for this lengthy development time is that there was no theoretical concept available that demonstrates what is necessary to increase the efficiency of a solar cell as a function of a simultaneous improvement of the material properties. As a result, many research contributions are typically needed to increase a cell's efficiency, which leads to slow-growing efficiency curves (NREL, 2020). In this thesis, we show by the numerical optimization of an analytical solar cell model, how the efficiency of a pin-type PSC can be increased by the improvement of its material properties in a multidimensional function space. We present different optimized cell designs of this solar cell, which represent different development states, with and without light trapping and for different absorber layer thicknesses.

Proof of the hypothesis: While the one and the two-dimensional optimizations with the most efficiency-sensitive variables resulted in the maximal efficiency improvement from 15.7 % to only 18.1% and 20% (Table 4.1, page 102), the multidimensional optimization enables a much higher efficiency improvement to the maximum value of 27.8%.

We obtained 27.8% and 27.6% for 450 and 160 nm thick absorber layers in *m*-constrained optimizations (m = 4.5) (Table 4.4, Table 4.5, page 113 and Figure 4.3, page 106). In f_B constrained optimizations (m = 5.5) these efficiencies increase to 28.1% and 28.7% as to see from these tables, because of the lower reflection losses as related to a higher m – factor. For these highest efficiency optimizations, we adopted the same material property improvement factor of f_B = 160. As a scientific method for this hypothesis-testing, we used an

analytical solar cell model of a PSC, as derived from the drift-diffusion model, and optimized the variable values of this model, using an NLP optimization algorithm.

We emphasize that the multidimensional optimization presents a much higher efficiency increase than the highest efficiency rise using state-of-the-art one- and tow-dimensional efficiency optimizations for any variable combinations. Such state-of-the-art optimizations lead in our optimizations to small efficiency increases of only ΔPCE = 2.4% and 4.3%, even if the most efficiency-sensitive variables are improved with a high material property improvement factor of f_B = 160. If the whole set of possible one-dimensional efficiency optimizations is summed up, this weak scenario dos does not improve substantially, resulting in an efficiency increase of only ΔPCE 6.7%. However, with the presented multidimensional optimizations, we have demonstrated that the efficiency of a PSC can be increased significantly, with ΔPCE = 12.1%, raising its initial value of 15.7% to a PCE of 27.6%. This is a significant increase, which we expected to find when starting this research. We assign the large difference in-between the tow-dimensional and the multidimensional optimization chiefly to the nonlinear behavior of the drift-diffusion model of electrons and holes.

From our research with the optimized solar cell, we found specific knowledge as related to the importance of each of the material properties in the PCE optimization, being important in multidimensional efficiency optimizations: (i) The surface recombination velocities (SRV) are the most efficiency-sensitive variables. Furthermore, we found that it is most important to reduce the SRV related to the front - charge conduction layer (s_f), rather than the back - charge conduction layer (s_b). This comprehensible as most of the irradiance absorption happens close to the p-type front charge conduction layer, generating the highest density of charge carriers at this local. Close to the back n-type charge conduction layer appears the lowest density of generated charge carriers, and therefore, a reduced s_b results in lower PCE improvements because of the lower probability that a charge carrier encounters a recombination site. The best two-dimensional improvement, as obtained by the combined reduction of s_f and s_b, lead alone not in a high efficiency improvement. Consequently, an optimization must always be accomplished in the context of the improvement of a whole set of material properties. While the PCE increases over the whole range as a function of improved material properties, the built-in voltage must be increased only to a maximal value of 1.08 V, which we found as the ideal value for V_{bi}, as higher values do not increase any of

the performance parameters of an PSC as optimized in a multidimensional space. For the diffusion coefficients, we found that it is most important to improve the D_n, because, again, the highest charge carrier densities appear close to the front p-type charge conduction layer. Therefore, a slight increase of the diffusion length of holes is effective in the PSC's efficiency optimization, as most of the holes can be conducted to its electrode by its p-type layer needing only short diffusion paths. However, the diffusion length of electrons should be ideally much longer, because of the larger diffusion distances the generated holes are subjected to, to arrive at the back-electron conduction layer.

For the highest efficiency cell, we obtained a significant PCE increase as a function of a rise in the maximal power point voltage, which rises from 0.74 V to 1.21 V (Table 4.5). A characteristic which was obtained principally as a function of the improved material properties, which resulted to an increase of the open-circuit voltage from 0.87 V to 1.31 V. If compared to further solar cell technologies, this V_{0C} is higher than the open-circuit voltage of the highest-efficient GaAs cell, which state-of-the-art value is 1.13 V. The obtained fill factor of 0.904 is only to a small extent larger than the FF of this GaAs cell, showing a value of 0.867.

Spherical nanoparticles used for light trapping lead to an increase in the short circuit density, as based on a shorter average optical decay length, which is related to a higher absorption. Effective light trapping using spherical nanoparticles should not be used in cells with absorber layer thicknesses thinner than t_0 = 160 nm, as otherwise, the short circuit current density reduces significantly. Furthermore, light trapping in thin absorber layers increases the maximal power point voltage, and as a result, we observed a high PCE over a large range of absorber layer thicknesses from 160 to 400 nm. If compared to a cell with a 400 nm thick absorber layer, thin absorber layers of 160 nm result in only small efficiency losses of ΔPCE = 0.2%, as the lower short circuit current density is compensated by two V_{MPP} increases, (i) as a function of the absorber layer's thickness reduction and (ii) the use of light trapping. Therefore, we recommend as an ideal cell design a PSC with t_0 = 160 nm, by reason of its lower Pb content. The use of light trapping, which reduces λ_{ave}, should always be followed by the tuning of the absorber layer thickness, because λ_{ave} and t_0 stand in a close relationship which is defined by the *m*-factor. This factor relates the average optical decay length (λ_{ave}) to the absorber layer thickness (t_0), which stand in a close relationship. Our non-optimized cell presents an *m* factor of 4.5, and, in our optimized cell with the highest

efficiency of 27.6%, uses the same *m* factor. Using instead of m-constrained optimizations variable ranges solely restrained by f_B lead to higher efficiencies as corresponding to something lower reflection losses, as related to a higher absorption of the solar irradiance.

As discussed at the end of section 4.2.1, page 105, we conclude that the efficiency can increase as a function of increased diffusion coefficients, which can be configured by increased diffusion length of charge carriers or a reduced lifetime. The lifetime can be considered as the transport time, starting from the point at which an electron is elevated from the valence to the conduction band, in the absorber layer, up to a point, at which it recombines, because of its limited diffusion length. As the here considered diffusion lengths are in any case longer than 1 μm, a value which is much larger than the considered absorber layer thicknesses, recombination because of the limited diffusion length need not be analyzed separately in the considered cell designs.

In our optimizations, we maximize the PCE as a function of solely the diffusion coefficients, not considering the separate modeling of the lifetime of electrons and holes and its diffusion lengths. However, the equation of the diffusion length of electrons (A.33), page 169, can be thought of as an equation for the calculation of a distance, using (i) a velocity, as defined by D_n and (ii) a transport time as defined by τ_n. Therefore, the same diffusion length can be obtained for a lower lifetime, saying a transport time, if the diffusion coefficient, saying the transport velocity, is increased. However, an increase of this diffusion length can be obtained by both, (i) a lifetime increase, or (ii) an increase of the diffusion coefficient.

We conclude from our exemplary calculations in the last paragraph of section 4.2.1, page 105, that a rise in the diffusivity, and, therefore, an increase in the PCE, can be obtained from a longer diffusion length, or a lower lifetime. While most of the authors consider a PCE increase as a function of the diffusion length increase and a lifetime increase, only some authors measure higher efficiency values for shorter lifetimes, as e.g. in (SONG; CUI; WANG; WEI *et al.*, 2015). It is actually more challenging to measure such an effect, as in comparison to the diffusion length, the lifetime presents a 12.8-fold lower sensitivity to the diffusion coefficient, and therefore, the PCE, as discussed in section 4.2.1. Furthermore, we must advise that a correct measurement of the lifetime and the diffusion length, using solely direct rather than indirect measurements can avoid misconceptions, e.g. to access the PCE sensitivity related to the lifetime (section APPENDIX B.8, page 198).

As the improvement of one material property might result in the worsening of another property, we show in a stepwise inclusion of properties the ideal sequence of variable selection for the tuning of improved material properties. In the presented lineup, the material properties with the highest sensitivities in relation to the PCE are prevailing (section 4.4, page 128). In summary, we think that our contribution will accelerate the efficiency optimization of manufactured perovskite solar cells. The general character of the presented method allows its adoption for further solar cell types and even other devices.

Our established objectives are fulfilled, proving not only that our hypothesis is correct, but we also show a significant efficiency increase as a function of the multidimensional property improvements, achieving our research objectives, as determined in section 1.2, page 29. We believe that our study paves the way for the implementation of a better, multidimensional protocol for the optimization of PSCs in research and module manufacturing in the near future. Our findings facilitate the publication of related research papers, as each material property can be used as a separate objective function, rather than the PCE, in manufactured solar cells. The combined use of excellent manufacturing techniques should result in the next step to a PSC with the highest cell efficiencies.

5.2 FUTURE DIRECTIONS

Our future research will focus on the multidimensional optimization of a nip-type PSC. Furthermore, the OTM method for the simulation of the short circuit current density allows the validation with charge transport layers of different materials and thicknesses in a multidimensional optimization. Such thickness optimizations are important, as it appears that each charge transport layer material seems to present its individual ideal thickness in one-dimensional optimizations of these layers (section 2.10.8, on page 78).

We encourage further FDTD simulations for (i) cells that use shape-optimized nanoparticles for light trapping, because of the higher effectiveness of these NPs in the context of light trapping. Approximated results for this case we present in section APPENDIX B.1, page 188.

Furthermore, distinctive cell designs with extra high J_{sc} values (section APPENDIX B.2, page 191) are also interesting, especially if combined with light trapping, because of the expected higher optimized efficiencies. As a composed absorber layer of the material

$(FAPbI_3)_{0.95}(MAPBr_3)_{0.05}$ leads in a high measured J_{sc} of 24.9 mA/cm^2 (section 2.10.1), the use of plasmonic light trapping in such a layer should lead to even higher efficiencies as the here presented 27.8% for a MAPI PSC. We did not accomplish such a simulation in this thesis as we do not know accurately to which extent the J_{sc} can increase in such a cell as a function of light trapping. A rough estimation of the efficiency of such a cell without light trapping, but with optimized material properties, we present in Appendix Table B.4, page 191.

We must advise that we found no report of a state-of-the-art manufactured PSC with a high-efficiency as based on light-trapping techniques. Therefore, we consider that PSCs with thinner absorber layers and light trapping are more difficult to be manufactured, as in comparison, to cells with standard thicknesses in the range of approximately 400…450 nm, without light trapping. We recommend proving in the first step that high-efficiency cells with ~450 nm can be manufactured based on the multidimensional material property improvement and effective light-trapping techniques. Additionally, it is also essential to show that high-efficiency cells with low Pb content can be manufactured. Therefore, it is necessary to coat a cell with a 160 nm thick MAPI layer, which should result in a high short circuit current density of 11 mA/cm^2 without light trapping (CAI; PENG; CHENG; GU, 2015). Then light trapping should improve this J_{sc} to the value of 23.9 mA/cm^2 (CAI; PENG; CHENG; GU, 2015), and further material property improvement should increase the PCE to 27.6%. The resulting cell must present a high efficiency because of its J_{sc} and V_{MPP} increases in comparison to a cell with a 450 nm thick absorber layer without light trapping (Table 4.5, page 113– cell design 3).

In the research with the manufactured prototypes, we urge for the development of a research protocol, which enables the measurement of the material properties by independent methods. Such measurements can then be used to validate the simultaneous improvement of multiple material properties in a PSC.

REFERENCES

ADINOLFI, V.; PENG, W.; WALTERS, G.; BAKR, O. M. *et al.* The electrical and optical properties of organometal halide perovskites relevant to optoelectronic performance. **Advanced Materials**, p. 1-13, 2017.

AGARWAL, S.; NAIR, P. R., 2014, Colorado. **Performance optimization for Perovskite based solar cells**. 1515-1518. Acesso em: accessed 26 03 2019.

AGARWAL, S.; NAIR, P. R. Device engineering of perovskite solar cells to achieve near ideal efficiency. **Applied Physics Letters**, 107, n. 12, p. 1-5, 2015.

AHN, N.; SON, D.-Y.; JANG, I.-H.; KANG, S. M. *et al.* Highly reproducible perovskite solar cells with average efficiency of 18.3% and best efficiency of 19.7% fabricated via Lewis base adduct of lead (II) iodide. **Journal of the American Chemical Society**, 137, n. 27, p. 8696-8699, 2015.

AL IRSYAD, M. I.; HALOG, A.; NEPAL, R. Renewable energy projections for climate change mitigation: An analysis of uncertainty and errors. **Renewable energy**, 130, p. 536-546, 2019.

ALGORA, C.; DÍAZ, V. Influence of series resistance on guidelines for manufacture of concentrator p-on-n GaAs solar cells. **Progress in Photovoltaics: Research and Applications**, 8, n. 2, p. 211-225, 2000.

ALONSO-ÁLVAREZ, D.; WILSON, T.; PEARCE, P.; FÜHRER, M. *et al.* Solcore: a multi-scale, Python-based library for modelling solar cells and semiconductor materials. **Journal of Computational Electronics**, 17, n. 3, p. 1099-1123, 2018.

AMU, T. L. Performance optimization of tin halide perovskite solar cells via numerical simulation. (Master thesis). : African University of Science and Technology, Abuja, Nigeria. Master thesis 2014.

ANWAR, F.; MAHBUB, R.; SATTER, S. S.; ULLAH, S. M. Effect of Different HTM Layers and Electrical Parameters on ZnO Nanorod-Based Lead-Free Perovskite Solar Cell for High-Efficiency Performance. **International Journal of Photoenergy**, 2017, 2017.

ARCHITEKTUR, D. T.; DER TECHNIK, E. D. S.; LA ARQUITECTURA, T. TEXTILE-BASED ARCHITECTURE. 2017.

ARORA, J. **Introduction to optimum design**. Academic Press, 2004. 0080470254.

ATWATER, H. A.; POLMAN, A. Plasmonics for improved photovoltaic devices. **Nature materials**, 9, n. 3, p. 205-213, 2010.

AZRI, F.; MEFTAH, A.; SENGOUGA, N.; MEFTAH, A. Electron and hole transport layers optimization by numerical simulation of a perovskite solar cell. **Solar Energy**, 181, p. 372-378, 2019.

BALDWIN, S. Carbon footprint of electricity generation. **London: Parliamentary Office of Science and Technology**, 268, 2006.

BALL, J. M.; STRANKS, S. D.; HÖRANTNER, M. T.; HÜTTNER, S. *et al.* Optical properties and limiting photocurrent of thin-film perovskite solar cells. **Energy & Environmental Science**, 8, n. 2, p. 602-609, 2015.

BARANOV, M. I. An Anthology of the distinguished achievements in science and technique - Discovery and study of quantum-wave nature of microscopic world of matter - Part 3: Albert Einstein and the creation of the quantum theory of the photoelectric effect. **ELECTRICAL ENGINEERING & ELECTROMECHANICS - GREAT EVENTS AND FAMOUS NAMES**, p. 5, 2016.

BAZZO, T. d. P. M.; KÖLZER, J. F.; CARLSON, R.; WURTZ, F. *et al.* Multiphysics design optimization of a permanent magnet synchronous generator. **IEEE Transactions on Industrial Electronics**, 64, n. 12, p. 9815-9823, 2017.

BREYER, C.; GERLACH, A. Global overview on grid-parity. **Progress in photovoltaics: Research and Applications**, 21, n. 1, p. 121-136, 2013.

BRITTMAN, S.; ADHYAKSA, G. W. P.; GARNETT, E. C. The expanding world of hybrid perovskites: Materials properties and emerging applications. **MRS Communications**, 5, n. 01, p. 7-26, 2015.

BUSH, K. A.; PALMSTROM, A. F.; ZHENGSHAN, J. Y.; BOCCARD, M. *et al.* 23.6%-efficient monolithic perovskite/silicon tandem solar cells with improved stability. **Nature Energy**, 2, p. 17009, 2017.

BUTLER, J. H.; MONTZKA, S. A. The NOAA annual greenhouse gas index (AGGI). **NOAA Earth System Research Laboratory: Boulder, CO, USA**, 2016.

BYRD, R. H.; HRIBAR, M. E.; NOCEDAL, J. An interior point algorithm for large-scale nonlinear programming. **SIAM Journal on Optimization**, 9, n. 4, p. 877-900, 1999.

CAI, B.; PENG, Y.; CHENG, Y.-B.; GU, M. 4-fold photocurrent enhancement in ultrathin nanoplasmonic perovskite solar cells. **Optics Express**, 23, n. 24, p. A1700-A1706, 2015.

CAI, M.; WU, Y.; CHEN, H.; YANG, X. *et al.* Cost-Performance Analysis of Perovskite Solar Modules. **Advanced Science**, 4, n. 1, p. 1-6, 2017.

CHANG, R. P. H. Nanotechnology, a Driver for Developing Future Solar Cells, Supercapacitors and Sensors. : Northwestern University, Argonne Northwestern Solar Energy Research Center (ANSER); International Materials Institute for Solar Energy and Environment (IMI-SEE) without date.

CHEN, Y.; SUN, Y.; PENG, J.; ZHANG, W. *et al.* Tailoring Organic Cation of 2D Air-Stable Organometal Halide Perovskites for Highly Efficient Planar Solar Cells. **Advanced Energy Materials**, 2017.

CHIRVONY, V. S.; SEKERBAYEV, K. S.; PÉREZ-DEL-REY, D.; MARTÍNEZ-PASTOR, J. P. *et al.* Short Photoluminescence Lifetimes in Vacuum-Deposited CH3NH3PbI3 Perovskite Thin Films as a Result of Fast Diffusion of Photogenerated Charge Carriers. **The journal of physical chemistry letters**, 10, n. 17, p. 5167-5172, 2019.

CHOWDHURY, M.; ALAM, M. A physics-based analytical model for bulk heterojunction organic solar cells incorporating monomolecular recombination mechanism. **Current Applied Physics**, 14, n. 3, p. 340-344, 2014.

CHUNG, S.-Y.; KIM, Y.-M.; KIM, J.-G.; KIM, Y.-J. J. N. P. Multiphase transformation and Ostwald's rule of stages during crystallization of a metal phosphate. 5, n. 1, p. 68, 2009.

CMU, D. o. C.-. **Molecular Simulations - Force field based Simulations – Minimizations**. Carnegie Mellon University (CMU), 2000. Disponível em: http://www.chem.cmu.edu/courses/09-560/docs/msi/ffbsim/4_Minimize.html. Acesso em: 15. 02. 2017.

CROW, M. L. **Computational methods for electric power systems**. Crc Press, 2009. 0429148690.

DELUCCHI, M. A.; JACOBSON, M. Z. Providing all global energy with wind, water, and solar power, Part II: Reliability, system and transmission costs, and policies. **Energy policy**, 39, n. 3, p. 1170-1190, 2011.

DEVI, C.; MEHRA, R. Device simulation of lead-free $MASnI_3$ solar cell with $CuSbS_2$ (copper antimony sulfide). **Journal of Materials Science**, 54, n. 7, p. 5615-5624, 2019.

DEVI, N.; PARREY, K. A.; AZIZ, A.; DATTA, S. Numerical simulations of perovskite thin-film solar cells using a CdS hole blocking layer. **Journal of Vacuum Science & Technology B, Nanotechnology and Microelectronics: Materials, Processing, Measurement, and Phenomena**, 36, n. 4, p. 04G105, 2018.

DIMROTH, F.; GRAVE, M.; BEUTEL, P.; FIEDELER, U. *et al.* Wafer bonded four-junction GaInP/GaAs//GaInAsP/GaInAs concentrator solar cells with 44.7% efficiency. **Progress in Photovoltaics: Research and Applications**, 22, n. 3, p. 277-282, 2014.

DIXIT, H.; PUNETHA, D.; PANDEY, S. K. Improvement in performance of lead free inverted perovskite solar cell by optimization of solar parameters. **Optik**, 179, p. 969-976, 2019.

DOMANSKI, K.; CORREA-BAENA, J.-P.; MINE, N.; NAZEERUDDIN, M. K. *et al.* Not all that glitters is gold: Metal-migration-induced degradation in perovskite solar cells. **ACS Nano**, 10, n. 6, p. 6306-6314, 2016.

DONG, Q.; FANG, Y.; SHAO, Y.; MULLIGAN, P. *et al.* Electron-hole diffusion lengths> 175 μm in solution-grown CH3NH3PbI3 single crystals. **Science**, 347, n. 6225, p. 967-970, 2015.

DORN, R. T.; SOUKUP, R. Solution of the solar cell transport equations using Maple. *In*: **Maple V: Mathematics and its Applications**: Springer, 1994. p. 90-96.

EDENHOFER, O.; PICHS-MADRUGA, R.; SOKONA, Y.; SEYBOTH, K. *et al.* **Renewable energy sources and climate change mitigation: Special report of the intergovernmental panel on climate change**. Cambridge University Press, 2011. 1139505599.

EDRI, E.; KIRMAYER, S.; MUKHOPADHYAY, S.; GARTSMAN, K. *et al.* Elucidating the charge carrier separation and working mechanism of $CH_3NH_3PbI_{3-x}Cl_x$ perovskite solar cells. **Nature Communications**, 5, p. 1-8, 2014.

ELUMALAI, N. K.; UDDIN, A. Open circuit voltage of organic solar cells: an in-depth review. **Energy & Environmental Science**, 9, n. 2, p. 391-410, 2016.

EPERON, G. E.; STRANKS, S. D.; MENELAOU, C.; JOHNSTON, M. B. *et al.* Formamidinium lead trihalide: A broadly tunable perovskite for efficient planar heterojunction solar cells. **Energy & Environmental Science**, 7, n. 3, p. 982-988, 2014.

FEDELI, P.; GAZZA, F.; CALESTANI, D.; FERRO, P. *et al.* Influence of the Synthetic Procedures on the Structural and Optical Properties of Mixed-Halide (Br, I) Perovskite Films. **The Journal of Physical Chemistry C**, 119, n. 37, p. 21304-21313, 2015.

FOSTER, J. M.; SNAITH, H. J.; LEIJTENS, T.; RICHARDSON, G. A model for the operation of perovskite based hybrid solar cells: Formulation, analysis, and comparison to experiment. **SIAM Journal on Applied Mathematics**, 74, n. 6, p. 1935-1966, 2014.

FTHENAKIS, V. M.; KIM, H. C.; ALSEMA, E. Emissions from photovoltaic life cycles. **Environmental Science & Technology**, 42, n. 6, p. 2168-2174, 2008.

GANOSE, A. M.; SAVORY, C. N.; SCANLON, D. O. Beyond methylammonium lead iodide: prospects for the emergent field of ns 2 containing solar absorbers. **Chemical Communications**, 53, n. 1, p. 20-44, 2017.

GOLDSCHMIDT, V. M. Die Gesetze der Krystallochemie. **Naturwissenschaften**, 14, n. 21, p. 477-485, 1926.

GONG, J.; DARLING, S. B.; YOU, F. Perovskite photovoltaics: life-cycle assessment of energy and environmental impacts. **Energy & Environmental Science**, 8, n. 7, p. 1953-1968, 2015.

GOODRICH, A.; HACKE, P.; WANG, Q.; SOPORI, B. *et al.* A wafer-based monocrystalline silicon photovoltaics road map: Utilizing known technology improvement opportunities for

further reductions in manufacturing costs. **Solar Energy Materials and Solar Cells**, 114, p. 110-135, 2013.

GRAHAM, R. L. **Concrete mathematics: a foundation for computer science**. Pearson Education India, 1994. 8131708411.

GRANCINI, G.; ROLDÁN-CARMONA, C.; ZIMMERMANN, I.; MOSCONI, E. *et al.* One-Year stable perovskite solar cells by 2D/3D interface engineering. **Nature Communications**, 8, 2017.

GREEN, M., A. Do built-in fields improve solar cell performance? **Progress in Photovoltaics: Research and Applications**, 17, n. 1, p. 57-66, 2009.

GREEN, M. A. Third generation photovoltaics: Ultra-high conversion efficiency at low cost. **Progress in Photovoltaics: Research and Applications**, 9, n. 2, p. 123-135, 2001.

GREEN, M. A. Silicon photovoltaic modules: a brief history of the first 50 years. **Progress in Photovoltaics: Research and applications**, 13, n. 5, p. 447-455, 2005.

GREEN, M. A.; DUNLOP, E. D.; LEVI, D. H.; HOHL-EBINGER, J. *et al.* Solar cell efficiency tables (version 54). **Progress in Photovoltaics: Research and Applications**, 27, n. 7, p. 565-575, 2019.

GREEN, M. A.; HO-BAILLIE, A.; SNAITH, H. J. The emergence of perovskite solar cells. **Nature Photonics**, 8, n. 7, p. 506-514, 2014.

GREEN, M. A.; JIANG, Y.; SOUFIANI, A. M.; HO-BAILLIE, A. Optical properties of photovoltaic organic-inorganic lead halide perovskites. **The journal of physical chemistry letters**, 6, n. 23, p. 4774-4785, 2015.

HANSEN, J.; SATO, M.; RUEDY, R. Radiative forcing and climate response. **Journal of Geophysical Research: Atmospheres**, 102, n. D6, p. 6831-6864, 1997.

HIMA, A.; LAKHDAR, N. Enhancement of efficiency and stability of CH3NH3GeI3 solar cells with CuSbS2. **Optical Materials**, 99, p. 109607, 2020.

HIRTH, L.; UECKERDT, F.; EDENHOFER, O. Integration costs revisited–An economic framework for wind and solar variability. **Renewable Energy**, 74, p. 925-939, 2015.

HOSSAIN, M.; DAIF, O.; AMIN, N.; ALHARBI, F. *et al.*, 2015, **Numerical optimization of lead free perovskite solar cell**. John Wiley & Sons, Inc. 335-338.

HSU, E.; KUO, C.-M. A Recycling System for Sustainable Management of Waste Solar Photovoltaic Panels in Taiwan. *In*: **Energy Technology 2020: Recycling, Carbon Dioxide Management, and Other Technologies**: Springer, 2020. p. 241-248.

HSU, H.-L.; JUANG, T.-Y.; CHEN, C.-P.; HSIEH, C.-M. *et al.* Enhanced efficiency of organic and perovskite photovoltaics from shape-dependent broadband plasmonic effects of silver nanoplates. **Solar Energy Materials and Solar Cells**, 140, p. 224-231, 2015.

IFTIQUAR, S. M.; YI, J. Numerical simulation and light trapping in perovskite solar cell. **Journal of Photonics for Energy**, 6, n. 2, p. 1-10, 2016.

IRENA. **Future of solar photovoltaic - Deployment, investment, technology, grid integration and socio-economic aspects**. Abu Dhabi: International Renewable Energy Agency, 2019. (.

JACOBSON, M. Z. Getting to 100% clean, renewable energy: 2018 Rosenbluth Lecture with Mark Z. Jacobson, Youtube, 31. October 2018, https://www.youtube.com/watch?v=UASzeS9yrTI. 2018.

JACOBSON, M. Z.; DELUCCHI, M. A. Providing all global energy with wind, water, and solar power, Part I: Technologies, energy resources, quantities and areas of infrastructure, and materials. **Energy policy**, 39, n. 3, p. 1154-1169, 2011.

JACOBSON, M. Z.; DELUCCHI, M. A.; CAMERON, M. A.; FREW, B. A. Low-cost solution to the grid reliability problem with 100% penetration of intermittent wind, water, and solar for all purposes. **Proceedings of the National Academy of Sciences**, 112, n. 49, p. 15060-15065, 2015.

JACOBY, M. The future of low-cost solar cells. **Chem. Eng. News**, 94, n. 18, p. 30-35, 2016.

JAIN, S. M.; EDVINSSON, T.; DURRANT, J. R. Green fabrication of stable lead-free bismuth based perovskite solar cells using a non-toxic solvent. **Communications Chemistry**, 2, n. 1, p. 1-7, 2019.

JEON, N. J.; NA, H.; JUNG, E. H.; YANG, T.-Y. *et al.* A fluorene-terminated hole-transporting material for highly efficient and stable perovskite solar cells. **Nature Energy**, 3, n. 8, p. 682, 2018.

JIANG, C.-S.; YANG, M.; ZHOU, Y.; TO, B. *et al.* Carrier separation and transport in perovskite solar cells studied by nanometre-scale profiling of electrical potential. **Nature communications**, 6, p. 8397, 2015.

JIANG, Y.; GREEN, M. A.; SHENG, R.; HO-BAILLIE, A. Room temperature optical properties of organic–inorganic lead halide perovskites. **Solar Energy Materials and Solar Cells**, 137, p. 253-257, 2015.

JUNG, E. H.; JEON, N. J.; PARK, E. Y.; MOON, C. S. *et al.* Efficient, stable and scalable perovskite solar cells using poly (3-hexylthiophene). **Nature**, 567, n. 7749, p. 511, 2019.

KAKAVELAKIS, G.; PETRIDIS, K.; KYMAKIS, E. Recent advances in plasmonic metal and rare-earth-element upconversion nanoparticle doped perovskite solar cells. **Journal of Materials Chemistry A**, 5, n. 41, p. 21604-21624, 2017.

KALTENBRUNNER, M.; ADAM, G.; GŁOWACKI, E. D.; DRACK, M. *et al.* Flexible high power-per-weight perovskite solar cells with chromium oxide-metal contacts for improved stability in air. **Nature Materials**, 14, n. 10, p. 1032-1039, 2015.

KAMRAN, M.; FAZAL, M. R.; MUDASSAR, M.; AHMED, S. R. *et al.* Solar Photovoltaic Grid Parity: A Review of Issues, Challenges and Status of Different PV Markets. **International Journal of Renewable Energy Research (IJRER)**, 9, n. 1, p. 244-260, 2019.

KANOUN, A.-A.; KANOUN, M. B.; MERAD, A. E.; GOUMRI-SAID, S. Toward development of high-performance perovskite solar cells based on CH3NH3GeI3 using computational approach. **Solar Energy**, 182, p. 237-244, 2019.

KAPUSTIN, N. O.; GRUSHEVENKO, D. A. Long-term electric vehicles outlook and their potential impact on electric grid. **Energy Policy**, 137, p. 111103, 2020.

KHATIWADA, D.; VENKATESAN, S.; ADHIKARI, N.; DUBEY, A. *et al.* Efficient perovskite solar cells by temperature control in single and mixed halide precursor solutions and films. **The Journal of Physical Chemistry C**, 119, n. 46, p. 25747-25753, 2015.

KHENKIN, M. V.; ANOOP, K.; KATZ, E. A.; VISOLY-FISHER, I. Bias-dependent degradation of various solar cells: lessons for stability of perovskite photovoltaics. **Energy & Environmental Science**, 12, n. 2, p. 550-558, 2019.

KIM, H. D.; OHKITA, H. Potential Improvement in Fill Factor of Lead-Halide Perovskite Solar Cells. **Solar RRL**, 1, n. 6, p. 1-6, 2017.

KIM, Y. Y.; YANG, T. Y.; SUHONEN, R.; VÄLIMÄKI, M. *et al.* Gravure-Printed Flexible Perovskite Solar Cells: Toward Roll-to-Roll Manufacturing. **Advanced Science**, 6, n. 7, p. 1802094, 2019.

KITAI, A. Principles of solar cells, LEDs and diodes. **Departments of Engineering Physics and Materials Science and Engineering, McMaster University, Hamilton**, 2011.

KLASSEN, S. The photoelectric effect: Reconstructing the story for the physics classroom. : Springer 2011.

KOBOS, P. H.; ERICKSON, J. D.; DRENNEN, T. E. Technological learning and renewable energy costs: implications for US renewable energy policy. **Energy policy**, 34, n. 13, p. 1645-1658, 2006.

KOJIMA, A.; TESHIMA, K.; SHIRAI, Y.; MIYASAKA, T. Organometal halide perovskites as visible-light sensitizers for photovoltaic cells. **Journal of the American Chemical Society**, 131, n. 17, p. 6050-6051, 2009.

KOST, C.; SHAMMUGAM, S.; JÜLCH, V.; NGUYEN, H.-t. *et al.* Stromgestehungskosten erneuerbare energien. 2018.

KRATZENBERG, M.; RAMBO, C.; RÜTHER, R.; BEYER, H., 2015, Daegu, Korea. **Sensitivity analyses of a p-i-n perovskite solar cell with a fixed band gap**. 1-5.

KRATZENBERG, M. G. **A numerical optimization of a planar heterojunction organic solar cell of the type p-n under consideration of a fixed band gap**. p. 14. 2015a.

KRATZENBERG, M. G. **A numerical optimization of an organic-inorganic perovskite solar cell of the type p-i-n under consideration of a fixed band gap**. Universidade Federal de Santa Catarina (UFSC) - Laboratory of Electrical Materials (LAMATE) p. 78. 2015b.

KRATZENBERG, M. G.; MOYA, J. S.; ROMERO, R. **Ensaio para a medição indireta de dez paramêtros de uma célula solar monocrystalina de silício usando o modelo de dois resistores e um dióde**. Universidade Federal de Santa Catarina. 2014.

KRATZENBERG, M. G.; RAMBO, C.; RÜTHER, R. Towards the maximum efficiency design of a perovskite solar cell by material properties tuning: A multidimensional approach. **Solar Energy**, 194, p. 499-500, 2019.

KUMAR, A.; SOLEIMANIOUN, N.; SINGH, N.; SINGH, K. *et al.* Effects of Thermal Annealing Duration on the Film Morphology of Methylamine Lead Triiodide (MAPbI3) Perovskite Thin Films in Ambient Air. **Journal of nanoscience and nanotechnology**, 20, n. 6, p. 3795-3801, 2020.

LESAJA, G. Introducing interior-point methods for introductory operations research courses and/or linear programming courses. **Open Operational Research Journal**, 3, p. 1, 2009.

LI, J.; TRITSARIS, G. A.; ZHANG, X.; SHI, B. *et al.* Monolayer honeycomb borophene: A promising anode material with a record capacity for lithium-ion and sodium-ion batteries. **Journal of the Electrochemical Society**, 2020.

LI, Y.; YAN, W.; LI, Y.; WANG, S. *et al.* Direct observation of long electron-hole diffusion distance in CH 3 NH 3 PbI 3 perovskite thin film. **Scientific reports**, 5, p. 14485, 2015.

LIN, R. Y. Advanced Solar Power Technology-Multiple Junction Photovoltaics. *In*: **Innovations in Sustainable Energy and Cleaner Environment**: Springer, 2020. p. 505-527.

LIU, C.; LI, W.; FAN, J.; MAI, Y. A brief review on the lead element substitution in perovskite solar cells. **Journal of Energy Chemistry**, 27, n. 4, p. 1054-1066, 2018.

LIU, F.; ZHU, J.; WEI, J.; LI, Y. *et al.* Numerical simulation: toward the design of high-efficiency planar perovskite solar cells. **Applied Physics Letters**, 104, n. 25, p. 1-4, 2014.

LIU, Y. Plasmonic metal nanoparticle films for solar cells with ultra-thin absorber layers: Low temperature synthesis and application. : (Doctoral thesis), Freie Universität, Berlin, Germany 2017.

LOUWEN, A.; VAN SARK, W. Photovoltaic solar energy. *In*: **Technological Learning in the Transition to a Low-Carbon Energy System**: Elsevier, 2020. p. 65-86.

LUCAS, B. D.; KIM, J.-S.; CHIN, C.; GUO, L. J. Nanoimprint Lithography Based Approach for the Fabrication of Large-Area, Uniformly-Oriented Plasmonic Arrays. **Advanced Materials**, 20, n. 6, p. 1129-1134, 2008.

MARINOVA, N.; TRESS, W.; HUMPHRY-BAKER, R.; DAR, M. I. *et al.* Light harvesting and charge recombination in $CH_3NH_3PbI_3$ perovskite solar cells studied by hole transport layer thickness variation. **ACS nano**, 9, n. 4, p. 4200-4209, 2015.

MARTYNOV, Y. B.; NAZMITDINOV, R. G.; MOIÀ-POL, A.; GLADYSHEV, P. P. *et al.* On the efficiency limit of ZnO/$CH_3NH_3PbI_3$/CuI perovskite solar cells. **Physical Chemistry Chemical Physics**, 19, n. 30, p. 19916-19921, 2017.

MCDONALD, N. C.; PEARCE, J. M. Producer responsibility and recycling solar photovoltaic modules. **Energy Policy**, 38, n. 11, p. 7041-7047, 2010.

MCEVOY, A. J.; CASTANER, L.; MARKVART, T. **Solar cells: materials, manufacture and operation**. Academic Press, 2012. 0123869641.

MCMEEKIN, D. P.; MAHESH, S.; NOEL, N. K.; KLUG, M. T. *et al.* Solution-Processed All-Perovskite Multi-Junction Solar Cells. **Joule**, 3, n. 2, p. 387-401, 2019.

MONTGOMERY, D. C. **Design and analysis of experiments**. John wiley & sons, 2017. 1119113474.

MORITZ, K. Building Integrated Photovoltaic (BIPV) applications with ETFE-Films. *In*: Proceedings of the TensiNet Symposium 2019, Milan, Italy. p. 558-569.

NAGPAL, A.; GUPTA, R.; SRIVASTAVA, G.; JAIN, V. *et al.* Measurement of minority carrier lifetime in silicon solar cells using an ac light source. **Solar Cells**, 29, n. 1, p. 73-81, 1990.

NAZARI-HERIS, M.; MOHAMMADI-IVATLOO, B.; GHAREHPETIAN, G. A comprehensive review of heuristic optimization algorithms for optimal combined heat and power dispatch from economic and environmental perspectives. **Renewable and Sustainable Energy Reviews**, 2017.

NIE, W.; BLANCON, J.-C.; NEUKIRCH, A. J.; APPAVOO, K. *et al.* Light-activated photocurrent degradation and self-healing in perovskite solar cells. **Nature communications**, 7, p. 11574, 2016.

NIE, W.; TSAI, H.; ASADPOUR, R.; BLANCON, J.-C. *et al.* High-efficiency solution-processed perovskite solar cells with millimeter-scale grains. **Science**, 347, n. 6221, p. 522-525, 2015.

NOEL, N. K.; ABATE, A.; STRANKS, S. D.; PARROTT, E. S. *et al.* Enhanced photoluminescence and solar cell performance via lewis base passivation of organic–inorganic lead halide perovskites. **ACS nano**, 8, n. 10, p. 9815-9821, 2014.

NREL. **Best Research-Cell Efficiencies**. 2020.

O'REGAN, B.; GRÄTZEL, M. A low-cost, high-efficiency solar cell based on dye-sensitized colloidal TiO_2 films. **Nature** 353, n. 6346, p. 737-740, 1991.

OLALERU, S.; KIRUI, J.; WAMWANGI, D.; RORO, K. *et al.* Perovskite solar cells: The new epoch in photovoltaics. **Solar Energy**, 196, p. 295-309, 2020.

PALMSTROM, A. F.; EPERON, G. E.; LEIJTENS, T.; PRASANNA, R. *et al.* Enabling Flexible All-Perovskite Tandem Solar Cells. **Joule**, 2019.

PARK, J.-K.; KANG, J.-C.; KIM, S. Y.; SON, B. H. *et al.* Diffusion length in nanoporous photoelectrodes of dye-sensitized solar cells under operating conditions measured by photocurrent microscopy. **The Journal of Physical Chemistry Letters**, 3, n. 23, p. 3632-3638, 2012.

PARK, N.-G.; GRÄTZEL, M.; MIYASAKA, T.; ZHU, K. *et al.* Towards stable and commercially available perovskite solar cells. **Nature Energy**, 1, p. 1-8, 2016.

PAZOS-OUTÓN, L. M.; SZUMILO, M.; LAMBOLL, R.; RICHTER, J. M. *et al.* Photon recycling in lead iodide perovskite solar cells. **Science**, 351, n. 6280, p. 1430-1433, 2016.

PEREZ, R.; PEREZ, M. A fundamental look at energy reserves for the planet. **The IEA SHC Solar Update**, 50, n. 2, 2009.

PEREZ, R.; ZWEIBEL, K.; HOFF, T. E. Solar power generation in the US: Too expensive, or a bargain? **Energy Policy**, 39, n. 11, p. 7290-7297, 2011.

PERRAKIS, G.; KAKAVELAKIS, G.; KENANAKIS, G.; PETRIDIS, C. *et al.* Efficient and environmental-friendly perovskite solar cells via embedding plasmonic nanoparticles: an optical simulation study on realistic device architecture. 2019.

PHILLIPS, L. J.; RASHED, A. M.; TREHARNE, R. E.; KAY, J. *et al.* Maximizing the optical performance of planar CH3NH3PbI3 hybrid perovskite heterojunction stacks. **Solar Energy Materials and Solar Cells**, 147, p. 327-333, 2016.

PV-RESOURCES. **Photovoltaics - Historical Development**. Solar cells / Modules, http://www.pvresources.com/en/introduction/history.php acessed on 15.12. 2019, 2015.

QIU, W.; MERCKX, T.; JAYSANKAR, M.; DE LA HUERTA, C. M. *et al.* Pinhole-free perovskite films for efficient solar modules. **Energy & Environmental Science**, 9, n. 2, p. 484-489, 2016.

REN, X.; WANG, Z.; SHA, W. E.; CHOY, W. C. Exploring the way to approach the efficiency limit of perovskite solar cells by drift-diffusion model. **Acs Photonics**, 4, n. 4, p. 934-942, 2017.

ROLDAN-CARMONA, C.; GRATIA, P.; ZIMMERMANN, I.; GRANCINI, G. *et al.* High efficiency methylammonium lead triiodide perovskite solar cells: the relevance of non-stoichiometric precursors. **Energy & Environmental Science**, 8, n. 12, p. 3550-3556, 2015.

RONG, Y.; HOU, X.; HU, Y.; MEI, A. *et al.* Synergy of ammonium chloride and moisture on perovskite crystallization for efficient printable mesoscopic solar cells. **Nature Communications**, 8, p. 1-8, 2017.

RÜHLE, S. Tabulated values of the Shockley-Queisser limit for single junction solar cells. **Solar Energy**, 130, p. 139-147, 2016.

RÜTHER, R.; KLEISS, G.; REICHE, K. Spectral effects on amorphous silicon solar module fill factors. **Solar Energy Materials and Solar Cells**, 71, n. 3, p. 375-385, 2002.

SALEEM, I.; TILAKARATNE, B. P.; LI, Y.; BAO, J. *et al.* Cluster ion beam assisted fabrication of metallic nanostructures for plasmonic applications. **Nuclear Instruments and Methods in Physics Research Section B: Beam Interactions with Materials and Atoms**, 380, p. 20-25, 2016.

SALIBA, M.; MATSUI, T.; SEO, J.-Y.; DOMANSKI, K. *et al.* Cesium-containing triple cation perovskite solar cells: improved stability, reproducibility and high efficiency. **Energy & Environmental Science**, 9, n. 6, p. 1989-1997, 2016.

SHA, W. E.; REN, X.; CHEN, L.; CHOY, W. C. The efficiency limit of $CH_3NH_3PbI_3$ perovskite solar cells. **Applied Physics Letters**, 106, n. 22, p. 1-5, 2015.

SHI, X.; CHEN, J.; WU, Y.; CAI, M. *et al.* Efficient Formamidinium-Based Planar Perovskite Solar Cells Fabricated Through a CaI2–PbI2 Precursor. **ACS Sustainable Chemistry & Engineering**, 8, n. 10, p. 4267-4275, 2020.

SHOCKLEY, W.; QUEISSER, H. J. Detailed balance limit of efficiency of p-n junction solar cells. **Journal of Applied Physics**, 32, n. 3, p. 510-519, 1961.

SHUKLA, A. K.; SUDHAKAR, K.; BAREDAR, P. A comprehensive review on design of building integrated photovoltaic system. **Energy and Buildings**, 128, p. 99-110, 2016.

SINGH, T.; SINGH, J.; MIYASAKA, T. Role of Metal Oxide Electron-Transport Layer Modification on the Stability of High Performing Perovskite Solar Cells. **ChemSusChem**, 9, n. 18, p. 2559-2566, 2016.

SMITH, I. C.; HOKE, E. T.; SOLIS-IBARRA, D.; MCGEHEE, M. D. *et al.* A layered hybrid perovskite solar-cell absorber with enhanced moisture stability. **Angewandte Chemie**, 126, n. 42, p. 11414-11417, 2014.

SONG, D.; CUI, P.; WANG, T.; WEI, D. *et al.* Managing Carrier Lifetime and Doping Property of Lead Halide Perovskite by Postannealing Processes for Highly Efficient Perovskite Solar Cells. **The Journal of Physical Chemistry C**, 119, n. 40, p. 22812-22819, 2015.

STASIULIONIS, J. Life cycle assessment of perovskite solar cells and comparison to silicon solar cells. (Master thesis). : Chalmers University of Technology, Sweden. Master of Science**:** 50 p. 2015.

STRANKS, S. D.; EPERON, G. E.; GRANCINI, G.; MENELAOU, C. *et al.* Electron-hole diffusion lengths exceeding 1 micrometer in an organometal trihalide perovskite absorber. **Science**, 342, n. 6156, p. 341-344, 2013.

SUN, S.-S.; SARICIFTCI, N. S. **Organic photovoltaics: mechanisms, materials, and devices**. CRC press, 2017. 1315221179.

SUN, X. **Opto-Electro-Thermal Approach to Modeling Photovoltaic Performance and Reliability from Cell to Module**. 2018. -, Purdue University.

SUN, X.; ASADPOUR, R.; NIE, W.; MOHITE, A. D. *et al.* A physics-based analytical model for perovskite solar cells. **IEEE Journal of Photovoltaics**, 5, n. 5, p. 1389-1394, 2015.

TAMAS VEKONY, A. The Opportunities of Solar Panel Recycling - What Happens to PV Panels When Their Life Cycle Ends. : GreenMatch 2020.

TAN, H.; JAIN, A.; VOZNYY, O.; LAN, X. *et al.* Efficient and stable solution-processed planar perovskite solar cells via contact passivation. **Science**, 355, n. 6326, p. 722-726, 2017.

TANABE, K. A review of ultrahigh efficiency III-V semiconductor compound solar cells: multijunction tandem, lower dimensional, photonic up/down conversion and plasmonic nanometallic structures. **Energies**, 2, n. 3, p. 504-530, 2009.

TANG, C. W. Two-layer organic photovoltaic cell. **Applied physics letters**, 48, n. 2, p. 183-185, 1986.

TANG, Z.; TRESS, W.; INGANÄS, O. Light trapping in thin film organic solar cells. **Materials today**, 17, n. 8, p. 389-396, 2014.

TARETTO, K.; SOLDERA, M.; KOFFMAN-FRISCHKNECHT, A. Material Parameters and Perspectives for Efficiency Improvements in Perovskite Solar Cells Obtained by Analytical Modeling. **IEEE Journal of Photovoltaics**, 7, n. 1, p. 206-213, 2017.

THE FREEING ENERGY PROJECT, B. N. E. F., National Renewable Laboratories. Why does the cost of renewable Energy continue to get cheaper? 2019.

TONG, J.; SONG, Z.; KIM, D. H.; CHEN, X. *et al.* Carrier lifetimes of> 1 μs in Sn-Pb perovskites enable efficient all-perovskite tandem solar cells. 364, n. 6439, p. 475-479, 2019.

TRESS, W.; DOMANSKI, K.; CARLSEN, B.; AGARWALLA, A. *et al.* Performance of perovskite solar cells under simulated temperature-illumination real-world operating conditions. **Nature Energy**, 4, n. 7, p. 568-574, 2019.

TURREN-CRUZ, S.-H.; HAGFELDT, A.; SALIBA, M. Methylammonium-free, high-performance, and stable perovskite solar cells on a planar architecture. **Science**, 362, n. 6413, p. 449-453, 2018.

UBIC, R.; SUBODH, G. The prediction of lattice constants in orthorhombic perovskites. **Journal of Alloys and compounds**, 488, n. 1, p. 374-379, 2009.

VAN ZEGHBROECK, B. **Principles of semiconductor devices**. Colarado University - Universidade Federal de Paraná, 2002 2004.

VICENTE, A. T.; WOJCIK, P. J.; MENDES, M. J.; ÁGUAS, H. *et al.* A statistics modeling approach for the optimization of thin film photovoltaic devices. **Solar Energy**, 144, p. 232-243, 2017.

WANG, D.; WRIGHT, M.; ELUMALAI, N. K.; UDDIN, A. Stability of perovskite solar cells. **Solar Energy Materials and Solar Cells**, 147, p. 255-275, 2016.

WANG, F.; CHEN, Y.; HAN, G.; ZHANG, Q. *et al.* The interface and its role in carrier transfer/recombination dynamics for the planar perovskite solar cells prepared under fully open air conditions. **Current Applied Physics**, 16, n. 10, p. 1353-1363, 2016.

WANG, J.; FU, W.; JARIWALA, S.; SINHA, I. *et al.* Reducing Surface Recombination Velocities at the Electrical Contacts Will Improve Perovskite Photovoltaics. 4, n. 1, p. 222-227, 2018.

WANG, L.; ZHOU, H.; HU, J.; HUANG, B. *et al.* A Eu3+-Eu2+ ion redox shuttle imparts operational durability to Pb-I perovskite solar cells. **Science**, 363, n. 6424, p. 265-270, 2019.

WEI, D.; MA, F.; WANG, R.; DOU, S. *et al.* Ion-Migration Inhibition by the Cation–π Interaction in Perovskite Materials for Efficient and Stable Perovskite Solar Cells. **Advanced Materials**, 30, n. 31, p. 1707583, 2018.

WONG, W.-Y.; WANG, X.-Z.; HE, Z.; DJURIŠIĆ, A. B. *et al.* Metallated conjugated polymers as a new avenue towards high-efficiency polymer solar cells. **Nature Materials**, 6, n. 7, p. 521-527, 2007.

WRUCK, F. **Análise da variação da eficiência de conversão energética de células fotovoltaicas de perovskita**. 2018. (Graduate Engineering Coursework) - Department of Electrical and Electronic Engineering, Universidade Federal de Santa Catarina.

WU, B.; ZHOU, Y.; XING, G.; XU, Q. *et al.* Long Minority-Carrier Diffusion Length and Low Surface-Recombination Velocity in Inorganic Lead-Free CsSnI3 Perovskite Crystal for Solar Cells. 27, n. 7, p. 1604818, 2017.

WU, Y.; YANG, X.; CHEN, H.; ZHANG, K. *et al.* Highly compact TiO2 layer for efficient hole-blocking in perovskite solar cells. **Applied Physics Express**, 7, n. 5, p. 052301, 2014.

XIAO, R. **Photocurrent Imaging of Single-Crystal Methylammonium Lead Iodide Nanostructures**. 2019. -, University of California, Davis.

XU, X.; XIAO, J.; ZHANG, G.; WEI, L. *et al.* Interface-enhanced organic solar cells with extrapolated T80 lifetimes of over 20 years. **Science Bulletin**, 65, n. 3, p. 208-216, 2020.

YANG, M.; LI, Z.; REESE, M. O.; REID, O. G. *et al.* Perovskite ink with wide processing window for scalable high-efficiency solar cells. **Nature Energy**, 2, n. 5, p. 17038, 2017.

YANG, S.; WANG, Y.; LIU, P.; CHENG, Y.-B. *et al.* Functionalization of perovskite thin films with moisture-tolerant molecules. **Nature Energy**, 1, p. 15016, 2016.

YANG, W. S.; NOH, J. H.; JEON, N. J.; KIM, Y. C. *et al.* High-performance photovoltaic perovskite layers fabricated through intramolecular exchange. **Science**, 348, n. 6240, p. 1234-1237, 2015.

YANG, W. S.; PARK, B.-W.; JUNG, E. H.; JEON, N. J. *et al.* Iodide management in formamidinium-lead-halide–based perovskite layers for efficient solar cells. **Science**, 356, n. 6345, p. 1376-1379, 2017.

YANG, Y.; YAN, Y.; YANG, M.; CHOI, S. *et al.* Low surface recombination velocity in solution-grown $CH_3NH_3PbBr_3$ perovskite single crystal. **Nature Communications**, 6, p. 1-6, 2015.

YE, Y. **Interior point algorithms: theory and analysis**. John Wiley & Sons, 2011. 1118030958.

YIN, W.-J.; SHI, T.; YAN, Y. Unique properties of halide perovskites as possible origins of the superior solar cell performance. **Advanced Materials**, 26, n. 27, p. 4653-4658, 2014.

YOU, J.; MENG, L.; SONG, T.-B.; GUO, T.-F. *et al.* Improved air stability of perovskite solar cells via solution-processed metal oxide transport layers. **Nature Nanotechnology**, 11, n. 1, p. 75-81, 2016.

YU, X. **Improve the stability of organic-inorganic hybrid perovskite by vapor-solid reaction**. 2019. -, University of Alabama Libraries.

YUAN, Y.; REECE, T. J.; SHARMA, P.; PODDAR, S. *et al.* Efficiency enhancement in organic solar cells with ferroelectric polymers. 10, n. 4, p. 296, 2011.

ZHAN, L.; LI, S.; LAU, T.-K.; CUI, Y. *et al.* Over 17% efficiency ternary organic solar cells enabled by two non-fullerene acceptors working in alloy-like model. **Energy & Environmental Science**, 2020.

ZHANG, B.; ZHANG, M. J.; PANG, S. P.; HUANG, C. S. *et al.* Carrier transport in CH3NH3PbI3 films with different thickness for perovskite solar cells. **Advanced Materials Interfaces**, 3, n. 17, p. 1600327, 2016.

ZHANG, C.-C.; WANG, Z.-K.; LI, M.; LIU, Z.-Y. *et al.* Electric-field assisted perovskite crystallization for high-performance solar cells. **Journal of Materials Chemistry A**, 6, n. 3, p. 1161-1170, 2018.

ZHANG, C. C.; WANG, Z. K.; YUAN, S.; WANG, R. *et al.* Polarized Ferroelectric Polymers for High-Performance Perovskite Solar Cells. p. 1902222, 2019.

ZHAO, P.; LIU, Z.; LIN, Z.; CHEN, D. *et al.* Device simulation of inverted CH 3 NH 3 PbI 3− x Cl x perovskite solar cells based on PCBM electron transport layer and NiO hole transport layer. **Solar Energy**, 169, p. 11-18, 2018.

ZHOU, Y.; YANG, M.; WU, W.; VASILIEV, A. L. *et al.* Room-temperature crystallization of hybrid-perovskite thin films via solvent-solvent extraction for high-performance solar cells. **Journal of Materials Chemistry A**, 3, n. 15, p. 8178-8184, 2015.

APPENDIX A – ANALYTICAL SOLAR CELL MODEL

CONTENTS

Here we introduce the derived model in (SUN; ASADPOUR; NIE; MOHITE *et al.*, 2015) and (SUN, 2018), discussing the different implementations in a detailed form in sections APPENDIX A.1 and APPENDIX A.2, page 178, we present the complete analytical model, as composed by these equations and used for the present simulations. In section APPENDIX A.3, page 181, we show in an exemplary form of how this model was derived from the normalized drift-diffusion equations.

APPENDIX A.1 – DISCRETE REPRESENTATION

This section provides a detailed understanding of the charge generation and recombination processes within a perovskite solar cell. The authors (SUN; ASADPOUR; NIE; MOHITE *et al.*, 2015) elaborated an analytical model for four different types of PSCs considering a fixed band gap (SUN; ASADPOUR; NIE; MOHITE *et al.*, 2015). Using a one-dimensional optimization of the absorber layer's thickness, the authors obtained the highest measured and modeled efficiencies of 15.7 % for the here optimized pin-type device. As the analytical model in (SUN; ASADPOUR; NIE; MOHITE *et al.*, 2015) considers some general simplifications, as discussed in SI-2, the authors validated its accuracy by comparison of the model value of the efficiency, with its measured value, using a manufactured solar cell, which show a depreciable dissimilarity of 0.1 %. In the present multidimensional optimizations, only the higher efficiency pin-type, as presented in (SUN; ASADPOUR; NIE; MOHITE *et al.*, 2015), is used. The modeled J-V curves of this cell exhibit a nearly perfect superposition with the measured J-V curves, for both conditions, in the dark and under reference illumination (SUN; ASADPOUR; NIE; MOHITE *et al.*, 2015). This analytical model and the values of its model variables are configured here as initial conditions for the optimization of the PCE in a hypercube variable space of material properties and the absorber layer thickness. For simplicity of the modeling, only a fixed band gap, based on the configuration of fixed values of the valence- and conduction-bands of: (i) the electrodes, (ii) the charge conduction layers and (iii) the absorber layer is considered, which values can be read from Figure 3.1a, page 81. In our proposal, specific range restrictions of the absorber layer thickness and the material properties define ranges at which the values of these variables can vary in several individual optimizations. These range restrictions are individualized by different amplification factors f_B, which are set up individually for each new optimization.

The analytical model is based on a self-consistent stationary quantum simulation of the charge carrier generation, which was derived from the drift-diffusion equations of electrons and holes, and the Poisson equation. Generally, the analytical model is a simplified version of the more accurate numerical model of the charge carrier generation, which can also be derived from the drift-and the Poisson equations (AGARWAL; NAIR, 2015; FOSTER; SNAITH; LEIJTENS; RICHARDSON, 2014; LIU; ZHU; WEI; LI *et al.*, 2014; WANG; CHEN; HAN; ZHANG *et al.*, 2016). With both the analytical and the numerical model, the total generation of charge carriers is obtained by the integration of the locally generated charges over the whole absorber layer thickness. Whereas the numerical model simulates in a very detailed procedure the charge carrier generation as function of the solar irradiance wavelength and its penetration depth, the present analytical model stands out because of its good approximation and its relatively low computational cost, which allows its use in a large number of numerical optimizations, or in further arbitrary analyses, which necessitate a large number of model simulations.

APPENDIX A.1.1 - The J-V curve models

In a manufactured solar cell, two different J-V curves can be measured: (i) the curve when the cell is exposed to a reference light source $J_{light}(G, V)$; and (ii) the curve when it is in the complete dark $J_{dark}(V)$ (Figure 4.4, page 111). By the superposition of these two measured curves, the curve of the intern photo-generated current density $J_{photo}(G, V)$, in units of [A/cm^3], can be specified (NIE; TSAI; ASADPOUR; BLANCON *et al.*, 2015; SUN; ASADPOUR; NIE; MOHITE *et al.*, 2015). This $J_{photo}(G, V)$ considers only radiative recombination losses and can be calculated by equation (A.1).

$$J_{photo}(G, V) = J_{light}(G, V) - J_{dark}(V) \qquad \text{(A.1)}$$

In this equation, G [s^{-1}cm^{-2}] is the charge generation rate per solar cell area, and V is the cell's external terminal voltage. This superposition considers an equal short-circuit current density $J_{sc} = J_{photo}(G, V) = J_{light}(G, V)$, at $V = 0$, while for the remaining curve points, the intern photocurrent density J_{photo} is larger than the measurable current density J_{light} ($J_{photo}(G, V) > J_{light}(G, V)$). This leads to a higher open-circuit voltage ($V_{0c\text{-}photo}$) of the internal and non-measurable J-V curve in comparison to the cell's measurable open-circuit voltage ($Voc\text{-}_{light}$ =

V_{oc}). The open-circuit voltage of this internal J-V curve is reduced by reason of the non-radiative recombination effects, which are modeled by use of the measured J-V curve when the solar cell is kept in the dark (J_{dark}), a simplification which can be adopted, considering the superposition principle, as adopted in (SUN; ASADPOUR; NIE; MOHITE *et al.*, 2015), and (NIE; TSAI; ASADPOUR; BLANCON *et al.*, 2015). As the present model is a simplification of the PSC, it depreciates very small parts of the solar irradiance, which are: (i) the absorption of light within the transparent conductive layer, the charge conduction layers, the back reflector; (ii) the light emitted by the solar cell's top surface, where one part is due to front surface reflection; and the other part is light, which comes from the cell's back reflector and is not absorbed by the absorber and the charge conduction layers. Furthermore, the transmission losses of the cell's front glass cover are also depreciated by this model. These losses are very small and are present in a manufactured solar cell but do not appear in the mathematical model of the PSC considered here for the simplicity of modeling. Therefore, it has to be remembered that the measured short-circuit current density $J_{sc\text{-}med}$ ($G,\ V = 0$), is to some minute extent smaller than the theoretically maximal attainable short-circuit current density $J_{sc\text{-}mod}$ as expressed in the present model by equation (A.2).

$$J_{sc\text{-}med}(G,\ V = 0) \quad < \quad J_{sc\text{-}mod} \ = \ q\ G_{max} \tag{A.2}$$

Where q = -1.6021765 x 10^{-19} [C] is the electric charge and G_{max} [s^{-1} m^{-2}] is the maximal attainable charge carrier generation, for the considered specific cell's band gap. In the present cell, the value of $q\ G_{max}$ is 23 mA/cm² was also obtained by the measurement of the short circuit density and by the optical transfer matrix method (SUN; ASADPOUR; NIE; MOHITE *et al.*, 2015). Considering the superposition in equation (A.1) the total current density under light exposure of the cell (Figure 4.4, page 111 - J_{light}) can be modeled by equation (A.3) (SUN; ASADPOUR; NIE; MOHITE *et al.*, 2015), with the sum of (i) the measurable current density in the dark (equation (A.5)), which express the recombination current density and has a negative sign (Figure 4.4, page 111 - J_{dark}); and (ii) current density which is generated by the photons (J_{photo}) (equation (A.14), page 163), having a positive sign. This current density can only be modelled and is therefore not visible in Figure 4.4.

$$J_{light}(G,V) = J_{dark}(V) + J_{photo}(G,V) \tag{A.3}$$

Both the photocurrent density J_{photo} and the current density in the dark J_{dark} are comprised of its electron ($J_{n\text{-}photo}$, $J_{n\text{-}dark}$) and hole current densities ($J_{p\text{-}photo}$, $J_{p\text{-}dark}$), which results in the following expression for the total current density of charge carriers (J_{light}).

$$J_{light} = J_{n\text{-}photo} + J_{p\text{-}photo} + J_{n\text{-}dark} + J_{p\text{-}dark} = J_n + J_p \qquad \text{(A.4)}$$

Where each one of the current densities J_n and J_p does present one part, which interprets the injection of generated charge carriers ($J_{n\text{-}photo}$, $J_{p\text{-}photo}$) by the solar irradiance and a further part which stands for the recombination of the generated charge carriers ($J_{n\text{-}dark}$, $J_{p\text{-}dark}$).

APPENDIX A.1.2 - The model of the recombination current densities

In this model, a total of six types of different recombination effects are accounted for, which are categorized by the following effects: (i) electrons, which casually pass through the hole conduction and electron blocking layer; (ii) holes, which eventually pass through the electron conduction and hole blocking layer; (iii) charge carriers, which escape at the wrong contact; (vi) recombination because of interface defects at the transition between arbitrary perovskite crystals within the absorber layer; (v) recombination due to interface defects at the transition between the absorber layer and the transport layers of charge carriers; and finally (vi) recombination within the bulk of the p- and n-charge transport layers, which may appear e.g. due to pinholes in these layers, and which thus decrease the shunt resistance of the PSC (WU; YANG; CHEN; ZHANG *et al.*, 2014). The exponential shape of the J-V curve density in the dark J_{dark} [mA/cm^2] can be measured if a variable external voltage V is applied to the cell's terminals in the absence of light (Figure 4.4, page 111). As derived in[29] this current density can be modeled as follows.

$$J_{dark} = \left(\alpha_f \, J_{f0} + \alpha_b \, J_{b0}\right) \left(e^{V/V_t} - 1\right) \qquad \text{(A.5)}$$

Where J_{f0} [mA/cm^2] and J_{b0} [mA/cm^2] are the current densities of the recombination effects[ii] related to the front and back charge conduction layers, which are calculated by equations (A.6) and (A.7). The dimensionless scaling coefficients of these recombination current densities, α_f and α_b, are calculated using equations (A.8) and (A.9), page 161. The variable V

in equation (A.5) is the solar cell's variable terminal voltage and V_t [V] is the thermal voltage, which is calculated by $V_t = k_B T/q$, where k_B = 1.38064852 × 10^{-23} [J/K] is the Boltzmann constant and q = 1.60217662 × 10^{-19} [As] is the electric charge, which determines the energy of an electron or a hole; and T [K] is the operating temperature of the solar cell at the moment when the two J-V curves are measured. The recombination current density of electrons (J_{f0}) at the front hole conduction and electron-blocking layer (HC-EBL) appears by reason of the parasitic conduction of those electrons, which have a higher energy than the potential of the blocking barrier of the HC-EBL #(Figure 3.1a, page 81). Conversely, the recombination current density of holes (J_{b0}) at the back electron conduction and hole blocking layer (EC-HBL) appears because of parasitic conduction of those holes, which have a lower energy than the blocking potential of the EC-HBL (Figure 3.1a, page 81). The second reason for the recombination of electrons occurs by occasional trapping of electrons because of positive trapping states at the perovskite crystal terminations. This effect appears especially in non-passivated absorber the layers and it has to be noted that the electron recombination current density (J_f) is an order of magnitude higher as in comparison to the hole recombination current density (J_b) (#Table 2, line 1), which possibly may be present by reason of these positive trap states[iii]. The recombination current densities are calculated as follows:

$$\left|J_f\right| = J_{f0} = q\, s_f\, \Delta n = q\, s_f\, (n - n_0) \tag{A.6}$$

$$\left|J_b\right| = J_{b0} = q\, s_b\, \Delta p = q\, s_b\, (p - p_0) \tag{A.7}$$

By assumption of the superposition principle (NIE; TSAI; ASADPOUR; BLANCON *et al.*, 2015; SUN; ASADPOUR; NIE; MOHITE *et al.*, 2015), it is considered that the two recombination current densities in the dark (J_{f0}, J_{b0}), are equal to the recombination current densities under exposure to light (J_f, J_b), meaning that $|J_f| = J_{f0}$ and $|J_b| = J_{b0}$. This principle considers also that the cell's recombination losses under its exposure to light are expressed by the J-V curve behavior in the dark (equation (A.5)). In equation (A.6) the variable Δn [cm^{-3}] presents the number of excess electrons per unit volume that are available for the recombination process within the p-type layer. This surplus of electrons occurs if the actual

number of electrons (n) in this layer is higher than the number of electrons under the thermal equilibrium condition (n_0)[iv], where $\Delta n = n - n_0$. Conversely Δp [cm^{-3}] in equation (A.7) is the number of excess holes per unit volume that are available to recombine within the n-type semiconductor, where this surplus occurs if the actual number of holes within this p-type layer is higher than the number of holes in thermal equilibrium p_0, where $\Delta p = p - p_0$. The effective SRV s_f [cm/s] in equation (A.6) represents the effective velocity or rate at which the minority electrons within the intrinsic layer recombine at the surface transition to the hole conduction layer. In contrast, s_b [cm/s] is the effective velocity or rate at which the minority holes from the absorber layer recombine at the interface between the electron conduction layer and the absorber layer. As the units of s_f and s_b are [cm/s], they can also be thought of as the effective speeds at which electrons and holes move toward dangling bond positive and negative trap states at the perovskite crystal surface[v]. The dimensionless coefficients α_f and α_b in equation (A.5) are used in order to reduce the large analytical expressions obtained from the derivation process of the analytical PSC model of the photocurrent (see equations (A.61) and (A.62), page 179) and the dark current (equation (A.64), page 180). They can be considered as scaling coefficients of the front and back components of the recombination current densities, which are calculated as follows.

$$\alpha_f = \frac{1}{\frac{e^{V'}-1}{V'} + \beta_f} \tag{A.8}$$

$$\alpha_b = \frac{1}{\frac{e^{V'}-1}{V'} + \beta_b} \tag{A.9}$$

Where the dimensionless coefficients β_f and β_b [-], used in (A.8) and (A.9), are calculated by equations (A.12) and (A.13), page 162. The unitless variable V' [-] translates the resultant electric field in a dimensionless form which is calculated as follows.

$$V' = (V - V_{bi}) / V_t \tag{A.10}$$

Where $V_t = k_B T/q$ [V] is the cell's thermal voltage, V [V] is its terminal voltage, and T [K] is its assumed operation temperature. The terminal voltage V is an imposed and measurable voltage, which varies in the range $0 \ldots V_{0C}$, where V_{0C} [V] is the cell's open-circuit voltage. In the dark, the terminal voltage must be imposed on the solar cell's electrodes by an external variable voltage supply. The built-in voltage (V_{bi}) in equation (A.10) is calculated by equation (A.11) and can be manipulated by the material selection of the charge conduction layers. Alternatively, V_{bi} can also be modified via additional doping of the selected charge conduction layers. Both manipulations result in the adjustment of the band gap energy of the transport layers[vi]. The built-in voltage of the pin-type cell is calculated as follows.

$$V_{bi} = V_t \log\left(\frac{N_{A,eff}\ N_{D,eff}}{n_i^2}\right) \tag{A.11}$$

Where $N_{D,eff}$ [1/cm³] is the effective doping concentration of the donor molecules, which are able to donate additional electrons that are fixed into the crystal lattice of the n-type charge conduction layer, while $N_{A,eff}$ [1/cm³] is the effective doping concentration of acceptor molecules, which are able to accept electrons that are fixed into the crystal lattice of the p-type charge conduction layer. The intrinsic carrier density n_i [1/cm³] in equation (A.11) is the inherent carrier density to the undoped p- and n-type layers, and it is considered as being very small. In silicon solar cells the intrinsic carrier density is equal in both charge conduction layers. The dimensionless coefficients β_f and β_b in equations (A.8) and (A.9) determine mainly the PSC's Fill Factor (SUN; ASADPOUR; NIE; MOHITE *et al.*, 2015) and are calculated with the following two equations for the front and the back charge transport layers respectively.

$$\beta_f = D_n\ /\ (t_0\, s_f) \tag{A.12}$$

$$\beta_b = D_p\ /\ (t_0\, s_b) \tag{A.13}$$

In equations (A.12) and (A.13), the variable t_0 [nm] is the thickness of the intrinsic absorber layer and D_p and D_n are the diffusion coefficients of holes and electrons, both

measured in units of [cm^2/s]. From the discussions resulting in equations (A.5) to (A.13), page 159, it can be seen that the recombination current density in the dark (J_{dark}) of this solar cell is a function of the whole set of PSC model variables, excluding the average optical decay length. These variables are the following material properties and design parameter: the effective SRV of holes s_b [m/s], mainly occurring at the surface of the back electron conduction layer; the effective SRV of electrons s_f [m/s], principally present at the surface of the front hole conduction layer; the number of excess electrons available for the recombination process Δn [cm^{-3}]; the number of excess holes that can participate at recombination process Δp [cm^{-3}]; the diffusion coefficient of electrons D_n and diffusion coefficient of holes D_p; which specify the diffusion of these charge carriers in random directions [cm^2/s]; the solar cell's built-in voltage V_{bi} [V]; the absorber layer thickness t_0 [nm]; the cells temperature (T) [K]; and the terminal voltage V [V].

APPENDIX A.1.3 - The model of the photocurrent density

Under light exposure of the solar cell, the photogeneration current density $J_{photo}(G,V)$ can be expressed by the following equation.

$$J_{photo}(G, V) = q\, G_{max}\,(A - B\, e^{-m}) \tag{A.14}$$

Where A and B are dimensionless parameters, which are used to replace some larger terms, as given by equations (A.15) and (A.16), and were obtained by the derivation of the analytical pin-type PSC model (SUN; ASADPOUR; NIE; MOHITE *et al.*, 2015).

$$A = \alpha_f \left(\frac{1 - e^{V'-m}}{V'-m} - \beta_f \right) \tag{A.15}$$

$$B = \alpha_b \left(\frac{1 - e^{V'+m}}{V'+m} - \beta_b \right) \tag{A.16}$$

In equations (A.15) and (A.16) the following dimensionless coefficients were calculated: (i) α_f and α_b by use of equations (A.8) and (A.9), page 161; (ii) V' by use of equation (A.10),

page 161; and (iii) β_f and β_b by use of equation (A.12) and (A.13), page 162 and 197. The dimensionless ratio (m) relates to the average optical decay length λ_{ave} and the absorber thickness t_0, both measured in [nm] as shown by the following equation

$$m = t_0 / \lambda_{ave} \ . \qquad \text{(A.17)}$$

The generation of charge carriers $G(x)$ [$s^{-1}cm^{-2}$], as appearing in equations (A.1) to (A.3), pages 157 to 158), and (equation (A.14), page 163), is calculated by equation (A.18), page 164, and is a function of the photon penetration depth x in the absorber layer, modeling the exponential charge generation curves in Figure 3.1b, page 81, for $x = 0 \ldots t_0$. It has to be remembered that the true charge generation curve in a solar cell has an oscillating decay, as specified by the superposition of the solar irradiance waves in top-down and bottom-up directions, where the photon flux in the bottom-up, or the backward direction, is the reflected photon flux at the back reflector and the layer interfaces. This effect occurs by reason of the superposition of light waves, which are not in phase, and it can be modeled using the optical transfer matrix method as cited in (SUN; ASADPOUR; NIE; MOHITE *et al.*, 2015). However, in a simplification, this decay curve can also be modeled by the adoption of an exponential decay as detailed by the Beer-Lambert law, where each wavelength has a specific optical decay length and decay curve. In a second simplification, a unique exponential decay curve is given based on the specification of an average optical decay length (equation (A.18)), which is modeled using the average of the optical decay lengths λ_{ave}.

$$G(x) = G_{eff} \ e^{-x / \lambda_{ave}} \qquad \text{(A.18)}$$

In this simplification the average of a complete set of wavelength-dependent optical decay lengths ($\lambda_y = \lambda_{min} \ldots \lambda_{max}$), also sometimes referred to as the optical absorption lengths, leads to the present model to an approximation which is specified as average optical decay length (λ_{ave}). G_{eff} [$s^{-1}cm^{-3}$] in (A.18) is the effective generation of charge carriers, which is the highest charge generation at the top of the absorber layer at $x = 0$. In contrast, the lowest charge generation is present at the bottom of the cell at $x = t_0$ (Figure 3.1b, page 81). λ_{ave} is the penetration depth, as defined by the exponential decay in the Beer-Lambert law, at which

the charge carrier generation decays to the value of 36.8 % of G_{eff} (G_{eff} /e ≈ 0.368 G_{eff}). This behavior is consistent with the number of available photons, which decays exponentially as a function of the solar irradiance penetration depth, reaching at λ_{ave} a value of 0.368 G_{eff} in the exponential curves in Figure 3.1b, page 81.

Both variables λ_{ave} and G_{eff}, are specific constants related to the absorber layer material, where each of these constants is an average value. However, this configuration is a simplification, because, in more detailed modeling, both constants are a function of the wavelength of the solar irradiance. While the average optical decay length λ_{ave} can be improved by light trapping effects or the selection of the absorber layer material, G_{eff} can be improved by band gap tunings of the considered solar cell. In order to understand equation (A.18) better, the charge generation characteristic of this equation is visualized for a set of different λ_{ave} in Figure 3.1b, page 81. The range of the charge generation $G(x)$, is normalized in this figure, and the value of G_{eff} corresponds, therefore, to 100%. At zero penetration depth (x = 0), the penetration-dependent charge generation $G(x)$ is equal to the effective charge generation ($G(x) = G_{eff}$), and $G(x)$ decays exponentially as a function of the penetration depth.

The sum of the photons which are converted to free charges within the absorber layer (G_{max}) is given by the integration of the generated charges $G(x)$ over the absorber layer thickness at the depths $x = 0 \ldots t_0$. The correct dimension of the absorber layer thickness t_0 determines the maximum absorption of photons G_{max} [$s^{-1}cm^{-2}$] by equation (A.19). If the absorber layer is too thin, a significant number of photons might not be absorbed and converted by the absorber layer, as can be directly visualized by Figure 3.1b, page 81. In this equation, G_{max} is obtained by the integration of $G(x)$ over the whole absorber layer thickness t_0 [nm] as follows.

$$G_{\max} = \int_{x=0}^{t_0} G(x)\, dx = \int_{x=0}^{t_0} G_{eff}\; e^{-x/\lambda_{ave}}\; dx \qquad \text{(A.19)}$$

In an approximation, which considers ($t_0 = \infty$), the integration of equation (A.19) results in the following equation.

$$G_{max} = G_{eff}\;\; \lambda_{ave} \qquad \text{(A.20)}$$

Such a simplification leads to a small uncertainty as it adds mathematically a minute part of the solar irradiance, the part from t_0 to infinity, in the Beer-Lambert curve (not visible in Figure 3.1b, page 81), which is not supposed to be present in a manufactured PSC. Considering the cell configuration as used by (SUN; ASADPOUR; NIE; MOHITE *et al.*, 2015), with λ_{ave} = 100 nm, the irradiance part related to ($x = t_0 \ldots \infty$) is only 1 %, as seen from its value of (0.01 G_{eff}) for t_0 = 450 nm in Figure 3.1b, page 81. However, the highest part this 1 % is reflected by the back-reflector contact, and therefore, a large part of this back-reflected irradiance indeed generates free charges. Thus, at the end, some minute fractions, which are considered by the model and are not present in a manufactured PSC, are: (i) the small portion of solar irradiance, which is absorbed by the back reflector; and (ii) the part of the back-reflected irradiance, which is not converted into free charges and is consequently emitted by the solar cell's front surface. Due to these model simplifications, (SUN; ASADPOUR; NIE; MOHITE *et al.*, 2015) obtained a small dissimilarity with an absolute error of 0.1 % between the modeled and measured PCE values.

From the discussions resulting in equations (A.14) to (A.20), page 163, the modeling of the internal and not measurable photocurrent density is obtained as a function of the model variables which were already specified for calculating the solar cell current density in the dark. Additionally, the following two variables are included in the PSC model to simulate the photocurrent density: (i) the average optical decay length λ_{ave} [nm], which defines the effective optical thickness of the absorber layer, and (ii) the effective generation of charge carriers G_{eff}, which is proportional to the number of generated charge carriers considering the cells band gap.

APPENDIX A.1.4 - Differential equations of the model

The present model as derived in (SUN; ASADPOUR; NIE; MOHITE *et al.*, 2015) is based on the solutions of a total of five second-order differential equations. The assumed simplifications in this model result in limited uncertainties as validated by numerical simulations and measurements with a manufactured solar cell (SUN; ASADPOUR; NIE; MOHITE *et al.*, 2015). The first differential equation is the second-order Poisson equation, which defines the relationship between the space charge and the electric field as follows:

$$\frac{\partial^2 \phi(x)}{\partial x^2} = -\frac{\rho}{\varepsilon} = -\frac{\rho}{\varepsilon_r \, \varepsilon_0} = 0 \qquad ; \quad \rho = 0 \tag{A.21}$$

Where $\phi(x)$ is the electrostatic potential at a specific penetration depth (x) of the solar irradiance in the absorber layer; ρ [m^{-3}] is the density of charge carriers and ε [F/m] is the absolute permittivity of the intrinsic layer, which is the product of the relative permittivity ε_r and the vacuum permittivity ε_0. As the intrinsic i-type absorber layer is undoped, its density of charges ρ is equal to zero (ρ = 0). Considering this detail, the integration of the Poisson equation results in the following general solution:

$$\phi(x) = C_1 \, x + C_2 \tag{A.22}$$

Where C_1 and C_2 are arbitrary integration constants. The exact solution of this equation is obtained by consideration of two boundary conditions. The first boundary condition is given for zero penetration of the solar irradiance in the absorber layer (x = 0), where the electrostatic potential is defined as follows:

$$\phi\,(x = 0) \;=\; \phi\,(0) = 0 \tag{A.23}$$

The second boundary condition is specified for the maximal penetration depth of the solar irradiance in the absorber layer ($x = t_0$), where the electrostatic potential is given as follows:

$$\phi\,(x = t_0) \;=\; \phi\,(t_0) \;= (V_{bi} - V) \tag{A.24}$$

Substituting these two Dirichlet-type boundary conditions separately in the general solution of the Poisson equation (A.22), page 167, and solving the obtained system of two equations, results in the following specific solution for the electrostatic potential $\phi\,(x)$ [V]:

$$\phi\,(x) = -\frac{(V - V_{bi})}{t_0}\, x = -E\, x \tag{A.25}$$

Where the built-in voltage (V_{bi}), is specified by equation (A.11), page 162. Solving equation (A.25) for E results in the equation of the built-in electric field E [V/m] as follows:

$$E = (V - V_{bi}) / t_0 \tag{A.26}$$

This electric field equation is used to calculate the charge carrier generation rate in a PSC by its substitution in the Schrödinger drift-diffusion model ((A.29), page 168, and (A.30)), which defines the charge transport of electrons and holes considering a self-consistent stationary quantum simulation. The self-consistent stationary quantum simulation defines that there is no variation in the density of electrons and holes over time ($\partial n/\partial t = 0$, $\partial p/\partial t = 0$) and with this consideration, the continuity equations of a type pin perovskite solar cell under light exposure are defined by equations (A.27) and (A.28).

$$\frac{\partial n}{\partial t} = 0 = \frac{1}{q}\frac{\partial J_n}{\partial x} + G(x) - R(x) \tag{A.27}$$

$$\frac{\partial p}{\partial t} = 0 = -\frac{1}{q}\frac{\partial J_p}{\partial x} + G(x) - R(x) \tag{A.28}$$

Where $G(x)$, and $R(x)$ are the penetration depth specific photogeneration, and the recombination rates of charge carriers in the bulk of the absorber layer. J_n and J_p are the generated current densities of electrons and holes, which are specified by the differential equations of the current densities in (A.29) and (A.30).

$$J_n = q\ \mu_n\ n\ E + q\ D_n\ \frac{\partial n}{\partial x} \tag{A.29}$$

$$J_p = q\ \mu_p\ p\ E - q\ D_p\ \frac{\partial p}{\partial x} \tag{A.30}$$

In these equations, the first terms ($q\ \mu_n\ E$ and $q\ \mu_p\ E$) describe the drift component of

electrons and holes, while the following terms translate the diffusion component. Substituting J_n in equation (A.27), page 168, with the expression in (A.29); and substituting J_p in (A.28) with the expression in (A.30) results in the Schrödinger drift-diffusion equations of electrons and holes as specified in (A.31) and (A.32).

$$D_n \frac{\partial^2 n(x)}{\partial x^2} + \mu_n \, E(x) \frac{\partial n(x)}{\partial x} + G(x) - R(x) = 0 \qquad \text{(A.31)}$$

$$D_p \frac{\partial^2 p(x)}{\partial x^2} - \mu_p \, E(x) \frac{\partial p(x)}{\partial x} + G(x) - R(x) = 0 \qquad \text{(A.32)}$$

These Schrödinger equations are based on the equilibrium of two opposing forces, which determine the charge carrier transport behavior in a semiconductor crystal: the drift force and the diffusion force[vii]. While the diffusion current density of charge carriers is produced by concentration differences of charge carrier within the p-type and the n-type semiconductor, the drift current density is produced by the net electric field[viii] appearing across the pin-type junction of the solar cell. In equations (A.29) to (A.32), the diffusion coefficients of electrons and holes D_n and D_p [cm²/s] are material-specific constants, which determine the random diffusion or spread of charge carriers in arbitrary directions within the semiconductor layers. This random behavior is mainly limited to the depletion region, which thickness is increased in the present heterojunction pin-type solar cell, by the intrinsic i-layer, made of the hybrid perovskite material. The diffusion lengths for electrons and holes (L_n and L_p) are calculated as by equations (A.33) and (A.34) (PARK; KANG; KIM; SON *et al.*, 2012).

$$L_n = \sqrt{D_n \, \tau_n} \qquad \text{(A.33)}$$

$$L_p = \sqrt{D_p \, \tau_p} \qquad \text{(A.34)}$$

Where D_n [m], and D_p [m] are the diffusion lengths, or diffusivities, of electrons and holes; and τ_n [s] and τ_p [s] are its lifetimes, or times of the transport of these charge carriers, within

the charge generation layer. The diffusion lengths of electrons and holes define the pathways these charge carriers can diffuse until its recombination at the end of these pathways, and the lifetimes represent the time intervals in which the generated charge carrier can diffuse until its recombination does occur. Because of the extraordinarily long diffusion length, inherent to the perovskite layer material, the recombination effects in the intrinsic absorber layer resulting from a limited diffusion length can be neglected (SUN; ASADPOUR; NIE; MOHITE *et al.*, 2015), leading, therefore, to the simplification of $R(x) = 0$ in equations (A.29) to (A.32). The mobility of electrons and holes μ_n and μ_p [m²/Vs] in equations (A.29) to (A.32), also called as motility (SUN; ASADPOUR; NIE; MOHITE *et al.*, 2015), determines how quickly a charge carrier can be moved through the solar cell as a function of the drift force. This drift force is a function of the device's internal electric field E(x) [V/m] as calculated by equation (A.26), page 168[ix]. To develop an analytical model that defines the shapes of the solar cell's dark J-V curve, another set of Schrödinger drift-diffusion equations is necessary, as given by equations (A.35) and (A.36).

$$D_n \frac{\partial^2 n(x)}{\partial x^2} + \mu_n E(x) \frac{\partial n(x)}{\partial x} - R(x) = 0 \qquad \text{(A.35)}$$

$$D_p \frac{\partial^2 p(x)}{\partial x^2} - \mu_p E(x) \frac{\partial p(x)}{\partial x} - R(x) = 0 \qquad \text{(A.36)}$$

The coefficients $n(x)$ [cm^{-3}] and $p(x)$ [cm^{-3}], in equations (A.31), (A.32), page 169, and equaitons (A.35) and (A.36) are the charge carrier densities of electrons and holes, which are a function of the penetration depth x.

The first irradiance independent Dirichlet-type boundary conditions in equations (A.37) and (A.38) specify the equilibrium hole and electron concentrations within the electron and the hole conductor layers at $x = t_0$ and $x = 0$, which are the locations of the injections of the generated electrons and holes (Figure 3.1, page 81).

$$n(x = t_0) \quad = \quad n(t_0) \quad = \quad N_{Deff} \qquad \text{(A.37)}$$

$$p(x=0) \quad = \quad p(0) \quad = \quad N_{Aeff} \tag{A.38}$$

At equilibrium, these electron- and hole-concentrations are equal to the effective doping concentrations of the acceptor molecules (N_{Aeff}) at $x = 0$ and donor molecules (N_{Deff}) at $x = t_0$, both measured in units of [m^{-3}]. The second Dirichlet-type boundary conditions consider the undesired evasion of electrons and holes at the sites of the recombination current densities of electrons and holes at penetration depth $x = 0$ and $x = t_0$ (Figure 3.1b, page 81). These irradiance-independent Dirichlet-type boundary conditions are specified by the front and back recombination current densities J_f and J_b in equations (A.39) and (A.40)[x].

$$J_n(x=0) \quad = J_f \quad = q\, s_n\, \Delta n \quad = \quad q\, s_n \left(n_i - \frac{n_i^{\,2}}{N_{Aeff}} \right) \tag{A.39}$$

$$J_p(x=t_0) \quad = J_b \quad = \quad q\, s_p\, \Delta p \quad = \quad q\, s_p \left(p_i - \frac{p_i^{\,2}}{N_{Deff}} \right) \tag{A.40}$$

Where $s_n = s_f$ is the SRV of electrons, as related to the front hole conduction layer, while $s_p = s_b$ is the SRV of holes, as related to the back electron conduction layer. These denominations can be understood, as electrons recombine at the front p-type layer and holes recombine at the back n-type layer (Figure 3.1a, page 81).

APPENDIX A.1.5 – Normalization of the drift-diffusion model

In order to find a simplified drift-diffusion equation, the Einstein equation is used to eliminate some of the material properties by substitution. Additionally, a normalized charge carrier generation is considered to isolate and simplify the first- and second-order terms, obtaining simplified second-order differential equations as a result.

Variable reduction by substitutions with the Einstein expressions: The drift coefficients of electrons and holes, μ_n and μ_p, are not part of the multidimensional model variables in the hypercube space optimization, but they can rather be calculated as a function of these model variables. The drift coefficients express the mobilities of electrons and holes, and its substitution by use of the Einstein expression (equations (A.40) and (A.42)), results in a reduction of the total number of model variables in the multidimensional optimization space.

$$\frac{\mu_n}{D_n} = \frac{q}{k_B T} = \frac{1}{V_t} \tag{A.41}$$

$$\frac{\mu_p}{D_p} = \frac{q}{k_B T} = \frac{1}{V_t} \tag{A.42}$$

Considering that for a constant semiconductor temperature T [K] a fixed thermal voltage V_t [V] is obtained, the mobility μ_n can be substituted by expressions (A.43).

$$\mu_n = D_n / V_t \tag{A.43}$$

In a similar form, the mobility of holes can be substituted as follows, based on equation (A.42).

$$\mu_p = D_p / V_t \tag{A.44}$$

Using these reduced Einstein expressions (equations (A.43) and (A.44)), the mobilities μ_n and μ_p are substituted in the complete set of the non-normalized drift-diffusion (equations (A.29) to (A.32), page 168; and equations (A.35) and (A.36), page 170). Such substitutions can be considered as the drift- and the diffusion forces are permanently in equilibrium. Consequently, the drift coefficients are in a specific fixed relationship to the diffusion coefficients, which means that knowing one of them, e.g., the diffusion coefficients of electrons and holes, the others (the drift coefficients) can be modeled by expressions (A.43) and (A.44). Therefore, to obtain a solution for the current densities, the reduced Einstein expressions are used for the substitution of the charge carrier mobilities μ_n and μ_p in the four

drift-diffusion equations ((A.31), page 169, as well as (A.32), (A.35), and (A.36)). The drift coefficients can then be recovered after the optimization using (A.43) and (A.44), page 172. Therefore, they are considered as model variables but do not appear as optimization variables in the multidimensional PSC model.

Normalization of the drift-diffusion expressions: To simplify the derivation process of the drift-diffusion equations ((A.31), page 169, as well as (A.32), (A.35), and (A.36)) mathematically, it is of advantage to transform these four equations in normalized second-order differential equations. For the differential equations from which the photocurrent density is derived ((A.31) and (A.32), page 169), this normalization considers the following steps: (i) the charge carrier generation rates $G(x)$ in equations (A.31) and (A.32), page 169, are substituted by the expression in (A.18), page 164, which results in the following expressions:

$$D_n \frac{\partial^2 n(x)}{\partial x^2} + \mu_n \, E(x) \frac{\partial n(x)}{\partial x} + G_{eff} \, e^{-x/\lambda_{ave}} - R(x) = 0 \qquad \text{(A.45)}$$

$$D_p \frac{\partial^2 p(x)}{\partial x^2} - \mu_p \, E(x) \frac{\partial p(x)}{\partial x} + G_{eff} \, e^{-x/\lambda_{ave}} - R(x) = 0 \qquad \text{(A.46)}$$

(ii) the generation rate of charge carriers at the top surface of the absorber layer (G_{eff}) in (A.18), page 164, is substituted by the expressions of the normalized generation rates of electrons (G_n) and holes (G_p) in (A.47) and (A.48).

$$G_{eff} = G_n \, D_n \qquad \text{(A.47)}$$

$$G_{eff} = G_p \, D_p \qquad \text{(A.48)}$$

Where the effective generation rate of charge carriers (G_{eff}), is here substituted using G_n and G_p, both measured in units of [m^{-5}]. These substitutions transform (A.45), and (A.46) in the following expressions:

$$D_n \frac{\partial^2 n(x)}{\partial x^2} + \mu_n \, E(x) \frac{\partial n(x)}{\partial x} + G_n \, D_n \, e^{-x/\lambda_{ave}} - R(x) = 0 \qquad \text{(A.49)}$$

$$D_p \frac{\partial^2 p(x)}{\partial x^2} - \mu_p \, E(x) \frac{\partial p(x)}{\partial x} + G_p \, D_p \, e^{-x/\lambda_{ave}} - R(x) = 0 \qquad \text{(A.50)}$$

(iii) the assumption of zero recombination rates in the perovskite layer (R(x) = 0) and the division by D_n and D_p on both sides of equations (A.49) and (A.50) result in the following expressions:

$$\frac{\partial^2 n(x)}{\partial x^2} + \frac{\mu_n}{D_n} E(x) \frac{\partial n(x)}{\partial x} + G_n \; e^{-x/\lambda_{ave}} = 0 \qquad \text{(A.51)}$$

$$\frac{\partial^2 p(x)}{\partial x^2} - \frac{\mu_p}{D_p} E(x) \frac{\partial p(x)}{\partial x} + G_p \; e^{-x/\lambda_{ave}} = 0 \qquad \text{(A.52)}$$

(iv) The substitution of the charge carrier mobilities μ_n and μ_p with the reduced Einstein expressions ((A.43), page 172, and (A.44)), results in the following expressions.

$$\frac{\partial^2 n(x)}{\partial x^2} + \frac{1}{V_t} E(x) \frac{\partial n(x)}{\partial x} + G_n \; e^{-x/\lambda_{ave}} = 0 \qquad \text{(A.53)}$$

$$\frac{\partial^2 p(x)}{\partial x^2} - \frac{1}{V_t} E(x) \frac{\partial p(x)}{\partial x} + G_p \; e^{-x/\lambda_{ave}} = 0 \qquad \text{(A.54)}$$

(v) the remaining expression (E / V_t), as appearing in the second term of (A.53) and (A.54), is finally substituted by expression (A.55), where ε_n [1/m] is considered as to be a normalized electric field.

$$\varepsilon_n = E / V_t \qquad \text{(A.55)}$$

This final manipulation does result in the normalized drift-diffusion equations as presented in (A.56) and (A.57). If compared to the non-normalized differential equations, ((A.31) and (A.32), page 169), these simplified second-order differential expressions are based on a lower number of variables in its first two terms. Furthermore, the normalized expressions also include the optical Beer-Lambert model.

$$\frac{\partial^2 n(x)}{\partial x^2} + \varepsilon_n \frac{\partial n(x)}{\partial x} + G_n \, e^{-x/\lambda_{ave}} = 0 \tag{A.56}$$

$$\frac{\partial^2 p(x)}{\partial x^2} - \varepsilon_n \frac{\partial p(x)}{\partial x} + G_p \, e^{-x/\lambda_{ave}} = 0 \tag{A.57}$$

An even more simplified set of normalized drift-diffusion equations is obtained for the state when the cell is localized in the dark. In this development, the non-normalized equations (A.35) and (A.36), page 170, are converted in a similar normalization process to the equations (A.58) and (A.59).

$$\frac{\partial^2 n(x)}{\partial x^2} + \varepsilon_n \frac{\partial n(x)}{\partial x} = 0 \tag{A.58}$$

$$\frac{\partial^2 p(x)}{\partial x^2} - \varepsilon_n \frac{\partial p(x)}{\partial x} = 0 \tag{A.59}$$

APPENDIX A.1.6 - Resulting analytical expression of current density

To calculate the PCE, as detailed in equations (3.1) to (3.11), pages 83 to 88, by the use of the analytical solar cell model as derived in (SUN; ASADPOUR; NIE; MOHITE *et al.*, 2015); and, in order to optimize the PSC by the here proposed optimization process, we need a unique, complete analytical expression for the current density of the here considered pin-type PSC.

Necessary Transformations: The whole process of transformations, as described in (SUN; ASADPOUR; NIE; MOHITE *et al.*, 2015) involves the solution of several differential equations (DEs) to express the cell's current density under light condition (J_{light}) as measurable at its terminals. Therefore, we only describe these manipulations conceptually. The analytical model of J_{light} is obtained by derivation of the cell's fundamental DEs ((A.21), page 167; (A.31), page 169; (A.32), (A.35), and (A.36), pages 169 to 170), considering also: (i) the normalization of the drift-diffusion current density DEs, which result to the equations (A.56), page 175, to (A.59), (ii) the general solutions of (A.21), page 167 and the normalized DEs, which returns two unknown integration constants or factors for each DE, (iii) the application of its boundary expressions ((A.23) to (A.24), page 167, and (A.37) to (A.40), page 170) to obtain a system of equations from which the expressions of the unknown integration constants are obtained, (iv) the manipulation of the obtained expressions, obtaining first the electric field equation, which is substituted in the equations of the obtained current densities of electrons and holes for the illuminated and the dark state.

Electric Field equation: The analytical model of the electric field is in (SUN; ASADPOUR; NIE; MOHITE *et al.*, 2015) obtained by the (i) solution of the second-order Poisson differential equation (A.21), page 167, which returns to a general expression with two unknown integration constants or factors (A.22), page 167. Using the boundary expressions ((A.23), page 167, and (A.24)) for the substitution in the general solution (A.22) builds up an equation system, which results in an expression (A.25), page 167, which manipulation results in the solution of the electric field (A.26), page 168.

Charge carrier current densities: In a similar solution process, the expressions of the electron and hole current densities are obtained for the illuminated and the dark states. Basically, by the solution of the four normalized Schrödinger equations ((A.56) to (A.59), page 175) and its boundary equations ((A.37) to (A.40), page 170), the four charge carrier current densities as specified in equation (A.4), page 159, can be calculated.

Photocurrent density of electrons ($J_{n\text{-}photo}$): In a similar form, as the electric field equation was derived from the second-order Poisson equation, the analytical model for the generated current density of electrons $J_{n\text{-}photo}$ (as used in equation (A.4)) is obtained by the

following steps: (i) solving the normalized second-order drift-diffusion equation of electrons to achieve its general solution, which presents two unknown integration constants; (ii) substitution of the boundary conditions for electrons (equations (A.37) and (A.39), page 170) to create a system of two equations, which solution result to the expressions of the unknown integration constants (iii) substituting the integration constants in the general expression and solving this expression for $J_{n\text{-}photo}$.

Photocurrent density of holes ($J_{p\text{-}photo}$): The analytical model of the generated current density of holes ($J_{p\text{-}photo}$) is obtained by a similar procedure using the steps of (i) solving the normalized differential equation for the hole photocurrent density (A.57), page 175, which results in its general solution, with two unknown integration constants; (ii) substitution of its boundary conditions (equations (A.38) and (A.40), page 171) in this general solution and (iii) solving the obtained equation system for the current density of holes $J_{p\text{-}photo}$.

Total charge carrier density under exposition to light: The sum of the electron and hole current densities under exposition to light results in an equation that defines the total density of charge carriers for the illuminated state ($J_{photo} = J_{n\text{-}photo} + J_{p\text{-}photo}$), which is presented in equations (A.60) to (A.63), page 179.

Electron current density in the dark state ($J_{n\text{-}dark}$): The equation of the current density of electrons under the privation of light ($J_{n\text{-}dark}$), is obtained by a similar pathway. In step one a general solution of the normalized differential equation (A.57), page 175, is found, which presents two unknown integration constants. The substitution with the boundary equations of holes (equations (A.37) and (A.39), page 170) results in an equation system, which solution results in the expressions of the unknown integration constants. The substitution of these integration constants results then in a general expression, which is then solved for the current density of electrons ($J_{n\text{-}dark}$).

Hole current density in the dark state ($J_{p\text{-}dark}$): (i) using the normalized drift-diffusion equation (A.59), page 175, the general solution to this second-order differential equation contains two unknown integration constants. The substitution with the boundary conditions (equations (A.38) and (A.40), page 171) result in an equation system, which

solution results in the expressions of the two unknown integration constants. The substitution of these integration constants, in the general expression, results in an equation, which is solved for the hole current density in the dark $J_{p\text{-}dark}$.

Total charge carrier density in the dark state (J_{dark}): Similar as in the state under illumination the sum of the electron and hole current densities ($J_{dark} = J_{n\text{-}dark} + J_{p\text{-}dark}$) result in a large expression which is presented in equations equation (A.64) to (A.66), page 180. Here it has to be emphasized that only the substitution of the normalized electric field equation (A.55), page 174, and then the electric field equation (A.26), page 168, in the resulting current density equations, enables the modeling of the electron and hole current densities as a function of the terminal voltage V for both cases, for the equations of the illuminated state and the dark state of the solar cell.

APPENDIX A.2 – COMPOSED REPRESENTATION

The simplification of the resulting expressions of the photocurrent density ($J_{photo} = J_{n\text{-}photo} + J_{p\text{-}photo}$) and the recombination current density ($J_{dark} = J_{n\text{-}dark} + J_{p\text{-}dark}$) results in the expressions (A.1) to (A.26), pages 157 to 168, in (SUN; ASADPOUR; NIE; MOHITE *et al.*, 2015), where the variable E [V/m] in the equations of $J_{n\text{-}dark}$, $J_{p\text{-}dark}$, $J_{n\text{-}photo}$, $J_{p\text{-}photo}$ is substituted by the electric field equation (A.26), page 168. These are the equations by which a complete analytical expression of the J-V curve model is defined, where the current density of this curve is modeled by (J_{light}) (equation (A.3), page 158) as a function of the terminal voltage V, and a here considered fixed generation rate of charge carriers G.

Expression of the current density under exposition to light: For the calculus of the measurable current density (J_{light}) in equation (A.3), page 158, we need the internal, and not directly measurable photocurrent density $J_{photo}(G,V) = J_{n\text{-}photo} + J_{p\text{-}photo}$, as defined in equation (A.14), page 163, which describes the solar cell internal injection of charge carriers under exposition to light and we need furthermore the recombination current density $J_{dark}(G,V) = J_{p\text{-}dark} + J_{n\text{-}dark}$ as presented in equation (A.5), page 159. To calculate $J_{photo}(G,V)$ the terms A, B and m, which appear in equations (A.14), page 163, are substituted, with the terms as presented in equations (A.15) to (A.17), page 163, which leads to the following expression:

$$J_{photo} = q\, G_{\max} \left(\alpha_f \left(\frac{1 - e^{V' - \frac{t_0}{\lambda_{ave}}}}{V' - \frac{t_0}{\lambda_{ave}}} - \beta_f \right) - \alpha_b \left(\frac{1 - e^{V' + \frac{t_0}{\lambda_{ave}}}}{V' + \frac{t_0}{\lambda_{ave}}} - \beta_b \right) e^{-\frac{t_0}{\lambda_{ave}}} \right) \qquad \text{(A.60)}$$

Furthermore, the terms β_f and β_b (equations (A.12) and (A.13), page 162) can be substituted in equation (A.60), which transforms this equation the following large analytical expression.

$$J_{photo} = q\, G_{\max} \left(\alpha_f \left(\frac{1 - e^{V' - \frac{t_0}{\lambda_{ave}}}}{V' - \frac{t_0}{\lambda_{ave}}} - \frac{D_n}{t_0\, s_f} \right) - \alpha_b \left(\frac{1 - e^{V' + \frac{t_0}{\lambda_{ave}}}}{V' + \frac{t_0}{\lambda_{ave}}} - \frac{D_p}{t_0\, s_b} \right) e^{-\frac{t_0}{\lambda_{ave}}} \right) \qquad \text{(A.61)}$$

The further substitution of the terms α_f and α_b, as defined in equations (A.8) and (A.9), page 161, lead the complete expression of the photocurrent of electrons and holes, as presented in equations (A.62).

$$J_{photo} = q\, G_{\max} \left(\begin{array}{l} \dfrac{1}{\dfrac{e^{V'} - 1}{V'} + \dfrac{D_n}{t_0\, s_f}} \left(\dfrac{1 - e^{V' - \frac{t_0}{\lambda_{ave}}}}{V' - \dfrac{t_0}{\lambda_{ave}}} - \dfrac{D_n}{t_0\, s_f} \right) \\ - \dfrac{1}{\dfrac{e^{V'} - 1}{V'} + \dfrac{D_p}{t_0\, s_b}} \left(\dfrac{1 - e^{V' + \frac{t_0}{\lambda_{ave}}}}{V' + \dfrac{t_0}{\lambda_{ave}}} - \dfrac{D_p}{t_0\, s_b} \right) e^{-\frac{t_0}{\lambda_{ave}}} \end{array} \right) \qquad \text{(A.62)}$$

Where the whole set of variables D_n, D_p, t_0, s_f, s_b, and λ_{ave} are six of the nine model variables. The remaining unknown term V' (A.10), page 161, is calculated as a function of the terminal voltage V and by the substitution of V_{bi} (equation (A.11), page 162) and leads to equation (A.63). Where the variables N_{Aeff}, N_{Deff}, and n_i, which terminology was already described in equations (A.10) and (A.11), page 161, are as fixed values, which model the built-in voltage

V_{bi}. The thermal voltage $V_t = k_B T/q$ is also considered as a fixed value, giving a constant operating temperature (T).

$$V' = \frac{V - V_{bi}}{V_t} = \frac{V - V_t \log\left(\frac{N_{A,eff}\ N_{D,eff}}{n_i^2}\right)}{V_t} \qquad \text{(A.63)}$$

Expression of the current density in the dark: In a similar form, the measurable current density when the cell is localized in the dark (J_{dark}), is calculated by the substitution of the terms α_f and α_b in equation (A.5), page 159, which leads to the following expression.

$$J_{dark} = \left(\frac{1}{\frac{e^{V'} - 1}{V'} + \beta_f} J_{f0} + \frac{1}{\frac{e^{V'} - 1}{V'} + \beta_b} J_{b0} \right) \left(e^{V/V_t} - 1 \right) \qquad \text{(A.64)}$$

After the substitution of β_f and β_b in equation (A.64) we obtain the equation (A.65).

$$J_{dark} = \left(\frac{1}{\frac{e^{V'} - 1}{V'} + \frac{D_n}{t_0\, s_f}} J_{f0} + \frac{1}{\frac{e^{V'} - 1}{V'} + \frac{D_p}{t_0\, s_b}} J_{b0} \right) \left(e^{V/V_t} - 1 \right) \qquad \text{(A.65)}$$

Additionally, the expressions of the current densities in the dark (equations (A.6) and (A.7), page 160), related to the front and back charge conduction layers, are substituted in equation (A.65), which leads to the following final expression for the recombination current densities.

$$J_{dark} = \left(\frac{1}{\frac{e^{V'} - 1}{V'} + \frac{D_n}{t_0\, s_f}} q\, s_f\, \Delta n + \frac{1}{\frac{e^{V'} - 1}{V'} + \frac{D_p}{t_0\, s_b}} q\, s_b\, \Delta p \right) \left(e^{V/V_t} - 1 \right) \qquad \text{(A.66)}$$

Where the expression V' was already defined in equation (A.63), page 180. We see that the dark current density, which describes the recombination effects, is calculated as a function of

eight model variables s_b, s_f, Δp, Δn, D_n, D_p, V_{bi}, t_0, and the terminal voltage V, while the values of remaining variables are constants. These model variables are used in the present optimization which includes the modeling of the measurable $J_{light}(G,V)$ current density, where $J_{light}(G,V)$ is the sum of $J_{dark}(V)$ and $J_{photo}(G,V)$, as defined by the equation (A.3), page 158. The only not considered model variable in this expression is λ_{ave}, which only appears in the equation of the photogeneration (A.62), page 179.

APPENDIX A.3 – DERIVATION OF THE MODEL

General solutions: Here we are present the derivation of the equations of the current densities by the solution of the second-order normalized differential equations using its boundary equations. The integration of the normalized drift-diffusion (equations (A.56), and (A.57), page 175) lead to the general solution of these second-order differential equations as presented in (A.67) and (A.68). These equations determine the charge carrier densities of electrons and holes under the cell's exposition to light as a function of the light's penetration depth (x).

$$n_{photo}(x) = -\frac{C_1}{\varepsilon_n} e^{-\varepsilon_n x} + \frac{G_n \lambda_{ave}^2 e^{-\frac{x}{\lambda_{ave}}}}{\varepsilon_n \lambda_{ave} - 1} + C_2 \qquad \text{(A.67)}$$

$$p_{photo}(x) = \frac{C_3}{\varepsilon_n} e^{\varepsilon_n x} - \frac{G_p \lambda_{ave}^2 e^{-\frac{x}{\lambda_{ave}}}}{\varepsilon_n \lambda_{ave} + 1} + C_4 \qquad \text{(A.68)}$$

In these equations, C_1 to C_4 are four unknown integration constants of these two general solutions. In the following text, we search for the inherent expressions of these variables using the equations of the boundary conditions for electrons (equations (A.37) and (A.39), page 170) and holes (equations (A.38) and (A.40), page 171).

If the PSC is localized in the dark, much simple general solutions are obtained by equations (A.69) and (A.70).

$$n_{dark}(x) = C_5 + C_6 e^{-\varepsilon_n x} \qquad \text{(A.69)}$$

$$p_{dark}(x) = C_7 + C_8\, e^{\varepsilon_n x} \tag{A.70}$$

Where C_5 to C_8, are additional unknown integration coefficients, which expressions also must be determined, using the same boundary equations ((A.37) to (A.40), page 170).

Electron current density in the illuminated state: By the integration of equation (A.56), page 175, substitution with the first boundary condition (equation (A.37), page 170), the following expression is obtained

$$n_{photo}(x) = \frac{G_n\, \lambda_{ave}^2 \left(e^{-\frac{x}{\lambda_{ave}}} - e^{-\frac{t_0}{\lambda_{ave}}} \right) + C_2\, e^{-\varepsilon_n x} \left(\frac{1}{\varepsilon_n} - \lambda_{ave} \right) + N_{Deff} \left(\varepsilon_n\, \lambda_{ave} - 1 \right)}{\varepsilon_n\, \lambda_{ave} - 1} + \frac{C_2\, e^{-\varepsilon_n t_0}}{\varepsilon_n} \tag{A.71}$$

Dissimilar to the solution (A.67), this equation only presents one integration constant as unknown (C_2), while C_1 was eliminated by substitution using the first boundary condition (A.37), page 170. Both, the charge carrier densities of electrons $n_{photo}(x)$ (equation (A.71)), and its first order derivation $\partial n_{photo}(x)/\partial x$, are essential for the elaboration of the equation which defines the current density as presented in equations (A.72) and (A.73). The equation of the current density is used for the application of the second boundary condition (A.39), page 171, to obtain a solution of the remaining unknown integration constant (C_2). The first order derivation of equation (A.71) results in the following expression

$$\frac{\partial n_{photo}(x)}{\partial x} = \frac{C_2\, e^{-\varepsilon_n x} (\varepsilon_n\, \lambda_{ave} - 1) - \lambda_{ave}\, G_n\, e^{-(x/\lambda_{ave})}}{\varepsilon_n\, \lambda_{ave} - 1} \tag{A.72}$$

The equation of the generated current density of electrons can be elaborated by the substitution of the expressions of $n_{photo}(x)$ (equation (A.71)) and $\partial n_{photo}(x)/\partial x$ (equation (A.72)) in the current density differential equation as shown in equation (S66), being these variables highlighted in (A.73) by square brackets.

$$J_{n,photo}(x) = q\ \mu_n\ \ E\left[n_{photo}(x)\right] + q\ D_n\left[\frac{\partial n_{photo}(x)}{\partial x}\right] \tag{A.73}$$

The substitution of $n_{photo}(x)$ and $\partial n_{photo}(x)/\partial x$ leads to the following expression

$$J_{n,photo}(x) = q\ \mu_n E\left[\frac{G_n\ \lambda_{ave}^2\left(e^{-\frac{x}{\lambda_{ave}}} - e^{-\frac{t_0}{\lambda_{ave}}}\right) + C_2\, e^{-\varepsilon_n x}\left(\frac{1}{\varepsilon_n} - \lambda_{ave}\right) + N_{D,eff}\left(\lambda_{ave}\ \varepsilon_n - 1\right)}{\varepsilon_n\ \lambda_{ave} - 1} + C_2\,\frac{e^{-\varepsilon_n t_0}}{\varepsilon_n}\right] \tag{A.74}$$
$$+\quad q\ D_n\left[\frac{C_2\ e^{-\varepsilon_n x}(\varepsilon_n\ \lambda_{ave} - 1) - \lambda_{ave}\ G_n\ e^{-(x/\lambda_{ave})}}{\varepsilon_n\ \lambda_{ave} - 1}\right]$$

We note that the remaining unknown integration constant appears in the expressions of $n_{photo}(x)$ and $\partial n_{photo}(x)/\partial x$. The solution to the remaining unknown integration constant (C_2), is obtained by substitution with boundary condition (A.39), page 171. In this substitution, the photocurrent for zero penetration depth, $J_{n,photo}(x = 0)$, is determined, and the obtained the resulting expression (A.75) is solved for the still unknown integration variables C_2 in equation (A.76).

$$J_{n,photo}(x=0) \to q\ s_n\ \Delta n = q\ \mu_n E\left[\frac{G_n\ \lambda_{ave}^2\left(1 - e^{-\frac{t_0}{\lambda_{ave}}}\right) + C_2\left(\frac{1}{\varepsilon_n} - \lambda_{ave}\right) + N_{D,eff}\left(\lambda_{ave}\ \varepsilon_n - 1\right)}{\varepsilon_n\ \lambda_{ave} - 1} + C_2\,\frac{e^{-\varepsilon_n t_0}}{\varepsilon_n}\right] \tag{A.75}$$
$$+\quad q\ D_n\left[\frac{C_2\ (\varepsilon_n\ \lambda_{ave} - 1) - \lambda_{ave}\ G_n}{\varepsilon_n\ \lambda_{ave} - 1}\right]$$

$$C_2 = \frac{\varepsilon_n\ E\ \mu_n\ G_n\left[\lambda_{ave}^2\left(e^{\frac{t_0}{\lambda_{ave}}} - 1\right) + \frac{N_{D,eff}}{G_n}\left(1 - \lambda_{ave}\right) + \frac{D_n\ \lambda_{ave}}{\mu_n\ E}\right]}{E\ \mu_n\ \varepsilon_n\left[E\ \mu_n\ \varepsilon_n\left(\lambda_{ave}\ e^{-\varepsilon_n t_0} - \lambda_{ave} - \frac{e^{-\varepsilon_n t_0}}{E} + \frac{1}{E}\right) + \varepsilon_n\left(D_n\ \lambda_{ave}\ \varepsilon_n - D_n\right)\right]} \tag{A.76}$$

The solution for the photocurrent density (J_{photo}) is obtained by substitution of the term for C_2 in the current density equation (equation (A.74)). This equation specifies the current density as a function of the penetration depth (x) of the solar irradiance. To specify the current density of electrons at the injection location of the generated electrons at the n-type layer, we substitute x with t_0. Therefore, the specific solution for the injection of electrons ($J_{n\text{-}photo}$) is obtained by calculating the electron current at $x = t_0$ as follows

$$J_{n-photo} = J_{n-photo}(x = t_0) = q\frac{A_1 + A_2}{A_3} \tag{A.77}$$

Where the terms A_1, A_2, and $\underline{A_3}$ are defined by equations (A.78) to (A.80).

$$A_1 = E^2 \mu_n^2 \left(N_{D,eff} + G_n \lambda_{ave}^2 e^{-\varepsilon_n t_0} + \varepsilon_n N_{D,eff} \lambda_{ave} + G_n \lambda_{ave}^2 e^{-\frac{t_0}{\lambda_{ave}}} \right) \tag{A.78}$$

$$\begin{aligned} A_2 = {} & \left(1 - \varepsilon_n \lambda_{ave}\right) \lambda_{ave} \mu_n e^{-\varepsilon_n t_0} \left(D_n E G_n - \Delta n E s_n\right) \\ & + D_n E \varepsilon_n N_{D,eff} \mu_n \left(\varepsilon_n \lambda_{ave} + 1\right) \end{aligned} \tag{A.79}$$

$$A_3 = \left(\lambda_{ave} \varepsilon_n - 1\right)\left(D_n \varepsilon_n + E e^{-\varepsilon_n t_0} \mu_n\right) + E \mu_n \left(1 - \lambda_{ave} \varepsilon_n\right) \tag{A.80}$$

Observation: This equation was simplified by the substitution of x with ∞, instead of t_0, in order to simplify the large expression obtained, as otherwise obtained with the substitution with t_0. This simplification can be accomplished as the assumption of an infinite thick absorber layer shows an absorption which is only < 1 % lower in comparison to the case of a manufactured solar cell with thickness t_0 as to see from Figure 3.1b, page 81.

Electron current density in the dark state: The equations (A.67) to (A.71), page 181, show how the equation of the photocurrent density of electrons in the illuminated state is

obtained. The electron current densities in the dark state, is calculated in a similar development, starting however, with the normalized differential equation for the dark state (A.58), page 175. This elaboration uses identical boundary expressions ((A.37), page 170 and (A.38)), to eliminate the unknown integration constants. As the dark curve expresses the cell's non-radiative recombination of electrons, as present at the transition to the hole conduction layer, the electron current density at the recombination location at $x = 0$ (Figure 3.1a, page 81) is determined by equation (A.78). This electron recombination current density corresponds also to the electron current density at the front p-conduction layer at $x = 0$ ($J_{n\text{-}dark} = Jf$) in Figure 3.1a, page 81, and is calculated as follows

$$J_{n-dark} = J_{n-dark}(x) = J_{n-dark}(x=0) = q\left[E\,N_{D,eff}\,\mu_n + \frac{D_n\,\varepsilon_n\,e^{-\varepsilon_n t_0}\left(\Delta n\,s_n - E\,N_{D,eff}\,\mu_n\right)}{E\,\mu_n\left(e^{-\varepsilon_n t_0}-1\right)+D_n\,\varepsilon_n}\right] \qquad \text{(A.81)}$$

Hole current density in the illuminated state: To calculate the general solution of the generated and injected current density of holes, the normalized drift-diffusion differential equation (A.57), page 175, is used, which is integrated, and to which the boundary conditions of holes (equations (A.38) and (A.40), page 171) are applied, to solve for the injected hole current density. The injection of holes (J_p) appears at the boundary to the front hole conduction layer at $x = 0$. Therefore, the equation of the generated hole current density $J_{p\text{-}photo}(x) = J_{p\text{-}photo}(x = 0)$ is calculated substituting in the resulting $J_{p\text{-}photo}(x)$ the x with zero, which leads to the following equation (A.82), where the terms B_1, B_2, and B_3 are defined by the equations (A.83) to (A.85).

$$J_{p-photo} = J_{p-photo}(x=0) = q\frac{\left(B_1 + B_2\right)}{B_3} \qquad \text{(A.82)}$$

$$B_1 = D_p\,E\,\varepsilon_n\left(N_{A,eff}\,\mu_p\left(e^{\varepsilon_n t_0}\varepsilon_n\,\lambda_{ave} - \varepsilon_n\,\lambda_{ave} - 1 + e^{\varepsilon_n t_0} - G_p\,\lambda_{ave}^2\,\mu_p\left(e^{-t_0/\lambda_{ave}}-1\right)\right)\right) \qquad \text{(A.83)}$$

$$B_2 = \left(1 - e^{\varepsilon_n t_0}\right)\left(E^2\ \varepsilon_n\ \lambda_{ave}\ \mu_p^2\ N_{A,eff} - D_p\ E\ G_p\ \lambda_{ave}\ \mu_p + E^2\ N_{A,eff}\ \mu_p^2\right) + D_p\ \Delta p\ \varepsilon_n\ s_p\left(1 + \varepsilon_n\ \lambda_{ave}\right) \qquad \text{(A.84)}$$

$$B_3 = D_p\ \varepsilon_n\ e^{\varepsilon_n t_0}\left(1 + \varepsilon_n\right) - \left(\lambda_{ave}\ \varepsilon_n + 1\right)\left(E\ \mu_p\left(1 - e^{\varepsilon_n t_0}\right)\right) \qquad \text{(A.85)}$$

Hole current density in the dark state: The expression of the current density, which expresses the recombination of holes is calculated in a similar form by (i) the integration of normalized differential equation (A.58), page 175, (ii) using the substitution with the boundary expressions (equations (A.38) and (A.40), page 171). As the holes recombine at the transition to the back-electron conduction layer, the following equation is obtained for the hole recombination current density:

$$J_{p-dark} = J_{p-dark}\left(x = t_0\right) = q\left[\frac{\left(1 - e^{\varepsilon_n t_0}\right)\left(N_{A,eff}\ \mu_p\ E(E - D_p\ \varepsilon_n)\right) + D_p\ \Delta p\ \varepsilon_n\ s_p}{E\ \mu_p\left(1 - e^{\varepsilon_n t_0}\right) + D_p\ \varepsilon_n\ e^{\varepsilon_n t_0}}\right] \qquad \text{(A.86)}$$

Simplifications in the combined expression of J_{light} (equation (A.1), page 157), by use of the obtained expressions of the four current densities ($J_{n\text{-}photo}$, $J_{n\text{-}dark}$, $J_{p\text{-}photo,}$ and $J_{p\text{-}dark}$) in equations (A.77) to (A.83), page 184, result in the formulation of the model as presented in sections **ctions** APPENDIX A.1 and APPENDIX A.2, pages 156 and 178.

APPENDIX B – ADDITIONAL RESULTS AND DISCUSSIONS

CONTENTS

Here we present some additional results and discussions, considering ideal light trapping and PSC materials, which translates to a higher absorption of light. We also show the maximal obtainable efficiency, not considering any practical limitations as obtained by the multidimensional optimization, and we discuss phenomena not considered in the presented optimizations. Then we discuss the improvement of light trapping by shape-optimized NPs, and we present a flow chart of the programed optimization process. Finally, we estimate the efficiency attainable by the combination of the best state-of-the-art measured material properties.

APPENDIX B.1 – IDEAL LIGHT TRAPPING

In our presented optimizations, excluding, we adopted as initial conditions in a nine-dimensional optimization scheme (i) the material properties and absorber layer thickness as obtained in (SUN; ASADPOUR; NIE; MOHITE *et al.*, 2015). We constraint the short circuit current densities for different absorber layer thicknesses with an increased value as found in (CAI; PENG; CHENG; GU, 2015). We calculate the λ_{ave} for different t_0 with the m-value as adopted in (SUN; ASADPOUR; NIE; MOHITE *et al.*, 2015), which results in different cell designs. In a more simplified example of optimizations, we constrain the whole set of variables with boundary amplification factors, using equation (3.5), up to the value of f_B = 160, inclusive t_0 and λ_{ave}, which leads to a nearly ideal thin absorber layer thicknesses. We consider that almost perfect light trapping, as eventually obtainable by advanced light-trapping schemes (section APPENDIX B.5, page 194), results in a high qG_{max} of 23 mA/cm^2, even in cells with extremely thin absorber layers. In this case, light trapping does not increase the J_{sc} but compensates for the lower absorption in very thin absorber layers. Such constraints consider ideal light trapping, and result in a higher efficiency of 29% (Table B.1, page 189). The table is also useful to understand better the behavior of the optimization in the multidimensional space.

In Table B.1 the setup variables appear at line 1, and for a maximal boundary-expansion factor of f_B = 160, the optimization algorithm searches for the ideal properties and the ideal absorber layer thickness. These ideal values lead to the highest simulated efficiency, which we present at line 6. The actual modification factor shows to which definite extent the

optimization algorithm improves a variable. As to see, for most of the variables, the optimization algorithm explores the fully the available constraint range, as the ideal values correspond to an actual modification factor of 160 or 1/160. Only t_0 is modified to a lower extent with an actual modification factor of f_B factor of (1/127), which results in an ideal value of 3.54 nm, instead, while its lower constraint is t_0 = 2.81 nm.

Table B.1 - Optimization data and results related to the nine-dimensional optimization (boldface symbols) by use of the maximal boundary expansion of the model variables (f_B = 160) for the whole set of nine optimization variables presenting a nearly ideal light-trapping scheme with shape-optimized nanoparticles; J_{sc} = 23 mA/cm^2.

Variable specification	s_f	s_b	Δn	Δp	V_{bi}	D_n	D_p	t_0	λ_{ave}	η
Units	[cm / s]	[cm / s]	[1 / cm ^{3}]	[1 / cm ^{3}]	[V]	[cm ^{2} / s]	[cm ^{2} / s]	[nm]	[nm]	[%]
1 - Values obtained in (Sun et al. 2015)	2.00E+02	1.92E+01	8.43E+06	1.30E+08	0.78	5.00E-02	5.00E-02	450.0	100.0	15.7
2 - Lower boundary values	1.25E+00	1.20E-01	5.27E+04	8.13E+05	0.00	3.13E-04	3.13E-04	2.81	0.63	-
3 - Lower constraint factor	1 / 160	1 / 160	1 / 160	1 / 160	∞	1 / 160	1 / 160	1 / 160	1 / 160	-
4 - Upper boundary values	3.20E+04	3.07E+03	1.35E+09	2.08E+10	1.40	8.00	8.00	1000	1.60E+04	-
5 - Upper constraint factor	160	160	160	160	1,8	160	160	2.22	160	-
6 - Optimized values	1.25	0.12	8.43E+06	1.30E+08	1.40	8.00	8.00	*3.54*	*0.63*	*28. 98*
7 – Actual modification factors	1 / 160	1 / 160	n. m.	n.m.	1.8	160,0	160	1 / 127	1 / 160	-

Row 1, Configuration as obtained from the one-dimensional thickness optimization in (Sun et al. 2015), which represent the initial conditions;

Row 2, The constraining lower boundary limits specified for the optimization and the related constraint multiplication factor (Line 3);

Row 4, The constraining upper boundary limits specified for the optimization and the associated constraint multiplication factor (Line 5).

Row 6, The ideal model variable values obtained from the multidimensional optimization process;

Row 7, The actual modification factors as calculated with the values from Line 6 (n.m., not modified).

Such a behavior appears, as t_0 and λ_{ave}, shows a dependency, which results in a maximal efficiency vertex line, as shown in Figure 4.2e-f, page 102, whereas the relationship of the further variables does not lead to such a saddle point. The identification of a saddle-point curve or the maximal efficiency values vertex-line in the relationship of model variables is of importance, as only an adequate tuning of the involved variables enables high cell efficiencies. We consider that further vertex lines are not present as for the further variables the optimization algorithm does not identify any similar optimal variable value. These findings correspond to the findings in (WRUCK, 2018), which analyzed several combinations of the two-dimensional space graphically, studying all possible combinations that involve the

variables t_0 and λ_{ave}.In Table B.2 and Table B.3, we present the stepwise efficiency growths up to the efficiency of 29%, as obtained for several optimizations, each using a different boundary improvement factor.

Table B.2 - Optimized model variables (boldface symbols), as obtained from 11 optimizations in a nine-dimensional function space considering individual f_B factors. We achieved an ideal PCE of 29% by considering nearly perfect light trapping with shape-optimized nanoparticles in an absorber layer with t_0 =3.5 nm; qG_{max} = 23 mA/cm^2.

f_B	s_f	s_b	Δn	Δp	V_{bi}	D_n	D_p	μ_n	μ_p	t_0	λ_{ave}	η
[-]	[cm/s]	[cm/s]	[1/cm^3]	[1/cm ^{3}]	[V]	[cm^2/s]	[cm^2/s]	[cm^2/Vs]	[cm^2/Vs]	[nm]	[nm]	[%]
5.00	40.00	3.84	8.43E+06	1.30E+08	0.80	0.25	0.25	9.65	9.65	99.63	20.00	20.09
10.00	20.00	1.92	8.43E+06	1.30E+08	0.82	0.50	0.50	19.30	19.30	334.98	10.00	20.77
20.00	10.00	0.96	8.43E+06	1.30E+08	0.86	1.00	1.00	38.61	38.61	351.59	5.00	22.33
30.00	6.67	0.64	8.43E+06	1.30E+08	0.90	1.50	1.50	57.91	57.91	18.22	3.33	24.96
40.00	5.00	0.48	8.43E+06	1.30E+08	0.94	2.00	2.00	77.22	77.22	13.79	2.50	25.71
60.00	3.33	0.32	8.43E+06	1.30E+08	1.01	3.00	3.00	115.82	115.82	9.28	1.67	26.69
80.00	2.50	0.24	8.43E+06	1.30E+08	1.09	4.00	4.00	154.43	154.43	7.00	1.25	27.37
100.00	2.00	0.19	8.43E+06	1.30E+08	1.17	5.00	5.00	193.04	193.04	5.62	1.00	27.89
120.00	1.67	0.16	8.43E+06	1.30E+08	1.25	6.00	6.00	231.65	231.65	4.70	0.83	28.31
140.00	1.43	0.14	8.43E+06	1.30E+08	1.32	7.00	7.00	270.26	270.26	4.04	0.71	28.67
160.00	1.25	0.12	8.43E+06	1.30E+08	1.40	8.00	8.00	308.87	308.87	3.54	0.63	28.98

Observation: The values in italic formatted numbers correspond (i) to values of the vertex line in Figure 4.2f, page 102, and the upper dashed curve in Figure 4.3, page 106. The values in boldface formatted numbers correspond to the optimized values (row 6) in Table B.1, page 189.

Table B.3 - Optimized model variables (boldface symbols) as obtained from 11 multidimensional optimizations, which consider the boundary adjustments in a two-dimensional in function space, as controlled by specific boundary-expansion factors $f_{B,}$ and nearly ideal light trapping based on shape-optimized nanoparticles; qG_{max} = 23 mA/cm^2.

f_B	s_f	s_b	Δn	Δp	V_{bi}	D_n	D_p	μ_n	μ_p	t_0	λ_{ave}	η
[-]	[cm/s]	[cm/s]	[1/cm^3]	[1/cm ^{3}]	[V]	[cm^2/s]	[cm^2/s]	[cm^2/Vs]	[cm^2/Vs]	[nm]	[nm]	[%]
1.25	1.25	0.12	8.43E+06	1.30E+08	1.40	8.00	8.00	308.87	308.87	*443.89*	*80.00*	*26.16*
1.50	1.25	0.12	8.43E+06	1.30E+08	1.40	8.00	8.00	308.87	308.87	*370.22*	*66.67*	*26.26*
2.00	1.25	0.12	8.43E+06	1.30E+08	1.40	8.00	8.00	308.87	308.87	*277.96*	*50.00*	*26.43*
5.00	1.25	0.12	8.43E+06	1.30E+08	1.40	8.00	8.00	308.87	308.87	*111.67*	*20.00*	*26.96*
9.00	1.25	0.12	8.43E+06	1.30E+08	1.40	8.00	8.00	308.87	308.87	*62.18*	*11.11*	*27.31*
20.00	1.25	0.12	8.43E+06	1.30E+08	1.40	8.00	8.00	308.87	308.87	*28.07*	*5.00*	*27.77*
30.00	1.25	0.12	8.43E+06	1.30E+08	1.40	8.00	8.00	308.87	308.87	*18.75*	*3.33*	*28.01*
40.00	1.25	0.12	8.43E+06	1.30E+08	1.40	8.00	8.00	308.87	308.87	*14.08*	*2.50*	*28.17*
60.00	1.25	0.12	8.43E+06	1.30E+08	1.40	8.00	8.00	308.87	308.87	*9.41*	*1.67*	*28.41*
80.00	1.25	0.12	8.43E+06	1.30E+08	1.40	8.00	8.00	308.87	308.87	*7.06*	*1.25*	*28.58*
160.00	1.25	0.12	8.43E+06	1.30E+08	1.40	8.00	8.00	308.87	308.87	*3.54*	*0.63*	*28.98*

Observation: The values in italic formatted numbers correspond to the values of the vertex line in Figure 4.2f, page 102.

In the first table, f_B constrains the whole set of variables. In the second table, a variable constrained is only adopted for t_0 and λ_{ave}, while the remaining variables are set up with the highest values of the here considered boundary amplification factors, with f_B = 160, similar as in Figure 4.2f, page 102.

APPENDIX B.2 – INCREASED SHORT CIRCUIT DENSITY

As the J_{sc} in our simulated PSCs is similar to the measured short circuit density in (SUN; ASADPOUR; NIE; MOHITE *et al.*, 2015), and the simulated short circuit current densities in (CAI; PENG; CHENG; GU, 2015), in the case with light trapping, the highest optimized efficiency of 27.8% is obtained because of the cell's higher (i) open-circuit voltage, (ii) fill factor, and (iii) short circuit current density. Some authors present cells with an even higher J_{sc} of, e.g., 24.88 mA/cm^2 (JUNG; JEON; PARK; MOON *et al.*, 2019) without light trapping, which is even higher than the highest value J_{sc} of 24.5 mA/cm^2, as presented in (CAI; PENG; CHENG; GU, 2015) for a 400 thick absorber layer and light trapping. Using this higher J_{sc} as fixed setup configuration in an optimization without light trapping (λ_{ave} = 100 nm), and a t_0 = 450 nm, we obtained a maximal efficiency of 28.13% (Table B.4, page 191), because of the V_{0C} and FF increase.

Table B.4 - Optimized model variables (boldface symbols) as obtained from optimizations in the nine-dimensional function space, obtained from eleven optimizations considering specific boundary-expansion factors f_B and an increased short circuit current density of J_{sc} = 24.88 mA/cm^2, which resulted in an optimized PSC of 28.13% without light trapping.

f_B	s_f	s_b	Δn	Δp	V_{bi}	D_n	D_p	μ_n	μ_p	t_0	λ_{ave}	η
[-]	[cm/s]	[cm/s]	[1/cm^3]	[1/cm ^{3}]	[V]	[cm^2/s]	[cm^2/s]	[cm^2/Vs]	[cm^2/Vs]	[nm]	[nm]	[%]
5.00	40.00	3.84	8.43E+06	1.30E+08	1.40	0.25	0.25	9.65	9.65	450.00	100.00	21.66
10.00	20.00	1.92	8.43E+06	1.30E+08	1.40	0.50	0.50	19.30	19.30	450.00	100.00	22.95
20.00	10.00	0.96	8.43E+06	1.30E+08	1.40	1.00	1.00	38.61	38.61	450.00	100.00	24.25
30.00	6.67	0.64	8.43E+06	1.30E+08	1.40	1.50	1.50	57.91	57.91	450.00	100.00	25.00
40.00	5.00	0.48	8.43E+06	1.30E+08	1.40	2.00	2.00	77.22	77.22	450.00	100.00	25.54
60.00	3.33	0.32	8.43E+06	1.30E+08	1.40	3.00	3.00	115.82	115.82	450.00	100.00	26.30
80.00	2.50	0.24	8.43E+06	1.30E+08	1.40	4.00	4.00	154.43	154.43	450.00	100.00	26.83
100.00	2.00	0.19	8.43E+06	1.30E+08	1.40	5.00	5.00	193.04	193.04	450.00	100.00	27.25
120.00	1.67	0.16	8.43E+06	1.30E+08	1.40	6.00	6.00	231.65	231.65	450.00	100.00	27.59
140.00	1.43	0.14	6.02E+04	1.30E+08	1.40	7.00	7.00	270.26	270.26	450.00	100.00	29.15
160.00	1.25	0.12	8.43E+06	1.30E+08	1.40	8.00	8.00	308.87	308.87	450.00	100.00	28.13

Light trapping should increase this simulated efficiency, but presently, there are no FDTD simulations available that show how the J_{sc} increase as a function of t_0 for this cell type. Using a light-trapping scheme this PCE will even increase, but as we do not exactly know to which extent the J_{sc} increases based on a light-trapping scheme, we do not accomplish an optimization using a light-trapping scheme for this cell. This result must be considered as being only approximated, as the used cell in (JUNG; JEON; PARK; MOON *et al.*, 2019) is a FAPI and not a MAPI PSC, and furthermore, as it is a nip-type, but not a pin-type PSC.

APPENDIX B.3 – INFINITE BOUNDARY AMPLIFICATION FACTOR

It is of interest to know how the efficiency of the analyzed pin-type PSE increases if its material properties are nearly infinitely improved, and the absorber layer is reduced to an infinite thin absorber layer, as accomplished by using a f_B = 1000. Such a simulation is of especial importance to identify if the optimization algorithm can eventually get stuck in a lower local maximum rather than the global maximum. In our optimizations, we obtained a high PCE of 32.1 % in Appendix Figure B.1, proving that either, (i) there is no local maximum in our optimization space; or otherwise, (ii) the optimization algorithm is not getting stuck by an eventually existing local maximum in the multidimensional hypercube space.

While we think that the latter is true as the optimization algorithm explores the whole range of constraints for all variables, excluding the absorber layer thickness, as presented in section APPENDIX B.1, the essential conclusion is that it is highly unlikely that with an f_B = 160 our multidimensional optimizations got stuck in a local maximum.

APPENDIX B.4 – EFFECTS NOT CONSIDERED OR SIMPLIFIED

Here, we discuss only for completeness some effects which are not considered in the used simulation model and, therefore, in the present multidimensional optimizations.

Effects related to the band tuning of the single-junction solar cell: The short circuit current density can be increased in many solar cells by use of a correct band gap tuning, which is not considered in the presented solar cell. Our cell presents a fixed effective band

gap of 1.1 eV. In arbitrary single-junction solar cells, this band gap value leads to a theoretical efficiency limit of 32.23 % (RÜHLE, 2016), which is only 0.68 % lower than the highest thermodynamic efficiency limit of 33 %, which demand an ideal band gap of 1.4 eV (RÜHLE, 2016). Therefore, an efficiency increase of 0.68 % might be obtained in future work because of an only slightly improved band gap tuning.

Figure B.1 - Optimized cell efficiency varying the boundary-expansion factor f_B from 1 to 1000 for the whole set of model variables, showing a theoretical efficiency increase to the maximal value of maximal 32.1 % for f_B = 1000.

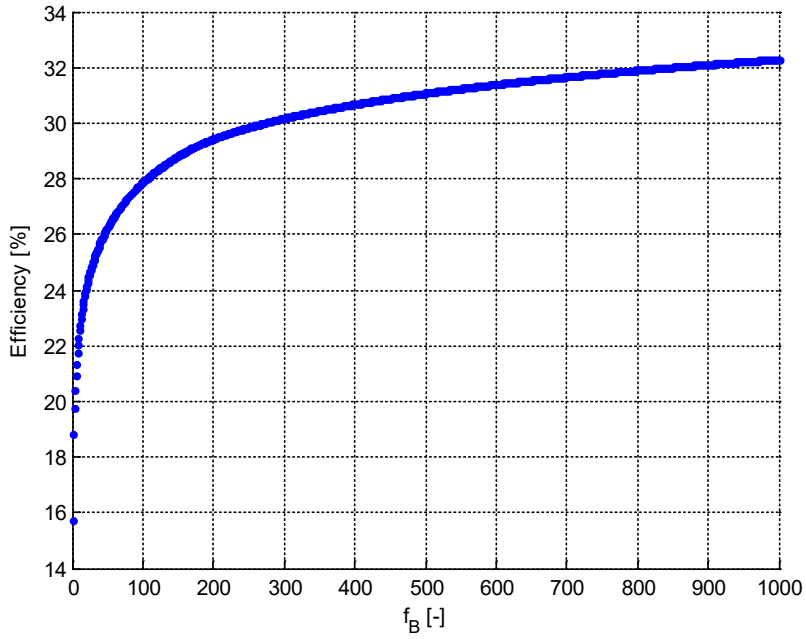

Effects related to the work functions of the front and back contacts: Under one aspect, a further efficiency increase might be obtained by a tuning, which leads to the exact matching of the values of the conduction band work function, of the (i) the back anode contact, and (ii) the electron conduction layer (Figure 3.1a, page 81). Furthermore, an even higher efficiency increase might be obtained by a tuning, which leads to the improved matching of the valence band work functions of the (iii) transparent front contact, and (vi) the hole conduction layer, as the potential difference between these layers is even higher than in the former case. Avoiding those potential losses in the electron and hole-conduction pathways by use of a better material selection of these layers results in a potential tuning that can potentially increase the modeled efficiency further, which is, however, not considered in the present work.

APPENDIX B.5 – IMPROVEMENT NANOPARTICLES

Shape-optimized NPs and further related up-conversion effects of these nanoparticles lead to an improved light trapping effect in comparison to spherical nanoparticles.

Light trapping by plasmonic nanoparticles: In light-trapping structures, nanoparticles (NPs) are utilized to confine resonant photons by an induced coherent oscillation of the electrons in the conduction band of the atoms. These coherent oscillations are localized at the outer surface of the NPs, defining the so-called localized surface plasmon resonance (LSPR). Furthermore, particular NPs can even produce an up-conversion effect of photons, transforming a part of the lower energy photons to photons with higher inherent energy, which match the band gap of the solar cell and lead to the generation of free charge carriers (KAKAVELAKIS; PETRIDIS; KYMAKIS, 2017). While the plasmonic effect leads to the increased absorption of the available photons and its conversion to free charge carriers, the up-conversion effect ensues, additionally, a larger number of convertible photons for the generation of free charges. As an outcome of these improvements, the NPs reduce the solar cell's internal series resistance; and increase its internal shunt or parallel resistance, also known as recombination resistance.

Shape-optimized nanoparticles: In such a purpose, the effectiveness of the plasmonic nanoparticles can be tuned by the NP's constitution, size, shape, and its surrounding environment (KAKAVELAKIS; PETRIDIS; KYMAKIS, 2017) in which the NPs are inserted. For these reasons, we consider that the results as obtained in (CAI; PENG; CHENG; GU, 2015) can be improved further, which, therefore, leads to a higher absorption as a function of the average optical decay length.

However, presently we do not know how the short circuit current density behaves with these improved nanoparticles. We set up in an optimistic simplification a constant short circuit current density of qG_{max} = 23 mA/cm^2, even for very thin absorber layers in Table B.1 to Table B.3, pages 189 to 190. This superior absorption property is obtained as we consider, e.g., that shape-optimized nanoparticles are more effective than spherical nanoparticles

(Kakavelakis et al., 2017). However, the effectiveness of shape-optimized nanoparticles in thiny absorber layers should be qualified by a correct quantification of the J_{sc}, e.g., using an FDTD simulation, as already presented for spherical nanoparticles in (Cai et al., 2015), which is used in the central part of this thesis.

APPENDIX B.6 – FLOWCHART OF THE OPTIMIZATION PROCESS

Figure B.2 - Flowchart of the NLP optimization process, with (i) configuration of the considered boundary-expansion factor; (ii) inner loop, for the validation if the optimization process has the variable value increased, or decreased, beyond its upper or above its lower limits as defined by the boundary-expansion factor f_B; (iii) outer loop, for the calculation of the J-V curve, the MPP-power; and validation of the convergence criterion, which specifies the minimal necessary efficiency gain as being ≥ 0.001%.

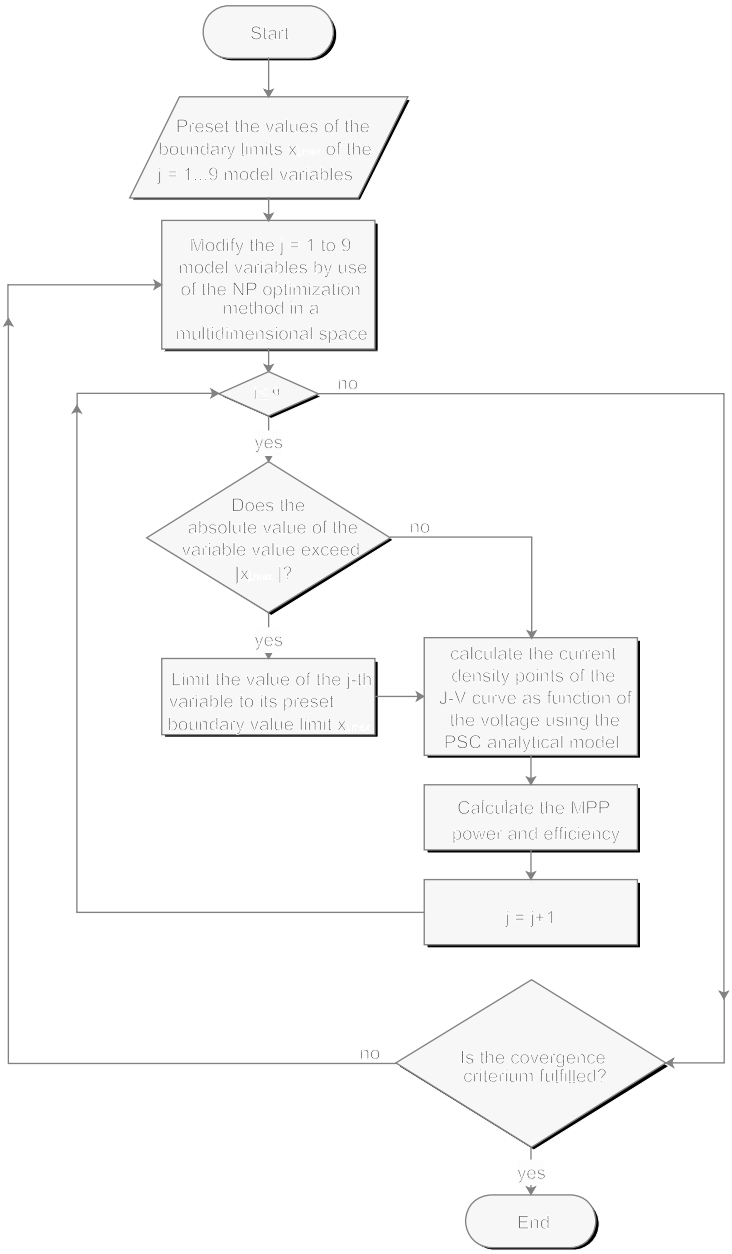

APPENDIX B.7 – STATE-OF-THE-ART MATERIAL PROPERTIES

Considering state-of-the-art properties (section 2.10, page 70), we like to know what the maximal attainable efficiency is, considering a combination of the best measured state-of-the-art material properties, as obtained by different references. In responding to this question, we achieved a simulated PCE of 22.1% (Table B.5), based on the measured short circuit current density and its modeling. We calculate the diffusion coefficients in the table based on the shortest lifetime and the longest diffusion length as measured by direct and, therefore, independent measurement methods. While this efficiency is much higher than the PCE obtained in (SUN; ASADPOUR; NIE; MOHITE *et al.*, 2015), if compared to the state-of-the-art efficiency of 25.2% this PCE is relatively low. We consider that the reason for this low efficiency is that the PCE obtained by authors in sections 2.10.2 to 2.10.8, pages 72 to 78, is much lower than the state-of-the-art efficiency. Furthermore, there is presently no research available, which considers a cell's material properties improvement rather than the PCE as an objective function.

Table B.5 - Measured material properties, as most similar to the ideal material properties, the short circuit current density, and the absorber layer thickness as found by different authors: (rows 1…6) measured properties; (row 7) simulated efficiency based on these measured properties; (row 8)values as used in the simulation in (SUN; ASADPOUR; NIE; MOHITE et al., 2015) (row 9); the optimal values as obtained in (KRATZENBERG; RAMBO; RÜTHER, 2019) (row 9).

Variable specification	s_f	s_b	Δn	Δp	V_{bi}	D_n	D_p	qG_{max}	t_0	λ_{ave}	η
Units	*[cm / s]*	*[cm / s]*	*[1 / cm ^{3}]*	*[1 / cm ^{3}]*	*[V]*	*[cm ^{2} / s]*	*[cm ^{2} / s]*	*[mA/cm^2]*	*[nm]*	*[nm]*	*[%]*
*1 - (Perrakis et al., 2019)**	-	-	-	-	-	-	-	-	*350*	-	*23.7*
*2 - (Wu et al., 2017)**	*2.00E+03*	*2.00E+03*	*1.00E+16*	*1.00E+16*	-	*1.31*	*1.31*	-	-	-	*23.0*
*3 - (Tong et al., 2019)**	*1.00E+02*	*1.00E+02*	-	-	-	***1.31***	***18.04***	-	-	-	*20.4*
*4 - (Green, Martin et al., 2015)**	-	-	-	-	-	-	-	-	-	*250*	*20.0*
*5 - (Zhang et al., 2019)**	-	-	-	-	***1.36***	-	-	-	-	-	*21.4*
*6 - (Wang et al., 2018)**	***1.00E+1***	*2.00E+1*	-	-	-	-	-	-	-	-	*27.0*
7 - ***Combined simulation***	*1.00E+1*	*1.92E+01*	*8.43E+06*	*1.30E+08*	*1.36*	*9.47*	*9.47*	*23.9*	*350*	*100.0*	*22.1*
8 - ***(Sun et al.,2015)****	*2.00E+02*	*1.92E+01*	***8.43E+06***	***1.30E+08***	*0.78*	*5.00E-02*	*5.00E-02*	*23.0*	*450.0*	*100.0*	*15.7*
9 - ***(Kratzenberg et al., 2019)***	*1.25*	***0.12***	*8.43E+06*	*1.30E+08*	*1.40*	*8*	*8*	***23.9***	***160***	***35.56***	*27.6*

*Boldface reference shows simulated values, and the * indicates measured properties and efficiency values as obtained by different authors.*

Row 1, Values obtained in (PERRAKIS; KAKAVELAKIS; KENANAKIS; PETRIDIS et al., 2019);
Row 2, Values obtained in (WU; ZHOU; XING; XU et al., 2017);
Row 3, Based on the diffusion length in (LI; YAN; LI; WANG et al., 2015 and lifetime in (SONG; CUI; WANG; WEI et al., 2015);
Row 4, Values obtained in (GREEN; JIANG; SOUFIANI; HO-BAILLIE, 2015)
Row 5, Values obtained in ((ZHANG; WANG; YUAN; WANG et al., 2019);
Row 6, Values obtained in (WANG; FU; JARIWALA; SINHA et al., 2018);
Row 7, Best measured values used in a simulation which combines these variables;
Row 8, As obtained from the one-dimensional thickness optimization in(SUN; ASADPOUR; NIE; MOHITE et al., 2015), representing the initial conditions;
Row 9, As obtained from a multidimensional optimization for thin absorber layers in (KRATZENBERG; RAMBO; RÜTHER, 2019);

APPENDIX B.8 –DIFFUSION LENGTHS AND LIFETIMES

The model of (SUN; ASADPOUR; NIE; MOHITE *et al.*, 2015) considers the diffusion coefficients ($D_{n,p}$) in its drift-diffusion model (equations (A.31) and (A.32), page 169), or its derived model of the current densities under exposure to light and in the dark, (equations (A.62), page 179; (A.65), page 180), as independent model variables. These variables can be substituted with the equation of the diffusion coefficients (equation (4.2)), and it can be seen that the diffusion coefficients can be increased by two different methods, (i) the increase of the diffusion lengths of charge carriers, or its lifetime reduction. Materials with high diffusion lengths are more interesting, as a doubling of its diffusion length leads to a four-fold increase in the diffusion coefficient. The lifetimes are less important, and they even behave contrarian, as a doubling in the lifetime halves the diffusion coefficients, because the lifetime is localized in the denominator of equation (4.2).

One of the most illustrative presentations of the understanding of the drift-diffusion equation (equations (A.31) and (A.32), page 169) and the related equation of the diffusion length ((A.33) and (A.34), page 169), is presented in [xi], introducing inclusively the derivation of the expression related to the diffusion coefficient. The authors define (i) the diffusion coefficient (equation (4.1), page 108) as the velocity at which charge carriers move, defining, therefore, the quality of the absorber material; (ii) while the minor carrier lifetime of a material (equation (4.2), page 109) is the average time that a charge carrier can spend in an excited state, after the generation of an electron-hole pair, before it recombines, and (iii) the diffusion length (equations (A.33) and (A.34), page 169) is the average distance a charge carrier moves between its generation and its recombination. If its velocity and its lifetime are large enough to move the generated charge carrier by its diffusion length to its charge conduction layer, then the charge carrier does not recombine and increase the PCE of the solar cell.

As to see from equations of the diffusion coefficients (equation (4.1), page 108), the same diffusion coefficients can be obtained by different combinations of lifetimes and diffusion lengths. If, for example, the diffusion length is doubled, then the lifetime must be four times longer to obtain the same diffusion coefficient, and therefore, the same recombination rate. This relationship can be understood as the charge carrier needs a longer

time for its diffusion if a longer distance is to be traveled at the same velocity. Vice-verse if the diffusion length is halved, then the lifetime must be four times shorter.

While e.g. the average diffusion length of electrons (L_n), and its average lifetimes ($\tau_{n,}$), can be determined by direct measurements, as discussed in sections 2.10.4, page 73, its diffusion coefficient $D_{n,}$ which determines the diffusion velocity, must be calculated by indirect measurement, using the measured $L_{n,p}$ and $\tau_{n,p}$. Therefore, the diffusivity ($D_{n,}$) is the unique variable of the equation of the diffusion length (A.33), page 169, which must be determined by indirect measurements.

Misconceptions of the lifetime and diffusion length measurements: If, e.g., the measurements of the lifetime of electrons is accomplished by an indirect rather than a direct measurement method, then the lifetime increases as a function of a rise in the diffusion length. This misconception can be seen by the substitution of (i) a measured diffusion length, and (ii) a considered constant D_n in the equation of the lifetime (eq. (4.2), page 109). In order to avoid such an error, the lifetime should be determined independently of the measured diffusion length, saying by a direct measurement method, as, e.g., presented in (NAGPAL; GUPTA; SRIVASTAVA; JAIN *et al.*, 1990), rather than by an indirect measurement method.

Conversely, in an indirect measurement of the diffusion length, as obtained by (i) a lifetime measurement, and (ii) a considered fixed value of D_n, used in (equation (A.33), page 169), an indirect measurement of the diffusion length by a lifetime measurement, considering constant diffusion coefficients, would also be misleading. In such a case the diffusion length increases as a function of the lifetime increase. Therefore, the diffusion length should also be measured by direct measurement methods, such as, e.g., the SPCM method, as used in (XIAO, 2019) in section 2.10.4, page 73.

APPENDIX C – ACCURACY AND APPLICABILITY

CONTENTS

Here we discuss the applicability and the accuracies comparing different methods for the determination of the short circuit current density, such as (i) the simplest Beer-Lambert method, (ii) the optical transfer matrix method, and (iii) the finite difference time domain method.

APPENDIX C.1 – BEER-LAMBERT LAW

The Beer-Lambert modeling calculates the optical absorption of solar irradiance, and its conversion in free charge carriers, as a function of the absorber layer thickness and its related optical decay length, which is a function of the wavelength. Beer-Lambert optical modeling is used for PSC in (SUN; ASADPOUR; NIE; MOHITE *et al.*, 2015), (ADINOLFI; PENG; WALTERS; BAKR *et al.*, 2017), and (BALL; STRANKS; HÖRANTNER; HÜTTNER *et al.*, 2015), in-between other references. The authors (REN; WANG; SHA; CHOY, 2017), use the Beer-Lambert law also to express an increase of the J_{sc}, for the case with ideal light trapping. For the model as proposed in (SUN; ASADPOUR; NIE; MOHITE *et al.*, 2015), the elaborated simplification of the average optical decay length (λ_{ave}) accounts for the optical decay lengths of the whole solar spectrum. In this formulation, the cell's short circuit current density, of qG_{max} = 23 mA/cm^2 (SUN; ASADPOUR; NIE; MOHITE *et al.*, 2015), is proportional to the total or maximal generation of charge carriers per cell area G_{max} [m^{-2}s^{-1}], which is calculated as calculated with equation (A.19), page 165. In this equation, G_{eff} [m^{-3}s^{-1}] is the effective generation of charge carriers per volume unit of the absorber layer, and λ_{ave} [m] the average optical decay length. A simplified solution of equation (A.19), page 165, is presented in (SUN; ASADPOUR; NIE; MOHITE *et al.*, 2015) by equation (A.20), page 165, as obtained by the integration of (A.19).

For the case without light trapping, the material-specific properties, defined as G_{eff} = 1.4356 x 10^{13} cm^{-3}s^{-1}, λ_{ave} = 100 nm and J_{sc} were validated in (SUN; ASADPOUR; NIE; MOHITE *et al.*, 2015) with the OTM modeling method. Additionally, the authors validated J_{sc} by measurements. The Beer-Lambert model considers that approximately 99% of the light is absorbed in the forward direction, while 1% is reflected on the back layer, as can be read from Figure 3.1, page 81. For example, if λ_{ave} = 100 nm and t_0 = 450 nm, this 1% corresponds to the part of the charge carrier generation curve, which appears for penetration depths beyond t_0 (x > 450 nm) in this figure.

APPENDIX C.2 – OPTICAL TRANSFER MATRIX METHOD

A simulation method that presents a higher resolution than the Beer-Lambert model in the modeling of the short circuit current density is the cavity-modeling based on the OTM modeling. In this method, the photocurrent density is calculated as a function of the (i) extinction coefficient, and (ii) the refractive index, which in its conjunction, are conceived as the complex refractive index. Both coefficients are functions of the wavelength of the solar irradiance. The modeling of the short circuit current density without light trapping, as used in our model, was validated in (SUN; ASADPOUR; NIE; MOHITE *et al.*, 2015) by (i) the OTM method and (ii) the measurements with a manufactured solar cell, which resulted to low deviations of only 0.1%. Exact values of the extinction coefficient and the refractive index for the PSC as used in (SUN; ASADPOUR; NIE; MOHITE *et al.*, 2015) are also validated in (JIANG; GREEN; SHENG; HO-BAILLIE, 2015).

APPENDIX C.3 – FINITE-DIFFERENCE TIME-DOMAIN MODELING

In comparison to the OTM model, an even higher-resolution simulation method for the determination of a correct J_{sc} is obtained with the finite-difference time-domain (FDTD) modeling (CAI; PENG; CHENG; GU, 2015). In comparison to the Beer-Lambert and OTM modeling, this third simulation method presents possibly the highest accuracy, for the modeling of the short circuit current density, because of its high spatial resolution using a finite-element method (FEM). The FDTD is a numerical method of computational electrodynamics, which uses time-dependent partial Maxwell differential equations in the discretization of a very small but finite-volume section of the absorber layer and the method pertains to the group of finite-difference modeling, as mostly known from the FEM. The objective of the FDTD is to model the cell's absorption, and especially its increase, because of light trapping effects, which is accomplished over a wide frequency spectrum of the electromagnetic solar irradiance. In the case of light trapping with plasmonic nanoparticles, it simulates the omnidirectional scattering of light coming from a unidirectional light source, an effect inherent to the nanoparticles when inserted into the absorber layers of a PSC. (CAI; PENG; CHENG; GU, 2015) accomplished an FDTD modeling for a PSC, which presents the same absorber material ($CH_3NH_3PBI_3$) as used in (SUN; ASADPOUR; NIE; MOHITE *et al.*,

2015), and therefore, its simulation lead in a very similar short circuit current density considering a cell with t_0 = 400 nm without light trapping. As a result, we consider a high accuracy for our optimizations, using the adopted current densities as simulated in (CAI; PENG; CHENG; GU, 2015) for the cases with and without light trapping.

APPENDIX C.4 - IMPROVED ABSORBTION AND LIGHT TRAPPING

In our optimizations in section 4.2, page 105, we use the same $J_{sc}(t_0)$ as a function of t_0 as obtained in (CAI; PENG; CHENG; GU, 2015) for light trapping with spherical nanoparticles. The authors show that efficient light trapping using spherical nanoparticles increases the cell's J_{sc} for a large range of absorber layer thicknesses of $t_0 \approx 50 \ldots 450$ nm. For t_0 = 50 nm, the J_{sc} decreases to 11 mA/cm^2, and an almost complete restoration of the cell's short circuit current density is obtained by light trapping. Considering that, because of improved light trapping, a full restoration of the J_{sc} can be obtained even for lower absorber layer thicknesses; higher efficiencies are the result as presented in (Appendix Table B.1 to Table B.3, pages 189 to 190). E.g., an efficiency of 28.4% can be obtained for a cell with an absorber layer thickness of ~ 10 nm with f_B = 60 in Appendix Table B.3, page 190. These results are based on a f_B constrained absorber layer thickness.

In a more conservative setup of our optimizations, in section 4.2, page 105, we analyzed several absorber layer thicknesses. Our ideal cell design, which presents a high efficiency of 27.6% we obtained for a higher minimum value of t_0 = 160 nm, using the corresponding J_{sc} as simulated in (CAI; PENG; CHENG; GU, 2015) for spherical plasmonic nanoparticles. The adopted λ_{ave}, we obtained by the equality constraint in equation (3.10), page 87. As a result, we adopt in our modeling the same relationship in-between λ_{ave} and t_0 as presented in (SUN; ASADPOUR; NIE; MOHITE *et al.*, 2015), while the short circuit current density ($J_{sc} = q\ G_{max}$) is the same as obtained by FDTD simulations in (CAI; PENG; CHENG; GU, 2015), getting, consequently, carefully selected setup conditions in our multidimensional optimizations, which do not result in overestimations of the optimized PCE.

In a f_B constrained optimization, where the whole set of variables is improved with the considered maximal f_B = 160, as defined by equations (3.1) to (3.9), page 83, we actually obtained an m – factor of 5.5, analyzing the gradient of the vertex line in Figure 4.2f, page 102. This factor is higher than the defined m = 4.5 in (SUN; ASADPOUR; NIE; MOHITE *et*

al., 2015) for a low-efficiency PSC of 15.7%. However, this *m* factor difference results only in a very small efficiency difference in a fully optimized PSC. We obtained a maximal PCE of 27.62% with $m = 4.5$, and 27.82 % with $m = 5.5$.

APPENDIX D – COMPUTER SIMULATION CODES

CONTENTS

Here we present two different simulation examples using the Maple™ and the Matlab™ program, which result in the J-V curves of the considered non-optimized and optimized cell. The first example (section Appendix D.1) considers nearly ideal light trapping in an extra thin absorber layer, and the second example (section Appendix D.2, page 211) considers the optimized cell with a 160 nm thick absorber layer, which results in Figure 4.5, page 115.

APPENDIX D.1 – Maple™ for ideal light-trapping

Considering ideal light trapping in extreme thin absorber layers, the PSC's efficiency increases from 15.7 % to 29 %, as also presented in Appendix Table B.1, page 189. We show in this section, by a simple simulation in the program Maple™, that PSCs of such a high efficiency can be obtained if its absorber layer thickness is sufficiently reduced and its material properties are adequately improved. Especially its absorption by light-trapping is meliorated, showing nearly ideal light trapping. Such an improved light trapping can eventually be configured by the use of shape-optimized nanoparticles, which improves the light trapping character of as related to the use of spherical NPs, where the latter was adopted in sections 3 and 4, pages 79 and 98. The simulations are accomplished by Maple equations (D.1) to (D.7), pages 208 to 208, and the simulated curves are presented in Appendix Figure D.1, page 210.

Non optimized solar cell with the set-up conditions: First, we specify the complete equation for the current densities under exposition to light, considering solely optical recombination J_{photo} by equation (D.1). The J-V curve, when the solar cell is localized in the dark J_{dark} (D.7), page 208, is similar in comparison to the J-V curve of the forward-current of a diode. This curve is used to simulate the recombination effects of the solar cell. The superposition of J_{photo} and J_{dark} (equation (D.7)) results in the J-V curve that characterizes a solar cell by the current J_{light}. The terms defined in equation (D.4), we already introduced by equation (A.10), page 161, presenting a dimensionless form of the expression of the electric field. In (D.7), the used constants, saying (i) the electric charge and (ii) the Boltzmann constant, are defined. The maximal generation of charge carriers, as related to the absorption of the cell, and the cell's temperature are defined as fixed values. The equation (D.12), page

209, sets up the nine model variables, saying the eight considered material properties and the absorber layer thickness for the solar cell as optimized in (SUN; ASADPOUR; NIE; MOHITE *et al.*, 2015), which are here utilized as initial in a multidimensional optimization. As the different variables were specified in SI units, the current and power densities are converted in values of [mA/cm^2], and [mW/cm^2] by equation (D.13). The plotting of the two current density curves, and the power density curve is specified by (D.14) to plot Figure D.1, page 210. The non-optimized cell results in a power density of 15.7 W/cm^2, an efficiency of 15.7%

Optimized solar cell: The equations (D.9) to (D.12) define the equation of the optimized solar cell configuration ($J_{light\text{-}opti}$), using the same expressions as already specified in (D.1) to (D.7). The nine optimized variables, as obtained by the multidimensional optimization, are defined by equation (D.12). Finally, the normalization and the plotting of the optimized curves are specified by equations (D.13) and (D.14). The optimized cell results in a power density of 29 W/cm^2, an efficiency of 29%.

$$J_{photo} := qG_{\max}\left(\frac{\dfrac{1-e^{V''-\frac{t_0}{\lambda_{ave}}}}{V''-\frac{t_0}{\lambda_{ave}}}-\dfrac{Dn}{t_0 s_f}}{\dfrac{e^{V''}-1}{V''}+\dfrac{Dn}{t_0 s_f}}-\dfrac{\left(\dfrac{1-e^{V''+\frac{t_0}{\lambda_{ave}}}}{V''+\frac{t_0}{\lambda_{ave}}}-\dfrac{Dp}{t_0 s_b}\right)e^{-\frac{t_0}{\lambda_{ave}}}}{\dfrac{e^{V''}-1}{V''}+\dfrac{Dp}{t_0 s_b}}\right) \tag{D.1}$$

$$J_{dark} := \left(\frac{q\,s_b\,\Delta p}{\dfrac{e^{V''}-1}{V''}+\dfrac{Dp}{t_0 s_b}}+\frac{q\,s_f\,\Delta n}{\dfrac{e^{V''}-1}{V''}+\dfrac{Dn}{t_0 s_f}}\right)\left(e^{\frac{v}{V_t}}-1\right) \tag{D.2}$$

The complete current density model of the cell when exposed to light :

> $J_{light} := J_{dark} + J_{photo};$ (D.3)

$$J_{light} := \left(\frac{q\,s_b\,\Delta p}{\dfrac{e^{V''}-1}{V''}+\dfrac{Dp}{t_0 s_b}}+\frac{q\,s_f\,\Delta n}{\dfrac{e^{V''}-1}{V''}+\dfrac{Dn}{t_0 s_f}}\right)\left(e^{\frac{v}{V_t}}-1\right) \tag{D.4}$$

$$+q\,G_{\max}\left(\frac{\dfrac{1-e^{V''-\frac{t_0}{\lambda_{ave}}}}{V''-\frac{t_0}{\lambda_{ave}}}-\dfrac{Dn}{t_0 s_f}}{\dfrac{e^{V''}-1}{V''}+\dfrac{Dn}{t_0 s_f}}-\dfrac{\left(\dfrac{1-e^{V''+\frac{t_0}{\lambda_{ave}}}}{V''+\frac{t_0}{\lambda_{ave}}}-\dfrac{Dp}{t_0 s_b}\right)e^{-\frac{t_0}{\lambda_{ave}}}}{\dfrac{e^{V''}-1}{V''}+\dfrac{Dp}{t_0 s_b}}\right)$$

Unitless variable V' which stands for the electric filed as function of the terminal voltage v and the thermal voltage

> $V'' := q\cdot\frac{v-V_{bi}}{k_b\cdot T};\ V_t := \frac{k_b\cdot T}{q};$ (D.5)

$$V'' := \frac{q\,(v-V_{bi})}{k_b\,T}$$

$$V_t := \frac{k_b\,T}{q}$$

The used constants expressed in SI units :

> $q := 1.6021765\cdot 10^{-19};\ k_b := 1.38064852\cdot 10^{-23};$ (D.6)

$$q := 1.602176500\ 10^{-19}$$

$$k_b := 1.380648520\ 10^{-23}$$

Variables considered as fixed :

> $G_{\max} := 1.435547207\cdot 10^{21};\ T := 300.56;$ (D.7)

$$G_{\max} := 1.435547207\ 10^{21}$$

$$T := 300.56$$

A set of improvable state – of – the – art cell parameters and material properties as used by Sun et al. 2015 :

> $V_{bi} := 0.78; t_0 := 450 \cdot 10^{-9}; Dn := 0.05 \cdot 10^{-4}; Dp := Dn; \lambda_{ave} := 100 \cdot 10^{-9}; s_f := 2; s_b := 0.192; \Delta n := 8.43 \cdot 10^{6}; \Delta p := 1.3 \cdot 10^{8};$ (D.8)

$$V_{bi} := 0.78$$

$$t_0 := \frac{9}{20000000}$$

$$Dn := 0.000005000000000$$

$$Dp := 0.000005000000000$$

$$\lambda_{ave} := \frac{1}{10000000}$$

$$s_f := 2$$

$$s_b := 0.192$$

$$\Delta n := 8.43000000\ 10^{6}$$

$$\Delta p := 1.300000000\ 10^{8}$$

The optimized current model use identical equations as the non – optimized current model :

> $J_{photo\_opti} := q\, G_{\max} \left(\frac{\frac{1 - e^{V'' - \frac{t_0}{\lambda_{ave}}}}{V'' - \frac{t_0}{\lambda_{ave}}} - \frac{Dn}{t_0 s_f}}{\frac{e^{V''} - 1}{V''} + \frac{Dn}{t_0 s_f}} - \frac{\left(\frac{1 - e^{V'' + \frac{t_0}{\lambda_{ave}}}}{V'' + \frac{t_0}{\lambda_{ave}}} - \frac{Dp}{t_0 s_b} \right) e^{-\frac{t_0}{\lambda_{ave}}}}{\frac{e^{V''} - 1}{V''} + \frac{Dp}{t_0 s_b}} \right);$ (D.9)

> $J_{dark\_opti} := \left(\frac{q\, s_b \Delta p}{\frac{e^{V''} - 1}{V''} + \frac{Dp}{t_0 s_b}} + \frac{q\, s_f \Delta n}{\frac{e^{V''} - 1}{V''} + \frac{Dn}{t_0 s_f}} \right) \left(e^{\frac{v}{V_t}} - 1 \right);$ (D.10)

> $J_{light\_opti} := J_{photo\_opti} + J_{dark\_opti};$ (D.11)

>

Optimized cell parameters and material properties :

> $V_{bi} := 1.4; t_0 := 4.07 \cdot 10^{-9}; Dn := 8 \cdot 10^{-4}; Dp := Dn; \lambda_{ave} := 0.625 \cdot 10^{-9}; s_f := 1.25 \cdot 10^{-2}; s_b := 0.12 \cdot 10^{-2}; \Delta n := 8.43 \cdot 10^{6}; \Delta p := 1.3 \cdot 10^{8};$ (D.12)

$$V_{bi} := 1.4$$

$$t_0 := 4.070000000\ 10^{-9}$$

$$Dn := \frac{1}{1250}$$

$$Dp := \frac{1}{1250}$$

$$\lambda_{ave} := 6.250000000\ 10^{-10}$$
$$s_f := 0.01250000000$$
$$s_b := 0.001200000000$$
$$\Delta n := 8.43000000\ 10^{6}$$
$$\Delta p := 1.300000000\ 10^{8}$$

Normalization of the obtained currnt densities to the unit $\left[\frac{mA}{cm^2}\right]$

and calculation of the power curves :

> $J_{light} := \frac{J_{light}}{10} : J_{dark} := \frac{J_{dark}}{10} : J_{light\_opti} := \frac{J_{light\_opti}}{10} : J_{dark\_opti} := \frac{J_{dark\_opti}}{10} : P_{light} := J_{light} \cdot v : P_{light\_opti} := J_{light\_opti} \cdot v :$ (D.13)

Plotting of the non-optimized and optimized solar cell curves :

> $plot([-J_{light}, -J_{dark}, -P_{light}, -J_{light\_opti}, -J_{dark\_opti}, -P_{light\_opti}], v = 0..1.5, linestyle = [dashdot, dash, dot, dashdot, dash, dot], view = [0..1.5, -30..30], axis = [gridlines = [10, color = grey]])$ (D.14)

Figure D.1 – J-V curves under exposition to light (dash-dotted curves), and in the dark (dashed curves); and power density curves (dotted curves) of a simulated cell with setup (curves with the lower voltage) and nearly ideal light trapping and improved material properties (curves with the higher voltage), as obtained with the Maple™ simulation, leading for the optimized cell to a PCE of 29 % (figure is similar as in Figure 4.5, on page 115). The abscissa specifies the terminal voltage, the left-side of the ordinate is the current density, while its right side shows the power density.

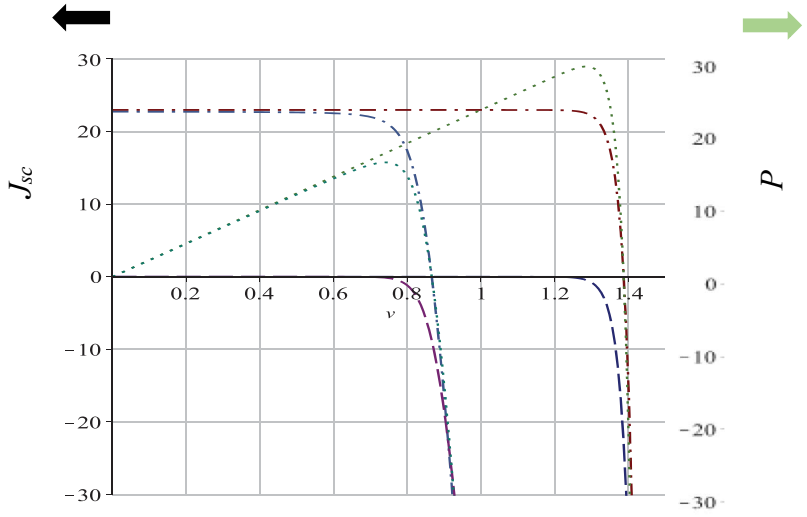

Observation: The simulation adopts almost the identical symbols as shown in the text, and only the variable *V'*, (equation (A.10), page 161) is here substituted by *V"*, and the variable *V* in this equation is substituted by *v*, because of Maple™ format convenience. Material properties are expressed in SI units, and the axis of the obtained curves are converted to the units as adopted in (SUN; ASADPOUR; NIE; MOHITE *et al.*, 2015).

APPENDIX D.2 – MATLAB SIMULATION OF BEST DESIGN

This simulation program was adapted from the Supplementary Information presented in (SUN; ASADPOUR; NIE; MOHITE *et al.*, 2015). The simulation uses an identical formulation, as presented in section , page 206. The setup conditions of the non-optimized solar cell are also the same. However, the variable setup conditions of the optimized solar cell are adopted as used obtained from the multidimensional optimizations presented in sections 3 and 4, pages 79 and 98, using light trapping with spherical nanoparticles, as based on the results obtained in (CAI; PENG; CHENG; GU, 2015), which results in a slightly lower PCE.

```
% ************************************************************
% Simulation of:
% (i) the cell as optimized in (Sun et al., 2015),
% and (ii) the selected PSC with t0 = 160 nm and light trapping
% (Adapted from Supplementary Information in (Sun et al. 2015))
% ************************************************************
clear all, close all;

qgmax       = 23; % mA/cm2

VdataH      = 0:0.0001:1.5;  % terminal voltage
vd_         = VdataH;

%% ************************************************************************
% the values, equations and curves as obtained in Sun et al.(2015):
% ************************************************************************
lambda  =  100;       % nm
Dnp     =  0.05;      % cm2s-1
kt      =  0.0259;  % Boltzmann constant x temperature;
vbi     =  0.78;    % [V] Buitl in voltage,
to      =  450;     % [nm] Cell thickness,
sf      =  2e2;     % the front surface recombination velocity,
sb      =  19.2;    % the back surface recombination velocity,
jfo     =  2.7 * 10^-13; % recombining current at the front surface;
jbo     =  4.0 * 10^-13; % recombining current at the back surface;
m       =  to/lambda;
bf      =  Dnp/to/1e-7/sf;
```

```
bb      =  Dnp/to/1e-7/sb;
y       =  (vd_-vbi)./kt; % V'
alphaf  =  1./((exp(y) -1)./y+bf);
alphab  =  1./((exp(y) -1)./y+bb);
B       =  alphab .* ((1-exp(y+m))./(y+m) -bb);
A       =  alphaf .* ((1-exp(y-m))./(y-m) -bf);
jphoto_  =  qgmax * (-B.*exp(-m)+A);

 %1e10 here just make it easy to converge
jdark_  = (exp(vd_/kt) -1).*(alphaf*jfo+alphab*jbo); % /1e10;
jlight_ = jphoto_ + jdark_;
Power__  = -jlight_.* vd_;
Power_   = Power__(1:8668);
vd_P     = vd_(1:8668);
[Pmpp_,amostra_] = max(Power_);

plot(vd_P, Power_,'r-.','linewidth',2); grid on, hold all,
plot(vd_, -jlight_,'b-.','linewidth',2),
plot(vd_, -jdark_,'k-.','linewidth',2), hold all, axis([0 1.4 -5 25]);%
xlabel('Terminal Voltage [V]','fontsize',11), ylabel('Current [mA/cm^2],
Efficiency [%]','fontsize',11),grid on
Isc_sun = max(-jlight_)

%%*********************************************************************
% The new U-I curve for the optimized model:
% *********************************************************************
clear alphaf alphab jfo jbo vbi to sf sb delta_p delta_n B A jdark
qgmax  = 23.9;    % [mA/cm2]; short circuit current density (q Gmax), as
obtained by FDTD simulations in (Cai et al., 2015)
m      = 5.5;     % [-] as used in (Sun et al., 2015) for ~ 1 % reflection
losses at the back reflector,
Dnp    = 8 ;      % [cm2s-1] diffusion coefficients, as obtained by the
multidimensional optimization,
to     = 160;     % [nm] Cell thickness, as obtained for high efficiency
and low Pb content,
lambda = to / m;  % [nm] as obtained by the constraints' setup,
vbi    =  1.4;    % [V] Built in voltage, as obtained by the
multidimensional optimization,
sf     =  1.25;   % [cm/s] front surface recombination velocity, as
obtained by the multidimensional optimization,
sb     =  0.12;   % [cm/s] back surface recombination velocity, as obtained
by the multidimensional optimization,

% The terminal voltage:
VdataH     = 0:0.0001:1.5;
vd         = VdataH;
kt      =  0.0259;      % Boltzmann constant x temperature;
delta_n =  8.43 * 10^6; % [cm^-3],
delta_p =  1.3 * 10^8;  % [cm^-3],
q       =  1.60217662*10^-22; % [mA s]
jfo     =  q * sf * delta_n;  % [mA/cm^2]
jbo     =  q * sb * delta_p;  % [mA/cm^2]
bf      =  Dnp/to/1e-7/sf;
bb      =  Dnp/to/1e-7/sb;
y       =  (vd-vbi)./kt; % named V' in (Sun et al., 2015)
E       =  (vd-vbi)./to;
alphaf  =  1./((exp(y) -1)./y+bf);
alphab  =  1./((exp(y) -1)./y+bb);
```

```
B       =  alphab .* ((1-exp(y+m))./(y+m) -bb);
A       =  alphaf .* ((1-exp(y-m))./(y-m) -bf);
jphoto  =  qgmax * (-B.*exp(-m)+A);

jdark  = (exp(vd/kt) -1).*(alphaf*jfo+alphab*jbo); % /1e10;
jlight = jphoto + jdark;
Power_c  = -jlight.* vd;
Power    = Power_c(1:length(vd));
vd_r     = vd(1:length(vd));
plot(vd_r, Power,'r-','linewidth',2);

[AX, s1h1, s1h2] = plotyy(vd, -jlight,vd, -jdark);
set(get(AX(1), 'Ylabel'), 'String', 'Current density J
[mA/cm^2]','fontsize',11);
set(get(AX(2), 'Ylabel'), 'String', 'Power density P
[mW/cm^2]','fontsize',11);

%sig1 color blue
sig1col = [0 0 1];
%sig1log color black
sig1logcol = [0 0 0];
%style the plot
set(s1h1,'Color',sig1col,'LineWidth',2);
set(s1h2,'Color',sig1logcol,'LineWidth',2);
set(AX(1),'YColor',sig1logcol);
set(AX(2),'YColor',sig1logcol);
set(AX(1),'YLim',[-30 30])
set(AX(1),'YTick',[-30:5:30])
set(AX(2),'YLim',[-30 30])
set(AX(2),'YTick',[-30:5:30])
xlabel('Terminal Voltage [V]','fontsize',11)

[Pmpp,amostra] = max(Power);
legend('P','J_l_i_g_h_t','J_d_a_r_k','P_m_a_x','J_l_i_g_h_t_-
_m_a_x','J_d_a_r_k_-_m_a_x','non optim.','optim.')

plot(vd_(amostra_),Pmpp_,'k*');
plot(vd(amostra),Pmpp,'ko');
plot(vd(amostra),-jlight(amostra),'ko');
plot(vd(amostra),-jdark(amostra),'ko');
plot(vd_(amostra_),-jlight_(amostra_),'k*');
plot(vd_(amostra_),-jdark_(amostra_),'k*');
```

ENDNOTES

[i] The T_{80} time defines the lifetime in which a solar cell or photovoltaic module loses 20 % of its MPP power, as specified for a solar irradiance of 1000 W/m^2 and air mass of AM 1.5.

[ii] (a) In heterojunction solar cells a large number of recombination centers appear, as a consequence of the anisotropic crystal structure at the termination of the semiconductors crystals involved by reason of the use of distinct materials for the n-type, the p-type and the i-type layers, which own dissimilar crystal structures. These effects lead to recombination effects on the front and back transition surfaces between the perovskite absorber and it's charge conduction layers and result to a significant impact on the behavior of the IV-curve of semiconductor devices. The dangling bonds at these transition surfaces introduce a large number of electrically active states, which result in higher defect densities, leading therefore, to a reduction of the open-circuit V_{0C} and maximum power point voltages V_{MPP} (ELUMALAI; UDDIN, 2016). Furthermore, these transition surfaces tend to contain more impurities and defects, which are acquired e.g. in silicon solar cells during the fabrication process, when devices are exposed to air and humidity(VAN ZEGHBROECK, 2004).
(b) Electronically active states capture holes and electrons and are, likewise, existent at the transition surface between single perovskite crystals within the absorber layer.
(c) Another recombination effect related to the transition between the charge conduction layers and the absorber layer occurs by reason of holes, which present a lower energy, and electrons, which present a higher energy than the blocking barriers, designed for the charge conduction layers in a PSC (Figure 3.1a, page 80), which lead also to the recombination current densities J_f and J_b.

[iii] In PSC the loss of iodine at the perovskite $CH_3NH_3PbI_{3-x}Cl_x$ crystal termination or crystal surface leads to vacancy sites, resulting in a local positive charge attached to the Pb-atom. This local inhomogeneity of the crystal structure, therefore, represents a positive coulomb trap of electrons, also called a trap state (NOEL; ABATE; STRANKS; PARROTT *et al.*, 2014).

iv Thermal equilibrium of a semiconductor is a state where no external energy is added to this semiconductor due to irradiance, voltage or temperature.

[v] PV-Education, Surface Recombination velocity, http://www.pveducation.org/pvcdrom/surface-recombination.

[vi] As the energy potentials and band gaps of the organic charge conduction layers have to be adjusted in accordance to the configured band gap of the perovskite absorber layer (Figure 3.1a, page 109), a correct matching of the band gap of these layers also increases the built-in voltage (SUN; ASADPOUR; NIE; MOHITE *et al.*, 2015).

[vii] Within the solar cell, both the drift and the diffusion current densities of charge carriers are always equal, determining therefore, different equilibrium conditions. In the dark the drift and the diffusion current densities are in a specific internal equilibrium, producing thus only the built-in electrical field, if no external voltage is applied to the cell's terminals. Due to the production of additional charges under light exposure, the number of positive charges in the p-type layer and the number of negative charges in the n-type layer are further increased, and a new equilibrium of the drift diffusion current densities is produced. If under this condition, a load is connected to the cell's terminals, an external drift current of electrons and holes defines, together with the internal drift current densities, another specific equilibrium.

[viii] The net electric field represents, by reason of the superposition of the internal and the external electric fields, a barrier for the diffusion current density. Whereas the internal electric field depends on the equilibrium of charge carrier concentrations of the solar cell, the external field is defined by the value of the cell's terminal voltage. If the cell is exposed to light, the external field is enhanced by the production of electrons within the n-type and holes within the p-type semiconductor.

[ix] The net electric field of a solar cell is defined by the superposition of its internal and external electric fields. However, numerical simulations show that the net electric field in PSC is mainly defined by its internal field, and therefore, the use of the internal field for the replacement of the net electric field represents a good approximation. This concludes that the external electric field, which is a function of the photo-generated carriers, does not significantly perturb the net electric filed as discussed in (SUN; ASADPOUR; NIE; MOHITE *et al.*, 2015), citing (NIE; TSAI; ASADPOUR; BLANCON *et al.*, 2015).

[x] Observation: The boundary equations of the Poisson equation ((A.23), page 196, and (A.24)) are both defined for the same variable, which is the electrostatic potential (ϕ), which facilitates therefore, the solution of this second-order differential equation. However, in the case of the drift diffusion differential equation, the first boundary equation specifies the electron density (n) ((A.37), page 200), while the second boundary equation specifies the current density of electrons (J_n) ((A.39), page 200). Thus, the solution of the general equation of $J_{n\text{-}photo}$ and $J_{n\text{-}dark} = J_f$ with known integration constants is obtained differently, resulting in an extended equation

manipulation. The same consideration is also valid for drift diffusion equations for holes and its boundary conditions, finding the hole generation current densities $J_{p\text{-}photo}$ and $J_{p\text{-}dark} = J_b$ (Figure 3.1a, page 109). For the recombination current density, the derivation process is repeated under consideration of $G(x) = 0$, using the drift diffusion equation in (A.35), page 199, and (A.36), instead of (A.31), page 198, and (A.32).

[xi] https://www.pveducation.org/pvcdrom/pn-junctions/diffusion accessed on 24.05. 2020.